DEFORMATION MECHANISMS IN CALCIUM CONTAINING MAGNESIUM ALLOYS



UNIVERSITY OF BIRMINGHAM

by

MOHAMMED WAKIB SAID

A thesis submitted to the University of Birmingham for the degree of DOCTOR OF PHILOSOPHY

School of Metallurgy and Materials

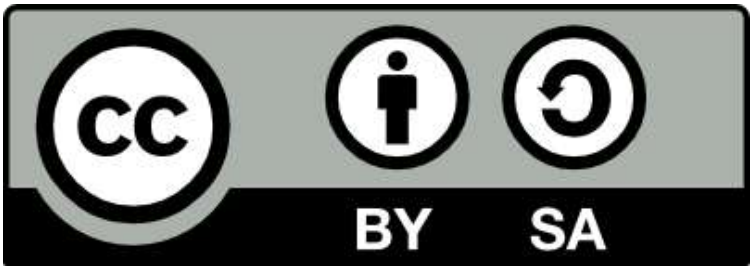
College of Engineering and Physical Sciences

University of Birmingham

September 2024

UNIVERSITY OF BIRMINGHAM

University of Birmingham Research Archive
e-theses repository



This unpublished thesis/dissertation is under a Creative Commons Attribution-ShareAlike 4.0 International (CC BY-SA 4.0) licence.

You are free to:

Share — copy and redistribute the material in any medium or format

Adapt — remix, transform, and build upon the material for any purpose, even commercially.

The licensor cannot revoke these freedoms as long as you follow the license terms.

Under the following terms:



Attribution — You must give appropriate credit, provide a link to the license, and indicate if changes were made. You may do so in any reasonable manner, but not in any way that suggests the licensor endorses you or your use.



ShareAlike — If you remix, transform, or build upon the material, you must distribute your contributions under the same license as the original.

No additional restrictions — You may not apply legal terms or technological measures that legally restrict others from doing anything the license permits.

Notices:

You do not have to comply with the license for elements of the material in the public domain or where your use is permitted by an applicable exception or limitation.

No warranties are given. The license may not give you all of the permissions necessary for your intended use. For example, other rights such as publicity, privacy, or moral rights may limit how you use the material.

Unless otherwise stated, any material in this thesis/dissertation that is cited to a third party source is not included in the terms of this licence. Please refer to the original source(s) for licencing conditions of any quotes, images or other material cited to a third party.

Preface

This dissertation is submitted for the degree of Doctor of Philosophy at the University of Birmingham. It describes the research carried out in the Department of Metallurgy and Materials Science in both Birmingham and Cambridge between October 2020 and September 2024, under the supervision of Dr. David M. Collins. Except where reference is made to the work of others, the contents of this dissertation are entirely original and has not been a result of collaboration. No part of the work described here has been or is currently being submitted for the purpose of gaining academic qualification at this or any other institute of higher learning. This dissertation does not exceed 50,000 words in length.

Abstract

This study investigates the micromechanical origins of enhanced formability in Ca-containing Mg alloys (ZXK: Mg-Zn-Ca and AZX: Mg-Al-Zn-Ca) compared to commercial AZ31, focusing on texture-mediated deformation mechanisms. Through in-situ synchrotron X-ray diffraction, HR-EBSD, and VPSC modelling, twinning, slip activation, lattice strains were explored. The study included strain rate sensitivity (SRS) under varying temperatures (25–250°C) and loading directions (RD/TD), with conditions chosen to guide the suitability for sheet forming processes.

Texture weakening in the Ca-containing alloys was strongly inferred to occur via a solute-driven mechanisms: The weaker basal texture in ZXK compared to AZX gives strong evidence for Ca segregation to grain boundaries during recrystallization, suppressing the basal texture intensity in ZXK, while in AZX, Al-Ca intermetallic formation likely reduced solute Ca availability, resulting in a stronger basal texture. This texture weakening promoted directional yield anisotropy, also evidenced in lattice strains, with ZXK exhibiting twinning-dominated plasticity under TD loading (evidenced by sigmoidal flow curves and lattice strain inflections in the (0002) plane). HR-EBSD confirmed twin nucleation at grain boundaries, driven by c-axis alignment and local stress concentrations.

Dynamic strain ageing (DSA) observed by serrated flow during tensile testing was seen at elevated temperatures (150–250°C). In AZ31, DSA was linked to Al/Zn solute pinning, while in ZXK (0 Al wt.%), Ca solutes likely mediated dislocation pinning. AZX showed attenuated DSA due to Al-Ca precipitation, producing weaker serration amplitudes, corroborating the Al-Ca precipitation effect on solute content in AZX.

Strain rate sensitivity analysis highlighted the anomalous behaviour of ZXK: At room temperature, its high SRS (primarily attributed to a better ratio/combination of basal/prismatic slip, but also noted differences in prismatic plane lattice strain redistribution) correlated with improved formability, while a sharp SRS reduction at 150°C aligned with reported warm-forming ductility minima. This was linked to temperature-dependent solute drag on dislocations, with dislocation recovery mechanisms dominating

at 250°C.

VPSC modelling predicted enhanced basal slip activity in Ca-containing alloys at room temperature (versus prismatic slip dominant in AZ31), with ZXK exhibiting doubled twin volumes under TD loading validated by EBSD, while elevated temperatures activated pyramidal $\langle c+a \rangle$ slip and reduced twinning dependence. These results establish how Ca-induced texture modifications govern competing deformation modes, providing a microstructure-property framework for further investigation of forming relevant behaviour.

Acknowledgements

Firstly, I am grateful for the financial support from the University of Birmingham and the University of Cambridge during my PhD. I would like to acknowledge Volkswagen for supplying material for the experimental work performed in this thesis. I would also like to thank Diamond Light Source for the allocation of beam time.

I am grateful for the continuous support and enthusiasm from my supervisor Dr. David Collins throughout this research project. I would like to acknowledge the support from my second supervisor Professor Yu Lung Chiu for vital access to equipment and introduction to the very helpful Dr. Uthman Mahmud.

A big thanks to Dr. Anastasia Vrettou and Dr. Paraic O'Kelly for the warm welcome and help throughout the PhD. I am grateful for the "more than sufficient" wisdom and experience shared by Dr. Himanshu Vashishtha on our journey in Birmingham and Cambridge.

A special mention to Birmingham colleagues that shaped my PhD experience, providing endless encouragement, idea factories and motivation; Dr. Anastassia Milleret, Dr. James Ball, Dr. Johan Magnussen, Dr. Vincent Gagneur, Sophia von Tiedemann, Tom Blackburn, Dr. Iris Carneiro and Cameron Yousefian.

A special mention to Cambridge Colleagues Jamie Hogg and Ming En Pek for their vital support during write up. I am also grateful for the guidance and assistance from Dr. HT Pang in the RRUTC lab.

I would like to thank my parents and family for their continued support in my academic development, I didn't "forget the football" but I think I finally have got "the books right". Special thanks to my brother Abdi for machining samples last minute. I would also like to thank my close friends; Jordan M, Jack H, Harry O'C, Ryan W, the rest of 'Abbeymead Academy' and Kyran R for their continuous encouragement and experiences outside of university. Last, but not least, I want to acknowledge my wonderful partner Anna Rees for being there on this journey with me, always providing support, comfort and time keeping reminders (that were consistently ignored).

Dedication

I dedicate this thesis to my parents and grandparents for building the foundations needed for me to take this path.

"*If I have seen further than others, it is by standing upon the shoulders of giants*"

-Isaac Newton

Contents

List of Figures **xii**

List of Tables **xxii**

1 Introduction **1**

1.1 Magnesium 1

1.2 Sheet Metal and Forming 4

1.3 Scope of this work 5

2 Literature review **7**

2.1 Physical Metallurgy of Magnesium Alloys 7

2.1.1 Crystal Structure and Deformation Mechanisms 7

2.1.2 Slip Systems in Magnesium 9

2.1.3 Deformation Twinning in Magnesium 10

2.1.4 Interplay between Slip and Twinning 11

2.2 Alloying and Texture in Magnesium Alloys 13

2.3 Mechanical Testing For Sheet Metal 17

2.4 Overview of Plasticity Modelling of Polycrystalline Alloys 19

2.5 Visco-Plastic-Self-Consistent Modelling 20

2.5.1 Use of the Dislocation Density Hardening Model 21

2.5.2 Simulating Twinning with VPSC 23

2.5.3 Capabilities of the VPSC model 26

2.5.4 Application of VPSC Model to Ca-containing Mg alloys 30

3 Experimental methods 34

3.1 Metallographic Preparation 34

3.2 DIC & Tensile Tests 35

3.3 X-ray Synchrotron Diffraction 37

3.4 In-situ EBSD 39

4 Initial Characterisation and In-situ X-ray Synchrotron Investigation 41

4.1 Initial Microstructure and Texture 41

4.2 Initial tensile testing 45

4.3 Synchrotron X-ray diffraction 50

4.4 Introduction 50

4.5 Results 52

4.5.1 Anisotropic yield behaviour 52

4.5.2 Strain rate sensitivity 62

4.6 Discussion 70

4.6.1 Directional anisotropy 70

4.6.2 Strain rate sensitivity 72

5 Microstructure insights of deformation in Mg alloys via In-situ HR-EBSD 76

5.1 Introduction 76

5.2 Results 81

5.2.1 Microstructure and GND evolution 81

5.2.2 Twinning in Ca-containing alloys 93

5.3 Discussion 98

5.3.1 Twinning Activation and Directional dependence 100

5.3.2 GND and stress 104

6 VPSC Modelling of Mg alloys at Elevated Temperatures 107

6.1 Introduction 107

6.2 Overview of the VPSC model 109

6.2.1 Local constitutive behaviour and homogenisation 109

6.3 Results 129

6.3.1 Calibration of the VPSC model with macroscopic tensile data . . 129

6.3.2 Extracting slip and twinning activity 135

6.3.3 Pole figure predictions 142

6.3.4 VPSC calculations of lattice strains 149

6.4 Discussion 153

6.4.1 Dislocation interactions and Drag stress 153

6.4.2 Active deformation modes & Texture 158

7 Discussion 162

8 Conclusions and future work 171

8.1 Table of Symbols and definitions 175

Bibliography 177

List of Figures

1.1 Production of magnesium alloy sheet via twin-roll casting (a) and (b)&(c) show an example of the inner structure of a Passat bootlid produced from texture weakened twin-roll cast magnesium alloy sheet. (a) and (c) are adapted from [1, 2] 4

2.1 Crystal structure of magnesium (a) unit cell. (b) Conventional hexagonal close packed unit cell; with atomic stacking layers (ABA). 8

2.2 Deformation modes in magnesium showing (a) slip systems and (b) twinning systems. 8

2.3 CRSS values for the primary slip and twinning modes in pure magnesium and their variation with temperature. Re-created from [3] 10

2.4 Texture evolution under compressive stress in the RD direction for clock-rolled Zr, reorientation of the basal poles along the RD due to $\{10\bar{1}2\}$ twinning from 9% onwards, modified from Beyerlein and Tome [4]. . . . 25

2.5 Experimental curves used to calibrate the model at strain rates: (a) $0.001s^{-1}$ and $0.01s^{-1}$, & (b) $0.1s^{-1}$, $1s^{-1}$ and $10s^{-1}$, alongside VPSC simulated curves. Adapted from Zecevic et al. [5]. 28

2.6 (a)Texture evolution post 10% tensile deformation for two Mg-alloys, (b) difference in predicted slip activity for both alloys, adapted from Chaudry et al. [6]. 31

3.1 (a) DIC set-up, (b) sample with speckle pattern, (c) original sample with dimensions and (d) sample with white base for the first step of DIC speckle pattern preparation. 36

3.2 (a) Deben MT5000DL with sample mounted and door off, (b) sample used for ex-situ strain rate testing, important dimensions described. . . . 38

3.3 (a)Digital image of a tensile sample mounted in the In-situ tensile grips and (b) Electron back scatter diffraction pattern showing the Kikuchi bands. 39

4.1 Initial condition of AZ31 alloy, (a) Inverse Pole Figure map, (b) (0001) & $(10\bar{1}0)$ Pole figure and (c) Band contrast map. 42

4.2 Initial condition of AZX alloy, (a) Inverse Pole Figure map, (b) (0001) & $(10\bar{1}0)$ Pole figure and (c) band contrast map. 43

4.3 Initial condition of ZXK alloy, (a) Inverse Pole Figure map, (b) (0001) & $(10\bar{1}0)$ Pole figures and (c) band contrast map. 44

4.4 Energy dispersive spectroscopy (EDS) maps of AZ31 precipitates with a back scattered electron (BSE) image in the top left. The black arrows in the Mg elemental map show the gaps in signal from Mg atoms coinciding with suspected Al-Mn intermetallics highlighted with white arrows in the appropriate maps. 46

4.5 EDS maps of AZX precipitates, the red square in the BSE image (top left) corresponds with the elemental maps. Two regions are highlighted within the reduced area, (a) is associated with an Al-Mn intermetallic, (b) multiple Al-Ca intermetallics. 47

4.6 EDS maps of sub-surface ZXK precipitates with a secondary electron image of an over etched surface. White arrows point towards suspected Mg-Ca intermetallics. 48

4.7 Stacked room temperature X-ray diffraction patterns for each magnesium alloy, with markers corresponding to Mg HCP phase peak positions. The background originates from a quartz window between the sample and X-ray beam. 49

4.8 Tensile data for AZ31, AZX & ZXK alloys, both tested in RD & TD, for strain rates, in s^{-1}, labelled above each plot. 50

4.9 Room temperature in-situ lattice strain measurements evolving with strain, from uniaxial tensile tests of the 3 alloys, parallel to the (a) rolling direction (RD) and (b) transverse direction (TD). (c) includes the macroscopic tensile curves. 53

4.10 In-situ lattice strain measurements evolving with strain at $150°C$, from uniaxial tensile tests of ZXK and AZX, parallel to the (a) rolling direction (RD) and (b) transverse direction (TD). (c) includes the macroscopic tensile curves. 54

4.11 In-situ lattice strain measurements evolving with strain at $250°C$, from uniaxial tensile tests of ZXK and AZX, parallel to the (a) rolling direction (RD) and (b) transverse direction (TD). (c) includes the macroscopic tensile curves. 55

4.12 Schematic depicting the collection of debye-sherrer rings from diffraction in transmission. The azimuthal angles refer to data corresponding to the tensile axis major strains $\psi = 90°$ and minor strains $\psi = 0°$. 59

4.13 Room temperature in-situ lattice strain measurements evolving with strain, during tensile deformation of the 3 alloys at two strain rates. (a) $10^{-3}\,s^{-1}$, (b) $10^{-4}\,s^{-1}$ and (c) macroscopic true stress strain curves. 63

4.14 Elevated temperature in-situ lattice strain measurements evolving with strain, during tensile deformation of the 3 alloys at two strain rates. (a) $10^{-3}\,s^{-1}$, (b) $10^{-4}\,s^{-1}$ and (c) macroscopic true stress strain curves. . . . 64

4.15 Elevated temperature in-situ lattice strain measurements evolving with strain, during tensile deformation of the 3 alloys at two strain rates. (a) $10^{-3}\,s^{-1}$, (b) $10^{-4}\,s^{-1}$ and (c) macroscopic true stress strain curves. . . . 65

4.16 Strain rate sensitivity (SRS) for each alloy in the RD, symbol and line represents calculations from values obtained with the Deben Rig. The arrows indicate values from tests with the Instron at RT from three strain rates, highlighting differences in equipment for the same material. 66

4.17 Magnified view of the strain range with suspected serrations for the macroscopic flow curves in Figs. 4.14-4.15 at (a) 150°C and (b) 250°C. . 68

5.1 IPF-Z maps for (a) AZ31, (b) AZX and (c) ZXK for loading in the RD case. Showing the evolution of grain orientation and twin formation with increasing strain. 82

5.2 IPF-Z maps for (a) AZ31, (b) AZX and (c) ZXK for loading in the TD case. Showing the evolution of grain orientation and twin formation with increasing strain. Area's for twin analysis are enclosed in blue box's, Map 1 = solid line, Map 2 = dashed line. 83

5.3 Geometrically Necessary Dislocation (GND) density maps for (a) AZ31, (b) AZX and (c) ZXK, for loading in the RD case. Showing the GND evolution with increasing strain. 84

5.4 Geometrically Necessary Dislocation (GND) density maps for (a) AZ31, (b) AZX and (c) ZXK for loading in the TD case. Showing the GND evolution with increasing strain. 85

5.5 Total geometrically necessary dislocation (GND) density evolution with increasing macroscopic strain from each map, for (a) AZ31, (b) AZX and (c) ZXK. The GND densities have been normalised to the initial condition level, showing the GND density evolution with increasing strain. 87

5.6 Schematic illustrating the angle of the c-axis to the sheet normal. Φ represents the inclination angle. 88

5.7 Evolution of GND density as a function of c-axis inclination angle with increasing macroscopic strain. The inclination angles have been binned with 10°intervals and GND densities normalised by number of orientations within each bin. This is shown for alloys (a) AZ31, (b) AZX and (c) ZXK. 89

5.8 Distribution of c-axis inclination angles at $\varepsilon = 0\%$ (blue) and $\varepsilon \approx 8\%$ (black) strains for both RD and TD loading. (a) AZ31, (b) AZX and (c) ZXK. 90

5.9 Initial condition maps coloured by highest Schmid factor for the respective slip/twin system. (a) AZ31, (b) AZX and (c) ZXK, for loading in both cases. Hexagonal close packed (HCP) unit cells are superimposed on grains to visualise the mean orientation of the grain. 91

5.10 Percentage of grains with the highest Schmid factor for the respective slip/twin system. 92

5.11 Average Schmid factor for the respective slip/twin system for (a) RD case and (b) TD case. 92

5.12 $\varepsilon = 0\%$ condition maps coloured by Schmid factor for the tensile twin system. (a) AZ31, (b) AZX and (c) ZXK, for loading in both cases. Hexagonal close packed (HCP) crystal overlaid on grains to highlight the mean orientation of the grain. 93

5.13 Area Map 1 with increasing strain for ZXK. (a) EBSD maps (b) σ_{VM} (GPa) (c) GND ($\log_{10}$) for loading in the TD case. 94

5.14 Area Map 2 with increasing strain for ZXK. (a) EBSD maps, (b) σ_{VM} (GPa) and (c) GND ($\log_{10}$) for loading in the TD case. 95

5.15 Distribution of σ_{VM} in ZXK-Map 1 with increasing strain. For (a) grains that twinned and (b) grains that did not twin for loading in the TD case. (c) is an inset to help visualise the data in (a) and (b). 96

5.16 Distribution of σ_{VM} in AZX-Map 1 with increasing strain. For (a) grains that twinned and (b) grains that did not twin for loading in the TD case. (c) is an inset to help visualise the data in (a) and (b). 97

5.17 Area Map 1 with increasing strain for AZX. (a) EBSD maps (b) σ_{vm}(GPa) (c) GND ($\log_{10}$) for loading in the TD case. 97

5.18 ZXK-Area Map 1 at $\varepsilon \approx 8\%$ condition coloured by Schmid factor for systems:(a) Basal, (b) Prismatic, (c) Pyramidal and (d) TTwin. Hexagonal close packed (HCP) crystal overlaid on grains to highlight the mean orientation of the grain. 99

5.19 AZX-Area Map 1 at $\varepsilon \approx 8\%$ condition coloured by Schmid factor for systems:(a) Basal, (b) Prismatic, (c) Pyramidal and (d) TTwin. Hexagonal close packed (HCP) crystal overlaid on grains to highlight the mean orientation of the grain. 100

6.1 A summary of (a) the inputs that feed the model and (b) the outputs generated. 128

6.2 Stress-strain curves for AZ31 for loading in the (a) RD and (b) TD. Only the RD has experimental data at the elevated temperatures. The dotted lines represent the simulation results. 132

6.3 Stress-strain curves for AZX for loading in the (a) RD and (b) TD. The dotted lines represent the simulation results. 133

6.4 Stress-strain curves for AZX for loading in the (a) RD and (b) TD. The dotted lines represent the simulation results. 135

6.5 Evolution of initial CRSS with increasing temperature for considered deformation modes, for (a) AZ31, (b) AZX and (c) ZXK. 136

6.6 AZ31-RD. Predictions from left to right, the evolution of: slip system shear activity, twinning volume fraction and dislocation density on considered deformation modes. For increasing temperatures (a)-(c). 138

6.7 AZ31-TD. Predictions from left to right, the evolution of: slip system shear activity, twinning volume fraction and dislocation density on considered deformation modes. For increasing temperatures (a)-(c). 139

6.8 AZX-RD. Predictions from left to right, the evolution of: slip system shear activity, twinning volume fraction and dislocation density on considered deformation modes. For increasing temperatures (a)-(c). 140

6.9 AZX-TD. Predictions from left to right, the evolution of: slip system shear activity, twinning volume fraction and dislocation density on considered deformation modes. For increasing temperatures (a)-(c). 141

6.10 ZXK-RD. Predictions from left to right, the evolution of: slip system shear activity, twinning volume fraction and dislocation density on considered deformation modes. For increasing temperatures (a)-(c). 143

6.11 ZXK-TD. Predictions from left to right, the evolution of: slip system shear activity, twinning volume fraction and dislocation density on considered deformation modes. For increasing temperatures (a)-(c). 144

6.12 Active deformation modes relative contribution to total shear for all 3 alloys, for the (a) RD case, and (b) TD case. 145

6.13 AZ31 - Texture predictions to end strains for loading in both directions, (b) RD case and (c) TD case. The initial experimental texture at RT (a) for reference. 147

6.14 AZX - Texture predictions to end strains for loading in both directions, (b) RD case and (c) TD case. The initial experimental texture at RT (a) for reference. 148

6.15 ZXK - Texture predictions to end strains for loading in both directions, (b) RD case and (c) TD case. The initial experimental texture at RT (a) for reference. 150

6.16 AZ31 - Lattice strain predictions for deformation at at RT and elevated temperatures, plotted against true strain. With respect to the (a) RD case or (b) TD case. Solid lines represent lattice strains evolving parallel to the loading axis, dashed lines are 90°to the loading axis. 152

6.17 AZ31 - Relative volume fraction of grains contributing to the lattice strain predictions in Figure6.16. With respect to the (a) RD case or (b) TD case. Solid lines represent lattice strains evolving parallel to the loading axis, dashed lines are 90°to the loading axis. 153

6.18 AZX - Lattice strain predictions for deformation at RT and elevated temperatures, plotted against true strain. With respect to the (a) RD case or (b) TD case. Solid lines represent lattice strains evolving parallel to the loading axis, dashed lines are 90°to the loading axis. 154

6.19 AZX- Relative volume fraction of grains contributing to the lattice strain predictions in Figure6.18 With respect to the (a) RD case or (b) TD case. Solid lines represent lattice strains evolving parallel to the loading axis, dashed lines are 90°to the loading axis. 155

6.20 ZXK - Lattice strain predictions for deformation at at RT and elevated temperatures, plotted against true strain. With respect to the (a) RD case or (b) TD case. Solid lines represent lattice strains evolving parallel to the loading axis, dashed lines are 90°to the loading axis. 156

6.21 ZXK- Relative volume fraction of grains contributing to the lattice strain predictions in Figure6.20 With respect to the (a) RD case or (b) TD case. Solid lines represent lattice strains evolving parallel to the loading axis, dashed lines are 90°to the loading axis. 157

7.1 Comparison of the tension twin volume fractions calculated from In-situ EBSD samples post-experiment and predictions from the VPSC model. . 167

7.2 Comparison of lattice strains from (a) predictions from the VPSC model, and (b) calculated In-situ with X-ray synchrotron. 169

List of Tables

3.1 Nominal composition of magnesium alloys studied in weight %. 34

6.1 Temperature independent parameters for AZ31. 130

6.2 Temperature independent parameters for AZX. 130

6.3 Temperature independent parameters for ZXK. 131

6.4 Temperature dependent parameters for AZ31. 131

6.5 Temperature dependent parameters for AZX. 132

6.6 Temperature dependent parameters ZXK. 132

6.7 Interaction parameter 133

6.8 AZ31 Drag stress matrix 133

6.9 Drag stress matrix for AZX 134

6.10 Drag stress matrix for ZXK 134

8.1 Important Symbols and Definitions from Chapter 6 175

8.2 Important Symbols and Definitions from Chapter 6 (Continued table 8.1...).176

8.3 Important Symbols and Definitions from Chapter 4 and 5. 176

Chapter 1

Introduction

1.1 Magnesium

Magnesium (Mg), atomic number 12, is an alkaline earth metal with a plethora of uses. In nature, its presence is essential as a nutrient for physiological and biochemical processes, occurring in all organism cells, making it commonly included in health supplements. In societal applications, it has numerous uses when alloyed, enabling the manufacture of unique products in biomedical and lightweight, structural engineering applications. In 1808 Sir Humphry Davy declared that magnesium oxide contained a newly recognised element, but it was not until 1828 that the elemental form of magnesium was isolated from magnesium chloride ($MgCl_2$) by Antoine-Alexander Bussy [3, 7]. Magnesium is the eighth most abundant element in the Earth's crust. It is the most abundant metal ion in the ocean and sources are concentrated in brine deposits in locations such as the Great Salt Lake in Utah. Historically, 80% of magnesium production has exploited these readily available sources, through electrolytic reduction of $MgCl_2$. Initial success in electrolysis of $MgCl_2$ was achieved by Michael Faraday in 1833 [7], but this process was first commercialised some years later in the mid 19^{th} century, in Paris [3]. The

production of magnesium today is dominated by the "Pidgeon" process, developed in Canada[3]. Solid magnesium compounds found in mineral deposits in the Earth's crust are reduced by ferrosilicon in a high temperature batch process, the most common compound being 'dolomite' ($MgCO_3 \cdot CaCO_3$). Commercial production of magnesium has fluctuated since the 20th century, as has interest in its potential use as a structural metal. Very low initial outputs of 10 tonnes per year, grew to 3000 tonnes per year during the first world war, decreasing afterwards, followed by a large spike during the second world war, reaching 300,000 tonnes per year. Interest plateaued over the next two decades at a steady 250,000 tonnes per year [3]. The beginning of the 21st century saw renewed interest in magnesium alloys for automotive and aerospace industries. By 2015 global output had risen to $\sim 900,000$ tonnes per year [3]. Over 90% of Mg in structural applications is used in cast products for interior and power-train components [7, 3]. Despite the renewed interest, wrought products are yet to be used to the same extent.

Globally, the impact of global warming has necessitated legislation changes to reduce green house gas emissions (GHGs). The transport industry is a large contributor to GHG emissions, more specifically motor vehicles, and has consequently been chasing lower emission targets to reduce the impact on the environment [8]. Historically, focus has centered on the development of more fuel efficient internal combustion engine vehicles (ICE). However, in the last two decades technological developments in electric vehicles (EV) has led to a rapid increase in their production and commercialisation. EV vehicles are now a growing competitor to ICE vehicles for achieving zero-emission targets [9, 10, 11]. CO_2 is a major contributor to green house gas emissions, emissions (measured as CO_2 g/km) from ICE vehicles can be reduced with better fuel efficiency. An important factor in fuel consumption is vehicle power requirement; how much fuel is needed to accelerate and keep a vehicle moving. Power requirement has a number of contributing factors, vehicle weight is directly proportional to many of those factors, thus, vehicle

weight reduction will have a significant influence on fuel consumption [12]. Weight reductions of 100 kg can result in a reduction in fuel use of 0.3-0.5 l/100 km, translating to 8-11 g/km less CO_2 [12, 13, 14, 15]. Weight reduction in EV vehicles is equally as important, the range achieved with each battery charge can be greatly improved. In addition, the total cost of an EV can be reduced; a lighter vehicle demands fewer battery packs, for example [12]. Product performance can also be improved, with better acceleration and braking [16]. Considering this, magnesium and its alloys, synonymous with the term 'lightweighting', become an obvious endeavour.

Advanced materials research has identified magnesium alloys as a candidate to supersede steel and aluminium materials for various structural components in vehicles and aircraft. A low density of 1.73 g cm^{-3} and high specific strength gives Mg and its alloys a great strength to weight ratio. Combined with excellent castability make Mg valuable for achieving weight reduction [13]. A comparison of stiffness for beams of equal weights of steel, titanium, aluminium and magnesium found the ratios to be 1:2.9:8.2:18.9, respectively. Comparing a common commercial magnesium alloy, AZ31, with steel and commercial aluminium alloys, there are weight savings of 50% and 15%, respectively [3]. However, Mg and its alloys have not been widely adopted in automotive applications as hoped. Wrought products have been less favourable due to intrinsically poor mechanical properties at room temperature (RT), owing to their crystal structure. Poor corrosion resistance, especially galvanic corrosion, a major setback when considering their selection in applications where joining to steel is necessary, regularly encountered in automotive bodies [17]. While their absolute mechanical properties and corrosion resistance lag behind steel/Al, recent advances in alloy design (e.g., calcium and rare-earth additions[3, 18, 1]), processing (e.g., severe plastic deformation [19] and twin-roll casting [2, 1]), and coating technology [15, 18] have expanded their viability in targeted applications. The significant weight saving opportunities from a very low density continues to drive innovation in Mg alloy development [16].

1.2 Sheet Metal and Forming

Typical production of wrought sheet metal involves direct chill casting (DC) of ingots, homogenisation, machining then repeated hot rolling. The deformation imposed by rolling tends to orientate basal planes to be parallel to the sheet surface with $\langle 10\bar{1}0 \rangle$ directions in the rolling direction (RD), giving a strong basal texture in the (0001) pole figure; with a slight tilt in the RD. Due to this texture, during most forming techniques there exits a hard grain effect leading to non-uniform deformation with tension-compression asymmetry. The yield behaviour of a Mg single crystal can differ if the stresses are compressive or tensile in the direction of the c-axis, which compounds on the already anisotropic behaviour present in most wrought sheet metals [1].



Figure 1.1: Production of magnesium alloy sheet via twin-roll casting (a) and (b)&(c) show an example of the inner structure of a Passat bootlid produced from texture weakened twin-roll cast magnesium alloy sheet. (a) and (c) are adapted from [1, 2]

New techniques developed for the production of Mg sheets involve casting and rolling simultaneously, producing sheet metal close to the final dimensions. This is known as Twin-roll casting (TRC), producing which is shown in Figure 1.1(a). TRC produces strip approximately 5-8 mm thick. Progress in the TRC technique for the production of

magnesium sheet metal enhances the commercial viability for these alloys in combination with texture weakened alloys. TRC has been the focus of alternative sheet production because of the fewer required thermo-mechanical processes compared to DC casting. The as-cast microstructures for DC casting produced Mg sheets are usually destroyed via repeated rolling, TRC allows for fewer rolling passes, with the resulting microstructure comprising a larger fraction of the as-cast microstructure preserved. Without prior deformation this can result in weakened textures for non-Ca or non-RE containing alloys [1]. In 2015, magnesium sheet was selected for the roof of a Porsche 911 GT3, selected as it outperformed aluminium and carbon-fibre-reinforced polymers for this role [3]. More recently, Volkswagen have successfully produced the tail gate of a Passat with magnesium sheet at low temperatures as result of Ca containing alloys [2], shown in Figure 1.1 (b) & (c).

Mg sheets with weaker basal texture display better formability during deep drawing at RT [7]. The addition of RE elements successfully weakened/altered this strong texture, however, the financial cost of REs increases production expense, reducing commercial viability. Ca has shown to have a similar texture weakening effect [20] and therefore introduce a potential cost sensitive solution.

1.3 Scope of this work

This investigation sets out to study the anomalous effect possessed by Ca-containing Mg alloys, which are known to possess enhanced formability compared to the commercial alloy AZ31. The macroscopic behaviour of those alloys is established but the governing reasons why the modified recrystallisation textures observed in these alloys have such a significant effect on the mechanical properties are not well understood. In the present work, we will study two developmental Ca-containing alloys as well as a commercial

AZ31 (as a benchmark).

Chapter 2 will include a literature review summarising: the current understanding of deformation mechanisms, texture development and modelling, and processing of Mg alloys. Chapter 3 outlines the experimental methods employed throughout this work. Chapter 4 presents the initial microstructural condition and macro-mechanical behaviour of these alloys. The mechanical response is explored in more detail using in-situ synchrotron X-ray diffraction. More localised characterisation of the deformation behaviour is explored in Chapter 5 using High-Resolution Electron Backscatter Diffraction (HR-EBSD). In Chapter 6, a mean-field crystal plasticity model is used to predict the governing deformation modes in these alloys during plastic deformation. The material microstructure is represented by an aggregate given an initial texture and plasticity rules. Chapter 7 serves as a discussion of the experimental results together. Chapter 8 concludes the findings of this thesis and includes future work.

Chapter 2

Literature review

2.1 Physical Metallurgy of Magnesium Alloys

2.1.1 Crystal Structure and Deformation Mechanisms

Magnesium has a hexagonal close-packed (HCP) crystal structure, as shown in Fig. 2.1 with common slip and twinning planes illustrated in Fig. 2.2. The basal plane (0001) is the closest-packed plane in HCP magnesium, and basal $\langle$a$\rangle$ slip on this plane is the dominant deformation mode for magnesium and its alloys at room temperature (RT) [21, 22, 23]. The c/a ratio of magnesium (≈ 1.624) is close to the ideal HCP ratio of 1.633, which promotes the close packing of the basal plane and makes dislocation movement more favourable on these planes [7]. In contrast, HCP titanium has a lower c/a ratio (≈ 1.587), which introduces anisotropy in interatomic spacings and promotes prismatic $\langle a \rangle$ slip on $10\bar{1}0$ over basal slip.

Plastic deformation in magnesium occurs primarily through dislocation glide (slip) and twinning [24, 25, 22, 21]. HCP metals commonly exhibit anisotropic deformation

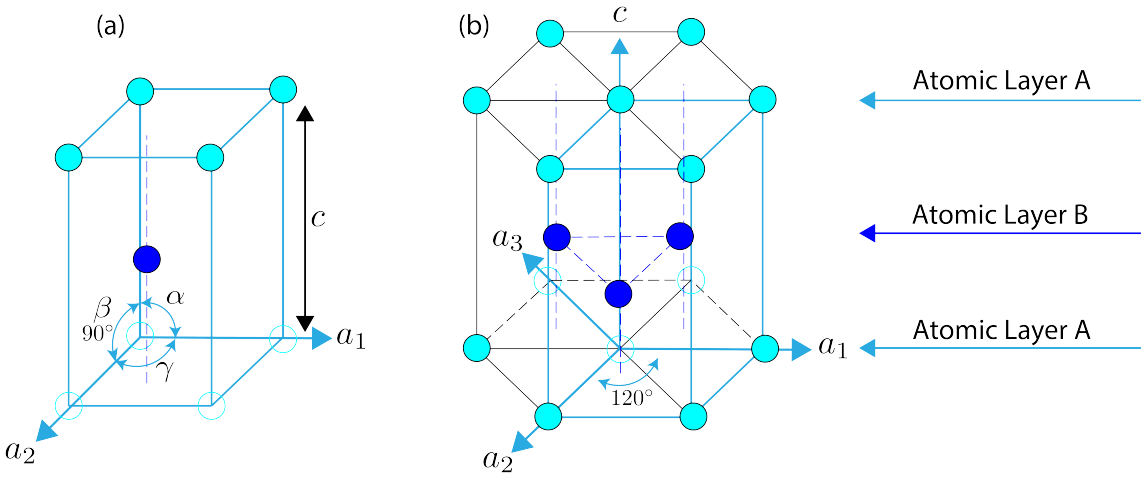


Figure 2.1: Crystal structure of magnesium (a) unit cell. (b) Conventional hexagonal close packed unit cell; with atomic stacking layers (ABA).

behaviour due to fewer slip systems compared to face-centred cubic (FCC) and body-centred cubic (BCC) metals, as well as the prevalence of deformation twinning [26]. Wrought magnesium and its alloys typically exhibit a strong basal texture, which arises from the limited number of deformation modes available in the HCP structure [27].

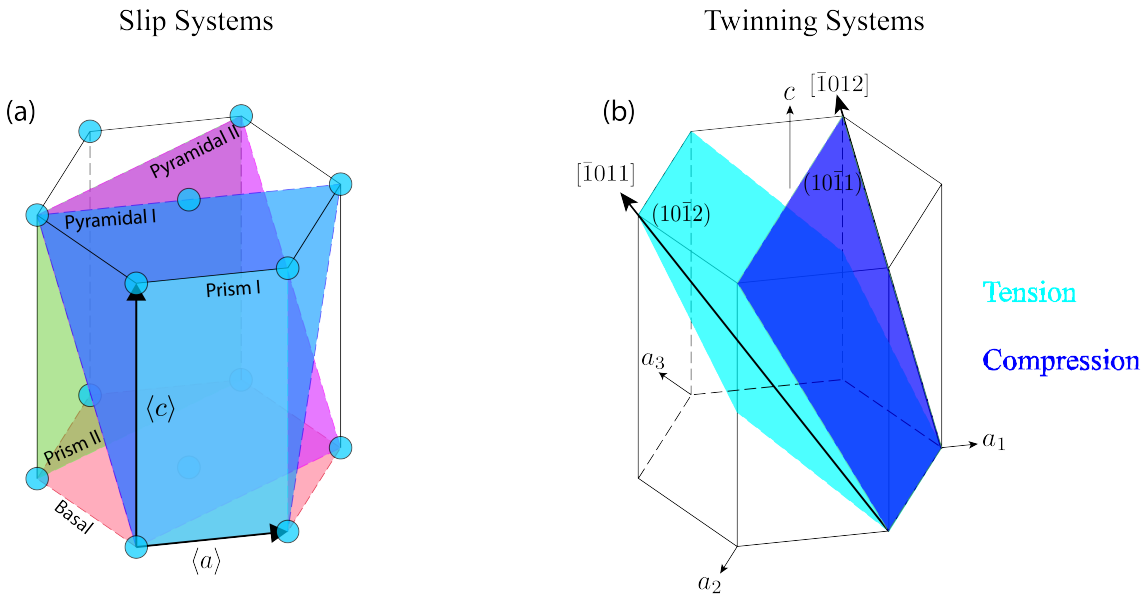


Figure 2.2: Deformation modes in magnesium showing (a) slip systems and (b) twinning systems.

2.1.2 Slip Systems in Magnesium

The primary slip system in magnesium is basal slip $(0001)\langle 11\bar{2}0\rangle$, which has the lowest critical resolved shear stress (τ_{CRSS}) at RT among the available slip systems [21, 22, 23]. However, basal slip provides only two independent slip systems, which is insufficient to satisfy the Von Mises and Taylor criterion requiring five independent slip systems for homogeneous deformation [28, 29]. This limitation results in plastic incompatibility at grain boundaries and restricts the formability of magnesium at RT [7].

Second to basal slip, the prismatic slip system $(1\bar{1}00)\langle 11\bar{2}0\rangle$ also involves $\langle a\rangle$-type Burgers vectors and provides plastic deformation parallel to the basal plane [25, 30, 31]. Non-basal slip systems, such as pyramidal $\langle a\rangle$ and $\langle c+a\rangle$, accommodate deformation along the c-axis but are more difficult to activate at RT due to their higher τ_{CRSS} values [32, 33]. Pyramidal $\langle c+a\rangle$ slip, in particular, has a significantly higher τ_{CRSS} than prismatic slip at low temperatures and is typically observed at stresses greater than those required for basal or prismatic slip [33], shown in Fig. 2.3.

The τ_{CRSS} for slip systems is governed by Schmid's law:

$$\tau_{\mathrm{CRSS}} = \sigma \cos\lambda \cos\phi, \tag{2.1}$$

where σ is the applied stress, λ is the angle between the applied force and the slip/twin direction, and ϕ is the angle between the applied force and the slip/twin plane normal [34]. It can be used to identify the condition for yield, defined as the nucleation and mobilisation of dislocations. It is noted that its detection via diffraction technique or microscopy, for example, is only measurable once slip or twinning has already occurred. Slip begins at a local scale with several possible influencing factors: local stress concentrations, temperature, strain rate and material conditions. Therefore, τ_{CRSS} can be influenced by experimental and material conditions, comparative evaluations of τ_{CRSS}

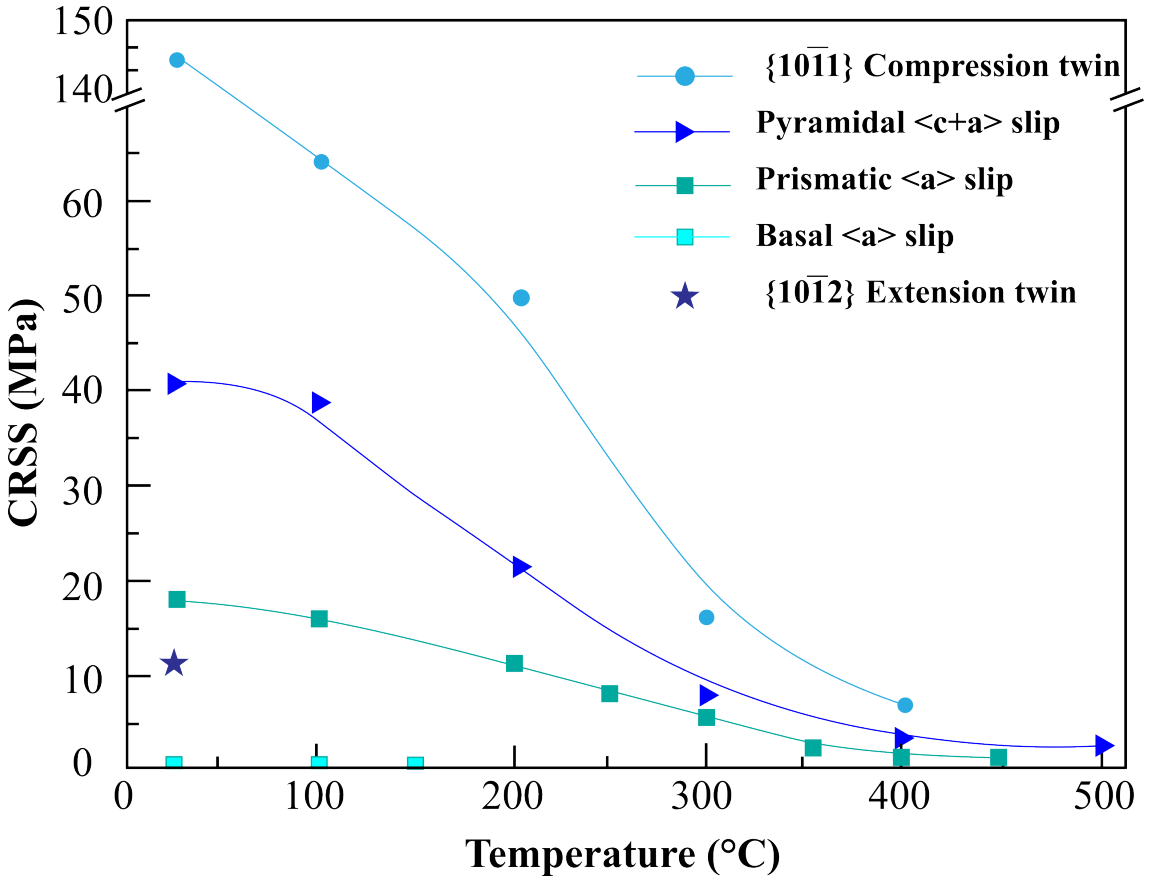


Figure 2.3: CRSS values for the primary slip and twinning modes in pure magnesium and their variation with temperature. Re-created from [3]

are more suitable here rather than the absolute values [7].

2.1.3 Deformation Twinning in Magnesium

Early research argued that deformation twinning is another critical mechanism for accommodating plastic strain in magnesium, particularly at RT with limited slip systems [35]. Twinning involves the homogeneous shear of a crystal region on a twin plane, resulting in a reoriented "twin" region that is a mirror reflection of the parent crystal [34]. Twinning typically initiates at grain boundaries [36, 37] or defects such as slip bands and twin interfaces [38, 4]. Twin growth occurs through the movement of twinning dislocations, which differ from slip dislocations in that they cause lattice reorientation

[34]. The two most common twinning modes, extension twins $\{10\bar{1}2\}$ and contraction twins $\{10\bar{1}1\}$, commonly referred to as tension and compression twins, respectively, are named after the stress states under which they are most frequently observed. These twins facilitate extension or shortening along the c-axis by shear-driven crystal reorientation, which leads to both orientation and shape changes in a grain. [7, 21]. The shear displacement can alter the grain morphology by introducing kinks or steps along twin boundaries. Extension twins are more frequently observed due to their lower τ_{CRSS} and simpler atomic shuffling requirements compared to contraction twins [31, 33]. Extension twinning, in particular, can help satisfy the Taylor criterion at low temperatures due to its lower τ_{CRSS} compared to non-basal slip systems and its relative insensitivity to temperature and strain rate [39, 40]. However, twinning is a polar mechanism and can only accommodate a finite amount of strain proportional to the volume of the twinned grain [25].

Twinning also influences texture evolution by causing rapid grain reorientation, which can alter the dominant deformation mechanism and induce stress concentrations at twin boundaries [33]. While twinning can enhance ductility in some cases, its suppression has been shown to improve formability in magnesium alloys at elevated temperatures by favouring prismatic slip [33].

2.1.4 Interplay between Slip and Twinning

The deformation of magnesium and its alloys follows a sequential micromechanical response. At RT, deformation typically initiates with basal slip, followed by the activation of twinning at low strains due to anisotropic stress concentrations arising from basal slip [41, 42]. Slip and twinning continue simultaneously until twinning saturates at approximately 8% matrix deformation, after which non-basal slip systems become active [7]. In some cases, non-basal slip (e.g., prismatic $\langle a \rangle$) can occur concurrently with basal slip,

particularly when the Schmid factor ratio of non-basal to basal slip reaches 1.5-2.0 [41].

Grain boundary sliding can also mediate deformation, particularly in fine-grained microstructures ($< 10\,\mu\text{m}$) at RT or in larger grains at elevated temperatures. This phenomenon accommodates anisotropic plastic strain at grain boundaries through intragranular dislocation motion [30, 41].

Several factors influence the yield behaviour and deformation mechanisms of magnesium alloys, including temperature, strain rate, grain size, solute atoms, and second-phase precipitates [7]. The τ_{CRSS} for basal and prismatic slip is nearly independent of temperature, while the τ_{CRSS} for other slip systems decreases significantly with increasing temperature, explaining the improved formability of magnesium at elevated temperatures ($200 - 300^{\circ}\text{C}$) [7]. Alloying additions can also alter τ_{CRSS} levels by modifying lattice parameters, varying the c- and a- unit cell dimensions and consequently a change in the stress required to overcome lattice resistance to dislocation movement (Peierls-Nabarro stress), thereby influencing the ease of dislocation motion on specific slip systems [34, 7].

Crystal structures consist of atoms with specific arrangements; displaying close packing on certain planes. The sequence of layers, known as the stacking sequence, determines how the layers are arranged. The first and any identical layers in the sequence are labelled as "A" layers, while layers with that are displaced relative to this are referred to as B, C, and so on. In HCP magnesium, the stacking sequence follows an ABABABA... pattern, as illustrated in Figure 2.1. A stacking fault occurs when this sequence is disrupted due to the addition, removal or displacement of a layer, breaking the stacking sequence. These faults can arise during crystal growth or as a result of plastic deformation, such as slip or twinning. Altering the natural stacking sequence introduces an associated SFE (mentioned earlier)- the energy per unit area required to maintain the fault. This energy is related to the forces acting at the boundary of the fault, including surface tension and the repulsion between partial dislocations [34].

Three basal-plane faults exist, two are Intrinsic I_1 & I_2, and one extrinsic (E). The first intrinsic fault is formed through the removal of a basal layer "A", growth induced, this introduces a very high energy fault, as a consequence slip of $\frac{1}{3}\langle 10\bar{1}0\rangle$ is forced on the crystal above to reduce the energy (I_1 stacking fault):

$$\mathrm{ABABABABA...} \rightarrow \mathrm{ABABBABA...} \rightarrow \mathrm{ABABCBCB...}$$

Slip of $\frac{1}{3}\langle 10\bar{1}0\rangle$ is also involved in the second intrinsic fault, deformation induced, on a perfect crystal (I_2 stacking fault):

$$\mathrm{ABABABAB...} \rightarrow \mathrm{ABABCACA...}$$

The extrinsic fault involves the scenario where an extra plane is inserted (E stacking fault):

$$\mathrm{ABABAB...} \rightarrow \mathrm{ABABCABAB...}$$

It is noted that stacking faults in HCP crystals create local face centered cubic (FCC) stacking sequences, ABCABC... The SFEs associated with these local changes can influence several deformation phenomena; twinning, ease of climb and cross-slip of dislocations and gives rise to work hardening [7].

2.2 Alloying and Texture in Magnesium Alloys

Magnesium is only useful for structural applications when processed as an alloy. Magnesium has an atomic diameter of $3.2\,\text{Å}$ and benefits from size-related strengthening when alloyed with various solute elements [7, 3]. Commercial magnesium alloys are categorised as cast and wrought, with their designations based on elemental additions: aluminium

denoted 'A', zinc 'Z', rare earth (RE) elements 'E', alkali earth elements 'X' and occasionally 'K' for trace elements. Common alloy systems include AZ (Mg-Al-Zn), AZX (Mg-Al-Zn-Ca), AE (Mg-Al-RE), AM (Mg-Mn-RE), EZ (Mg-RE-Zn), ZK (Mg-Zn-Zr), ZXK (Mg-Zn-Ca), WE (Mg-RE-Zr). The Mg-Al base alloy system has dominated cast magnesium alloys since its inception in Germany during the First World War. Magnesium has a large solubility for a relatively large number of elements. Aluminium and zinc were used as early alloying additions in magnesium systems, with manganese also added to combat poor corrosion properties. In the early 2000's, rare earth (RE) elements, such as neodymium (Nd), yttrium (Y), and cerium (Ce), along with alkali earth elements like calcium (Ca), were introduced to improve mechanical properties and later found to improve microstructural texture control [3, 7].

Most structural metals are polycrystalline, consisting of aggregates of many crystals. The crystallographic orientation of individual crystals significantly influences the properties of polycrystalline materials [35, 43, 44]. Texture arises when the distribution of crystal orientations is non-random, often resulting in a preferred orientation of grains after processing [44]. For hexagonal close-packed (HCP) materials like magnesium, which exhibit highly directionally dependent single-crystal properties, texture plays a critical role in determining the polycrystalline response [35]. Texture governs the stress experienced by deformation modes in each grain, thereby affecting the macroscopic material behaviour.

Wrought magnesium sheets typically exhibit a strong basal texture, with the c-axis predominantly aligned parallel to the sheet plane normal [1]. This strong texture contributes to the plastic anisotropy of magnesium, making it challenging to achieve isotropic mechanical properties [1, 45]. However, advanced processing techniques, such as unique plastic deformation processes and high-temperature rolling, have been shown to diminish the basal texture [46]. Research has also explored cryogenic treatment to improve the uniformity of grain orientations, and enhance pyramidal $\langle c + a \rangle$ slip, leading to an

increase strength and improve ductility [47, 48]. Cryogenic treatment is a process that involves cooling materials to extremely low temperatures, typically below (123 K), often using liquid nitrogen (or 77 K). The treatment is usually carried out in a controlled environment, where the material is gradually cooled to the target temperature, held for a specific duration (soaking time), and then slowly warmed back to room temperature [47].

The addition of RE metals, is particularly effective for reducing the strength of basal texture by promoting recrystallisation mechanisms that disrupt grain reorientation typically seen in wrought products. This leads to improved ductility and formability [49, 50]. This improvement is attributed to the substantial weakening of the basal texture influencing enhanced activity of non-basal dislocation slip [27]. RE-containing alloys typically exhibit a broad scatter of basal poles, with two peaks split toward the transverse direction (TD) in the (0001) pole figure. This texture morphology promotes more homogeneous deformation and larger strains to failure. Research on Mg-Y alloys has revealed high activity of pyramidal $\langle c+a \rangle$ dislocations gliding on pyramidal planes, linked to substantially improved ductility [51]. This increased activity is attributed to a reduced SFE, which promotes the formation of stacking faults that serve as heterogeneous nucleation sites for pyramidal $\langle c+a \rangle$ dislocations [52, 53]. The forming limit diagram of RE-containing alloys, such as ZEK100, demonstrates a clear improvement in sheet formability compared to conventional alloys like AZ31. The formability curve of ZEK100 resembles that of typical aluminium alloys, highlighting the potential of RE-containing magnesium alloys for structural applications [49]. However, the texture morphology and ductility improvements in RE-containing alloys depend on exceeding a critical threshold concentration of RE elements.

The high cost and limited availability of RE elements have driven the adoption of Ca as a cost-effective alternative for texture modification. Recent research has demonstrated that Ca-containing alloys exhibit similar texture weakening effects to RE-containing al-

loys, which is particularly important for cost-effective commercial production [54], even in the absence of second-phase precipitates [3]. Compared to other potential alloying elements, Ca offers reasonable solubility in magnesium and avoids severe corrosion issues associated with elements such as iron (Fe). Ca-modified magnesium alloys achieve similar texture weakening effects without the need for high concentrations of costly RE elements [49]. This makes Ca an attractive, lower-cost alternative to RE elements for texture modification in wrought magnesium alloy applications.

While intermetallics contribute to strengthening, strong evidence suggests that second-phase particles are not the primary cause of texture weakening. Mg-X-Ca alloys with no second-phase precipitates have shown similar texture weakening. Instead, the general consensus is solute segregation of Ca and zinc (Zn) to high-energy grain boundaries (grains with the $\langle 11\bar{2}0\rangle$ direction parallel to the RD and c-axis parallel to the sheet plane normal), lowers grain boundary energy and exerts a pinning effect. Suppressing the growth of preferentially oriented grains causing the basal texture during recrystallisation [3].

Texture significantly influences slip activity and twinning during deformation. Sheet forming involves stretching and deep drawing, achieved through a variety of stress states and strain paths. Mg sheets with lower yield strength show better stretch formability than higher yield strength alloys. Sharp yield points common in many metals are infrequently observed in Mg alloys [3], the elastic-plastic transition spans a greater stress range. This is linked to micro-yielding occurring first in grains more favourably aligned for basal slip known as "soft" orientations, before harder orientations begin to share the load [42]. The resultant stress-strain response will depend on the size, distribution and number of soft and hard grains for the applied stress. Grains oriented with their basal plane normal that is parallel and/or perpendicular to the loading axis are defined as "hard" grains. This is due to the 0 Schmid factor for basal slip, which then requires the activation of slip systems with higher τ_{CRSS} or twinning. In contrast, grains with basal plane normals $\approx 45^{\circ}$

to the loading axis are defined as "soft" grains, with easier basal slip. A microstructure with evenly distributed hard and soft grains creates a weak texture that allows for more homogeneous deformation and larger strains to failure [27].

Recent studies using high-resolution digital image correlation (HRDIC) techniques have shown that grain boundary shear accommodates only a small percentage of the total strain, despite the strain at grain boundaries being the highest. Slip deformation mechanisms and twinning are strongly influenced by texture and microtexture through local stresses [27]. These findings highlight the importance of texture control in achieving desirable mechanical properties and formability in magnesium alloys.

The development of Ca-containing magnesium alloys reflects the industry's focus on balancing cost, mechanical properties, and manufacturability. While RE elements remain effective in improving ductility and texture control, Ca offers a cost-effective alternative with similar benefits. Advances in processing techniques and a deeper understanding of texture evolution during deformation hold significant potential for expanding the applications of magnesium alloys commercially.

2.3 Mechanical Testing For Sheet Metal

Understanding the complexity of formability is critical for effectively manipulating sheet metal during manufacturing processes. The tensile test is a well-established method for characterising key deformation properties of metals [7]. From tensile test data, several useful parameters for forming can be extracted, including the Lankford r-value, strain hardening exponent n-value and strain rate sensitivity m-value.

The r-value, which measures the ratio of width contraction to thickness contraction during a tensile test, and is an indicator of a material's ability to resist thinning. A

high *r*-value recurrently correlates with superior deep drawability. However, in Mg alloys, higher *r*-values do not always guarantee better deep drawability [7]. This is due to the anisotropic nature of Mg alloys, where asymmetry in *r*-values between the rolling direction (RD) and transverse direction (TD) can lead to non-uniform deformation. Interestingly, materials with similar *r*-values exhibit better drawability, suggesting that other factors, such as microstructure and texture, also play a significant role.

The strain hardening exponent, or *n*-value, is a measure of a material's ability to uniformly distribute strain during deformation. In Mg alloys, twinning contributes significantly to the early stages of strain hardening. However, the polar nature of twinning and its limited period of activity adds complexity to forming. For instance, partially twinned material may yield at lower stresses during later stages of deformation compared to the original microstructure. Work hardening, which is closely related to the *n*-value, is a key predictor of formability for several forming techniques. It helps avoid localised deformation by stabilising the material and promoting uniform strain distribution. The Considère criterion can be used to estimate the *n*-values from tensile and yield strengths, where *n* is equal to the strain at the onset of diffuse necking. These estimated values have been shown to agree well with direct measurements of *n* [7].Furthermore, the *n*-value is a critical parameter in forming limit diagrams (FLDs), which are used to characterise the behaviour of sheets in stretching applications.

The rate sensitivity, or *m*-value, describes the material's response to changes in deformation speed. A higher *m*-value indicates a greater resistance to necking and improved ductility at elevated strain rates. This parameter is particularly important in dynamic forming processes, such as high-speed stamping, where strain rates can vary significantly. In Mg alloys, the *m*-value is influenced by factors such as temperature, grain size, and activation of non-basal slip systems [55, 7]. By predicting material behaviour during forming, these values provide a framework for evaluating formability of Mg sheet alloys.

2.4 Overview of Plasticity Modelling of Polycrystalline Alloys

Contemporary computational tools offers many model types for simulating deformation mechanisms and microstructure evolution in metals and alloys. The most effective and efficient choice depends on the end goal. The length scale of the physical phenomena is an important consideration when choosing a model type.

At atomic scales, DFT studies twin boundary dynamics and $\langle c+a \rangle$ dislocation nucleation in Mg [56, 57], while MD simulations investigate slip/twin nucleation [58, 59, 60, 61]. Discrete dislocation dynamics models larger-scale phenomena like dislocation-grain boundary interactions [62, 63], providing fundamental insights into elastic constants and defects, though limited to small volumes [64].

Crystal plasticity models bridge scales by homogenising single crystal responses. Mean-field approaches like VPSC [65], EPSC [66], and EVPSC [36] efficiently predict texture evolution using self-consistent schemes [29, 67, 68], often matching full-field models [69] despite averaging limitations [70]. Full-field methods (CP-FEM [71, 72], CP-FFT [73]) better capture local heterogeneities and complex geometries [74], with CP-FFT revealing twinning mechanisms [73] and CP-FEM simulating forming processes [72] and 3D microstructures [74]. Phenomenological models [75] offer simplified deformation predictions but struggle with anisotropy evolution [71].

Given the pronounced anisotropy in HCP materials due to their low crystal symmetry, the self-consistent mean-field VPSC model is widely regarded as the most suitable approach for Mg alloy modelling. Its simple computational setup makes it an effective tool for probing texture evolution during deformation. The following section details key features of the model and examples of its use.

2.5 Visco-Plastic-Self-Consistent Modelling

The VPSC model was originally developed to model plastic deformation of low-symmetry materials i.e. for HCP metals like magnesium. Building on early popular self-consistent (SC) models, Molinari et al.,[68], Lebensohn and Tome [65] developed the VPSC model accounting for texture evolution during deformation activity. The mechanical regime of viscoplasticity is described as time-dependent plastic deformation, viscoplastic materials exhibit a rate-sensitive response.

Self-consistency prescribes that the overall behaviour of the polycrystal is based on the average of the total behaviour of its individual grains by considering the interactions between them. A feature of self-consistent models is the interaction equations that linearly link the stress and strain rate of individual grains to the equivalent magnitudes in the aggregate/homogeneous effective medium (HEM). The primary interactions used are:

The Taylor-Bishop-Hill [29, 67] full constraints (FC) assumption of equal deformation applied to every grain ignores anisotropy but fulfils the compatibility condition. The resultant interaction is extremely rigid (upper bound), this interaction performs well with more isotropic crystals. The pioneering Sachs model [76] is known as the lower bound, it assumes uniform stress on each grain equal to the macroscopic deformation. The relaxed constraints (RC) [77] allows for some grains to differ from the average but is limited to highly distorted grains. Molinari et al [68] contributed to developing a grain-matrix interaction that is neither completely rigid nor fully relaxed by the idea of a cluster of grains surrounded by a homogeneous anisotropic matrix. A fundamental problem for all polycrystal models is the interaction of a grain with its neighbours, where the interaction governs how much plastic deformation is accommodated by each. Therefore, if anisotropy of the single crystal ultimately contributes to the anisotropy of the polycrystal, both grain and matrix anisotropy should explicitly be in the formulation

[65] to accurately predict deformation of HCP metals. Previous attempts with an elasto-visco-plastic scheme on FCC materials converged to the results of a FC assumption.

Lebensohn and Tome's [78] approach involves each grain as an inhomogeneous inclusion within a HEM to describe the polycrystal. This formulation results in an interaction that linearly relates the resulting strain rate in the grain with the HEM. A condition that ensures the average of the strain rate over all grains is consistent with the macroscopic magnitudes enforces the self-consistent aspect of the problem. Within this version they explicitly account for; plastic anisotropy of grains and matrix, grain shape effects and how they change with deformation. The VPSC scheme provides the structure to modify the strength of this interaction while the relative stiffness of grain and HEM is still accounted for.

Material hardening during deformation is another important aspect of plasticity modelling. Various hardening laws can be implemented with the VPSC formulation to describe the resistance slip or twinning modes experience during deformation; which generally increases with more deformation. They empirically describe the initial CRSS for each deformation mode and the evolution of this threshold stress during deformation. Obstacles to dislocation movement on individual slip systems via interaction with lattice defects such as grain boundaries, twin boundaries, precipitates and dislocation structures are empirically described by constants and equations. The extended Voce law by [79] and dislocation density-based hardening law, Beyerlein and Tome [80], are the most commonly used.

2.5.1 Use of the Dislocation Density Hardening Model

Material hardening during deformation is a crucial aspect of plasticity modelling. In the VPSC formulation, various hardening laws can describe the resistance encountered

by slip and twinning modes during deformation, which generally increases with strain. These laws empirically define the initial critical resolved shear stress (CRSS) for each deformation mode and its evolution as deformation progresses. Factors such as grain boundaries, twin boundaries, precipitates, and dislocation structures act as obstacles to dislocation movement on individual slip systems, and their effects are captured through empirical constants and equations. Among the commonly used models are the extended Voce law proposed by Tomé et al.,[79] and the dislocation density-based (DD) hardening law developed by Beyerlein and Tomé [80].

The DD hardening model introduced strain rate and temperature-dependent hardening parameters to improve deformation predictions. Building on this, Oppedal et al.,[81] applied the DD hardening model to simulate final textures in pure Mg. While the model successfully captured final textures, discrepancies arose in intermediate textures. These differences were attributed to the model's limited representation of multi-variant twinning, which was observed in EBSD but absent in the simulations.

Knezevic et al.,[82] also utilised the DD model to investigate the relationship between compression twin variants, temperature, and texture evolution. Their study demonstrated that twin re-orientation, as seen in EBSD, was linked to temperature effects. At moderate strains of 0.18 and higher strains of 0.44, the model accurately predicted the volume fraction of secondary twins during two distinct deformation states. However, the specific twin variant observed in each case differed, which was attributed to temperature-dependent variant selection.

An interesting observation from these studies was the assumption that twinning is rate-independent, with the preference for certain twin variants instead being influenced by the strain rate and temperature dependence of slip. This highlights the model's ability to predict twin preference by altering slip mode activity, underscoring the interconnected nature of deformation mechanisms in Mg alloys.

Despite these advancements, some experiments have reported differences between predicted and measured twinning statistics [83, 81, 4]. These discrepancies have been attributed to the model's incomplete integration of all microstructural dependencies relevant to twinning behaviour.

2.5.2 Simulating Twinning with VPSC

Accurately simulating texture evolution in HCP metals requires incorporating grain reorientation mechanisms, as twinning can induce abrupt texture changes or even inhibit texture evolution during plastic deformation. The VPSC model facilitates statistical analysis of key factors such as twin mode activity, twin volume fraction, variant selection, and the hardening effects arising from twin boundaries acting as barriers to dislocation motion.

The Volume Fraction Transfer (VFT) scheme, introduced by Tomé et al.,[84, 85, 65], addresses the significant influence of twinned fractions on texture evolution. The VFT scheme is particularly effective in scenarios where twinning dominates the deformation response. However, a key limitation of the VFT scheme is its transfer mechanism, which results in the loss of grain reorientation history [35]. This loss can adversely affect the accuracy of the applied hardening scheme. Additionally, Lebensohn et al.,[86] highlighted further shortcomings in self-consistent (SC) models using the VFT scheme, noting that such models fail to account for stress relaxation following twin activity.

An alternative approach is the Monte-Carlo method developed by Van Houtte [87], which applies a probabilistic criterion to determine when the original grain orientation is replaced by one of the twinned orientations. The Composite Grain (CG) model, introduced by Proust et al.,[83], builds upon the earlier Parent-Twin Reorientation (PTR) scheme developed by Tomé et al.,[84]. In the CG model, twin fractions are tracked until

a threshold value (typically 50%) is reached, at which point the entire grain adopts the predominant twin system (PTS) orientation. While the PTR scheme simplifies twinning by focusing on predominant twins, it does not account for directional hardening effects induced by twin boundaries acting as dislocation barriers. To address this, the CG model introduces a latent hardening term associated with twin shear. The CG model also improves upon the PTR scheme by retaining information about the original grain (parent) and twin fractions (child). The twinned grain is treated as a composite structure with alternating twin and matrix lamellae, improving the model's ability to capture the microstructural complexity of twinned regions.

Kaschner et al.,[88] explored the model's capability to capture secondary twins during microstructural evolution. Their study on Zr found that the predicted contributions of primary and secondary twins (twins forming inside primary twins) in compression simulations closely matched neutron diffraction data, which measured textures and twin volume fractions. These results were further supported by orientation imaging microscopy (OIM) observations of microstructural evolution.

Proust et al.,[83] developed the Composite Grain (CG) model, which calculated the volume fractions of both primary and secondary twins with reasonable agreement to experimental data. While their findings aligned with Kaschner et al.,[88], discrepancies arose due to differences in experimental techniques. For instance, EBSD data provides an upper bound estimate for twin volume fractions due to its limited field of view, whereas neutron diffraction may undervalue secondary twinning since regions with net zero orientation change can be overlooked.

Brown et al.,[89] also employed the VPSC model alongside neutron diffraction. Although their calculated final textures matched the measured bulk texture well, the model overestimated twin activity at earlier stages, causing a deviation in the predicted stress-strain curve. However, both the model and experimental data converged to the same

final strength at maximum strain.

To better capture the stochastic nature of twinning, Beyerlein and Tomé [4] treated twinning as a process governed by a critical resolved shear stress (CRSS), similar to slip. They introduced a probabilistic twin nucleation model, which employed a nucleation algorithm at each strain increment. This improved upon earlier deterministic twin nucleation models by predicting twin fractions at low strains (e.g., 5%) that aligned well with EBSD measurements. Fig. 2.4 shows the VPSC prediction vs EBSD measurements. Their results supported the idea that twin nucleation occurs before significant stress-strain curve changes become apparent.

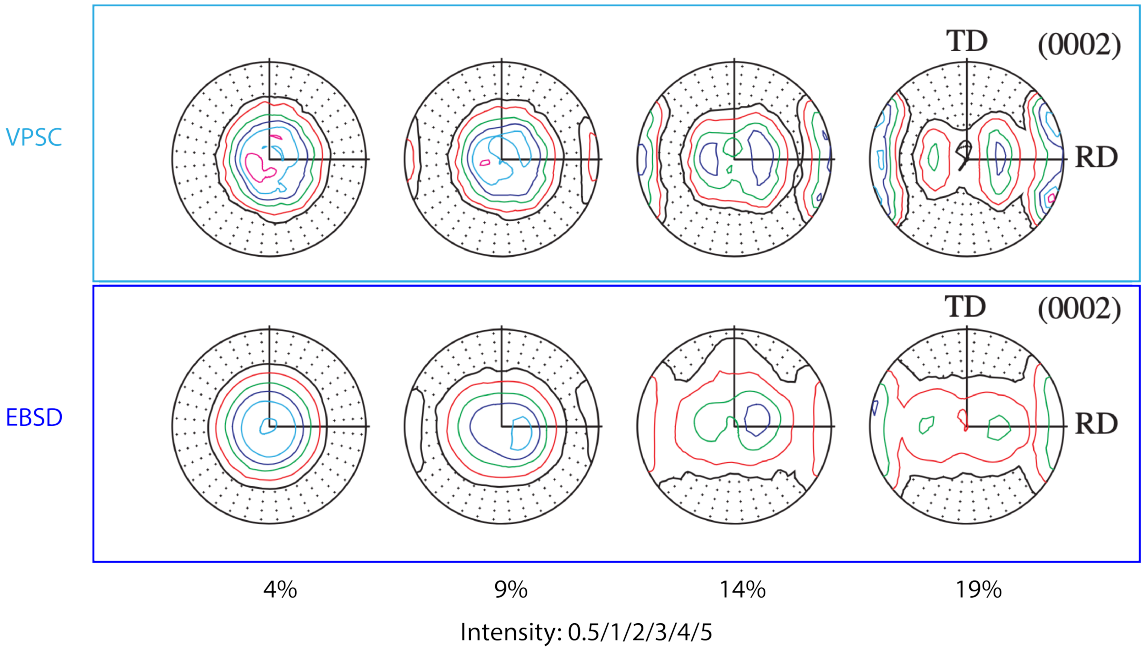


Figure 2.4: Texture evolution under compressive stress in the RD direction for clock-rolled Zr, reorientation of the basal poles along the RD due to $\{10\bar{1}2\}$ twinning from 9% onwards, modified from Beyerlein and Tome [4].

For clock-rolled Zr, the model effectively predicted twin distribution by assigning Schmid factors to grains. The predicted twin distribution in grains with Schmid factors greater than 0.4 showed strong correlation with EBSD data at both 5% and 10% strain.

2.5.3 Capabilities of the VPSC model

Early applications of the VPSC model to magnesium alloys were demonstrated by Agnew et al.,(2001) [90] and Agnew et al.,(2005) [25]. In the former study, texture evolution during the deformation of pure magnesium was compared to alloys containing lithium and yttrium [90]. By incrementally probing the CRSS ratio of basal to pyramidal slip ($\tau_{\text{basal}}/\tau_{\langle c+a\rangle}$), the authors found that this ratio largely dictated the resulting texture. Increasing $\langle c+a\rangle$ slip activity simulated the characteristic basal pole split in the (0002) pole figure for the alloys, a result corroborated by TEM observations [91]. These findings illustrate how alloying additions influence slip activity.

In a subsequent study, Agnew et al.,(2005) [25] investigated AZ31 and manipulated the CRSS ratios for slip systems: $\tau_{\text{prism}}/\tau_{\text{basal}}$ and $\tau_{\langle c+a\rangle}/\tau_{\text{prism}}$. When the $\tau_{\langle c+a\rangle}/\tau_{\text{prism}}$ ratio fell below a critical threshold, $\langle c+a\rangle$ slip activity increased, accompanied by a reduction in the r-value, suggesting improved formability. Agreement with high-temperature texture evolution was also achieved by promoting increased $\langle c+a\rangle$ slip activity.

Dogan et al. [92] effectively captured the texture evolution of AZ31 during equal channel angular processing (ECAP), a challenging process to examine experimentally. To calibrate the model, tensile and compressive tests were conducted in various directions at the typical processing temperature of 150°C. By investigating two different starting textures, the authors clarified the influence of initial texture on slip and twinning activity. Their findings demonstrated that the formability limit of AZ31 could be reduced to 150°C by suppressing compression and double twinning while promoting prismatic slip. EBSD measurements confirmed dynamic recrystallisation (DRX) in the microstructure, driven by twinning. The localised DRX within the compression twins leads to shear bands, which ultimately results in shear band formation and subsequent crack initiation, twinning here is detrimental to the low-temperature ductility.

Similarly, Vaughan et al. [33] observed DRX within extension twins after uniaxial tensile deformation at $100 - 200$°C. Their model showed that promoting prismatic slip at 150°C effectively suppressed twinning, enhancing ductility and mitigating DRX within twinned regions, corroborating the findings by Dogan et al. [92].

To better capture DRX effects in HCP metals, Zecevic et al. [5] extended previous work [93, 94, 95] by introducing a VPSC-based recrystallisation model for a non-cubic Mg WE43 alloy. Their model accurately simulated texture evolution driven by DRX. By calibrating an extended dislocation density (DD) hardening model using true stress-strain curves over a range of strain rates (0.001–0.01 s^{-1}) and temperatures (300–625 K or $27 - 352$°C), they achieved good agreement with experimental data even at higher strain rates (1.0 and 10.0 s^{-1}), shown in Fig. 2.5. Discrepancies were mainly observed at temperatures where DRX was absent, highlighting the hardening model's limitations in such conditions. Nevertheless, the model effectively captured dislocation density trends and their temperature dependence. The model provided dislocation densities for the active slip systems that correlated with the increase in dislocation removal at higher temperatures.

Tam et al. [96] extended the DD model further to better capture high-temperature deformation in AZ31. By incorporating improved temperature dependence for dislocation-dislocation interactions and drag stresses, their model achieved good agreement with stress-strain responses at 25–200°C across three plate directions (ND, TD and $45°$), alongside accurate texture predictions.

Miller et al. [97] explored the role of starting textures on plastic anisotropy using 'synthetic' microstructures fed into the VPSC model. Building on previous work [98], they generated microstructures with strong, medium, and weak basal textures based on (0001) pole figures. Their simulations revealed that strong basal textures corresponded to high r-values and poor formability, while increased prismatic slip activity intensified

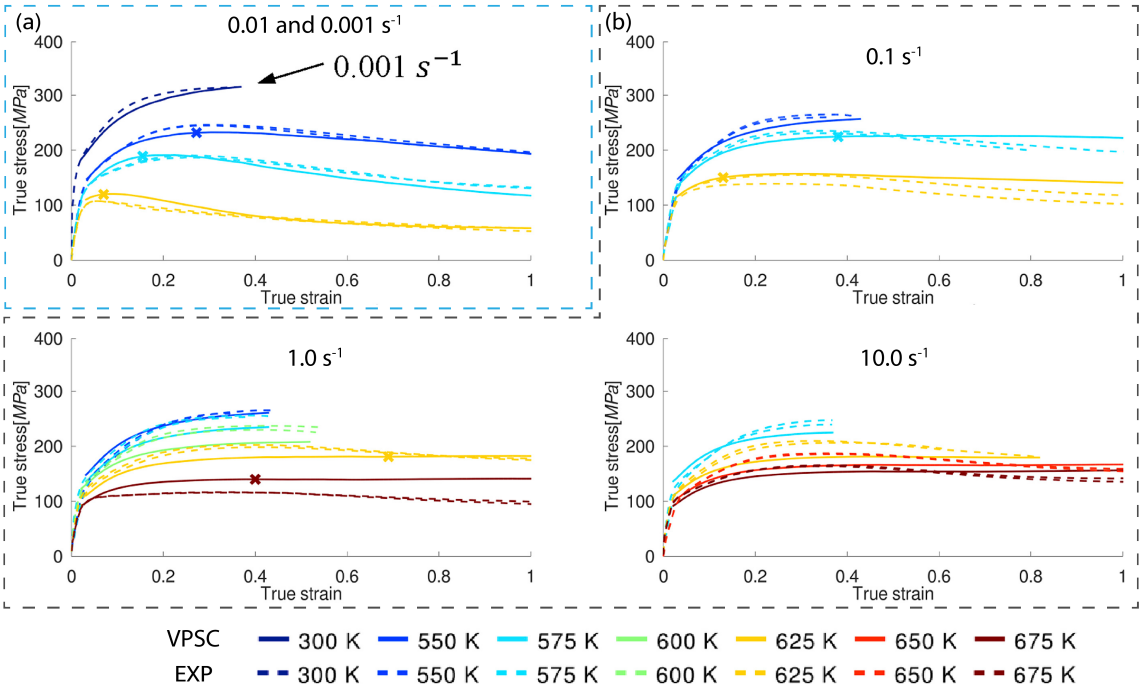


Figure 2.5: Experimental curves used to calibrate the model at strain rates: (a) $0.001s^{-1}$ and $0.01s^{-1}$, & (b) $0.1s^{-1}$, $1s^{-1}$ and $10s^{-1}$, alongside VPSC simulated curves. Adapted from Zecevic et al. [5].

basal peak strength and promoted twinning, ultimately reducing formability.

Despite the limitations of mean-field models in capturing complex microstructural effects, Ren et al.[99] successfully applied the VPSC model to an age-hardenable Mg alloy. By investigating precipitate morphology changes during ageing experimentally, they then linked disk-shaped (10 hours) and rod-like (30 hours) precipitates to slip and twinning activity using VPSC. After 30 hours of ageing, prismatic slip activity was significantly reduced, while basal and pyramidal slip compensated. TEM observations confirmed the morphological evolution of precipitates, and corresponding τ_{CRSS} changes were consistent with Orowan strengthening theory. Evolved textures from simulations closely matched experimental data, showing reduced extension twinning in the presence of β_1' precipitates.

Beyerlein et al. [100] applied the VPSC model to simulate the equal channel angular extrusion (ECAE) process, incorporating a grain co-rotation scheme that paired grains

randomly to simulate co-rotation. This modification slowed texture evolution, producing results that better represented ECAE textures. The model successfully captured both morphological and crystallographic texture evolution, showing that certain deformation routes (involving rotations after each pass) produced textures resembling continuous deformation, which are less detrimental during processing.

Many authors calibrate the VPSC model by fitting stress-strain curves to determine material parameters. However, Miller et al. [101] proposed an alternative least-squares optimisation approach using orientation distribution functions (ODF) to reduce discrepancies between experimental and simulated textures. While both methods produced reasonable results, the stress-strain approach better predicted measured strengths at low strains, whereas the ODF method excelled at predicting phase-specific textures. Both struggled at higher strains due to unaccounted microstructural complexities. This approach utilised the MATLAB based tool box MTEX [102], a similar optimisation method was developed by Begley et al. [103] for stress-strain response calibration.

Tuning material parameters is a necessary but challenging aspect, depending on the material, deformation(number of active slip and twin systems) and hardening law, the number of parameters can be greater than 12. To simplify VPSC calibration, Chen et al. [104] employed a minimal parameter approach, drawing from prior work [105, 106]. By analysing material behaviour across multiple deformation states or using single-test parameters from the literature, they introduced physically based arguments connecting hardening on different slip systems. They successfully reduced the required number of hardening parameters from 12 or more to just 3. While this method showed acceptable agreement with stress-strain data, deviations in evolved textures highlighted extremes in pyramidal $\langle c + a \rangle$ activity resulting from parameter reduction.

2.5.4 Application of VPSC Model to Ca-containing Mg alloys

Several studies have employed the VPSC model to investigate how the dynamics of various deformation mode activity changes with Ca additions. While the improved formability associated with Ca additions is largely attributed to changes in the starting texture, more complex mechanisms may also be involved. Ca is known to weaken the strong basal texture typically seen in recrystallised Mg microstructures after thermomechanical processing, which often coincides with enhanced formability [107].

Several studies to date have explored the capability of the VPSC scheme to underpin changes in CRSS and slip activity. Kim et al. [107] applied the model to AZ31 and AZX311 alloys, while Chaudry et al.,[6] examined AZ31 and AZ31-0.5Ca (wt%). Fig. 2.6 provides a brief overview of the data extracted by Chaudry et al.,(2019). Both studies found that Ca-containing alloys exhibited higher initial basal slip activity. In both alloy types, deformation initially dominated by basal slip transitioned to increasing prismatic slip activity. However, the Ca-containing alloys displayed a more pronounced increase in prismatic slip activity compared to their Ca-free counterparts.

Kim et al. [107] observed slip activity predictions that could elucidate the anisotropy seen in the macroscopic tensile curves. Chaudry et al. [6] attributed the presence of $(Mg,Al)_2Ca$ intermetallics to the changes in basal/prismatic slip activity. Primarily an increase in τ_{CRSS} for basal slip altering the basal/prismatic τ_{CRSS} ratio, because despite a difference in initial texture they show the Schmid factor for prismatic slip was equal for both microstructures. Similar findings regarding $(Mg,Al)_2Ca$ intermetallics were made by Kim et al. [107] and Park et al. [108], with Park's study focusing on a lower Al content Zn-Al-Ca alloy that also formed Al-Ca intermetallics. The VPSC model's ability to predict texture evolution was further demonstrated by Chaudry et al. [109], where experimentally observed texture changes at varying strain levels were successfully reproduced.

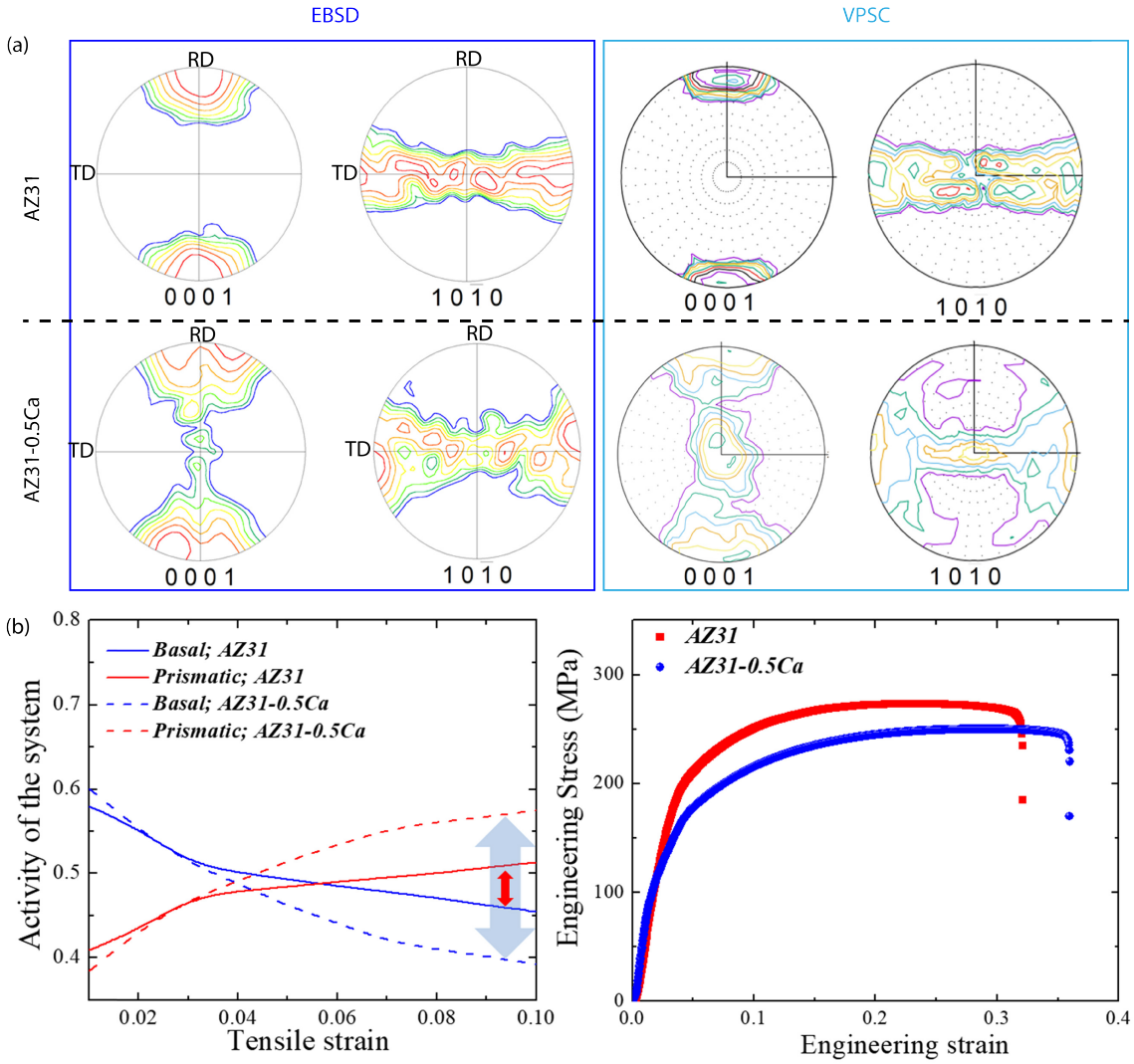


Figure 2.6: (a)Texture evolution post 10% tensile deformation for two Mg-alloys, (b) difference in predicted slip activity for both alloys, adapted from Chaudry et al. [6].

In a related study, Victoria-Hernandez et al. [110] used VPSC modelling to replicate experimental textures in a Mg-Zn-Ca alloy under two loading conditions at elevated temperatures (350°C). Their optimised CRSS and hardening parameters predicted slip activity trends consistent with previous studies, where initial high basal slip activity was rapidly surpassed by prismatic slip. At higher temperatures, pyramidal slip activity also became prominent, proving the models capability to combine orientation change to slip activity. While this pyramidal slip activity contrasted with observations in tension studies [6, 109], it aligned with Park et al [108] compression data. Both Victoria-Hernandez et al. [110] and Park et al. [108] reported accurate predictions of the macroscopic stress-strain response.

The Visco-Plastic Self-Consistent (VPSC) model emerges as a pivotal tool for simulating texture evolution and anisotropy in Mg alloys, balancing computational efficiency with predictive accuracy. Key strengths include its ability to incorporate grain-matrix interactions, empirical hardening laws (e.g., Voce, dislocation density), and advanced twinning schemes (e.g., Composite Grain model). However, limitations such as mean-field approximations and challenges in capturing localized microstructural effects highlight the need for experimental validation. The review underscores VPSC's utility in probing alloy-specific deformation (e.g., Ca-containing Mg systems) and informs the its methodology used in this investigation, particularly in calibrating CRSS parameters, interpreting texture development, and selecting hardening laws for subsequent results chapters. All the aforementioned simulations used the Voce hardening law, which lacks rate and temperature dependence. Future calibration of VPSC models for Ca-containing alloys may benefit from incorporating a rate and temperature-dependent hardening law, such as the DD hardening law [80].

Collectively, these studies also highlight a strong link between initial texture and the faster transition from basal to non-basal slip activity in Ca-containing alloys compared to conventional Mg alloys. While evidence suggests that $(Mg,Al)_2Ca$ intermetallics con-

tribute to τ_{CRSS} modifications, the limitations of the VPSC model's inherent limitations, particularly its length scale and inability to sufficiently account for microstructural features such as intermetallic inclusions, makes it challenging to fully validate these ideas.

Chapter 3

Experimental methods

Three automotive grades of magnesium alloys were supplied by Volkswagen in sheet form, produced via twin roll casting with a final thickness of 1.1 mm, then annealed in a proprietary condition, achieving equiaxed microstructures.

Alloy name	Mg	Al	Ca	Zn	Zr
AZ31	bal	3		1	
ZXK	bal		0.6	0.6	0.1
AZX	bal	2.3	0.5	0.8	

Table 3.1: Nominal composition of magnesium alloys studied in weight %.

3.1 Metallographic Preparation

Surface preparation for metallographic studies comprised the use of abrasive media using silicon carbide paper. Typically, 800 grit was initially used to create a planar surface, then successively fine grades were used down to 4000 grit. Special care was taken to clean equipment and gloves in-between steps, to avoid large particle size contamination in subsequent steps. Polishing was performed with water free diamond suspensions; 3 to

0.25 µm mixed with a water free lubricant. Each step was 3-5 minutes. Electropolishing was necessary for a surface finish suitable for EBSD measurements. The electrolyte was composed of 6% perchloric acid (60% concentration) and 94% ethanol. To cool the electrolyte down to -30°C, liquid nitrogen was poured directly into the solution; the temperature was measured with a thermometer and was maintained with subsequent pours if needed. Electropolishing was performed using a Struers Lectro-Pol 5 with a 0.5 mm^2 mask. The process was conducted at 20 V, a flow rate of 10 for a polishing duration of 90 seconds. This was followed by an immediate submersion of the sample into an ethanol bath to prevent further etching.

3.2 DIC & Tensile Tests

Uniaxial tensile tests were performed on an Instron with a 5kN load cell, along the RD and TD of each alloy, at room temperature. Tests were performed at 3 constant strain rates: $5\times10^{-2}\,s^{-1}$ (60 mm/min), $5\times10^{-3}\,s^{-1}$ (6 mm/min), $5\times10^{-4}\,s^{-1}$ (0.6 mm/min). These experiments served as an initial investigation into the room temperature behaviour of each alloy ie. anisotropic behaviour, strain rate sensitivity, and to compare them with current literature. Dogbone tensile specimens were machined according to the standard 'DIN 50125 type H test pieces'. Strain measurement was performed using digital image correlation (DIC), an image based point tracking technique utilising a surface pattern for the camera(s) to track. The surface was prepped by grinding using fine silicon carbide paper (2500 grit) and cleaning with ethanol. A uniform white base was sprayed on, then a random black speckle pattern sprayed on top, see Fig. 3.1. The speckle pattern was optimised by adjusting the spray to sample distance and spray dwell time. The DIC footage was captured using a THORLABS compact scientific camera and Thorcam software, in the set up displayed in Fig. 3.1 The videos were captured in greyscale within a region of interest (ROI) of 1392 × 1040 pixels, using pixel binning of 2 for

x and y and a frame rate of 29.9 frames per second. The videos were converted into their individual frames with the software VLC, using a scene filter that saves a frame at every chosen frequency (e.g. every 10^{th} frame). For the lower strain rate every 100^{th} frame was analysed, and every 10^{th} for the others. The open-source MATLAB-based 2D DIC software package 'Ncorr' was used for this analysis. The algorithms and theory implemented in Ncorr are documented here [111]. An average strain was calculated per frame, the start/end points from both camera and Instron synchronised, then the strain data interpolated with the Instron force readings due to having more frames than sample rate from the Instron.

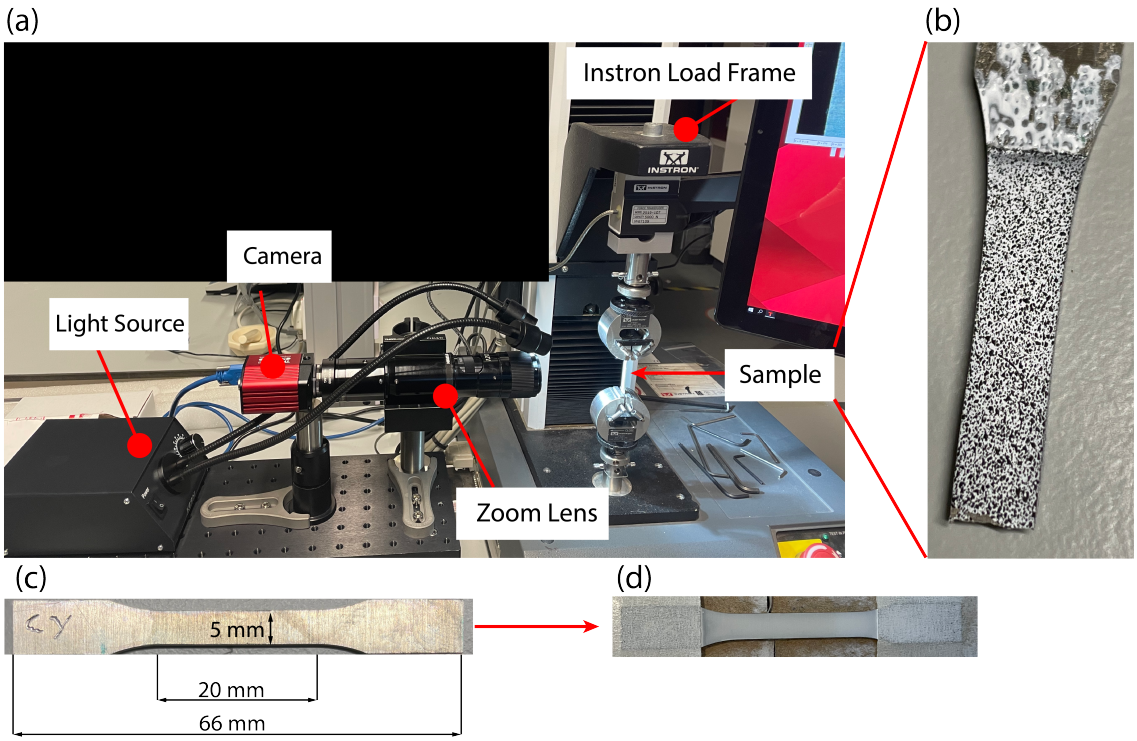


Figure 3.1: (a) DIC set-up, (b) sample with speckle pattern, (c) original sample with dimensions and (d) sample with white base for the first step of DIC speckle pattern preparation.

3.3 X-ray Synchrotron Diffraction

High energy in situ X-ray diffraction experiments on the I12 beamline at the Diamond Light Source were performed. A Deben MT5000DL 5 kN load frame equipped with sample heating was used; this was positioned onto the beamline sample stage in the beam-path, with the tensile axis of the samples set perpendicular to the incident X-ray beam. A schematic of the sample dimensions are shown in Fig. 3.2 and an illustration of the experiment configuration is shown in Fig. 4.12. High temperature testing required a sealed vacuum controlled environment; the tensile stage was housed within an enclosure that had glass windows front and back. The diffraction from this glass was considered in background removal. A $0.5 \times 0.5\,\mathrm{mm}^2$ monochromatic incident beam of energy ($60.0\,\mathrm{keV}$) was used, calibrated with a CeO_2 standard. This beam size ensured diffraction from a statistically appropriate number of grains through 1.1 mm thick samples. Transmission diffraction patterns were collected in full Debye Scherrer rings on the Pilatus 2M CdTe 2D area detector at a frequency of 1 Hz during constant deformation. The acquired patterns were radially integrated into 36 sections ('caking' technique), each section having 10° of azimuthal rotation in the range $0^\circ \leq \psi < 360^\circ$. This was performed using the Dawn 2 software [112]. By doing this, families of planes in the bragg diffraction condition due to grain orientation, ± 5 to major/minor strain directions, could be isolated. In house scripts based on earlier studies [113] were written in MATLAB for peak fitting with a pseudo-Voigt function on reflections from the following planes;$\{0002\}$, $\{10\bar{1}0\}$, $\{10\bar{1}1\}$, $\{11\bar{2}0\}$, & $\{11\bar{2}2\}$. The position, width and integrated intensity of each peak was recorded. To evaluate the fitting confidence, a χ^2 metric was calculated between the measured and fitted peaks to obtain a proxy for the fitting error. A 95% confidence interval was used for peak position and width error, calculated using the coefficient prediction, residual and Jacobian matrix.

Uniaxial testing was performed both at room temperature and elevated temperatures.

For room temperature tests, two strain rates were studied: $3\times10^{-3}\,s^{-1}$ and $3\times10^{-4}\,s^{-1}$. These tests were performed for each alloy using dogbone tensile samples machined with the gauge length parallel to either the rolling direction or transverse direction of the sheet. These tests were repeated at 150°C and 250°C. The heating of samples was achieved via conduction through heated grips, and the temperature was monitored via a k-type thermocouple in contact with the gauge region secured via 0.5 mm copper wire, shown in Fig. 3.2. Samples were initially heated to the test temperature, reaching the target temperature in increments of 25°C. This procedure was manually controlled to monitor and compensate for any thermal expansion of samples in the grips; the load on the sample was kept to $<$20 N while heating. Samples were aligned, with the aid of an X-ray imaging camera, prior to deformation such that the incident X-ray beam was approximately at the centre of the specimen gauge region. Prior to the beamline experiment the cross-head speeds were converted to strain rates using the DIC technique with the Deben stage ex-situ.

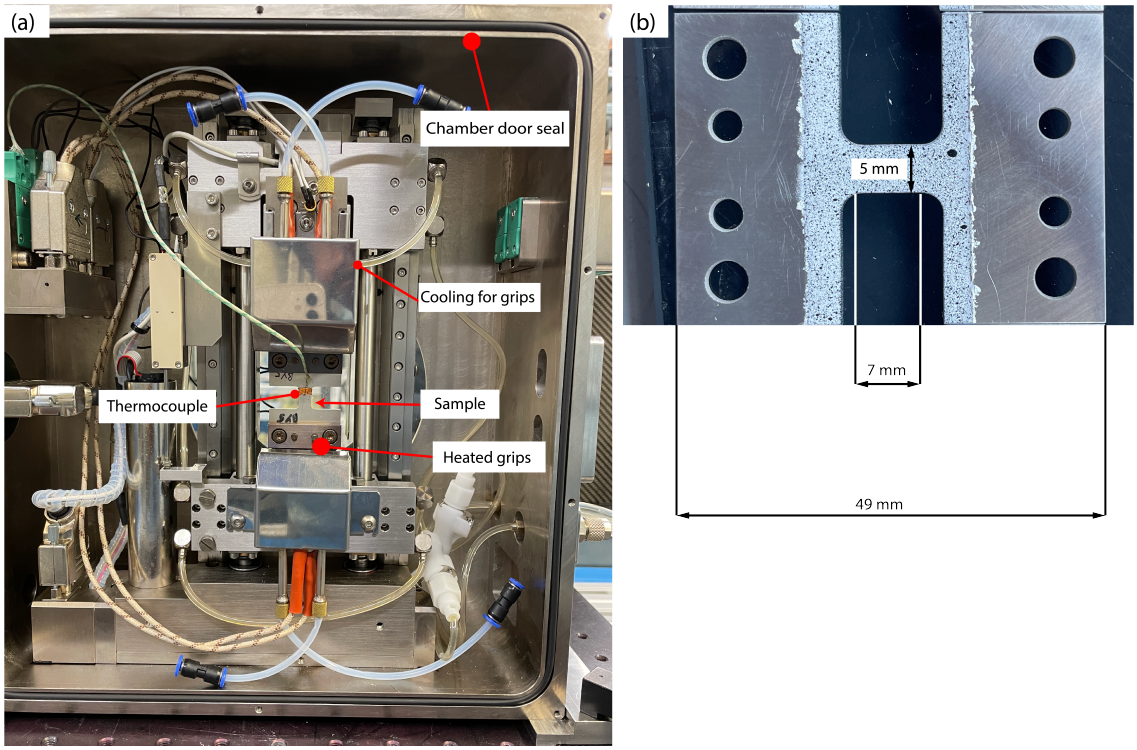


Figure 3.2: (a) Deben MT5000DL with sample mounted and door off, (b) sample used for ex-situ strain rate testing, important dimensions described.

3.4 In-situ EBSD

An in-situ uniaxial tensile loading experiment was performed using a scanning electron microscope (SEM) in conjunction with a Deben Microtest MT2000 tensile stage. The stage has a 2 kN loadcell and 70° pre-tilted specimen grips, orientated for EBSD measurement. This microscope used was a ThermoFischer Apreo 2 S HiVac FEG-SEM, equipped with Oxford instruments Symmetry S3 EBSD detector, with the following SEM conditions: working distance of $20\,\mathrm{mm}$, $20\,\mathrm{kV}$ accelerating voltage and $9.0\,\mathrm{nA}$ probe current. EBSD orientation maps were collected from an area of $75\,\mu\mathrm{m} \times 75\,\mu\mathrm{m}$ with a $0.25\,\mu\mathrm{m}$ step size. Electron backscattered patterns (EBSPs) showing Kikuchi patterns were acquired at a 1244×1024 pixel resolution, with frame averaging of 2 applied. The detector and data collection was controlled with Aztec. The sample in-situ with an example Kikuchi pattern is shown in Fig. 3.3. The raw EBSPs were saved for post processing, along with the background image (background image from the detector when the beam is off, used for a static background subtraction during indexing). Dogbone shaped tensile specimens with a gauge length of $3\,\mathrm{mm}$ and gauge width of $2\,\mathrm{mm}$, were machined from $1.1\,\mathrm{mm}$ thick sheets in both RD and TD directions. Specimen surfaces were prepared according to the metallographic preparation recipe given. Ex-situ tensile tests were performed to

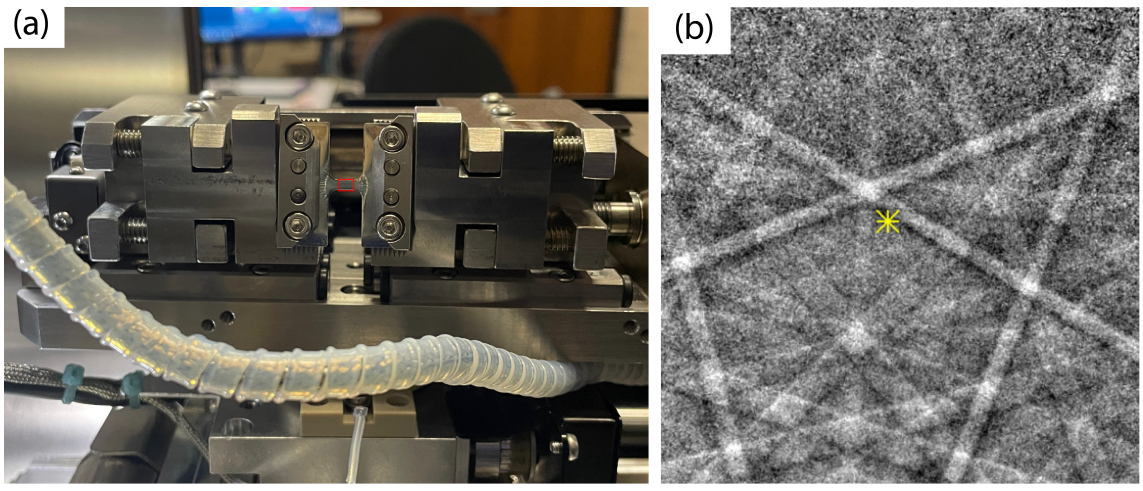


Figure 3.3: (a)Digital image of a tensile sample mounted in the In-situ tensile grips and (b) Electron back scatter diffraction pattern showing the Kikuchi bands.

obtain accurate stress targets for the in-situ interrupted tensile tests. Tensile loading was performed at a constant cross-head speed of 0.18 mm/min corresponding to a strain rate of $3 \times 10^{-3}\,\mathrm{s}^{-1}$, to appropriate force targets. Meaning the stage maintained a constant cross-head speed until a desired force was achieved.

EBSD data was analysed in MATLAB with utilising the MTEX library, an open source toolbox for modelling and analysing crystallographic textures [102].

Chapter 4

Initial Characterisation and In-situ X-ray Synchrotron Investigation

4.1 Initial Microstructure and Texture

Figures 4.1, 4.2 & 4.3 show the initial condition of the three alloys to be studied; AZ31, AZX and ZXK. Their grain structures comprise relatively equiaxed grains, notably the AZ31 alloy has areas of larger grains and smaller grains. The band contrast images are used to reveal features of the microstructure. These maps indicate the quality of the diffraction patterns obtained by analysing intensity variations between diffraction patterns and producing a grey scale based on these variations. Assuming good sample preparation, the quality of diffraction pattern and therefore band contrast is typically affected by defects, deformation or strain and amorphous structures. The band contrast obtained for these alloys in the initial condition shows high band contrast across the microstructures (excluding grain boundaries and polishing artefacts) suggesting well-defined grains with very low deformation present. The AZ31 pole figures shows the strong basal texture in the (0001) pole figure with a slight spread in the rolling direction

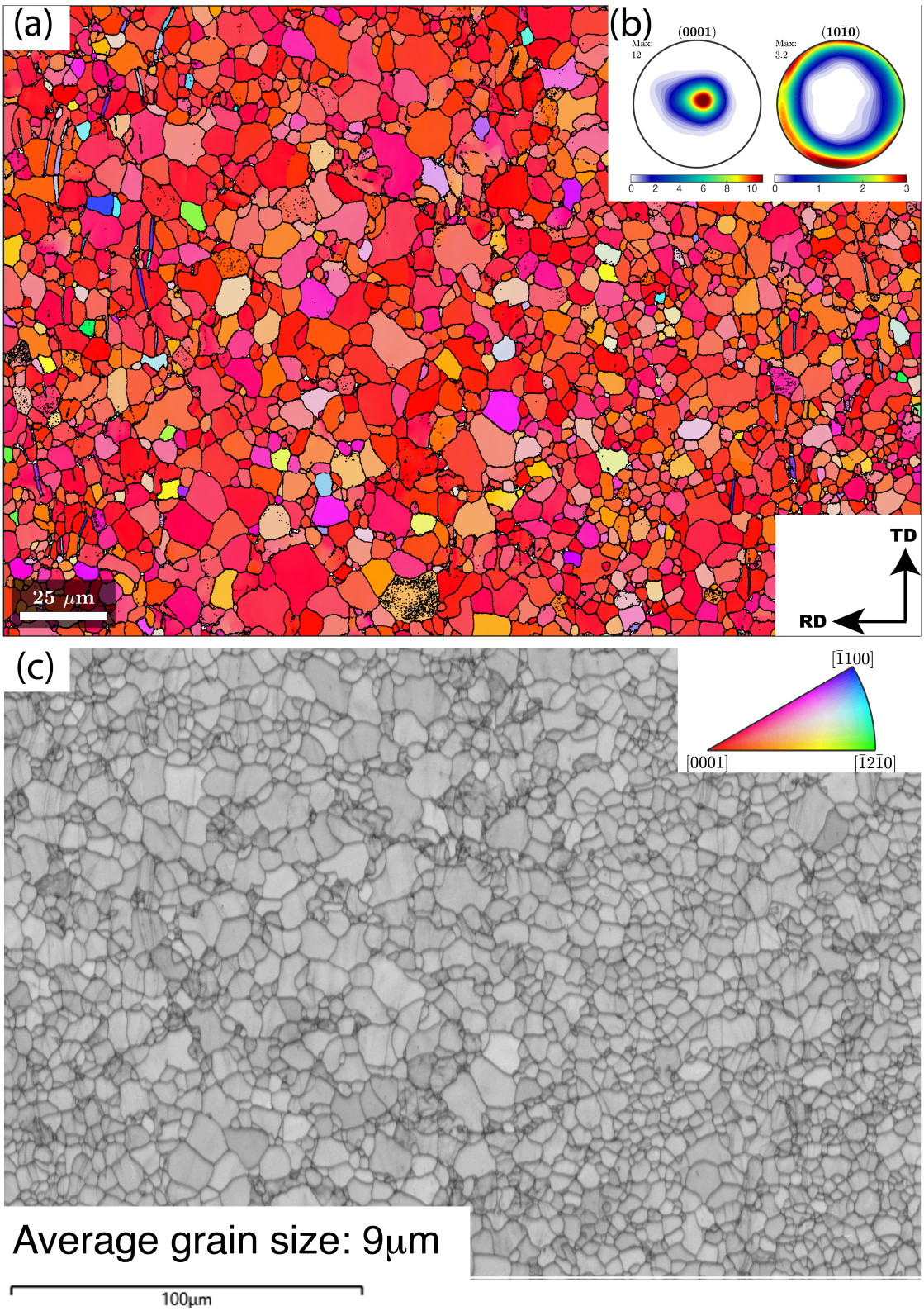


Figure 4.1: Initial condition of AZ31 alloy, (a) Inverse Pole Figure map, (b) (0001) & $(10\bar{1}0)$ Pole figure and (c) Band contrast map.

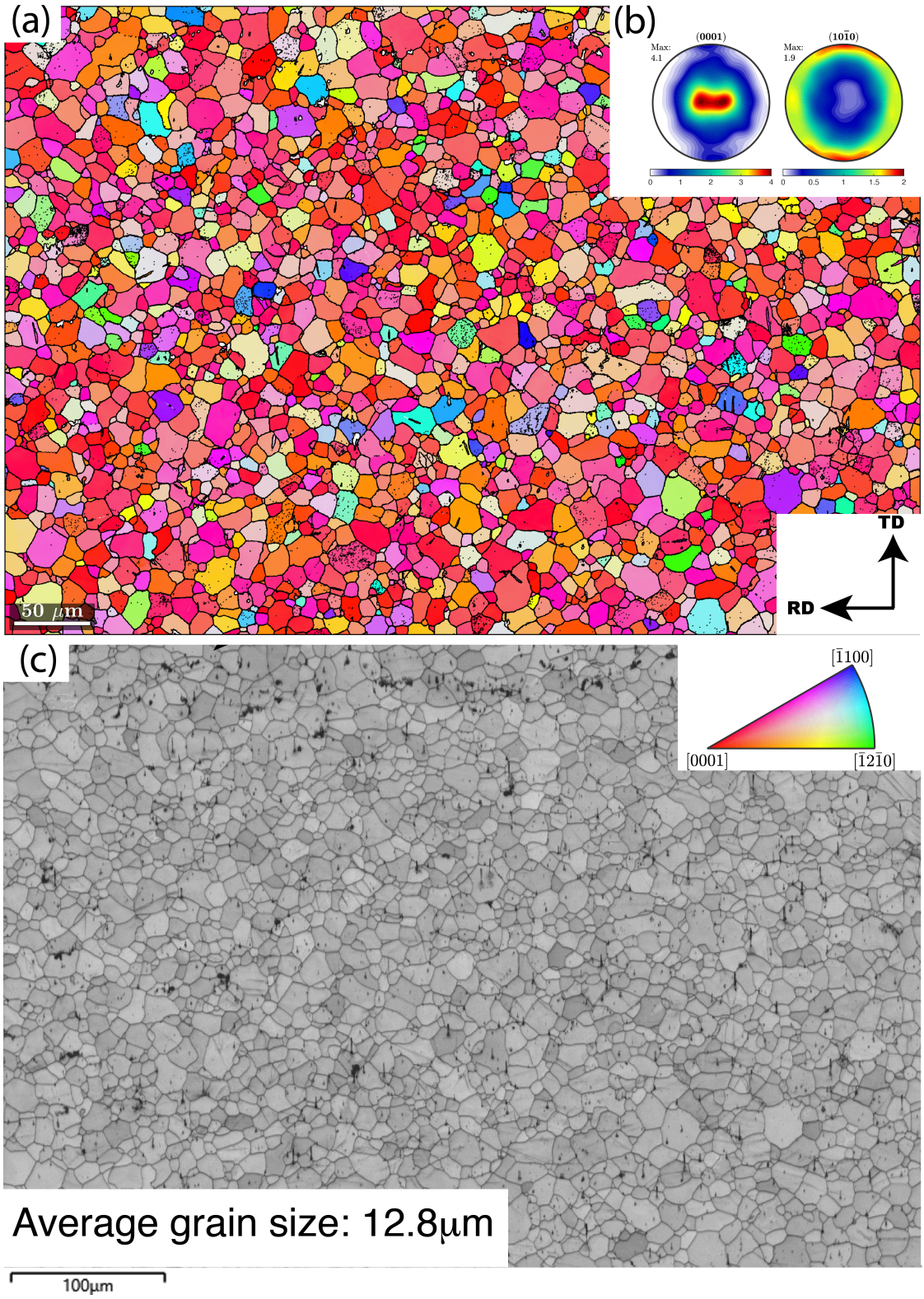


Figure 4.2: Initial condition of AZX alloy, (a) Inverse Pole Figure map, (b) (0001) & $(10\bar{1}0)$ Pole figure and (c) band contrast map.

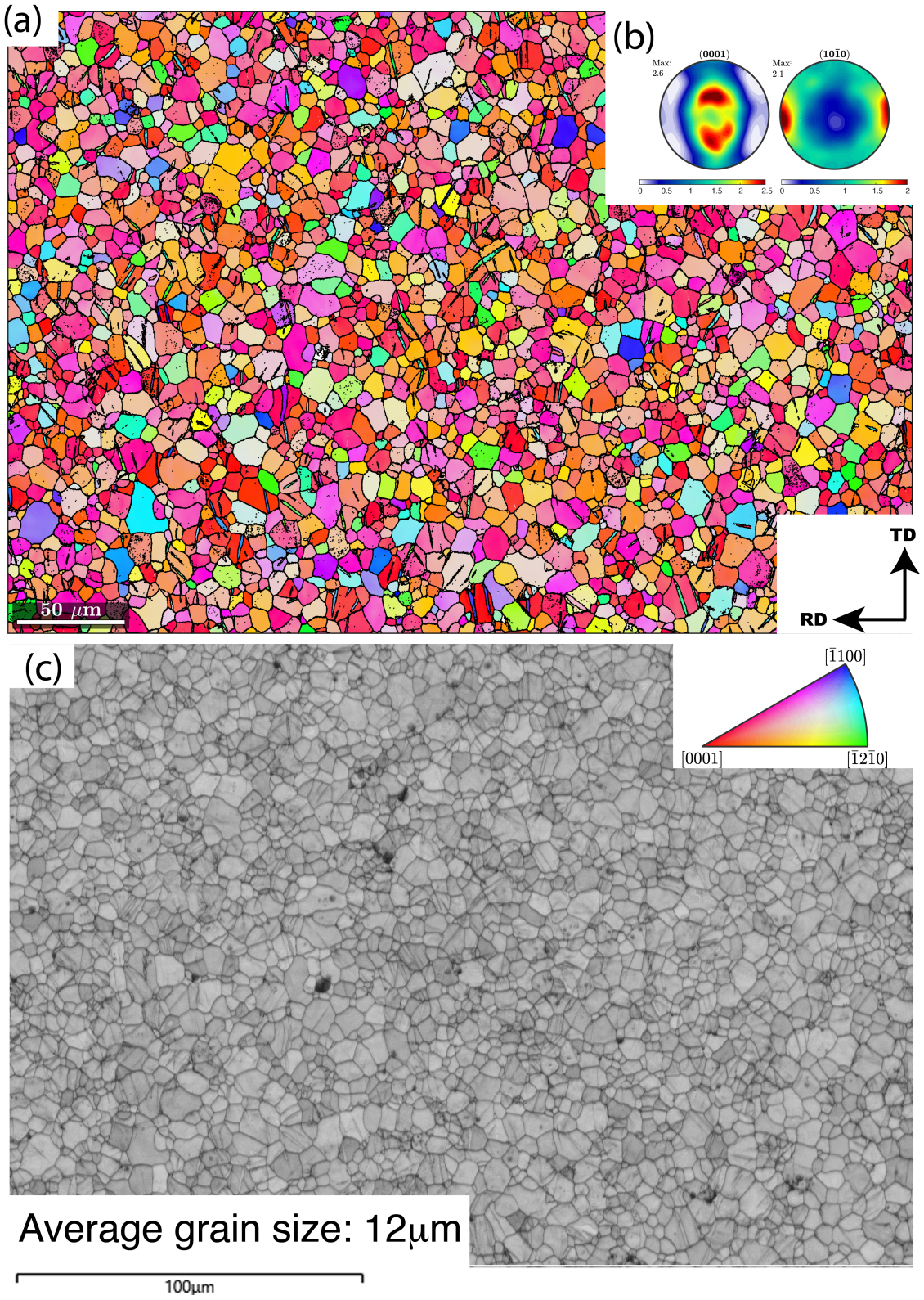


Figure 4.3: Initial condition of ZXK alloy, (a) Inverse Pole Figure map, (b) (0001) & $(10\bar{1}0)$ Pole figures and (c) band contrast map.

(RD), the $(10\bar{1}0)$ pole figure displays a relatively uniform intensity distribution at 90° to the plane normal. The AZX also displays a strong basal texture but exhibits a split in the basal pole in the RD. The $(10\bar{1}0)$ pole figure shows pronounced intensity at 90° to the plane normal along the transverse direction (TD). The ZXK alloy exhibits a large split in the basal pole towards the TD, with symmetrical basal poles $\approx 10^\circ$ from the sheet plane normal. The $(10\bar{1}0)$ pole figure for ZXK also exhibits a prismatic texture, opposite to the distribution in the AZX alloy.

Figures 4.4, 4.5, 4.6 reveal the presence of intermetallic precipitates in each alloy. AZ31 exhibits Al-Mn precipitates, likely the Al_8Mn_5 phase observed in similar alloys [114, 115]. For AZX, region (a) shows evidence of Al_8Mn_5, while region (b) contains precipitates with high concentrations of Al and Ca but no Mg, suggesting the formation of Al_2Ca. This is consistent with published results that show Ca readily forms intermetallics with Al and Mg [116, 117, 6, 3, 118, 115, 119]. The precipitates appear embedded in the surface, however, this is an artifact of the electrolyte preferentially attacking the surrounding matrix rather than the precipitates themselves, effectively etching them out depending on material removal rate. For ZXK, sub-surface Mg-Ca precipitates are evident, likely Mg_2Ca. The diffraction patterns in Fig. 4.7 were obtained by summing 50 frames from synchrotron X-ray diffraction measurements at room temperature. These patterns were used to identify major secondary phases in the bulk material; none were detected.

4.2 Initial tensile testing

For the initial mechanical characterisation tensile tests, Digital Image Correlation (DIC) was employed for strain measurements. DIC is a non-contact, digital image processing and numerical technique used to calculate strain. It works by tracking both individual

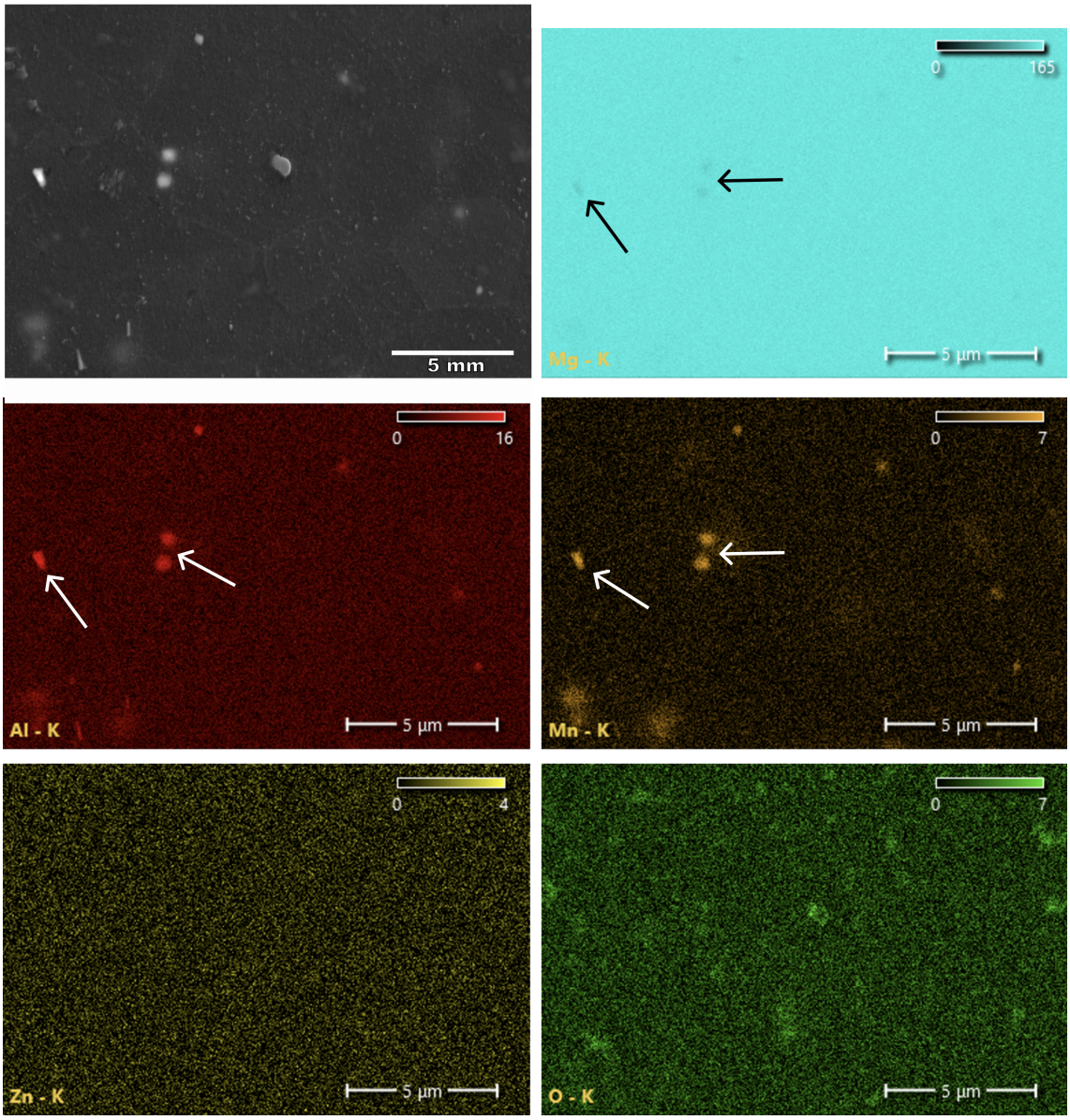


Figure 4.4: Energy dispersive spectroscopy (EDS) maps of AZ31 precipitates with a back scattered electron (BSE) image in the top left. The black arrows in the Mg elemental map show the gaps in signal from Mg atoms coinciding with suspected Al-Mn intermetallics highlighted with white arrows in the appropriate maps.

points and the grey levels on the surface of a test specimen. The method involves selecting a reference area in an image of the undeformed state and locating that same area in a subsequent image of the deformed state. By correlating these images, features can be accurately tracked, and a transformation operation in the form of displacement can be assigned to each. From the displacement gradients, strains and rotations are then computed. For each frame captured during the test, the strain distribution across

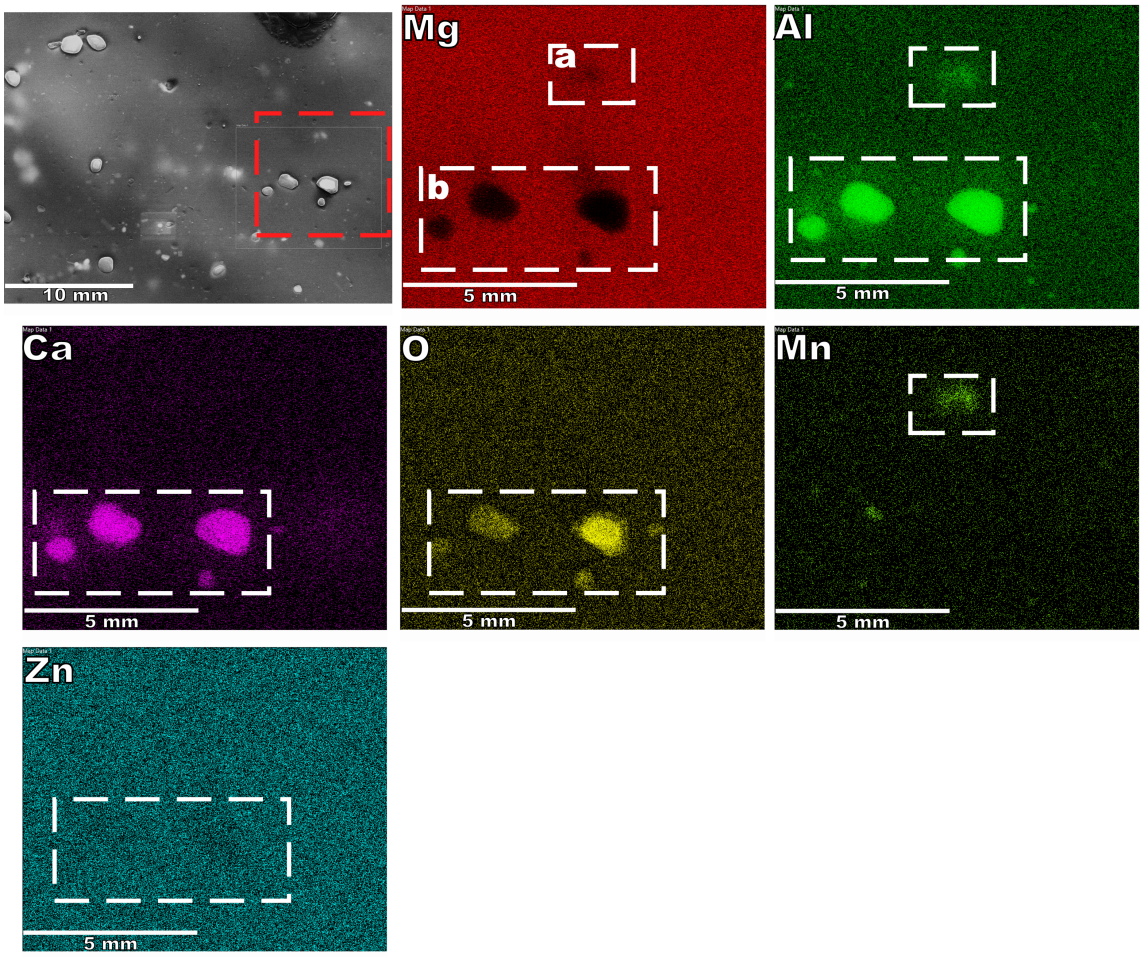


Figure 4.5: EDS maps of AZX precipitates, the red square in the BSE image (top left) corresponds with the elemental maps. Two regions are highlighted within the reduced area, (a) is associated with an Al-Mn intermetallic, (b) multiple Al-Ca intermetallics.

the surface was calculated. The strain values were then averaged over the entire region of interest (ROI) to obtain a representative global strain for each frame. Details of the set up are available in Chapter 3.

Tensile stress-strain curves for the alloys AZ31, AZX and ZXK are shown in Figure 4.8. They involve loading in both RD and TD for a range of strain rates. These tests reveal several key observations:

1. In Fig. 4.8, despite the differences in flow stress behaviour, both the AZ31 and AZX alloys display low levels of planar anisotropy between RD and TD loading when compared to the ZXK alloy. This suggests that the difference in starting

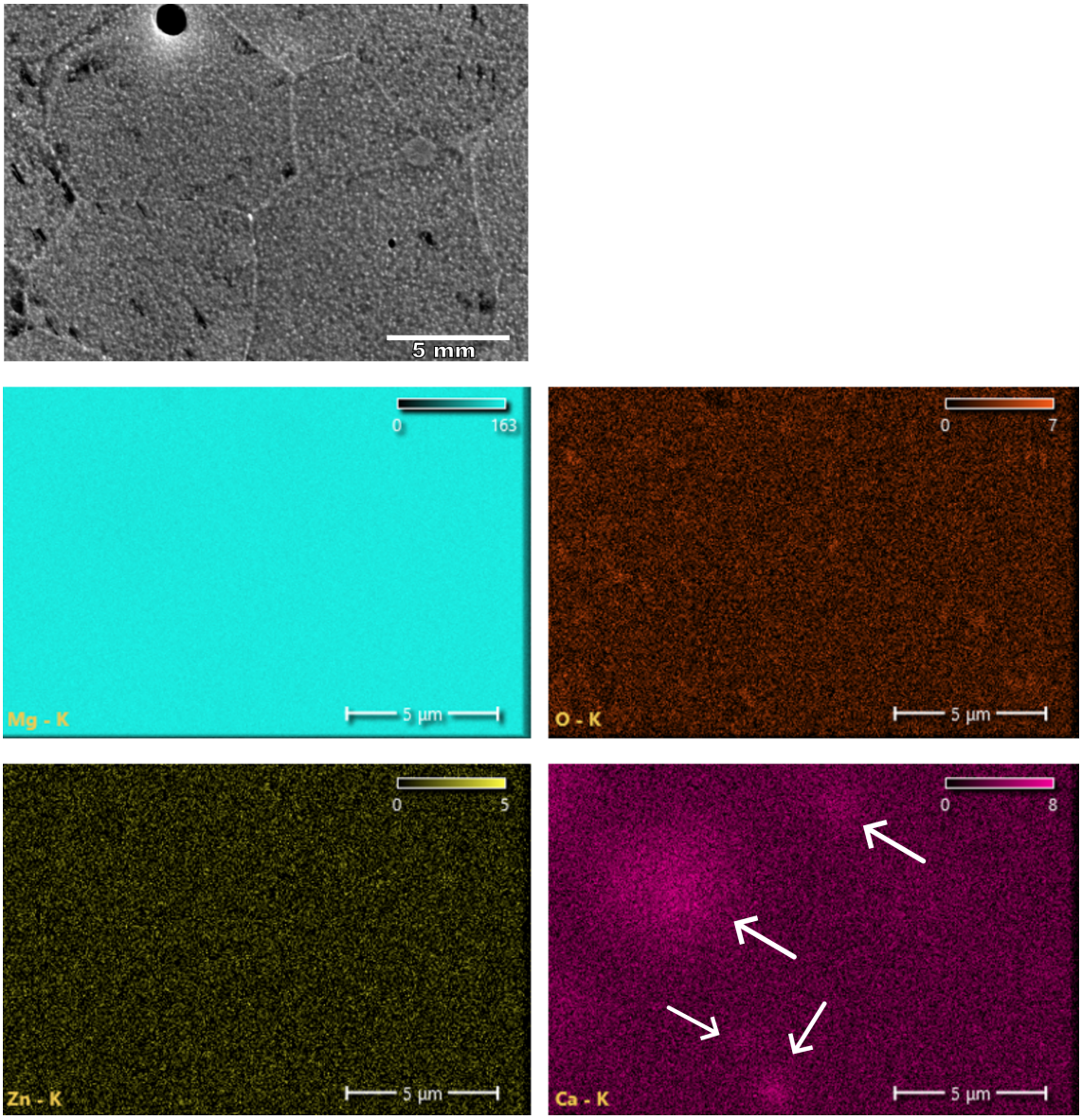


Figure 4.6: EDS maps of sub-surface ZXK precipitates with a secondary electron image of an over etched surface. White arrows point towards suspected Mg-Ca intermetallics.

textures for these alloys is not reflected in the planar anisotropy as it is for ZXK.

2. The sigmoidal-shaped flow stress curve observed in the TD for alloy ZXK across all strain rates strongly indicates the activation of deformation twinning. This unique shape arises because twinning initially leads to a rapid reorientation of grains, resulting in a temporary softening or plateau in the stress-strain response. As deformation continues, the reoriented grains harden, causing a subsequent increase in flow stress. This is consistent with findings in the compression testing of Mg alloys,

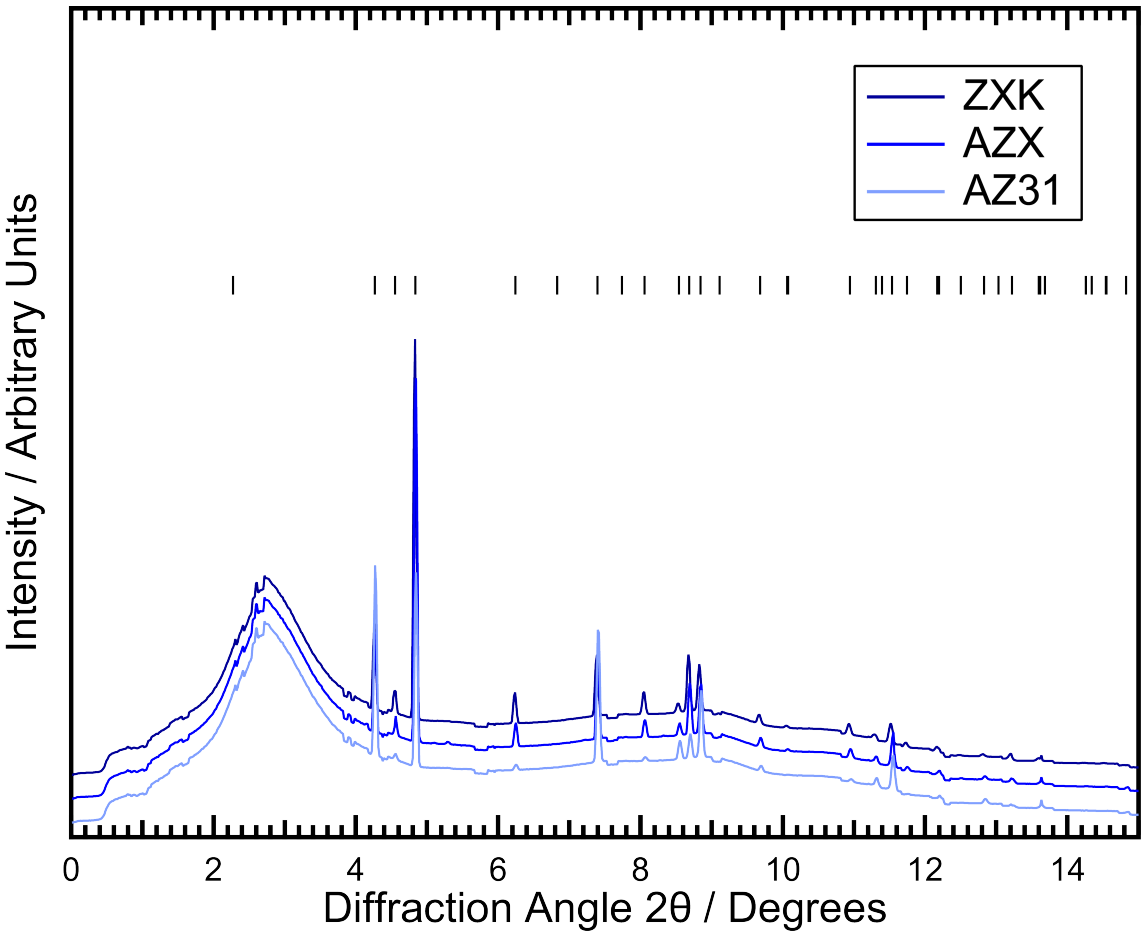


Figure 4.7: Stacked room temperature X-ray diffraction patterns for each magnesium alloy, with markers corresponding to Mg HCP phase peak positions. The background originates from a quartz window between the sample and X-ray beam.

where twining is more easily initiated due to the crystallographic orientation and stress state [21]. In contrast, loading parallel to RD follows a more conventional stress-strain response, characterised by continuous work hardening after yielding, which suggests a deformation mechanism dominated by slip.

3. The AZX alloy displays the sigmoidal-shaped hardening curve in both the RD and TD, suggesting that twinning significantly influences the yield behaviour of this alloy irrespective of loading direction.

4. At strain rate 3, loading in the TD for AZ31 produced a pronounced yield point followed by strong work hardening, which mimics the sigmoidal-shaped curve seen in the Ca-derivative alloys. This could indicate the activation of significant levels

of twinning at faster strain rates for AZ31.

The behaviour of the Ca-derivative alloys is consistent with studies indicating that the addition of Ca can promote twinning, the likely by-product of the modified basal texture shown in Fig. 4.2, 4.3. The tensile results presented here are in good agreement with studies on similar AZ31 and Ca-containing alloy compositions [20, 107, 120]. In general, a direct comparison of ductility between the alloys is difficult because of varying microstructural states. In the context of sheet forming, ductility obtained from uniaxial tensile tests are often not indicative of formability, instead, other parameters extracted from these tests are more useful, some of which are explored in the following sections.

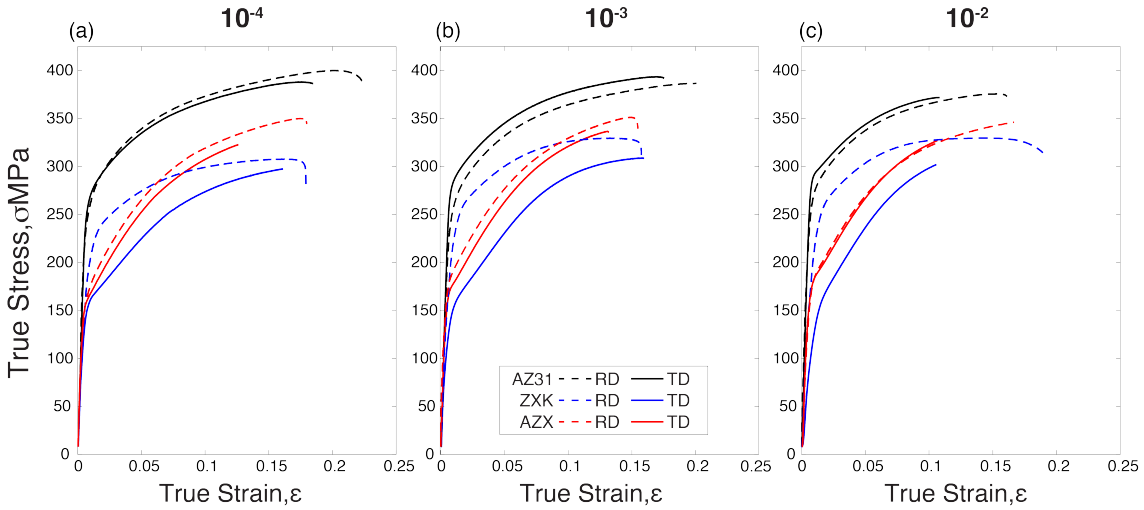


Figure 4.8: Tensile data for AZ31, AZX & ZXK alloys, both tested in RD & TD, for strain rates, in s^{-1}, labelled above each plot.

4.3 Synchrotron X-ray diffraction

4.4 Introduction

A synchrotron is a type of toroidal particle accelerator; Diamond Light Source is the UK's national synchrotron facility. Its primary role is to produce synchrotron radiation, which is

a very bright photon source used to generate high flux X-ray radiation. The characteristic bright light is produced when an electron beam is accelerated to relativistic speeds under ultra high vacuums and accelerated with high strength magnetic fields. At Diamond, the electron beam is accelerated twice to reach such speeds before it is injected into a storage ring. The storage ring consists of several large electromagnets where the electrons paths are bent, or their path changed by insertion devices containing arrays of magnets that wiggle/undulate the beam to produce more intense light where the wavelength of X-rays are tuneable. The X-rays are guided into beam lines located around this storage ring, each of which have dedicated experimental capability.

Relevant to this study, high energy X-ray diffraction enables the measurement of deformation at the crystal level at high temporal resolution, providing insights into the micro-mechanical response of a crystalline material during in-situ dynamic testing. A key advantage of this method is the large penetration depth of the X-rays, enabling bulk measurements of large material volumes to be interrogated that is otherwise impossible with lab based XRD. By using an incident monochromatic X-ray beam, the desired wavelength can be precisely selected, enabling tailored investigations of specific crystallographic features and deformation mechanisms.

In context to the initial characterisation of these alloys, clear deviations in the starting crystallographic textures shown above are present. These observations were coupled with anisotropy in the mechanical tensile properties between RD and TD. Slip is a major contributor to plastic deformation; magnesium and its alloys obey a general hierarchy of strengths of the different slip modes. The difference in strengths for these modes influences the anisotropy seen. It is often the case, for magnesium alloys at room temperature, that the limited active slip systems do not offer the sufficient number of independent modes of deformation needed for homogeneous plastic flow. Deformation at elevated temperatures proceeds with a sufficient number of independent slip systems, where ductility is greatly increased. However, it remains unclear how twinning or slip

controlling parameters such as CRSS values vary for these Ca-derivative alloys, which are known to be influenced by the c/a ratio and bulk composition changes. Performing in-situ X-ray diffraction with samples at forming relevant temperatures, we attempt to obtain insight into the ductility governing plasticity mechanisms.

4.5 Results

4.5.1 Anisotropic yield behaviour

Macroscopic observations

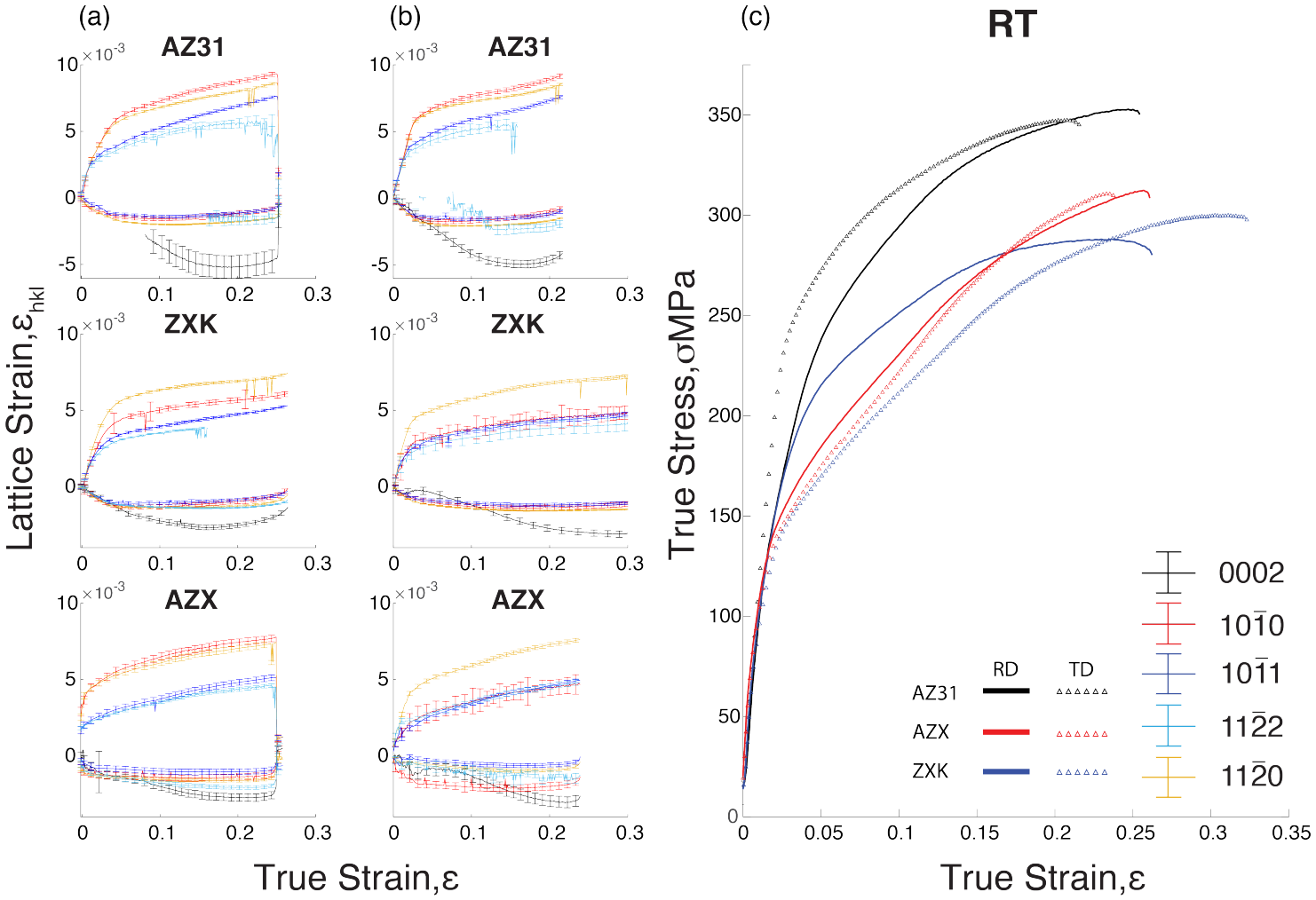


Figure 4.9: Room temperature in-situ lattice strain measurements evolving with strain, from uniaxial tensile tests of the 3 alloys, parallel to the (a) rolling direction (RD) and (b) transverse direction (TD). (c) includes the macroscopic tensile curves.

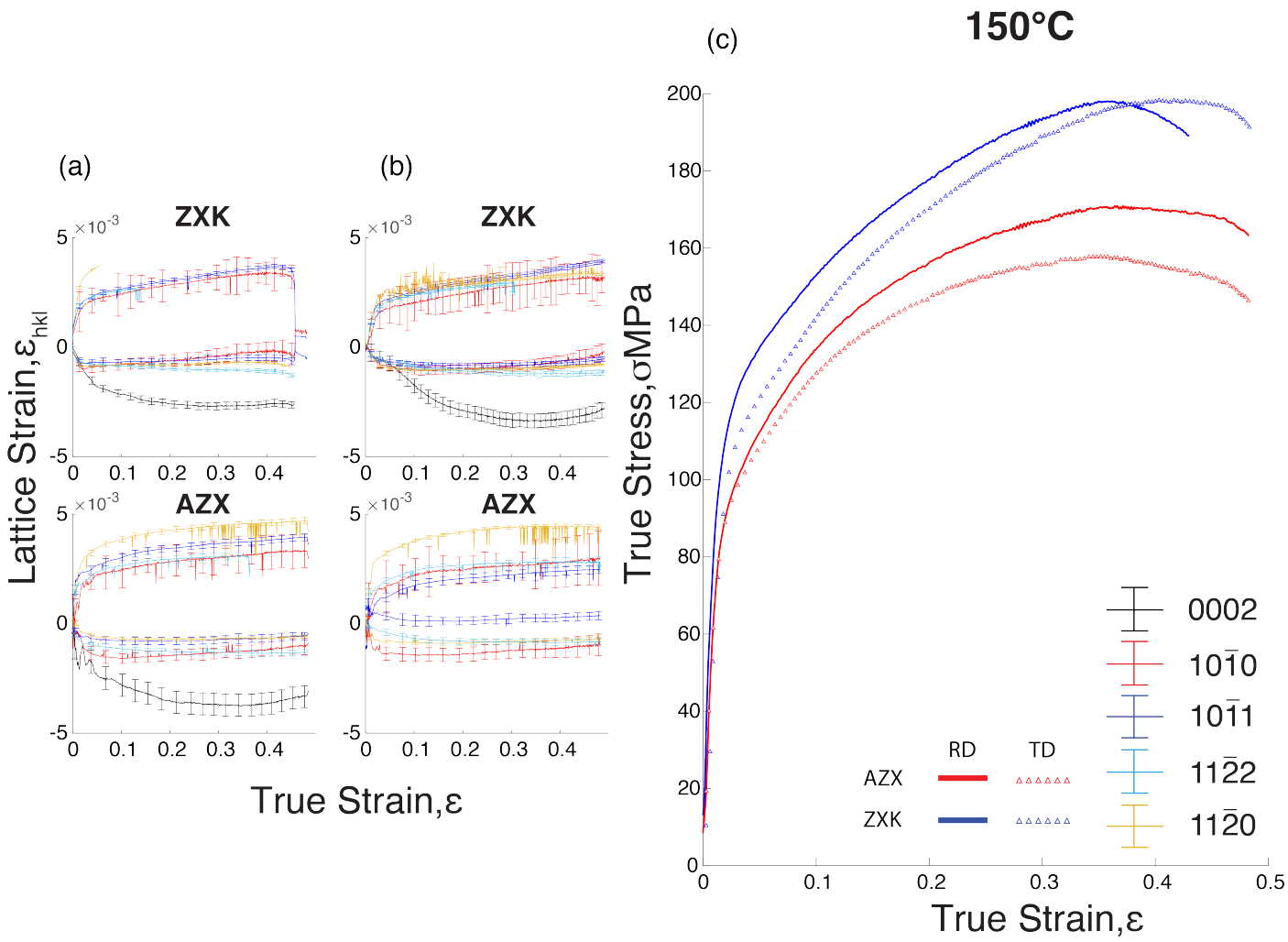


Figure 4.10: In-situ lattice strain measurements evolving with strain at $150°C$, from uniaxial tensile tests of ZXK and AZX, parallel to the (a) rolling direction (RD) and (b) transverse direction (TD). (c) includes the macroscopic tensile curves.

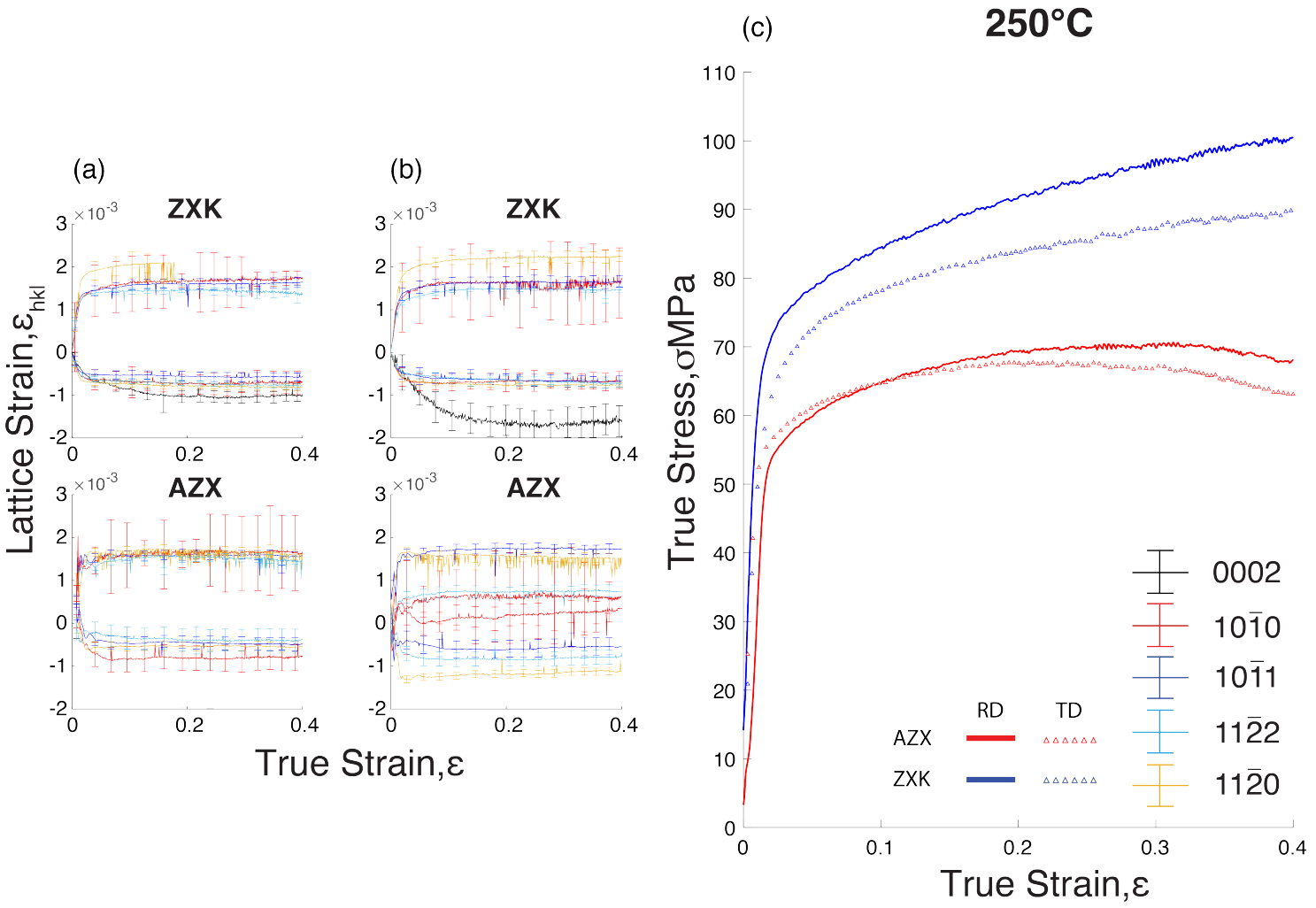


Figure 4.11: In-situ lattice strain measurements evolving with strain at $250°C$, from uniaxial tensile tests of ZXK and AZX, parallel to the (a) rolling direction (RD) and (b) transverse direction (TD). (c) includes the macroscopic tensile curves.

In the following results it is important to note that samples at 250°C had ductilities that exceeded the maximum displacement of the test rig, certain tests were terminated once the ultimate tensile strength was reached. Therefore, the strains at which each experiment was stopped should not be considered significant in the analysis. Additionally, due to time constraints, the assessment of the AZ31 alloy in both loading directions was given a lower priority compared to AZX and ZXK alloys. As a result, stress-strain data for AZ31 in both loading directions at elevated temperatures has been omitted from the analysis. Sample information can be found in Chapter 3.

The tensile stress-strain curves in Figures 4.9(c), 4.10(c)& 4.11(c) exhibit a decrease in yield anisotropy between RD and TD for the ZXK alloy with increasing temperature. While the TD curve maintains a lower yield and overall flow stress compared to RD. The yield behaviour closer resembles the RD response. This shift in yield behaviour in the TD suggests more deformation was accommodated via slip than twinning as a result of more non-basal slip activity due to a temperature increase. The larger elongation to failure observed in the TD compared to RD at room temperature is reduced at 150°C. At 250°C the flow stress for both directions continues to increase, this contrasts with the behaviour seen in the AZX alloy, where the flow stress appears to stabilise or even decrease. At 250°C ZXK maintains a more temperature-resistant flow stress. At 150°C the AZX curves have very similar flow stress trends with loading direction, similar to ZXK where the sigmoidal shape diminishes.

At elevated temperatures there were observations of serrated flow after yielding. At 150°C, Fig. 4.10(c), serrations appear to commence at ≈ 0.18 true strain, for both alloys in both directions. They are closely followed by distinct serrations at ≈ 0.25 true strain in both alloys. In Fig. 4.11, larger serrations were observed at 250°C. The distinct serrations seen at 150°C were also present in the same strain range. Serrations in the flow curves could indicate solute influenced dislocation behaviour such as dynamic strain ageing (DSA), not uncommon in ternary Mg alloys at elevated temperatures [121,

122]. However, it appears the distinct serrations at specific strains in both temperature conditions could be tensile-rig related artefacts. This point will be discussed further in 4.5.2.

Overall, the macroscopic stress-strain curves display a significant decrease in flow stress with increasing temperature and an expected increased strain to failure.

Lattice Strains

The lattice strain plots corresponding to each macroscopic tensile test are shown together. The lattice strains have been calculated using Equation4.1

$$\varepsilon_{\psi}^{hkl} = \frac{d_{\psi}^{hkl} - d_{0}^{hkl}}{d_{0}^{hkl}} \tag{4.1}$$

where ε_{ψ}^{hkl} is the lattice strain for the reflection hkl, d_{0}^{hkl} is the reference d-spacing before a tensile load is applied, and d_{ψ}^{hkl} is the measured d-spacing for each frame. As the samples were thin, there was no evidence of visual distortion after machining the samples, therefore residual strains are assumed to be minimal. The lattice strains calculated are therefore relative to the initial condition of the specimens, not absolute values. Lattice strain errors were calculated via error propagation, incorporating the corresponding standard error from the values of d and d_0 introduced in 3. The error propagation follows,

for any function e.g.,

$$q = f(x_1, ..., x_n)$$

uncertainty is calculated by:

$$\delta q = \sqrt{\left(\frac{\partial q}{\partial x} \cdot \delta x_1\right)^2 + ... + \left(\frac{\partial q}{\partial x_n} \cdot \delta x_n\right)^2} \tag{4.2}$$

our function is shown in Eq. 4.1.

Using the error of

$$d_{\psi}^{hkl} = \delta d_{\psi}^{hkl} \; and \; d_0^{hkl} = \delta d_0^{hkl},$$

we differentiate 4.1 to get

$$\frac{\partial \varepsilon_{\psi}^{hkl}}{\partial d_{\psi}^{hkl}} \; and \; \frac{\partial \varepsilon_{\psi}^{hkl}}{\partial d_0^{hkl}}.$$

From this we obtain

$$\frac{\partial \varepsilon_{\psi}^{hkl}}{\partial d_{\psi}^{hkl}} = \frac{1}{d_0^{hkl}} \; and \; \frac{\partial \varepsilon_{\psi}^{hkl}}{\partial d_0^{hkl}} = -\frac{d_{\psi}^{hkl}}{\left(d_0^{hkl}\right)^2}.$$

Finally the error in lattice strain (ε_{ψ}^{hkl}) is $\delta\varepsilon_{\psi}^{hkl}$, using Eq. 4.2

$$\delta \varepsilon_{\psi}^{hkl} = \sqrt{\left(\frac{1}{d_0^{hkl}} \cdot d_{\psi}^{hkl}\right)^2 + \left(-\frac{d_{\psi}^{hkl}}{\left(d_0^{hkl}\right)^2} \cdot \delta d_0^{hkl}\right)^2} \tag{4.3}$$

At elevated temperatures, larger error bars are observed due to variations in peak shape and intensity, making them more difficult to fit. This results in greater uncertainty in peak position, increasing the calculated error. However, for the majority, the profile of these error bars are consistent with the trends of the underlying curves, indicating

reliable trends in the data.

As described in Chapter 3, the collected diffraction rings, shown in Figure 4.12, were radially integrated into $36\times10^{\circ}$ azimuth ψ sectors. The positive lattice strains correspond to measurements from $\psi = 90^{\circ}$ & $\psi = 270^{\circ}$, and the negative lattice strains from $\psi = 0^{\circ}$ & $\psi = 180^{\circ}$, due to Poisson contraction in this direction. They are referred to as tensile and transverse strains respectively. The diffraction frames were interpolated with the true strain obtained from the loading frame to plot lattice strain against true strain for the crystallographic planes; basal (0002); prismatic $(10\bar{1}0), (11\bar{2}0)$; and pyramidal $(10\bar{1}1), (11\bar{2}2)$. The (0002) lattice strains at $\psi = 90^{\circ}$ have not been included due to weak diffraction intensities and high corresponding errors from peak fitting.

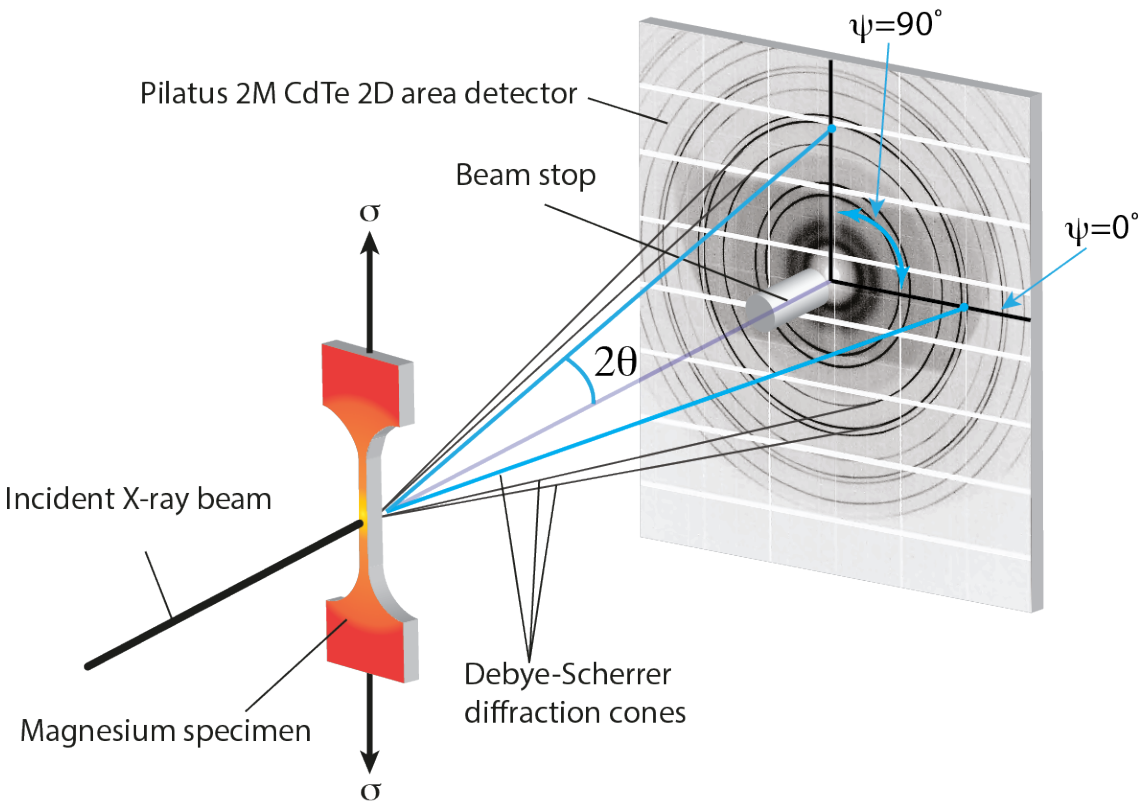


Figure 4.12: Schematic depicting the collection of debye-sherrer rings from diffraction in transmission. The azimuthal angles refer to data corresponding to the tensile axis major strains $\psi = 90^{\circ}$ and minor strains $\psi = 0^{\circ}$.

The lattice strains plotted against true strain in Figures 4.9, 4.10, 4.11 resemble stress-strain curves, primarily due to the hardening behaviour of the lattice strains in the

initial stages of strain.

At room temperature, Fig. 4.9, the AZ31 alloy's relative order of lattice strain magnitudes remained consistent between the loading directions. This observation coincides with the sample experiencing similar deformation behaviour in both directions, indicated by the macroscopic behaviour. Notably, the initial hardening of the tensile strains differed, with the TD response exhibiting more pronounced hardening. The (0002) basal plane displayed very high transverse strains compared to the other planes, indicating significant loads on basal planes in that direction.

For ZXK at RT, tensile strains for the $(10\bar{1}0)$ prismatic plane were lower in the TD direction. The $(11\bar{2}0)$ prismatic plane exhibited steeper initial hardening in the TD direction, resulting in an increased separation between the prismatic planes. The AZX alloy exhibited similar characteristics, with reduced lattice strains for the $(10\bar{1}0)$ prismatic plane in the TD. However, contrasting RD behaviour was observed, where the prismatic planes were very close aligned, and the $(10\bar{1}0)$ prismatic plane reached larger lattice strain magnitudes than the $(11\bar{2}0)$ plane. A notable comparison can be made for (0002) basal transverse strains in both AZX and ZXK alloys. The TD curve for the ZXK alloy displays a sigmoidal curve, initially tending toward a positive lattice strain until reaching a peak at ≈ 0.05 true strain, after which there was an increase in transverse strain. This contrasts with the RD behaviour, which followed a 'u' shaped trend similar to that observed in the AZ31 alloy. The AZX alloy also displayed a sigmoidal (0002) curve in the TD, although it was slightly delayed and occurred at higher transverse strains compared to ZXK. The RD for AZX exhibited a more subtle variation in transverse strain.

Compared to RT, at elevated temperatures, in Fig. 4.10 & 4.11 the magnitude of lattice strains decreases. At 150°C, for ZXK, the prismatic planes in the TD exhibit tensile strains closer to the pyramidal planes, indicating a shift in load sharing between slip systems; for the RD the $(11\bar{2}0)$ prismatic plane displayed a sharp hardening behaviour

before, the errors drastically increased post saturation and were subsequently omitted. In the RD at ≈ 0.15 true strain, the transverse strains from the $(11\bar{2}2)$ pyramidal plane increase as the $(10\bar{1}0)$ transverse strains decrease; this is also observed in the TD but delayed. The separation of the (0002) transverse strains compared to the other planes is significantly greater in both directions compared to the behaviour at room temperature. The sigmoidal curve for the (0002) plane in the TD reduced considerably, the trend was very similar to the response of the AZ31 alloy in the TD at room temperature.

For the AZX alloy the behaviour of lattice strains in the TD are very contrasting to the room temperature observations. In the TD, after initial hardening, the lattice strains approached a saturation point and the monotonic increase seen at room temperature was significantly reduced. In the initial stages the $(11\bar{2}0)$ prismatic plane solely exhibits moderate hardening, the other planes display very low hardening rates. In contrast to the RD at 150°C, the TD lattice strains for $(10\bar{1}1)$ pyramidal planes decrease, the transverse strains are very slightly positive. In the RD the transverse strain for the (0002) plane also shifted to a 'u' shape.

At 250°C, the lattice strains for both AZX and ZXK alloys plateau soon after the initial hardening. For ZXK the $(11\bar{2}0)$ prismatic plane has the largest tensile strains in both directions; comparing with the observations at 150°C in the TD suggests there was a change in the behaviour of this plane with increasing temperature, or an error at 150°C. The (0002) basal plane has a considerably larger transverse strain in the TD. For AZX in the RD, the tensile strains overlap considerably. In the TD, the $(10\bar{1}0)$ prismatic plane exhibits the least hardening and very low lattice strains, in contrast to the trends at 150°C where the $(10\bar{1}1)$ plane displayed this behaviour.

4.5.2 Strain rate sensitivity

Strain rate sensitivity (SRS) *m* is a useful measure of the material flow stress behaviour with varying deformation rates [7]. A higher *m* indicates deformation can be accommodated more gradually, the material is less prone to localised deformation leading to subsequent failure [123]. This is important for many forming processes, such as deep drawing and stamping, where complex deformation states can introduce varying deformation rates in different areas. At elevated temperatures forming of Mg alloys is greatly improved, the SRS tends to also increase at elevated temperatures. This is unsurprising as additional slip mechanisms become active in Mg alloys [7]. Formability and SRS have been related through forming limit diagram (FLD) tests, at elevated temperatures alloys with a high *m* exhibit an increased ductility when the strain rate is reduced[55, 124]. However, the SRS effect on alloys can be limited by the deformation mechanisms that are present; such as twinning and dynamic recrystallisation, they can complicate the relation of SRS with forming parameters such as elongation to failure [125].

The Strain rate sensitivity index *m* can be averaged from 2 or more constant strain rate tensile tests, using Equation4.4:

$$m = \frac{\delta \ln(\sigma)}{\delta \ln(\dot{\epsilon})} = \frac{\ln(\sigma_2/\sigma_1)}{\ln(\dot{\epsilon}_2/\dot{\epsilon}_1)} \tag{4.4}$$

where σ_2 and σ_1 are the flow stresses at the selected strain for strain rates $\dot{\epsilon}_2$ and $\dot{\epsilon}_1$

The strain rate sensitivity was assessed at three strain rates, at room temperature and two strain rates at elevated temperatures. This was calculated for samples in the RD at a true strain value of 0.10 to ensure a region of uniform plasticity across all temperatures and strain rates.

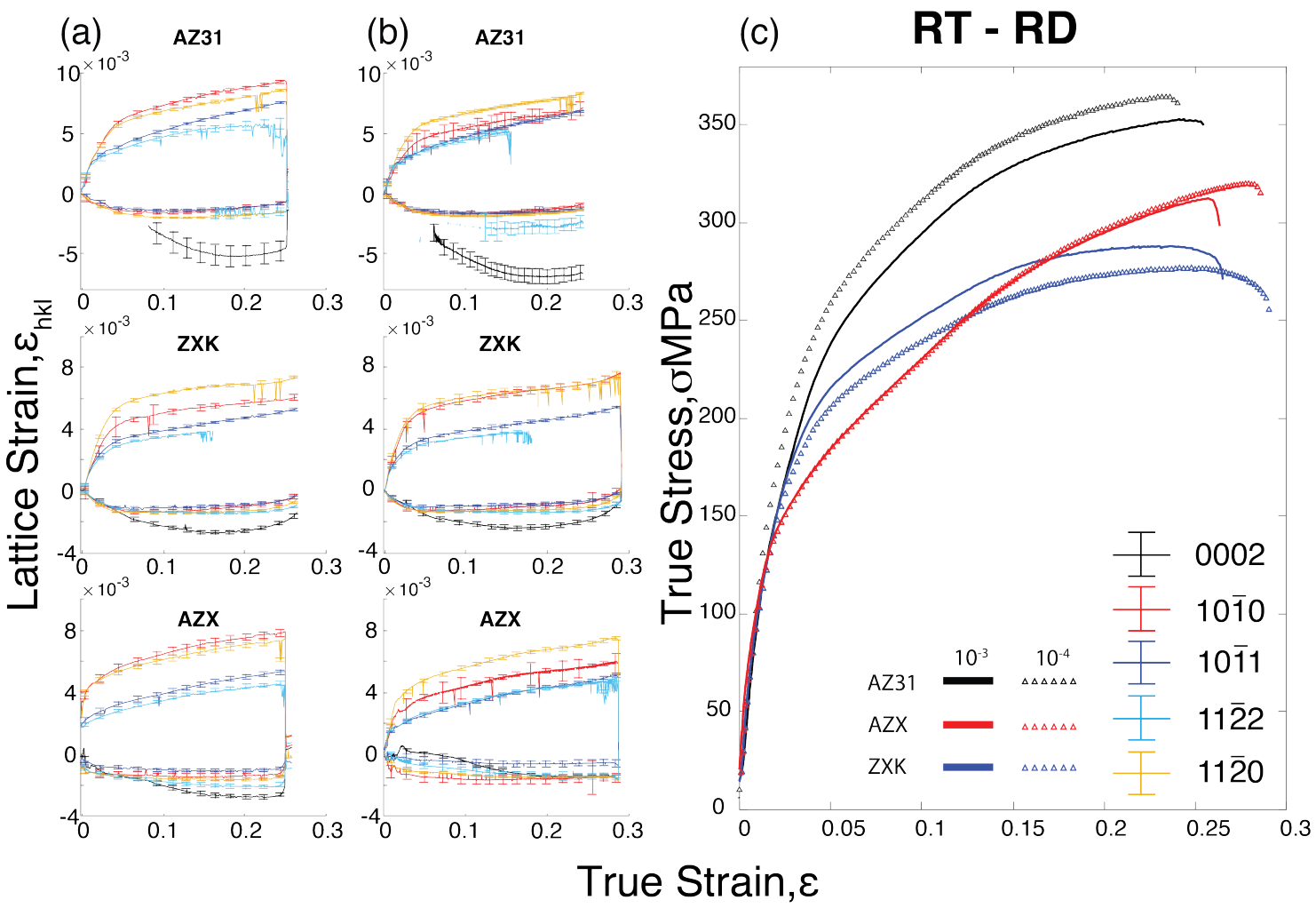


Figure 4.13: Room temperature in-situ lattice strain measurements evolving with strain, during tensile deformation of the 3 alloys at two strain rates. (a) $10^{-3}\,s^{-1}$, (b) $10^{-4}\,s^{-1}$ and (c) macroscopic true stress strain curves.

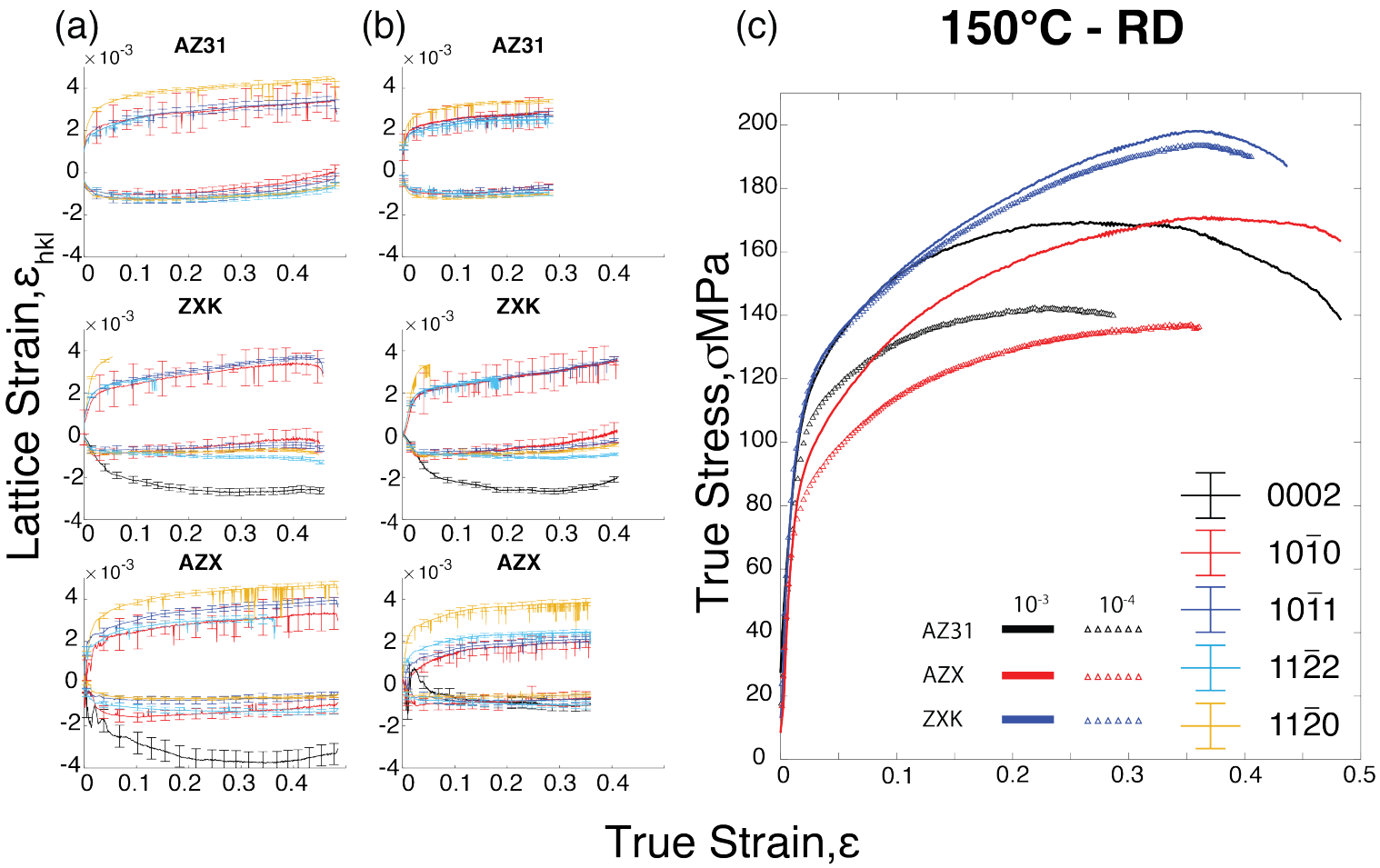


Figure 4.14: Elevated temperature in-situ lattice strain measurements evolving with strain, during tensile deformation of the 3 alloys at two strain rates. (a) $10^{-3}\,s^{-1}$, (b) $10^{-4}\,s^{-1}$ and (c) macroscopic true stress strain curves.

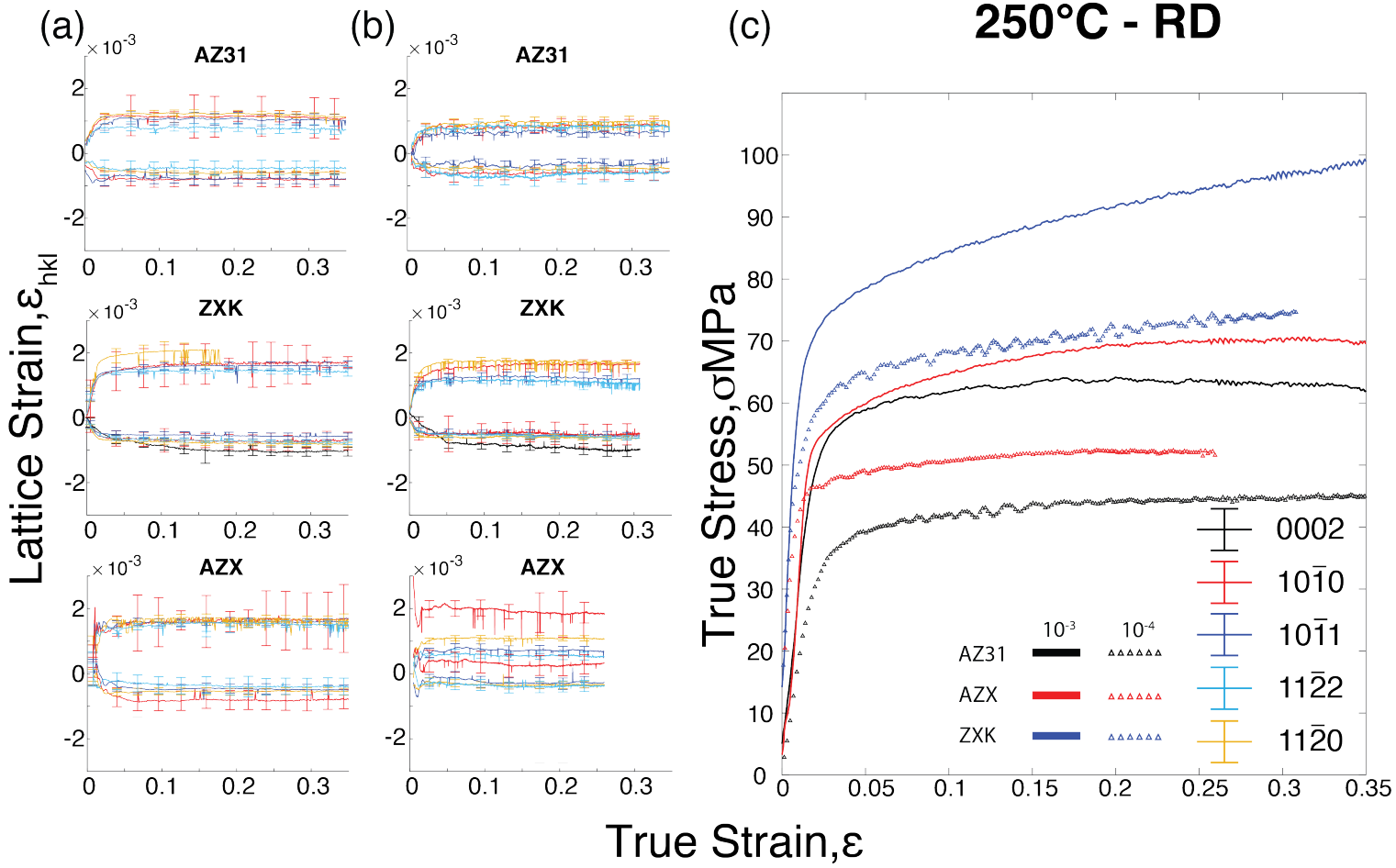


Figure 4.15: Elevated temperature in-situ lattice strain measurements evolving with strain, during tensile deformation of the 3 alloys at two strain rates. (a) $10^{-3}\,s^{-1}$, (b) $10^{-4}\,s^{-1}$ and (c) macroscopic true stress strain curves.

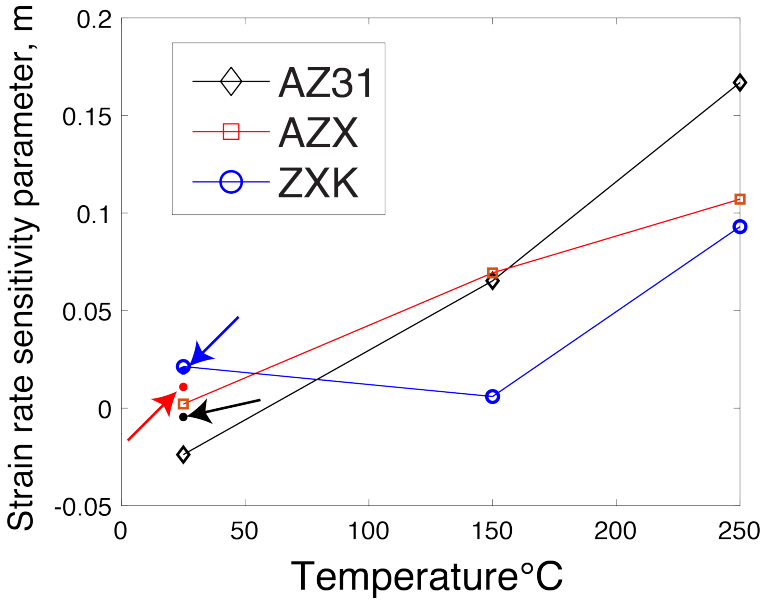


Figure 4.16: Strain rate sensitivity (SRS) for each alloy in the RD, symbol and line represents calculations from values obtained with the Deben Rig. The arrows indicate values from tests with the Instron at RT from three strain rates, highlighting differences in equipment for the same material.

Fig. 4.16 shows that the SRS trends at room temperature for the AZ31, AZX and ZXK alloys were consistent across tests using two different tensile rigs.

The AZ31 alloy exhibited the lowest SRS at room temperature but it experienced a dramatic increase of more than tenfold at 250°C. In contrast, the AZX and ZXK alloys displayed a higher SRS at room temperature compared to AZ31, with ZXK showing the highest value, indicating potential for superior formability at RT. Interestingly, both AZX and ZXK alloys had significantly lower SRS values than AZ31 at 250°C, highlighting a difference in how these alloys respond at elevated temperatures. Further to this, the SRS for ZXK initially decreased with increasing temperature before showing a substantial rise, suggesting a more complex temperature dependence compared to the other alloys.

At room temperature, Fig. 4.13 depicts how the flow stress for the AZX alloy does not change with varying strain rates. In contrast, the AZ31 and ZXK alloys display sensitivity to strain rate changes. At 150°C, in Fig. 4.14 the behaviour of the AZX alloy aligns more closely with AZ31, as both alloys exhibit a significantly lower flow stress at

a strain rate of $10^{-4}\,s^{-1}$ compared to $10^{-3}\,s^{-1}$. The opposite is true for the ZXK alloy, the flow stress at $10^{-4}\,s^{-1}$ was considerably closer to $10^{-3}\,s^{-1}$. At $250°C$ in Fig. 4.15 all the alloys exhibit a lower flow stress at $10^{-4}\,s^{-1}$.

Regarding serrations in the flow curves, the same distinct serrations previously mentioned in 4.5.1, were also observed at $10^{-4}\,s^{-1}$ for $150°C$ & $150°C$, appearing at similar true strain values of $\approx 0.25 - 0.3$, shown in Fig. 4.17. Given the consistency of these distinct serrations evident at both strain rates and elevated temperatures, it is plausible they are more likely an artefact of the tensile rig itself, rather than an intrinsic material behaviour. These distinct serrations appeared masked by the pronounced serrations at $10^{-4}\,s^{-1}$ for $250°C$.

Nonetheless, at $10^{-4}\,s^{-1}$ & $250°C$, AZ31 and ZXK showed very pronounced serrations. For ZXK, these serrations were apparent immediately after yielding, remaining consistent in magnitude up to ≈ 0.25 true strain. For AZ31, the serrations appeared later and maintained their magnitude only briefly. The serrations for AZX were less pronounced compared to the other alloys, indicating a weaker manifestation of this effect. The serrations at $10^{-4}\,s^{-1}$ are more prominent than at $10^{-3}\,s^{-1}$ for the $250°C$ condition, at $150°C$ we do not observe the same relationship. This suggests the mechanism for DSA is both temperature and strain rate related.

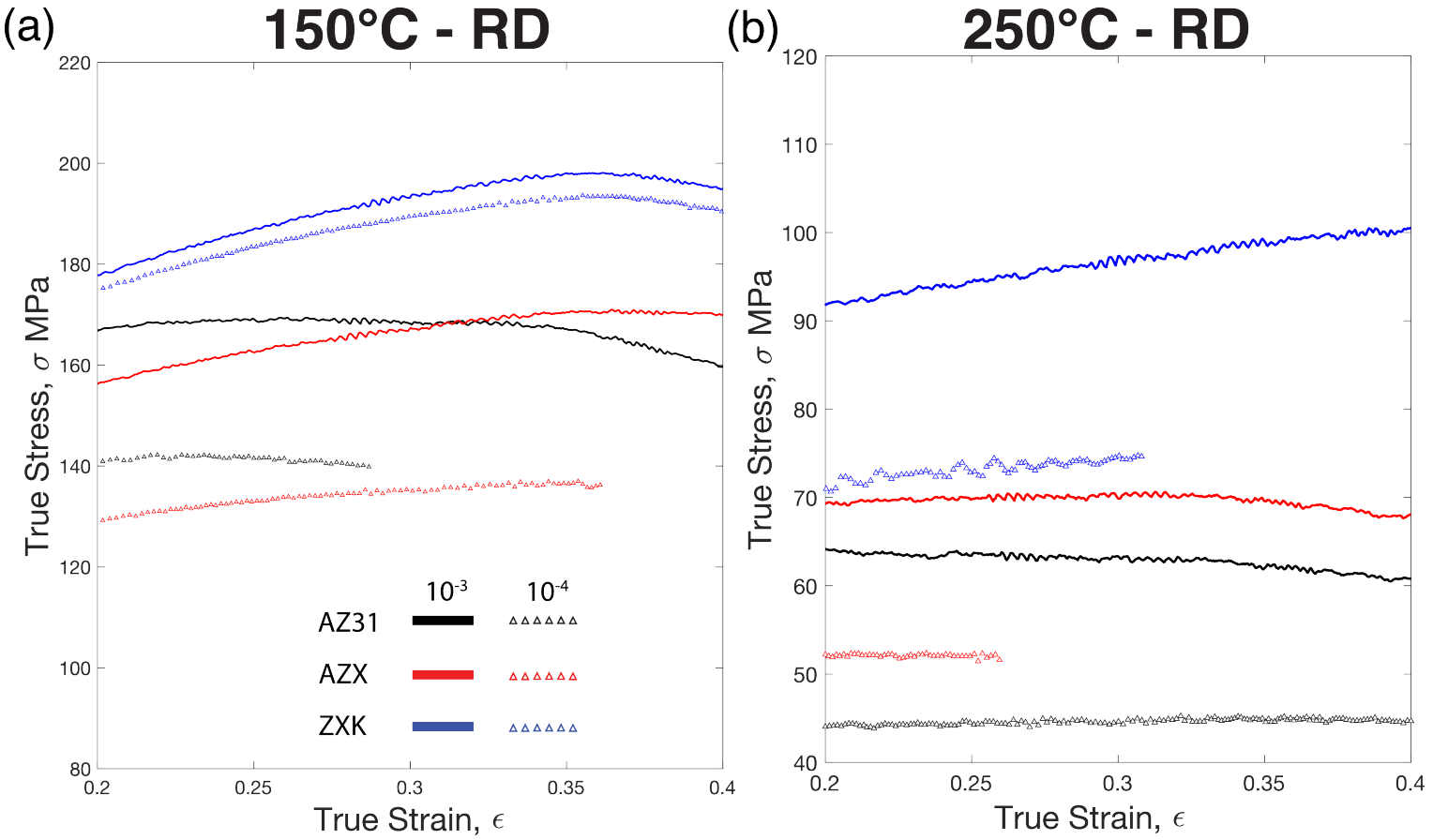


Figure 4.17: Magnified view of the strain range with suspected serrations for the macroscopic flow curves in Figs. 4.14-4.15 at (a) 150°C and (b) 250°C.

Lattice strains

The influence of strain rate on lattice strains at a range of temperatures is illustrated in Figures 4.13, 4.14 & 4.15. At room temperature, a clear relationship emerges between varying strain rate and changes in the tensile strain behaviour of the $(10\bar{1}0)$ prismatic plane for all alloys. The relative positions of the prismatic planes swap in terms of magnitude of tensile strain achieved between different strain rates. For both the AZ31 and AZX alloys, at $10^{-3}\,s^{-1}$, the $(11\bar{2}0)$ prismatic plane displayed larger lattice strains compared to the $(10\bar{1}0)$ plane. At $10^{-4}\,s^{-1}$, the trend is reversed. On closer inspection, the $(10\bar{1}0)$ plane demonstrated greater sensitivity to strain rate changes, as the tensile strains for the $(11\bar{2}0)$ plane were relatively consistent between the strain rates. For the ZXK alloy, similar sensitivity was observed; however, the tensile strains on the $(10\bar{1}0)$ plane increase at $10^{-4}\,s^{-1}$ instead of decreasing, indicating a different response to the strain rate change in comparison to the other alloys. A notable observation for the AZX alloy at room temperature is the contrasting (0002) basal plane behaviour. At $10^{-4}\,s^{-1}$ the transverse strains mirrored the trend observed in the TD direction shown in Figure 4.9, suggesting that slower strain rates in the RD for AZX activates similar deformation mechanisms to a change in loading direction.

At 150°C, the influence of strain rate on the tensile strains between prismatic planes became less consistent for all alloys. Overall, the tensile lattice strain magnitudes were significantly reduced at the slower strain rate of $10^{-4}\,s^{-1}$, suggesting a diminished sensitivity of the prismatic planes to strain at this elevated temperature. For the AZX alloy, at $10^{-4}\,s^{-1}$, the transverse strain behaviour of the (0002) basal plane exhibited an amplified version of the effect observed at room temperature.

At 250°C the lattice strain trends for AZX alloy at $10^{-4}\,s^{-1}$ show minimal correlation with those at the faster strain rate. There is a significant reduction in tensile strains and a noticeable positive transverse strain for the $(10\bar{1}0)$ prismatic plane, which again,

mirrors the transverse strain behaviour observed for the TD in Figure 4.11. There is clear evidence of serrations in the lattice strains for the AZ31 and ZXK alloys at the slower strain rate of $10^{-4}\,\mathrm{s}^{-1}$. For the AZ31 and ZXK alloys, subtle serrations are also observed at the faster strain rate, although it is difficult to draw the same conclusion for the AZX alloy. This evidence coincides with the macroscopic observations of lesser serration effects in the AZX alloy.

4.6 Discussion

4.6.1 Directional anisotropy

The lattice strain behaviour from families of crystallographic planes with common orientation (i.e., specific planes that were aligned in the same direction relative to the sample's geometry or loading axis) were directly captured in this experiment for different strain rates, temperatures and loading directions. However, this means the reliability of this technique depends on grain orientation in the sample. If too few grains have their planes oriented to satisfy the diffraction condition, the resulting peaks will be weak or absent. For example, in the sectors $\psi = 90°$ & $\psi = 280°$, there were not enough grains with their basal planes $\{0002\}$ oriented to generate a strong diffraction peak for analysis. The peak fitting and subsequent calculations contained large errors and have been omitted.

At room temperature, in Fig. 4.9, the trends in lattice strain behaviour aligned with the macroscopic stress-strain observations. In the AZ31 alloy, the relative order of lattice strain magnitudes remained consistent between RD and TD loading, indicating similar deformation modes in both directions. This consistency is attributed to the strong uniform basal texture for the alloy. The c-axis alignment will determine if basal slip less/more favourable, most grains having c-axis alignment close to the normal direction

(ND) results in a similar resolved shear stress on the basal plane under loading in the RD or TD. In contrast, the Ca-containing alloys (ZXK and AZX) exhibited distinct differences in the magnitude of lattice strains on specific planes. For AZX, in the TD, tensile strains on the $(10\bar{1}0)$ prismatic plane were significantly lower than in the RD, overlapping with the pyramidal planes; a phenomenon also observed in the ZXK alloy. With more random c-axis orientations the lattice strain behaviour suggests these alloys experienced differences in the activation of slip systems due to the greater sensitivity to loading direction. Basal slip is more favoured and twinning behaviour observed for grains with c-axis alignment further from the ND.

The sigmoidal yield in the macroscopic curve for ZXK and AZX is strongly associated with twinning, suggesting that transition in lattice strain hardening for the $(11\bar{2}0)$ prismatic plane due to lower stresses required for slip may have been influenced by twinning. This is supported by the sigmoidal trend observed in the (0002) basal plane in the TD. At ≈ 0.04 true strain, after initial hardening, the transverse strains on the (0002) basal plane began to increase (more negative) following an initial decrease towards 0 lattice strain. This behaviour suggests that reorientation due to twinning disrupted the (0002) basal plane transverse lattice strains, and necessitated a stiffer tensile response from the $(11\bar{2}0)$ prismatic plane. As twinning subsided, both planes displayed behaviours more consistent with the RD response. A smaller inflection was observed in the AZX alloy in the RD, no such inflection is seen for ZXK in the RD, suggesting twin activity at a lower level for AZX in the RD. Agnew et al. [126] also reported inflections in lattice strains from (0002) basal planes transverse to the loading direction with the onset of twinning in Mg alloys using neutron diffraction, corroborating our observations. At elevated temperatures, Fig. 4.10 & 4.11, reduced twin activity was reflected in the diminished magnitude of these inflections for the (0002) basal planes.

At elevated temperatures, the reduction in tensile lattice strain magnitudes was consistent across all alloys, reflecting the general decrease in stress required for slip, par-

ticularly on prismatic planes due to the ease of slip on non-basal slip systems, such as pyramidal systems. The increased activation of pyramidal slip systems at 250°C would reduce the lattice strain differences between prismatic and pyramidal planes [25]. The distribution of tensile lattice strains indicates increased stress sharing between grains ideally orientated for prismatic slip and harder pyramidal slip at elevated temperatures.

4.6.2 Strain rate sensitivity

The improved SRS at room temperature for the Ca-containing alloy ZXK compared to AZ31 seen in Fig. 4.16, is consistent with literature suggesting improved formability at low temperatures, attributed to a modified basal texture [120, 127]. The lattice strain results revealed rate sensitivity behaviour for the $(10\bar{1}0)$ prismatic plane for all alloys. For the ZXK alloy, the results in Fig. 4.13 suggest that the lower macroscopic flow stress at the slower rate of $10^{-4}\,\mathrm{s}^{-1}$ improving the SRS is linked to; the larger tensile lattice strains on the $(10\bar{1}0)$ prismatic plane, because of this the distribution of lattice strains changes, resulting in overlapping prismatic planes; consequently, reducing the overall magnitude of tensile lattice strains on these planes shortly after the elastic-plastic transition. The reverse of this behaviour was observed in AZ31 and AZX both with lower SRS. The AZX alloy at the slower rate $10^{-4}\,\mathrm{s}^{-1}$ displayed a pronounced sigmoidal curve for the transverse strains on the (0002) plane, described earlier to be influenced by twinning. This result suggests more twinning evolves in this alloy at lower strain rates than moderate strain rates. The SRS value close to 0 indicates a lower level of formability at room temperature compared to the ZXK alloy.

The outlying decrease in SRS for the ZXK alloy at 150°C aligns well with deep drawing experiments on a very similar composition by Victoria-Hernandez et al [20]. They reported good stretch formability at room temperature but a notable reduction in formability at warm temperatures ($100 - 150$°C). They suggested a relationship between

presence of coarse Mg_2Ca precipitates and oxides, they also note an improvement at 200°C. The results for the ZXK alloy at 150°C appear feasible with this knowledge, the significant rise in SRS at 250°C suggests the rate insensitive dynamics for the particle interactions causing the reduced formability could be reduced at temperatures ≥ 200°C. The lower SRS for AZX and ZXK at high temperatures compared to AZ31 suggests they may not benefit as much from temperature-induced ductility compared to AZ31. Kim et al [107] report an improved formability for a similar AZX alloy at 150°C corroborating the SRS results in Figure 4.16.

The serrated flow i.e., the Portevin-Le Chatelier (PLC) effect, observed at elevated temperatures is often associated with dynamic strain ageing [128, 129, 122], the serrated flow is attributed to the dynamic interaction between diffuse solute atoms and mobile dislocations leading to intermittent dislocation pinning and unpinning, at certain temperatures and strain rates. DSA has been shown to influence a lower or negative SRS at elevated temperatures [130, 125]. However, despite the dynamic strain ageing (DSA) these alloys exhibit larger 'm' values at 250°C.

The emergence of serration effects at elevated temperatures and lower strain rates suggests a diffusion-controlled mechanism such as DSA. At higher temperatures, solutes and vacancies gain increased mobility due to their higher thermal energy, while the strain rate governs the population and mobility of dislocations available to interact with solutes and form forest structures. The solutes responsible for DSA differ between the alloys. In AZ31, the substitutional elements Al and Zn are the most likely contributors to DSA [122]. Notably, Corby et al. [122] observed that both elements were necessary for the effect: Zn promotes cross-slip of basal dislocations onto prismatic planes, increasing forest dislocation densities, while Al atoms diffuse via pipe diffusion to these structures, pinning mobile dislocations.

For ZXK, which lacks Al, an alternative explanation for DSA is required. The solu-

bility of Ca in the Mg matrix increases with reduced Al content [117], suggesting that the higher Ca concentration in solid solution for ZXK could lead to solute pinning at elevated temperatures, where Ca has sufficient diffusivity [131].

In contrast, the smaller serrations in AZX imply a weaker DSA effect, despite the alloy containing Al, Zn, and Ca. Precipitation is known to diminish DSA by depleting solute concentrations in the matrix [132, 133]. The already lower Al and Ca content in AZX (compared to AZ31 and ZXK, respectively) may be further reduced by the formation of Al_2Ca and $(Mg,Al)_2Ca$ intermetallics, as evidenced in Fig. 4.5.

Without detailed chemical analysis of these alloys, definitive conclusions regarding the specific mechanisms of DSA remain beyond the scope of this work.

The lack of detrimental effects on ductility despite serrations could be due to the stronger effect of an increase in thermally activated mechanisms such as recovery of dislocations and $\langle$c+a$\rangle$ pyramidal slip activity [80]. Dynamic recrystallisation is another recovery mechanism that results in a reduced flow stress, its occurrence at temperatures > 200°C [25, 134] is relevant to the 250°C condition in this investigation, however, evidence of such mechanisms without post-mortem analysis is difficult to obtain [135]. In Fig. 4.11(c) & 4.15(c) there is a lack of a significant stress reduction after a critical strain before necking normally associated with DRX mechanisms in Mg alloys [136], making DRX unlikely but not impossible.

The analysis performed here provides early insights on the differences in the evolving elastic internal strain behaviour on specific planes of Ca-containing alloys compared to the AZ31 alloy. starting textures with varying temperature, strain rate and loading direction. While AZ31 exhibited consistent lattice strain behaviour between RD and TD due to its strong basal texture, the Ca-containing alloys showed distinct directional anisotropy, with significant variations in lattice strain magnitudes and hardening behaviour between load-

ing directions. At room temperature, ZXK demonstrated superior strain rate sensitivity (SRS) and formability, attributed to its modified basal texture and distinct lattice strain distribution on prismatic planes, where overlapping tensile strains reduced hardening effects. In contrast, AZ31 and AZX showed lower SRS, with AZX displaying pronounced twinning activity at low strain rates. These differences are attributed to the weakened basal textures in the Ca-containing alloys, which promote twinning and alter slip system activation. At elevated temperatures, reduced twin activity and increased activation of non-basal slip systems further differentiated the behaviour of Ca-containing alloys from AZ31, emphasizing the role of texture and temperature in governing deformation mechanisms in Mg alloys. Further probing of the elastic internal strains with more robust analysis such as the works of [137], could elucidate how the stress is distributed between grains in 'soft' or 'hard' orientations, an important concept for polycrystal HCP Mg alloys exhibiting strong textures

This chapter investigated the average lattice strain response of slip systems across many grains in the bulk material. The results revealed significant differences in twinning activity between rolling direction (RD) and transverse direction (TD) for the ZXK alloy, while AZX showed only minor directional variations. In the following chapter, we employ high-resolution electron backscatter diffraction to perform grain-scale analysis. This approach enables direct observation of twinning behaviour and characterization of intragranular stress evolution in these alloys with high spatial resolution at the sample surface.

Chapter 5

Microstructure insights of deformation in Mg alloys via In-situ HR-EBSD

5.1 Introduction

In-situ tensile testing combined with Electron Backscatter Diffraction (EBSD) enables a detailed, real-time examination of microstructural evolution during mechanical loading, providing insight into the underlying deformation mechanisms. EBSD is a powerful crystallographic tool used alongside Scanning Electron Microscopy (SEM) to capture Electron Backscattered Diffraction Patterns (EBSP), also known as Kikuchi patterns, seen in Fig. 3.3(b). These patterns contain Kikuchi bands, produced by scattered electrons that are diffracted by crystallographic planes, generating bands whose width is governed by Bragg's Law and the distance from specimen to detector screen. When indexed, these patterns reveal the crystal orientation of the sample at the beam's incident point. Scanning across a sample spatially reveals the crystallographic orientation

distribution and other structural details at the microscopic level. This coupling provides great insights of how grains reorient, which slip systems are active, and how deformation mechanisms such as twinning evolve during deformation. This combination offers several advantages: Detailed crystallographic information from EBSD offers insights into grain orientation and how these orientations change during deformation, enhancing the understanding of anisotropic behaviour in magnesium alloys. Observation of deformation mechanisms: The technique captures lattice rotation induced by slip, twinning, and dislocation behaviour, all critical for understanding the mechanical response of magnesium alloys. Texture evolution: Magnesium alloys exhibit strong texture due to their HCP structure, with grain orientations affecting their mechanical properties. In-situ EBSD permits the examination of macro and micro-scale crystallographic texture evolution during deformation, which is important factor for understanding formability. Twinning and detwinning processes: Magnesium alloys often undergo twinning as a major deformation mechanism, especially at low temperatures. In-situ EBSD can capture the initiation (shortly after nucleation), propagation, growth and reversal of twins, providing detailed insights into their influence on the overall mechanical response. However, direct observation of twinning nucleation has seldom been reported due to its exceptionally rapid speed.

While traditional mechanical testing methods, such as conventional tensile or compression tests, can provide valuable stress-strain data, they lack the detailed, real-time insights into microstructural changes that in-situ EBSD offers. Traditional post-deformation analysis captures only the deformation state after unloading, offering a static view of the microstructure. These methods cannot easily track grain reorientation or real-time evolution of deformation mechanisms such as twinning. The ability to observe real-time microstructural evolution, combined with the crystallographic detail provided by EBSD, enables a deeper understanding of grain boundary behaviour, texture changes, and the activation of slip and twinning mechanisms. Advances in technology and EBSD

analysis tools now enable the probing of larger sample sets at high speeds and accuracy. In this study, the High-Resolution EBSD (HR-EBSD) post-processing software Cross-court4 was used to aid the investigation of the grain-level local stress state evolution during deformation. This is alongside geometrically necessary dislocation (GND) and orientation analysis using the MTEX toolbox in MATLAB.

Cross correlation analysis with Cross-Court

A summary of the techniques employed by the software Cross-Court4 is given here based on literature from [138, 139, 140, 141, 142] Cross-correlation is a technique leveraging EBSD for assessing elastic strain and lattice rotations in crystalline materials. A Kikuchi pattern from a reference point within each grain is chosen, small shifts in pattern features across points in grains is compared relative to this reference pattern. Strain variations and rigid body rotations cause small shifts in the Kikuchi pattern features such as the position of the zone axis and width of bands. Four or more square regions of interest (ROIs) are distributed over the patterns (40 were used in this analysis), with at least one on the zone axis of the patterns (area with the most intersecting Kikuchi bands). The location of these ROIs is the same for each pattern. Cross-correlation between the reference pattern and subsequent patterns is performed for each ROI using fast Fourier transforms. The measured shifts are assumed to be determined by strain in the volume sampled, the x and y components of the shifts can be related to components of a displacement gradient tensor. This technique allows elastic strain variations and lattice rotations to be calculated for the shifts, from this deviatoric stress can be extracted, and using the condition that the surface normal has zero stress because EBSD is a surface technique, the hydrostatic stress can be reconstructed. With HR-EBSD enhancing traditional EBSD by offering improved sensitivity to strain and rotation. It is possible to measure the movement of features in the patterns with sub-pixel accuracy.

One of the key challenges in using cross-correlation is dealing with significant lattice rotations, which can lead to errors in strain measurement. To address this, an iterative approach is often employed: the diffraction pattern of the deformed crystal is first remapped to align more closely with the reference pattern, accounting for large rotations. Subsequent cross-correlation can then accurately capture the residual elastic strain. A feature that was not employed here due to software issues, resulting in high magnitudes when rotations are large at higher stresses, developing abrupt variations but overall gradients are relevant.

In summary, cross-correlation in HR-EBSD is a powerful tool for probing the microstructural mechanisms of deformation in crystalline materials. It allows for the detailed mapping of strain and rotation, even in the presence of complex dislocation structures, making it a useful tool for advancing our understanding of microstructural behaviour under stress.

It is important to note that the results from the CrossCourt4 analysis provide relative stress values for each EBSD map. The stresses calculated within each grain are based on reference points that are selected according to a measure of the internal variation in lattice distortion within a grain. Specifically, the Kernel Average Misorientation (KAM) method was used to identify a reference point within a grain with the lowest misorientation compared to the surrounding points within the same grain. This reference point selection method seeks to identify a 'strain free' reference within grains to capture the maximum level of strain from the remaining points within the grain. However, this method introduces variability when choosing a reference point from maps of the same area at different stages of deformation [143]. It was not feasible to automatically or manually select the same reference point within a grain at each stage, due to software limitations and the geometry of grains changes at higher strains. As a result, absolute stress values cannot be directly compared across maps because the reference points vary between strain stages. This approach, while sacrificing consistency in absolute values, is

essential when working with large datasets where manually selecting reference points in each grain is impractical. The focus of this processing method is on capturing the relative stress evolution within each grain, rather than absolute values across strain maps, allowing for an efficient and robust analysis of stress variations across large datasets.

Geometrically necessary dislocations (GNDs)

Plastic deformation in polycrystalline materials is mediated by the formation, motion, storage and/or annihilation of dislocations [144]. During deformation, permanent changes in lattice arrangements are facilitated by dislocations allowing atomic planes to slip past each other. Varied distributions of crystal orientations in a polycrystal will govern the plastic strain response of each grain, intragranular accommodation is necessary to prevent incompatibilities between grains that will lead to voids and/or destructive grain boundary interactions between grains [145]. Dislocations arrange into energetically favourable configurations, such as cell structures, to minimize strain energy [146]. A portion of the stored dislocations are accumulated as geometrically necessary dislocations (GNDs) with a non-zero Burgers vector that induces lattice curvature and enables strain compatibility across grain boundaries. These GNDs organise into dislocation walls, forming geometrically necessary boundaries (GNBs) that partition grains into subgrains [145]. In contrast, statistically stored dislocations (SSDs) arise from random trapping during deformation and exhibit no net Burgers vector, contributing to forest hardening without causing long-range lattice curvature. The interplay between GNDs and SSDs governs work hardening, with short-range interactions (e.g., dislocation reactions) and long-range stress fields collectively influencing mechanical behaviour. Critically, GND density is dictated by microstructural features (e.g., grain size, texture), while SSD accumulation is intrinsic to the material's deformation physics.

EBSD provides mesoscale information on dislocations and dislocation structures

across a microstructure by variation in the EBSD-measured crystal orientation as a function of stored dislocation density through imparted plastic strain. To quantify GNDs from HR-EBSD data, the Nye tensor formalism is employed, which relates lattice curvature (derived from orientation gradients) to dislocation density [147]. This was implemented using the MTEX toolbox in MATLAB, orientation gradients were computed from EBSD maps and used to solve for the dislocation density tensor. The GND density is then derived from the tensor's norm, assuming known Burgers vectors. The Burgers vectors from the basal $\langle a \rangle$, prismatic $\langle a \rangle$, pyramidal $\langle a \rangle$ & pyramidal $\langle c + a \rangle$ slip systems were used. This approach, while powerful, inherently captures only GNDs ignoring SSDs and is sensitive to experimental parameters like step size and noise. Nonetheless, it provides a robust framework for correlating dislocation structures to local mechanical responses, bridging macroscopic plasticity to micromechanical deformation response.

5.2 Results

5.2.1 Microstructure and GND evolution

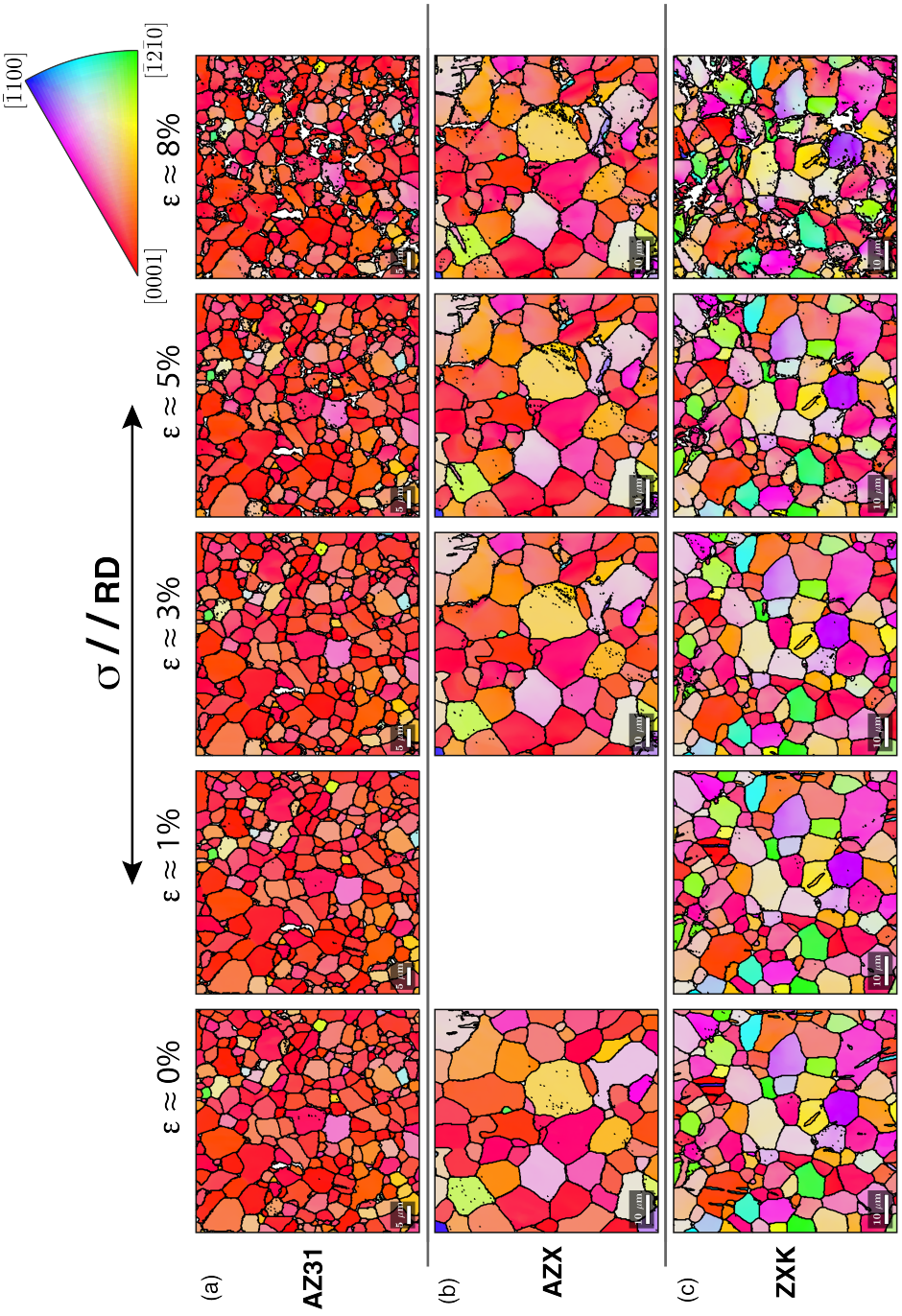


Figure 5.1: IPF-Z maps for (a) AZ31, (b) AZX and (c) ZXK for loading in the RD case. Showing the evolution of grain orientation and twin formation with increasing strain.

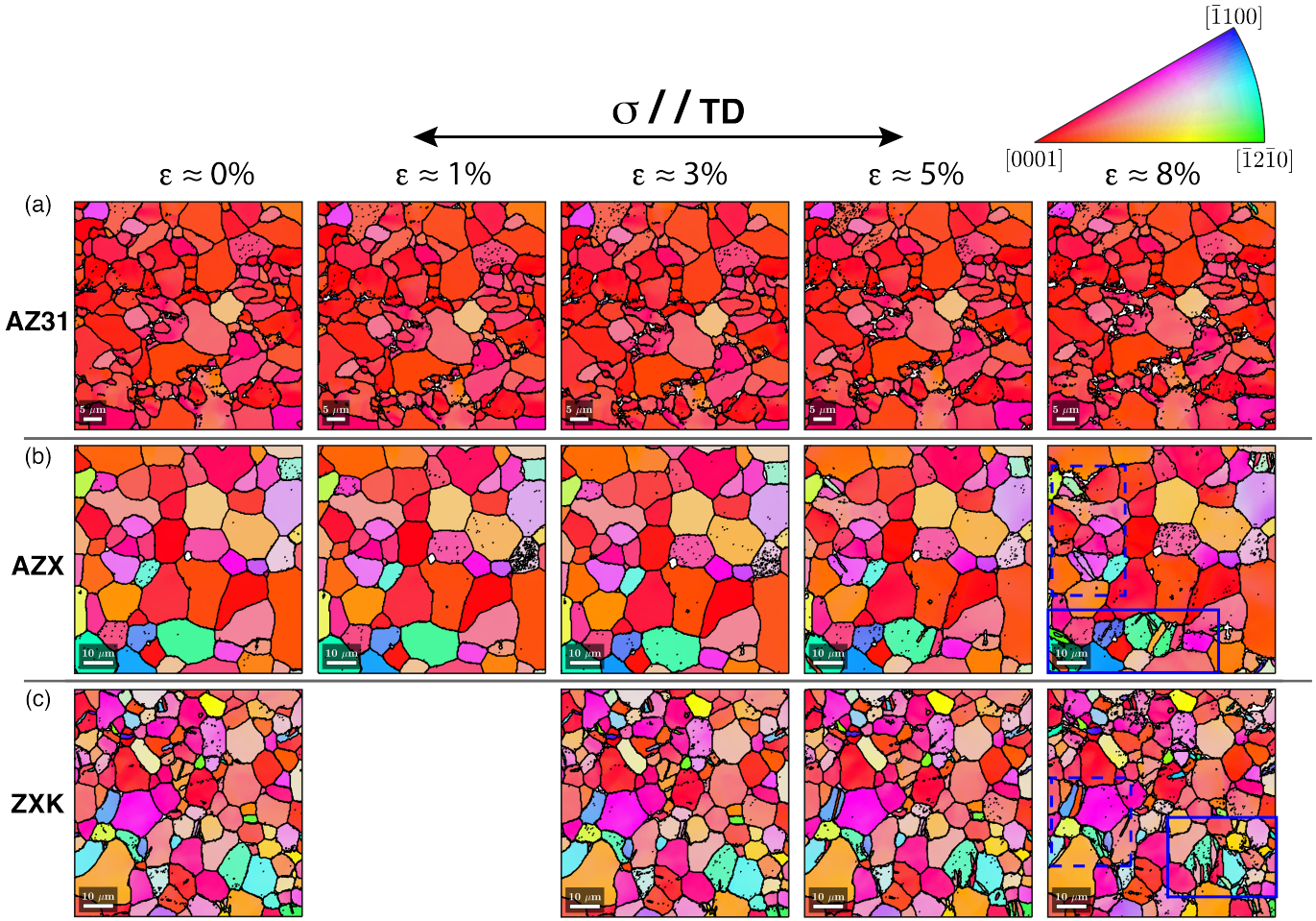


Figure 5.2: IPF-Z maps for (a) AZ31, (b) AZX and (c) ZXK for loading in the TD case. Showing the evolution of grain orientation and twin formation with increasing strain. Area's for twin analysis are enclosed in blue box's, Map 1 = solid line, Map 2 = dashed line.

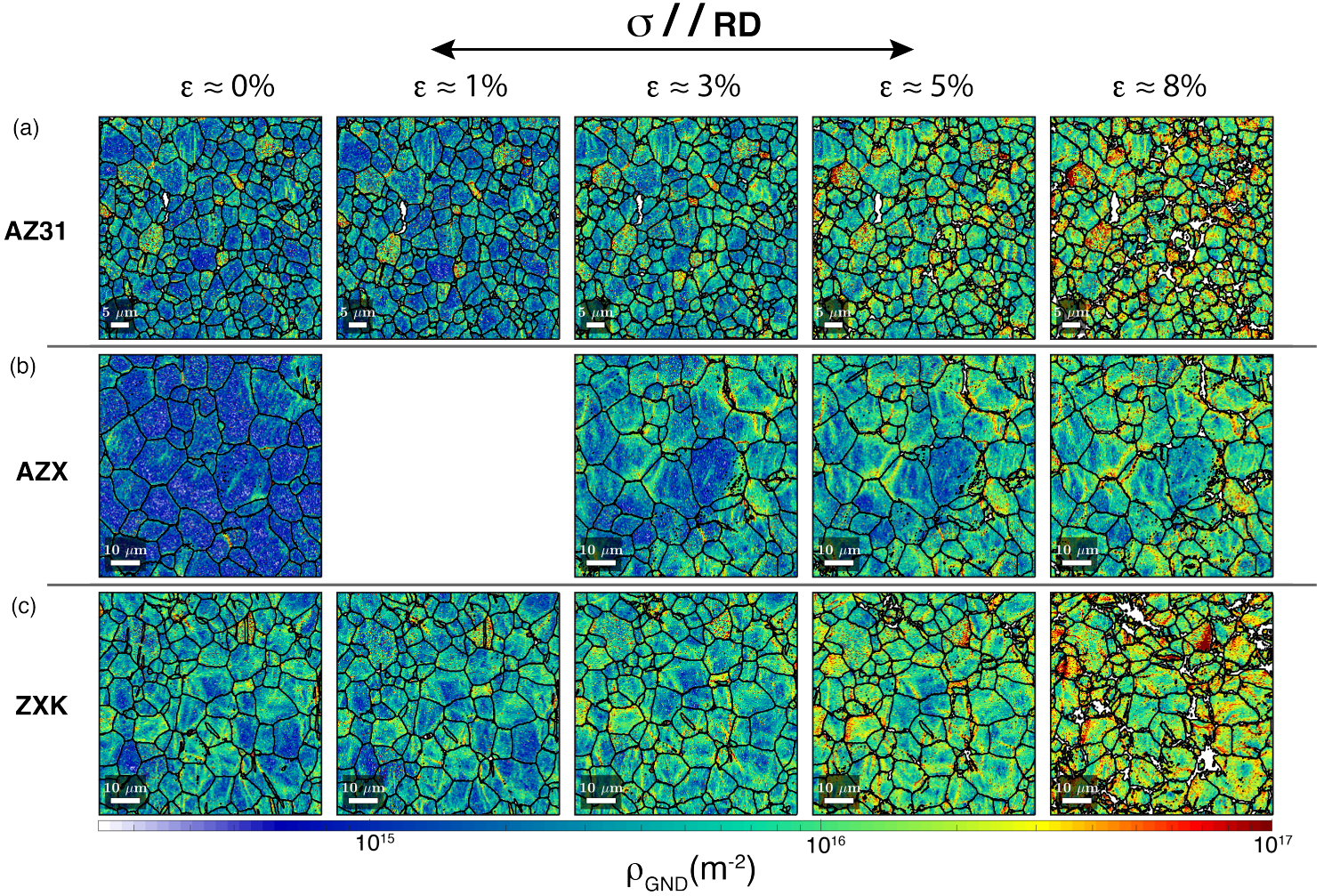


Figure 5.3: Geometrically Necessary Dislocation (GND) density maps for (a) AZ31, (b) AZX and (c) ZXK, for loading in the RD case. Showing the GND evolution with increasing strain.

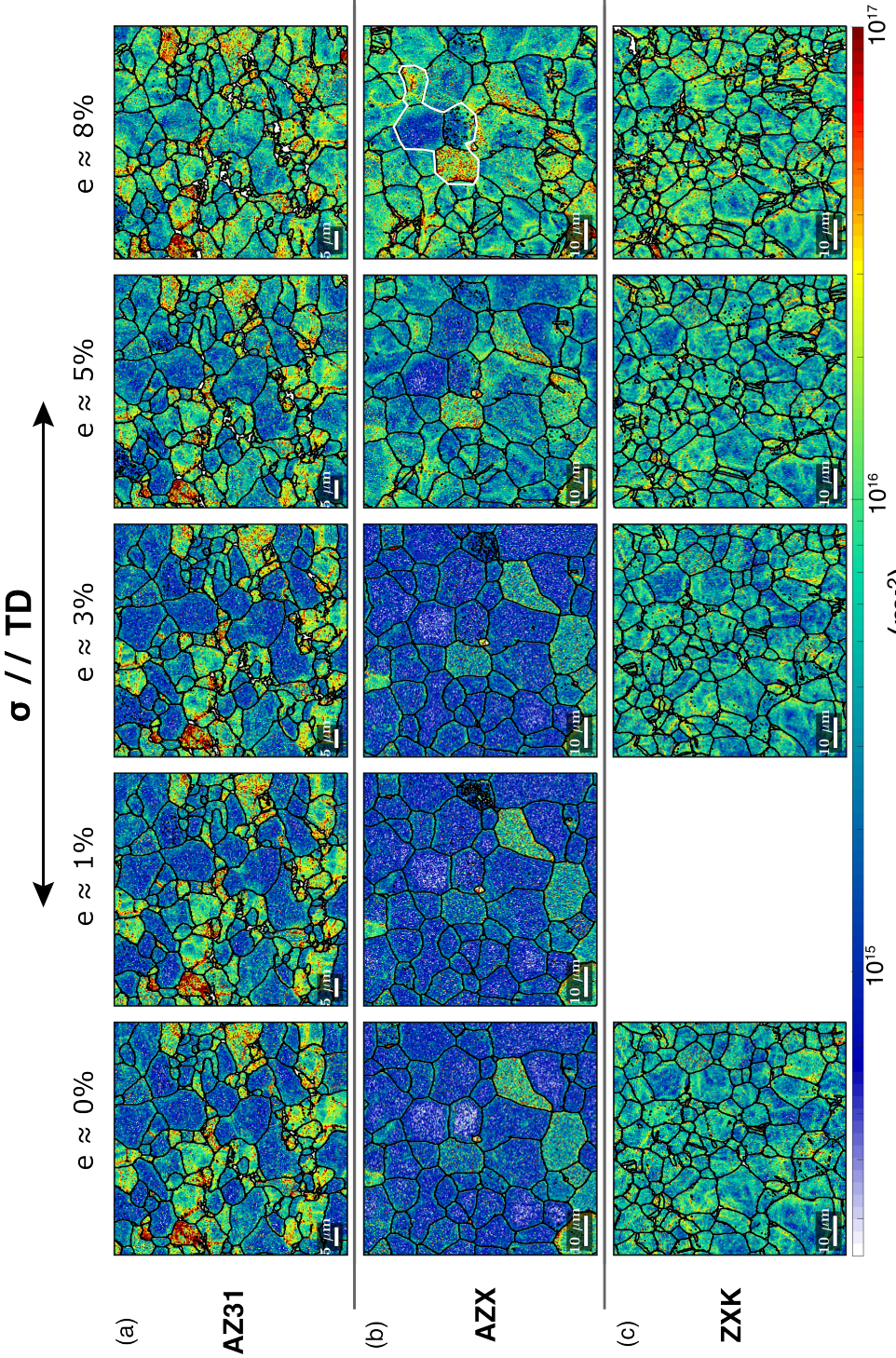


Figure 5.4: Geometrically Necessary Dislocation (GND) density maps for (a) AZ31, (b) AZX and (c) ZXK for loading in the TD case. Showing the GND evolution with increasing strain.

Grain orientation maps obtained via EBSD are presented in Figures 5.1 and 5.2, capturing the evolution of microstructure with increasing stress. The three stages of twinning, nucleation (post), propagation, and growth of twins are clearly evident in the Ca-containing alloys (AZX and ZXK), while AZ31 shows no twinning activity.

Qualitatively, AZX (Fig. 5.1(b)) exhibits more propagation of lenticular twins between strain states ($\varepsilon \approx 3 - 5\%$) compared to ZXK. In contrast, ZXK displays pre-existing twins in the initial condition that de-twin by $\varepsilon \approx 1 - 3\%$. Additionally, ZXK like AZ31, accumulates sufficient damage/dislocations to disrupt EBSD diffraction patterns, an effect not observed in AZX. Twinning is more pronounced in the transverse direction (TD, Fig. 5.2) for both AZX and ZXK. These results establish a clear correlation between strain state and twinning behaviour, reinforcing the selection of strain targets for mapping based on the macroscopic tensile and lattice strain data from Chapter 4.

It is important to note for AZ31, the EBSD grain orientation maps highlight the variation in grain size and morphology distribution across the sample. By chance, for the TD case, the captured region does not exhibit an equiaxed polygonal microstructure. The analysis performed is localised, and therefore comparisons between the RD and TD in relation to the macroscopic response would need to be considered.

The geometrically necessary dislocation (GND) density maps in Fig. 5.3 and Fig. 5.4 raise an interesting observation for the initial condition of the material. The GND maps have equal limits, allowing qualitative comparisons. For both RD and TD cases, maps at $\varepsilon \approx 0$ suggest ZXK and AZ31 samples contain a larger initial GND density. The increase in GND density with increasing macroscopic strain is clear for all alloys; the GND density approached $> 10^{17}$ m^{-2} within dislocation structures. This occurred in relatively more grains for ZXK in Fig. 5.3 vs 5.4.

The difference in GND density accumulation for AZX between the RD and TD case

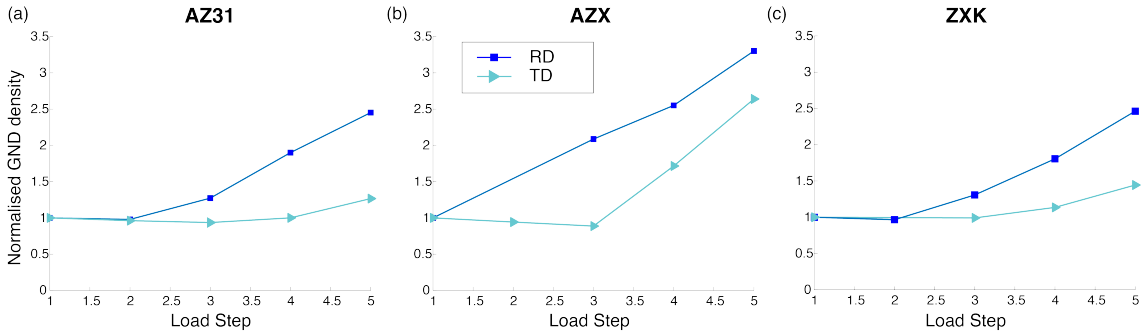


Figure 5.5: Total geometrically necessary dislocation (GND) density evolution with increasing macroscopic strain from each map, for (a) AZ31, (b) AZX and (c) ZXK. The GND densities have been normalised to the initial condition level, showing the GND density evolution with increasing strain.

is very clear in the maps; the RD case accumulates a higher density earlier at $\varepsilon = 3\%$. This is quantitatively depicted in Fig. 5.5, where the total GND density, summed and normalised by the initial condition, increased at larger strains. Outliers in the data were filtered out before summing, these were identified as values 3 times the scaled mean absolute deviation. The total GND densities were normalised to the initial condition to isolate the strain-induced evolution because the alloys had varying initial GND densities. For the deformation range examined, the data implies when loading in the RD, the rate of dislocation accumulation into GNDs in grains is greater than loading in the TD case. This anisotropy is consistent with the macroscopic tensile results for AZX and ZXK. The grain size difference between AZ31 samples is likely to have influenced the result between RD and TD case; more grain boundaries within the mapped area for the RD case would influence dislocation interaction and nucleation from the boundaries themselves. Fine grains will generally give rise to a higher rate of dislocation pile up [148], but the extent will depend on dislocation dynamics and compatibility at grain boundaries [149, 150, 151].

The relationship between GND density and c-axis inclination angle to the sheet normal is quantitively considered in Fig. 5.7. c-axis inclination is schematically represented in Fig. 5.6, for sheet Mg alloys it is directly linked to soft & hard grain orientations, the active deformation modes when loading in the sheet plane are heavily influenced by

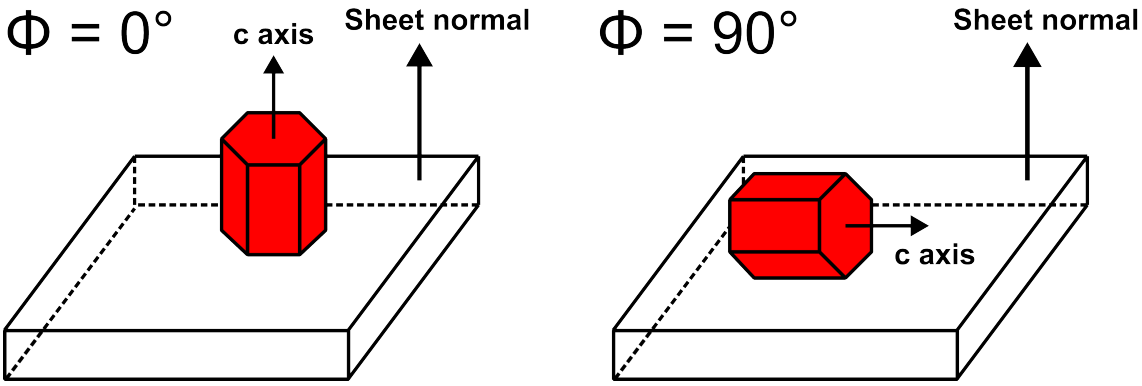


Figure 5.6: Schematic illustrating the angle of the c-axis to the sheet normal. Φ represents the inclination angle.

the c-axis inclination angle which determines the resolved shear stress on slip and twin systems based on Schmid's law. The c-axis inclination angles closer to the sheet normal ($0°$) in the majority of grains (e.g., AZ31) result in strong basal textures in the (0001) pole figure, known to be detrimental to formability in Mg alloys. In Fig. 5.4 the GND density within the grains highlighted by a white border showed significant variation, the orientation of these grains, seen in Fig. 5.9, correlates the c-axis inclination (soft & hard grains) with GND evolution during deformation. The soft grain with c-axis off-basal maintained a relatively low GND density of $\approx 10^{15}$ in the interior of the grain compared to the hard grains that appear to accumulate GND structures with densities $\approx 10^{16} - 10^{17}$. This suggests the soft grain accommodated deformation via easy basal slip, while suppressed basal slip in the harder grains required GNDs to accommodate strain gradients from higher stresses.

The 0-10° and 80-90° inclination ranges in Fig. 5.7 had the highest GND densities for all three alloys, with some exceptions. This observation agreed with the hard orientation theory, showing the presence of two hard orientations for the Mg HCP crystal structure. However, considering Fig. 5.8, the number of orientations contributing to several of the GND measurements in the initial and final strain state were significantly lower and insufficient for a reliable measurement despite the normalisation applied to each range. This particularly applies to AZ31 for both the RD & TD and AZX for the

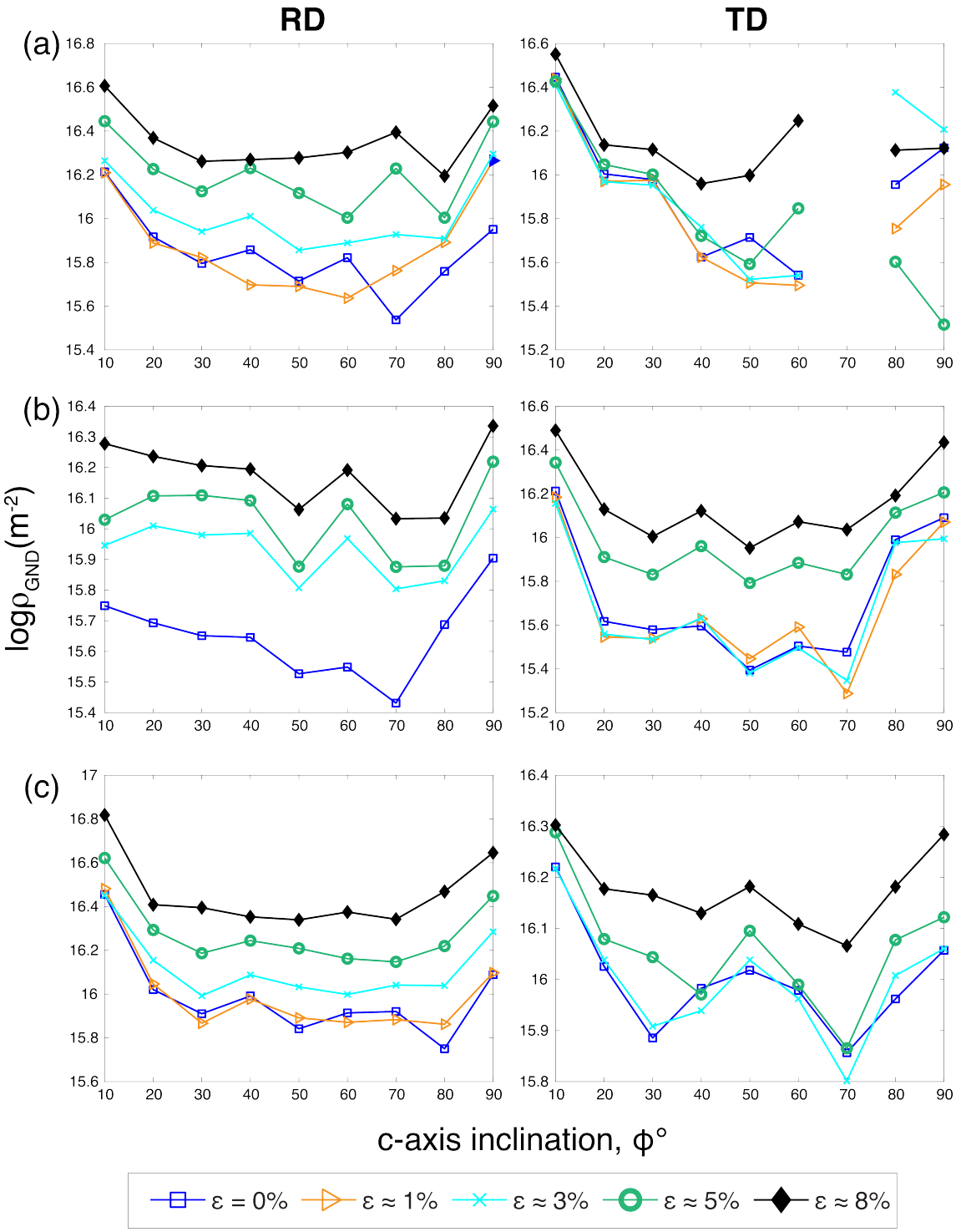


Figure 5.7: Evolution of GND density as a function of c-axis inclination angle with increasing macroscopic strain. The inclination angles have been binned with 10°intervals and GND densities normalised by number of orientations within each bin. This is shown for alloys (a) AZ31, (b) AZX and (c) ZXK.

RD. This suggests the similar GND density calculated in AZ31/AZX-RD for 80-90° was not accurate. From Fig. 5.7, statistically, the argument for a smaller increase in GND

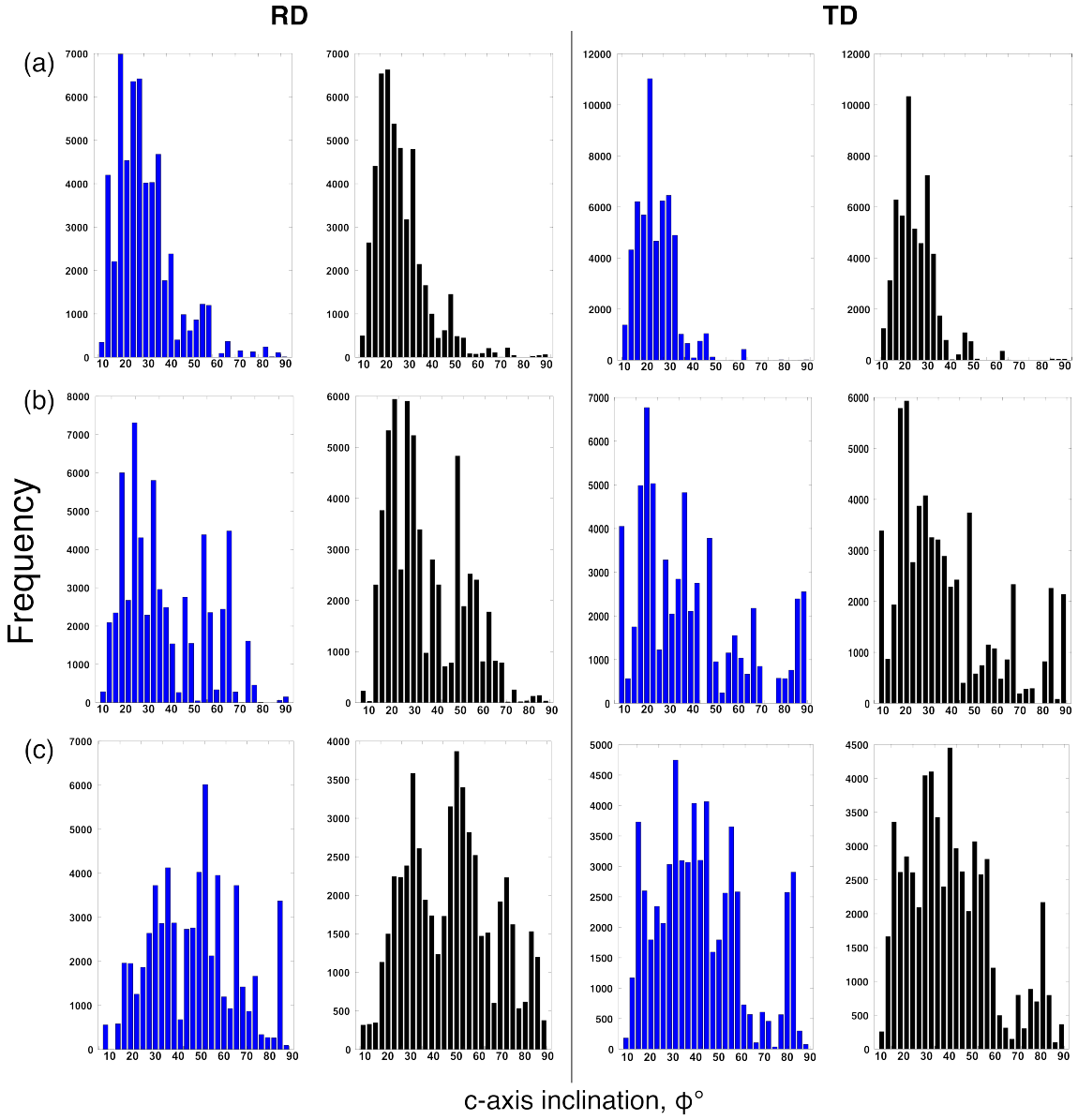


Figure 5.8: Distribution of c-axis inclination angles at $\varepsilon = 0\%$ (blue) and $\varepsilon \approx 8\%$ (black) strains for both RD and TD loading. (a) AZ31, (b) AZX and (c) ZXK.

density for inclination angles $\approx 45^{\circ}$ compared to 0-10°& 80-90°was not as strong as the qualitative observation.

The distribution of inclination angles in Fig. 5.8 closely resemble trends in pole figure observations for these alloys, shown in Figures. 4.1, 4.2 & 4.3. There is a left-skewed distribution for AZ31 due to the strong basal texture, whilst the texture weakened AZX and ZXK exhibit a broader spread of angles, with the c-axis normals oriented closer to

the sheet plane.

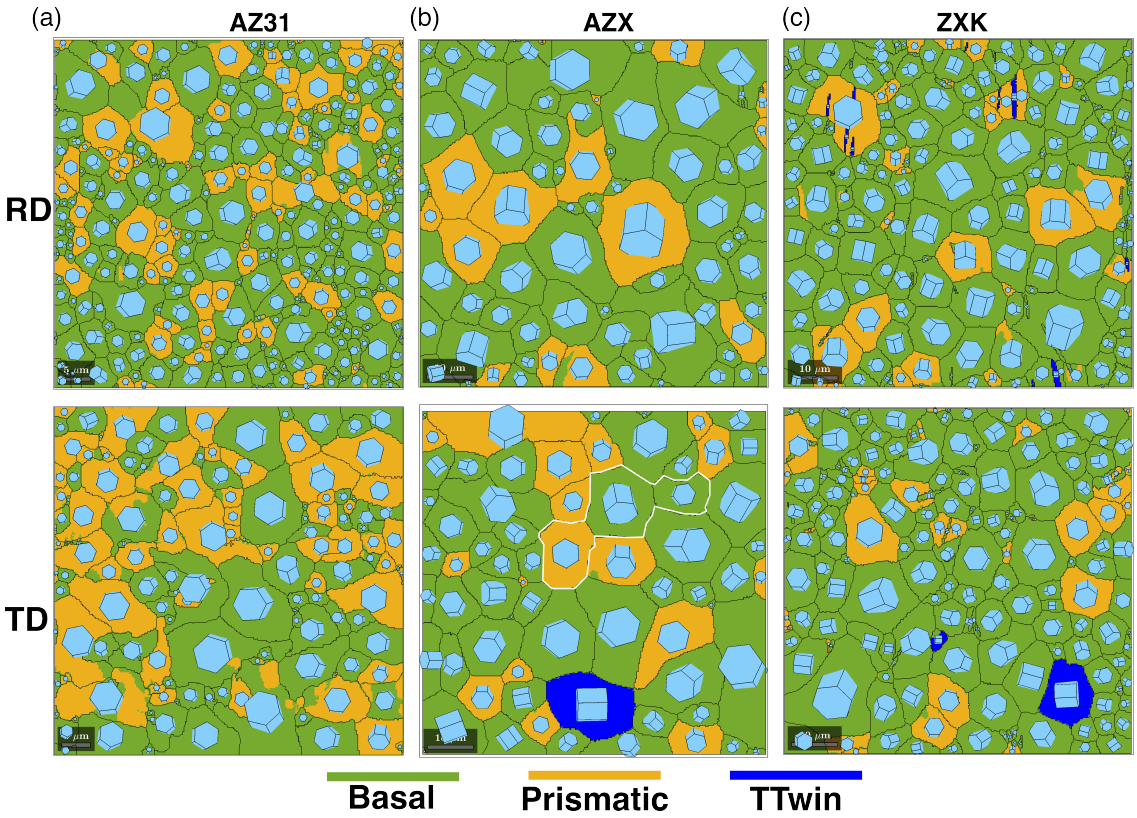


Figure 5.9: Initial condition maps coloured by highest Schmid factor for the respective slip/twin system. (a) AZ31, (b) AZX and (c) ZXK, for loading in both cases. Hexagonal close packed (HCP) unit cells are superimposed on grains to visualise the mean orientation of the grain.

Figures 5.9 5.10 show a very similar distribution between the alloys for grains with basal/prismatic slip as the highest Schmid factor, therefore these grains are likely to undergo dislocation slip over twinning. In the Schmid factor calculations the non-basal deformation systems are scaled by the critical resolved shear stress (τ_{CRSS}) ratio between these systems. The τ_{CRSS} values chosen were informed by polycrystal plasticity modelling work [152]. Scaling accounted for the significantly different τ_{CRSS} required for activation of deformation modes in Mg alloys, the predicted highest Schmid factor calculations highlighted may not visually align with the HCP crystal overlay because of this scaling. Where the highest Schmid factor corresponds to tensile twins, twins are expected, as is predicted for the TD case, but not all.

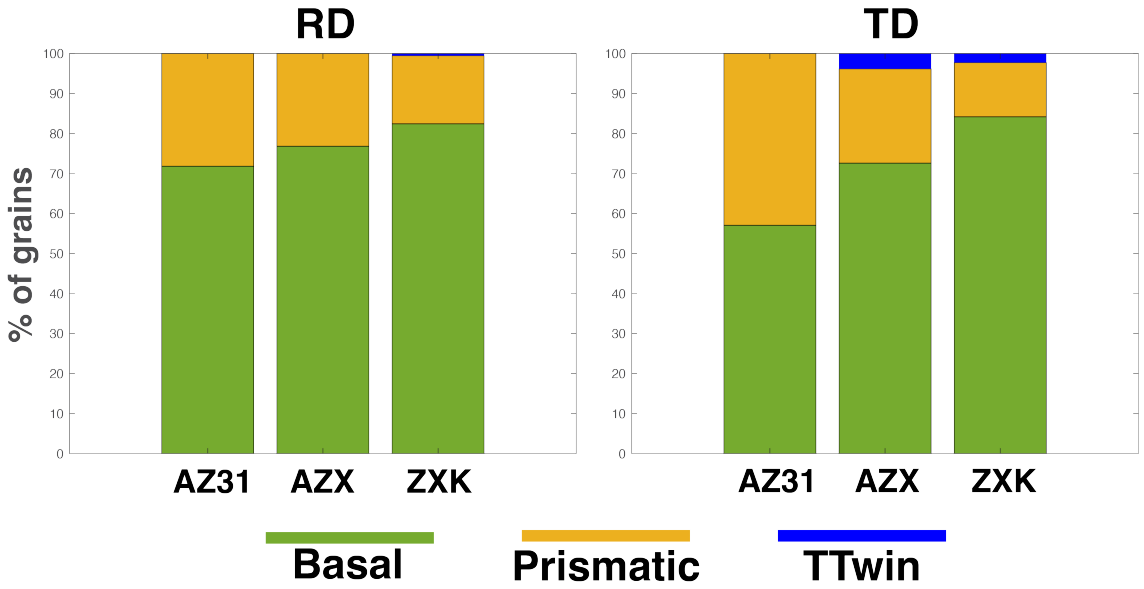


Figure 5.10: Percentage of grains with the highest Schmid factor for the respective slip/twin system.

Figure5.11 highlights an increase in the average tensile twin Schmid factor for the Ca-containing alloys. The average Schmid factor value for basal slip decreases for AZ31 & AZX textures but increases for the ZXK texture in the TD case.

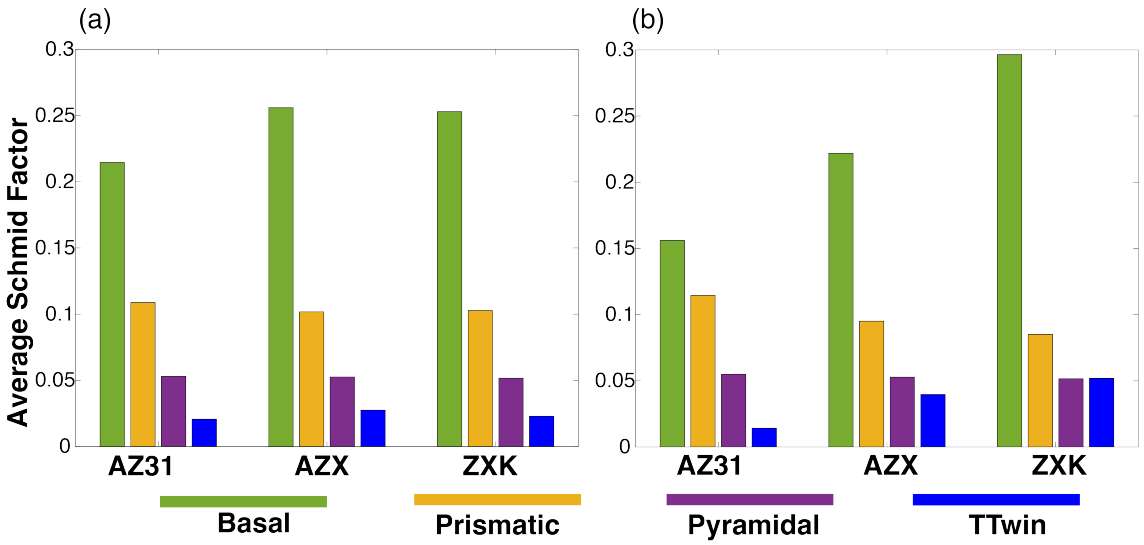


Figure 5.11: Average Schmid factor for the respective slip/twin system for (a) RD case and (b) TD case.

5.2.2 Twinning in Ca-containing alloys

Considering the prominent tendency for twinning in the Ca-containing alloys compared to AZ31, Fig. 5.12 provides insight into the Schmid factor distribution for twinning across individual grains. It specifically shows how the inclination and direction of the c-axis affect whether a grain is favourably oriented for twinning, based on the resolved shear stress acting on the $\{10\bar{1}2\}$ plane for tensile twinning, under the applied loading condition. A combination of factors, including a c-axis parallel to the sheet plane and aligned with the loading direction, resulted in higher calculated Schmid factors. Given these conditions, it can be anticipated which grains in the RD and TD maps at $\varepsilon = 0$ will exhibit twinning, although there were some exceptions.

Local variations in the spatial distribution of von Mises stress (σ_{VM}) and GND density

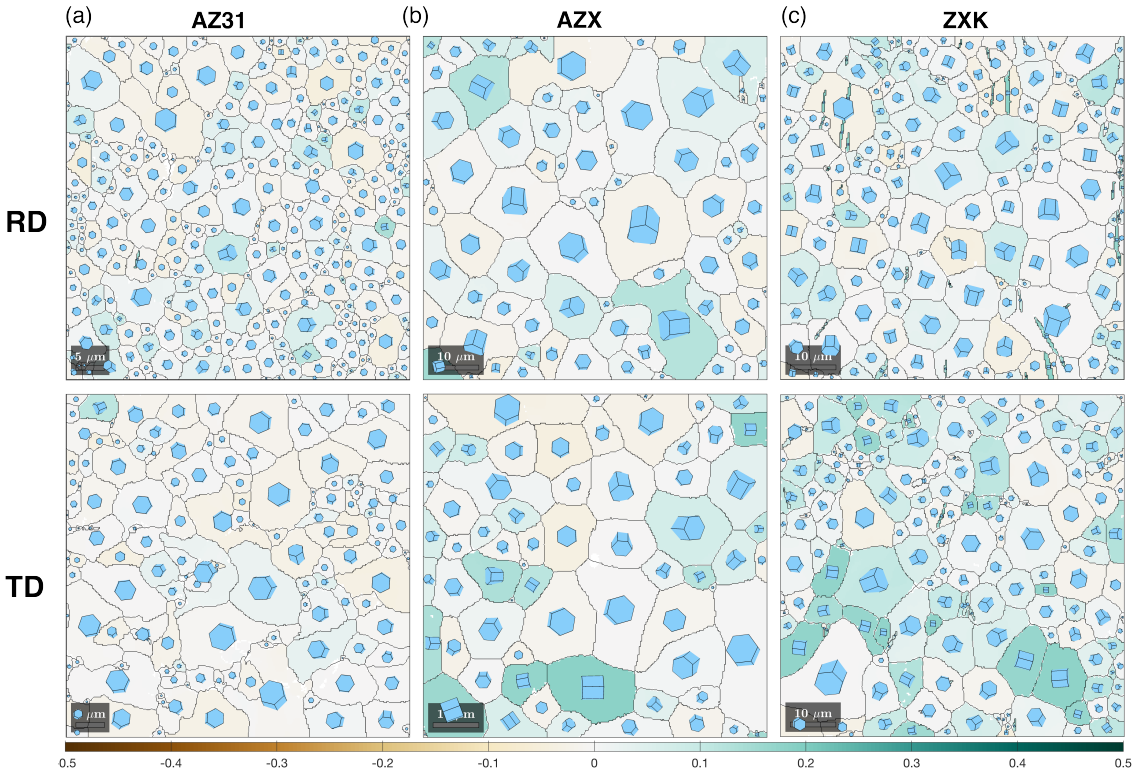


Figure 5.12: $\varepsilon = 0\%$ condition maps coloured by Schmid factor for the tensile twin system. (a) AZ31, (b) AZX and (c) ZXK, for loading in both cases. Hexagonal close packed (HCP) crystal overlaid on grains to highlight the mean orientation of the grain.

(ρ_{GND}) are captured for areas of interest in Figures 5.13 and 5.17. Here we define the whole area in these figures as Map 1 (M1), grains of interest are denoted as G1,G2 etc., and twins are given T1,T2 etc. Stress gradients preceding twins and at twin-grain boundaries are observed. In Fig. 5.13, within the annotated red rectangles at the boundary between M1G1 & M1G2 at $\varepsilon \approx 3\%$, a notable σ_{VM} gradient is observed, exhibiting a significant increase in σ_{VM} magnitude from $\varepsilon = 0$ to $\varepsilon \approx 3\%$. In contrast, the surrounding regions in M1G1 & M1G2 exhibited minimal changes. Between $\varepsilon \approx 3 - 5\%$, M1T5 nucleated within the region of the σ_{VM} gradient and grew significantly compared to the other newly formed twins. The GND density in the same area showed a similar concentration to the σ_{VM} gradient but with softer gradients. At $\varepsilon \approx 5\%$, M1T5 exhibited noticeably lower σ_{VM} values compared to the area before the twin nucleated, the surrounding area in M1G2 and the boundary of M1G1 had changes in σ_{VM} gradients. However, there was a contrasting increase in GND density inside the twin without a

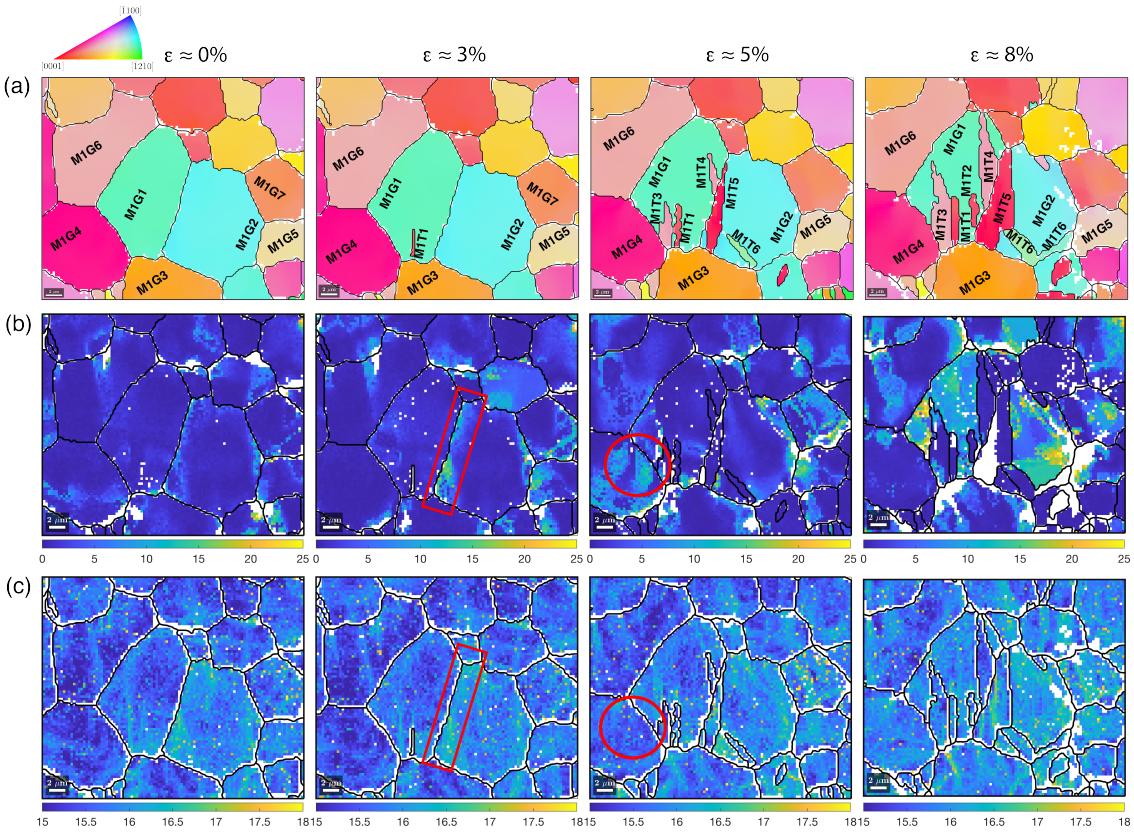


Figure 5.13: Area Map 1 with increasing strain for ZXK. (a) EBSD maps (b) σ_{VM} (GPa) (c) GND ($\log_{10}$) for loading in the TD case.

corresponding increase in magnitude of σ_{VM}. Focusing on the GND density, in M1T3 & M1T4 at $\varepsilon \approx 8\%$ a lower GND density is observed within the twins relative to the parent grain M1G1, this phenomenon is particularly pronounced in M1T4. While comparison with smaller twins such as M1T1 and M1T2 is challenging, a reduction in GND density is not replicated in other twin variants.

Within M1G3 & M1G4, which share the boundaries with M1G1 & M1G2 (where their respective twins appear to nucleate have nucleated), there are complex σ_{VM} gradients evolving from these boundaries at $\varepsilon \approx 5 - 8\%$. This suggests the twins M1T1,T3,T5 & T6 are influencing the boundary behaviour at these stages. At $\varepsilon \approx 8\%$ in M1G1 & M1G2 there are large σ_{VM} fluctuations in these grains compared to similar size grains that did not twin.

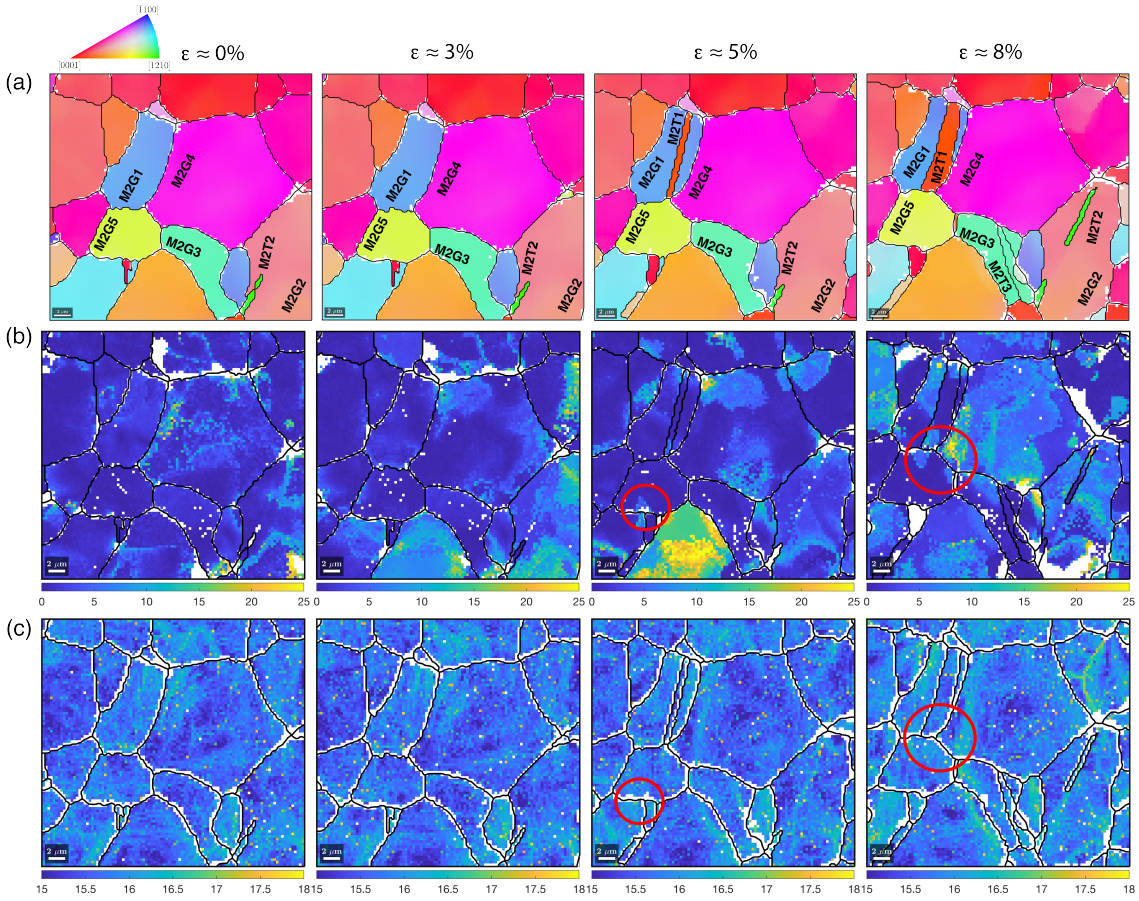


Figure 5.14: Area Map 2 with increasing strain for ZXK. (a) EBSD maps, (b) σ_{VM} (GPa) and (c) GND ($\log_{10}$) for loading in the TD case.

ZXK Map 2 (M2) shown in Fig. 5.14, has patterns similar to those from Map 1 are observed. Of note, the growth of twin M2T2 between the stages $\varepsilon \approx 5\%$ to $\varepsilon \approx 8\%$ coincides with a significant σ_{VM} concentration evolved at the boundary between M2G1 & M2G4 where the expanding twin interacts with the boundary. No σ_{VM} gradient was captured in the previous loading steps. Despite M2G2 exhibiting an overall higher σ_{VM} level, this particular σ_{VM} concentration stands out, indicating the twin boundary interaction may have altered local σ_{VM} conditions at this boundary.

In Figure5.17 we observe patterns in stress and GND density variations across strains for grains that also undergo twinning in AZX M1. Specifically, in grain M1G2, two twin variants, M1T3 and M1T4, exhibit a lesser GND density than the surrounding parent grain. Notably, a rise in GND density is observed at the boundary of M1T4, indicating dislocation accumulation near the twin-grain boundary. Similarly, in grain M1G1, twin variants M1T1 and M1T2 also show a lower overall GND density compared to the parent grain, which reinforces the trend of reduced dislocation density within certain twinned regions.

The data from ZXK Map 1 in Fig. 5.15, highlights a reduction in overall σ_{VM} for

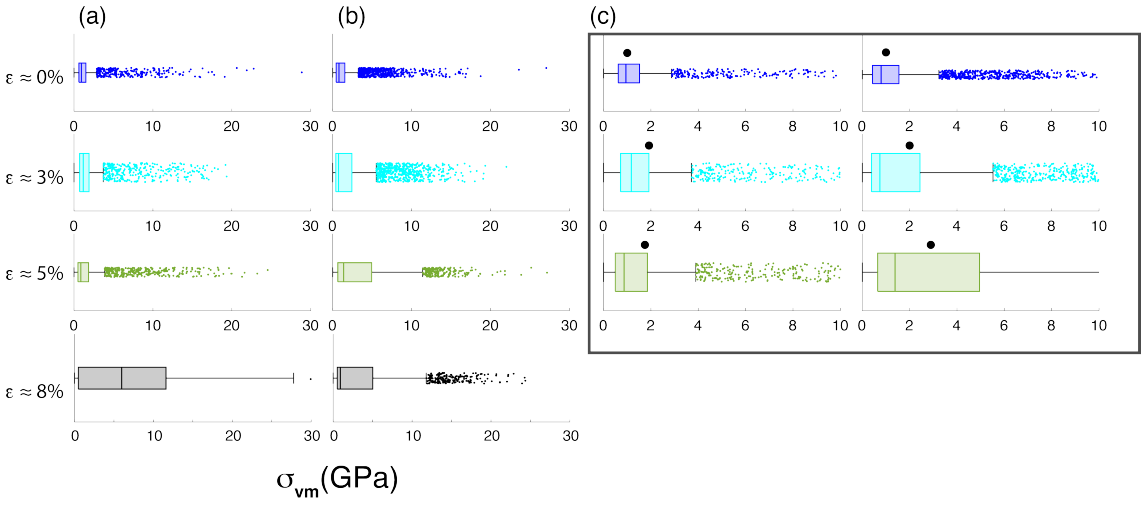


Figure 5.15: Distribution of σ_{VM} in ZXK-Map 1 with increasing strain. For (a) grains that twinned and (b) grains that did not twin for loading in the TD case. (c) is an inset to help visualise the data in (a) and (b).

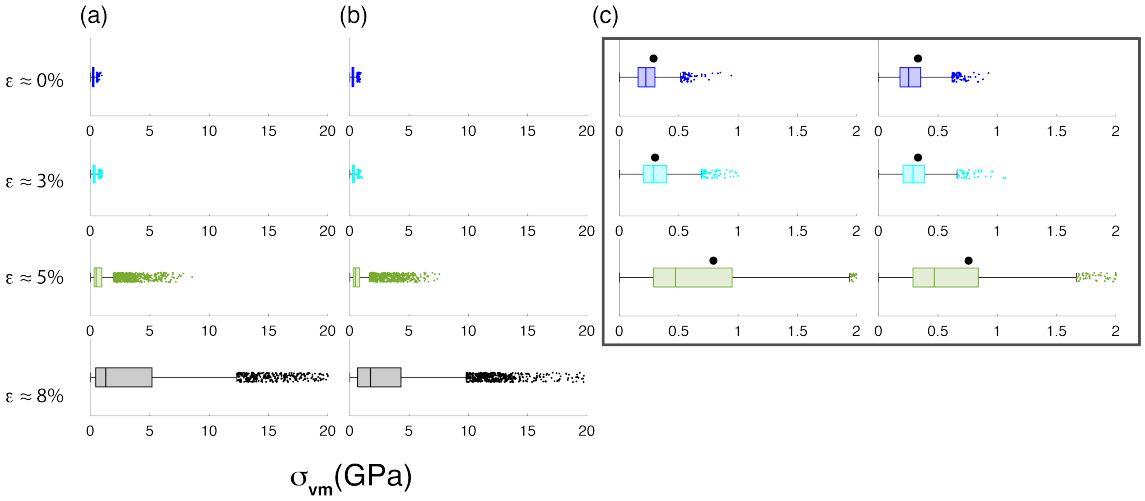


Figure 5.16: Distribution of σ_{VM} in AZX-Map 1 with increasing strain. For (a) grains that twinned and (b) grains that did not twin for loading in the TD case. (c) is an inset to help visualise the data in (a) and (b).

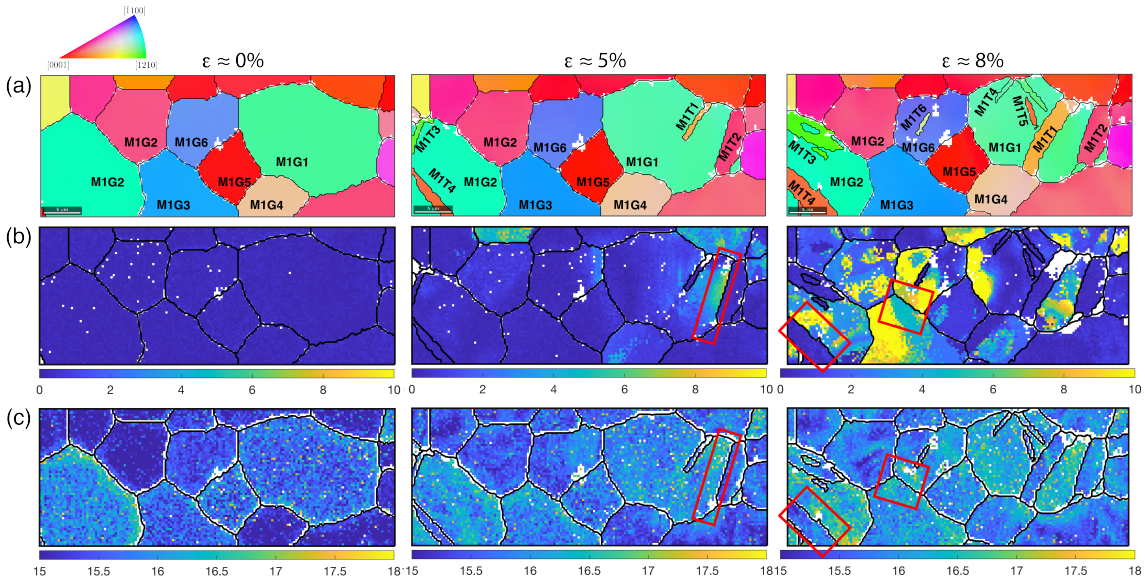


Figure 5.17: Area Map 1 with increasing strain for AZX. (a) EBSD maps (b) σ_{vm}(GPa) (c) GND ($\log_{10}$) for loading in the TD case.

grains that underwent twinning as well as their associated twin regions when compared to grains that did not experience twinning. Specifically prior to twinning at ($\varepsilon \approx 3\%$) and the strain where a burst of twinning is observed ($\varepsilon \approx 5\%$). At ($\varepsilon \approx 5\%$), the median σ_{VM} for grains that twin is lower than that of non-twinning grains. Additionally, the spread of the data is significantly narrower for twinning grains compared to non-twinning ones. Interestingly the mean σ_{VM} in non-twinning grains increases across the

strain range, while for twinning grains, it decreases. This suggests that twinning may have induced stress relaxation at ($\varepsilon \approx 5\%$), but with further development at ($\varepsilon \approx 8\%$), a subsequent increase in stress is observed.

In contrast, Fig. 5.17 for AZX Map 1 reveals a different trend. Between $\varepsilon \approx 3\%$ and $\varepsilon \approx 5\%$, the median σ_{VM} for twining grains remains similar to that of non-twinning grains, but the data spread for twinning grains widens. At $\varepsilon \approx 8\%$, the spread of stress data in the twinning grains does not increase substantially as in ZXK Map1, although the median stress remains lower in the twinning grains. This implies a more moderate evolution in the stress state for twinning grains in the AZX Map 1 compared to ZXK Map 1.

In Fig. 5.19, the predicted Schmid factors for the new twin orientations show that twinning in AZX M1 created orientations with similar Schmid factors for basal slip or harder orientations (M1T1 & M1T4) relative to the parent grains. Twins for ZXK M1 in Fig. 5.18 showed a similar trend, twin pairs M1T1 & T2 were significantly harder than M1G1. The Schmid factor trends for prismatic slip and twinning were very similar for both alloys.

5.3 Discussion

Data collected with EBSD techniques are highly sensitive to both surface preparation and the consistency of the acquisition parameters. In this study, a consistent surface preparation procedure was applied to all samples. with the final stage involving electro-polishing. This method, which removes surface deformation through chemical agitation rather than mechanical abrasion, generally produces superior surface quality for EBSD. However, the appearance of polishing twins in the ZXK samples indicates that excessive pressure may have been during polishing, exceeding the tolerance needed to avoid

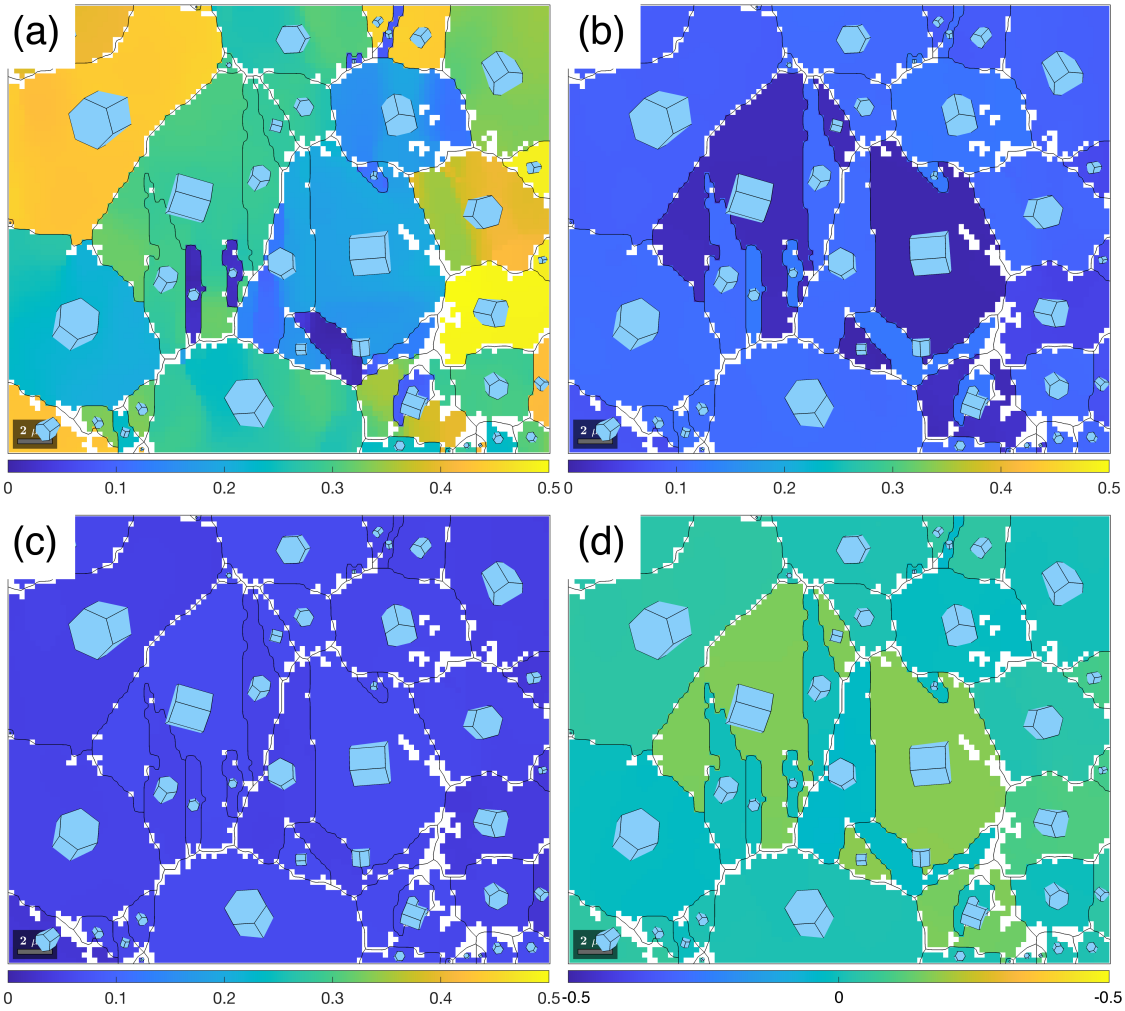


Figure 5.18: ZXK-Area Map 1 at $\varepsilon \approx 8\%$ condition coloured by Schmid factor for systems:(a) Basal, (b) Prismatic, (c) Pyramidal and (d) TTwin. Hexagonal close packed (HCP) crystal overlaid on grains to highlight the mean orientation of the grain.

introducing deformation. Additionally, sample mounting in the tensile rig may have inadvertently introduced stresses and during compliance adjustments. However, samples were not mounted in any given order that would suggest the AZX samples received differential care, ruling out systematic differences in sample preparation as a potential source. A systematic investigation of parameters such as heat treatments would be required to draw a meaningful conclusion regarding this observation. Since this is outside the scope of this study, it will be omitted from further discussion.

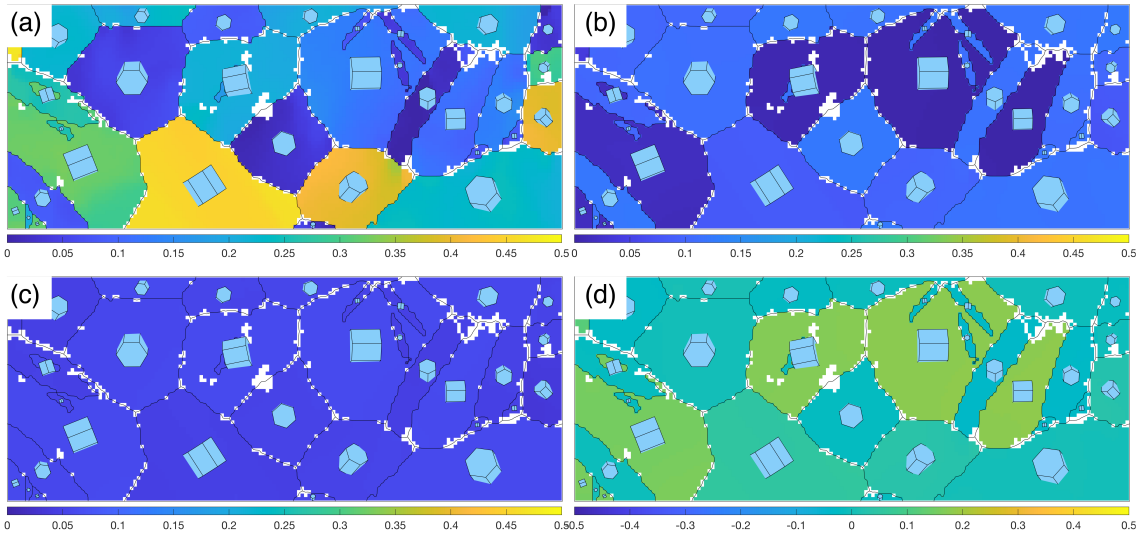


Figure 5.19: AZX-Area Map 1 at $\varepsilon \approx 8\%$ condition coloured by Schmid factor for systems:(a) Basal, (b) Prismatic, (c) Pyramidal and (d) TTwin. Hexagonal close packed (HCP) crystal overlaid on grains to highlight the mean orientation of the grain.

5.3.1 Twinning Activation and Directional dependence

Tensile testing along the TD for the ZXK alloy revealed yield behaviour that is characteristic of twinning activity, with flow stress curves consistent with prior studies [153, 21, 154], which documented strong plastic anisotropy driven by deformation twinning. The pronounced yield asymmetry between RD and TD loading (e.g., lower TD yield strength) confirmed this anisotropy. In contrast, the AZX alloy, exhibited more consistent yield behaviour between RD and TD loading, though with a similar, but less pronounced yield behaviour to ZXK-TD. EBSD maps (Figures 5.1 and 5.2) illustrate this microstructural divergence in the alloys under different loading directions. Showing the distinct influence of twinning in the Ca-containing alloys.

Twinning is strongly influenced by the orientation of the c-axis relative to the loading direction [155]. As shown in Fig. 5.12, twin nucleation is favoured when the c-axis is aligned parallel to the sheet plane and the loading direction, leading to higher Schmid factors for twinning, a phenomenon well-established [31, 21, 155]. This alignment favoured tensile twinning due to the c-axis being in tension within these grains, this required exten-

sion along the c-axis. The lower critical resolved shear stress (CRSS) for tensile twinning compared to other deformation systems capable of facilitating deformation along the c-axis, such as pyramidal $\langle c+a \rangle$ slip (which has a higher CRSS at room temperature) makes it favourable. In certain cases, a direct correlation with c-axis alignment was not observed. For example, in AZX M2 (Fig. 5.2), neighbouring grains with similar Schmid factors (Fig. 5.12) and c-axis inclination differed in their twinning response. One grain, with the c-axis more closely aligned to the loading direction, twinned despite a slight inclination from the sheet plane, while its neighbour does not twin. This suggests that the specific alignment of the c-axis to the loading axis can have a greater impact on twinning behaviour than the Schmid factor alone. However, concluding that the c-axis orientation of the affected grain alone dictates twinning would oversimplify the twinning criteria, other factors like local stress conditions and grain boundary interactions also play important roles [37].

The twinning behaviour observed in this study primarily nucleates at grain boundaries. M1T5 in Fig. 5.13 is a key example of a localised stress concentration at the grain boundary between M1G1& M1G2. The stress field is predominantly located within the domain of M1G2, and intensifies with increasing strain. The results suggest that the twin transformation of M1T5 originates from this region. The orientations of M1G1 and M1G2 resulted in considerably different Schmid factors for basal slip shown in Fig. 5.18, M1G2 was a harder orientation, this suggests the the localised stress and GND density accumulation at the boundary was to accommodate strain incompatibility. Offering an explanation for the relatively rapid propagation and growth of M1T5. Additionally, at $\varepsilon \approx 5\%$ a stress field develops at the boundary of M1G1 and the newly formed M1T5, from which the twin M1T2 nucleates. Multiple twins nucleate and grow within M1G1 and M1G2, looking at the overall stress the same pattern is not clear. Analysing individual stress components and resolving them on the relevant crystallographic planes may provide further insight into the local stress influences [156, 70].

The characteristic shear and lattice reorientation associated with twin transformations constrained inside grains will induce local stress fields. The typical behaviour involves internal back stresses within the twin and forward stresses in the surrounding grain [157], forward stress can be defined by the idea these stress drive forward twin propagation. The development of localised stress fields at twin tips and boundaries influences twin propagation [158].

The twin pairs M1T3 and M1T4 exhibit growth in the same direction. An interesting observation for twin M1T3 is the direction of growth for its tip shifts more towards M1G6 at $\varepsilon \approx 8\%$. Closer examination of the stress field ahead of the twin during the earlier strain step suggests the twins growth was influenced by a more substantial stress field on left side of the twin tip, acting as a forward stress for its propagation.

In contrast, no significant stress field is observed ahead of the growth of M1T4, leading to a more conventional growth direction for this twin. Similar observations can be noted for the expansion of M1T6. The interaction between the moving twin boundaries of M1T5 and M1T6 shows that the growth of M1T6 across the grain is impeded by M1T5. As M1T5 restricts M1T6 the boundary of M1T5 begins to spread around M1T6. This preferential growth of certain twin variants affects the resulting texture alteration during and after saturation of twinning. The orientation of the dominant twin variant will influence the preferred slip mode within the twin, creating a soft or hard orientation for subsequent plastic deformation. The result of such texture changes in the Ca-containing alloys during deformation are important to understand, predictions for ductility/formability will be more complex compared to AZ31 when considering twinning from in plane deformation as well as the twinning present in compression. Comparing between the Ca-containing alloys, variation in the levels of twinning is important, twinning accommodates strain but profuse twinning can result in significant texture changes, significantly altering the mechanical properties post-yield.

Only three strain steps have been presented for AZX map 1, as the microstructure remained relatively stable at $\varepsilon \approx 1\%$ & $\varepsilon \approx 3\%$. A non-uniform stress field develops between the twins M1T1&T2 at the boundary of M1T2 at $\varepsilon \approx 5\%$. At this strain step, M1T2 is in the second stage of twinning, spanning M1G1, with the subsequent thickening following increased strain. For instance, M1T4 exhibits significant thickening in M1G2 between $\varepsilon \approx 5 - 8\%$, and M1T1 similarly demonstrates propagation and thickening between these strain steps. However, M1T2 being pinned on one side, does not exhibit the expected thickening in the 'free' direction. This indicates that the stress field in this scenario may have hindered the twin boundary movement, possibly due to the emergence of M1T1 in close proximity, enhancing a back stress on the growth of M1T2 [159]. Neighbouring grain orientations could contribute to the back stress that impedes twin thickening [157, 73]. This is in contrast with the earlier example where discussed how the neighbouring orientation resulted in stresses and GND densities that promoted twin growth, this is more evidence that a solid conclusion can be better determined with further analysis of the stress states.

There is no clear evidence of twin transmission across grain boundaries. Although this phenomenon is commonly reported, especially in compression experiments [154]. Interestingly there is evidence of twin transfer in the initial condition for ZXK-TD originating from polishing twins, which likely formed under a compressive force. Fig. 5.12 indicates that most grains surrounding the twinned grains were not favourably oriented for twinning under the applied loading condition. Twin transfer typically facilitates rapid texture evolution by allowing twins to propagate across boundaries. However, the limited twin transfer observed within the strain range in this study suggests that the associated texture changes were predominantly confined to the grains that initially nucleated twins.

The presence of twinning in both Ca-containing alloys, despite their significantly different compositions, strongly suggests that Ca-induced modification of the basal texture was the primary factor promoting twinning. In HCP metals, alloying elements can

strongly influence twinning behaviour; for example, in Ti alloys, Al suppresses twinning [160], and similarly in Mg-Al-Zn alloys, increasing Al content raises the τ_{CRSS} for extension twinning [161]. In this study, the TD results could imply some Al induced suppression of twinning in AZX. However, the greater twinning activity observed in AZX compared to ZXK under RD loading suggests that the initial texture, rather than a composition dominated twinning response. This texture effect is explored in detail in later chapters.

5.3.2 GND and stress

Twinning can lead to stress relaxation within grains by accommodating local strain [162]. The evolution of stress levels between twinned and untwinned grains, as illustrated in Fig. 5.15, strongly suggests in the ZXK alloy, twinning led to a reduction in overall stress within the affected grains at $\varepsilon \approx 5\%$. In contrast, the untiwnned grains experienced a steady increase in both the median and mean stress values, along with a pronounced expansion in the stress range.

For AZX, as shown in Fig. 5.16, the trends were not similar. Grains that underwent twinning did not exhibit a significant change in stress levels behaving relatively indifferent to the twinning process. In both the ZXK and AZX examples, however, grains that had experienced twinning showed larger increases in stress following the initiation of twinning. This suggests that while twinning may initially aid stress relaxation, subsequent deformation stages lead to a build up of stress within the twinned regions, such as increased interaction with neighbouring grains and constraints on twin boundary movements [163, 18].

At $\varepsilon \approx 3\%$ the GND density distribution at the grain boundary between M1G1 and M1G2 in Fig. 5.13 closely aligns with the stress field. Notably, the GND density surrounding the twin M1T5 in M1G2 remained relatively unchanged, with similar GND

developing within M1T5 at $\varepsilon \approx 3\%$. The similarly low Schmid factor for basal slip in both twin and parent grain shown in Fig. 5.18, could suggest the equivalent strain accommodation in both orientations leading to GND accumulation. Comparable observations were made in the AZX sample at the boundary of M1T4, where a stress concentration and high GND density were observed. However, the lower GND density within M1T4 indicates that there was limited slip transfer across this boundary, suggesting the stress field was likely caused by a dislocation pile-up [164, 18]. This is in contrast with the twinning process in ZXK for M1T5, where the shear strain was accommodated without significantly increasing GND density, indicating that slip transferred and/or initiated within the twin generating GNDs. For AZX (Fig. 5.19), the Schmid factor for basal slip in twin M1T4 was significantly lower than of the parent grain M1G2, possibly impeding slip transmission across the twin boundary.

Additional evidence of lower GND density within twins is observed in M1T1 and M1T2, where the GND density in the parent grain M1G1 between these twins is higher than in neighbouring grains such as M1G4, M1G5 and M1G2. In contrast, in ZXK Map 1, the Schmid factors for basal slip within M1T5 and the parent grain M1G2 were dissimilar. These observations suggest that higher stress levels may be required to facilitate slip transmission in the AZX twinned grains. The decoupling of stress and GND density reflects how twinning can relax stress by accommodating shear through lattice reorientation, while simultaneously creating new boundaries that promote dislocation accumulation and slip, depending on the orientation of the twins formed.

GNDs contribute to strain hardening by increasing the resistance to further deformation [144]. The observed differences in GND density accumulation between twinned and non-twinned regions in the AZX and ZXK alloys may contribute to the overall differential hardening behaviour following twinning. The increased GND density in non-twinned regions compared to twinned areas suggests that strain hardening is more conventional where twinning is less active. Additionally, a statistical analysis of the total twin volume

fraction within the bulk material could provide insights into this behaviour. The observed higher average twinning Schmid factor in Figure 5.11 implies that the ZXK alloy might possess a larger twin volume fraction compared to AZX. An earlier saturation of twinning volume in the AZX alloy aligns with the tensile behaviour.

Chapter 6

VPSC Modelling of Mg alloys at Elevated Temperatures

6.1 Introduction

Modern computational tools in materials science and engineering enable high-throughput, statistically robust analysis of intrinsic material features that typically require complex, highly specific experiments to observe. Researchers can leverage this capability to assess and design new alloys using limited materials and simple experimental data.

For magnesium alloys in sheet form undergoing high levels of deformation, understanding the anisotropy of the mechanical properties is crucial for formability. These properties are strongly influenced by the HCP crystal structure, a pronounced microstructural texture, and the evolution of this texture during deformation due to twinning. Crystal plasticity is the study of how crystalline materials deform through mechanisms like dislocation slip and twinning, which dictate their anisotropic mechanical behaviour. Consequently, there exists a clear need for crystal plasticity models that can accurately

predict the properties of such anisotropic materials.

The constitutive rules used for modelling crystalline materials require a description of single-crystal elastic and plastic behaviour through mathematical models. The polycrystal response is then predicted based on the response of individual single crystals. However, this poses a severely challenging boundary value problem due to grain-grain interactions, especially in HCP polycrystals, where complex deformation mechanisms like slip and twinning dominate. To overcome this, homogenisation methods described as mathematical techniques that average the behaviour of many grains into an equivalent macroscopic response, are employed. These methods simplify the polycrystal's behaviour by accounting for grain interactions statistically, rather than resolving each grain individually. In HCP polycrystalline materials, the varying grain orientations lead to heterogeneity and anisotropy in the plastic response due to the change in grain properties relative to a reference loading axis. The low symmetry of HCP structures induces'soft' and 'hard' orientations, resulting in strongly directional grain interactions [35].

Early pioneering models, such as those proposed by Sachs [76] and Taylor[29], are more suited for predicting the plastic response of cubic materials with a high number of active slip systems. To tackle this problem, self-consistent (SC) homogenisation methods for viscoplastic behavior, developed by Hutchinson [165] for small deformations and Molinari [68] for large deformations, have been successful. In the SC approach, grains are treated as inclusions within a homogeneous effective medium (HEM), which represents the average neighborhood of grains. The response between inclusions and the HEM is solved with local stress equilibrium equations. The non-linear response of grains and the medium is governed by an appropriate deformation scheme, and the properties of the HEM are developed by ensuring that the average response of the grains is consistent with the boundary conditions [65].

The model used in this work was initally developed by Tome and Lebensohn, which

is an extension of Molinari's [68] works. In the Viscoplastic self-consistent (VPSC) code the polycrystal is represented by a set of crystal orientations that are weighted by volume fraction. These orientations statistically represent the grains and their morphology in the bulk material, to reproduce the materials crystallographic texture. Each grain is modeled as an ellipsoidal visco-plastic inclusion within in an effective visco-plastic medium, with both the inclusion and medium possessing anisotropic properties. The medium reflects the 'average' surroundings experienced by each grain [78]. The constitutive rules account for hardening, reorientation and shape change of individual grains, allowing prediction of the evolving hardening and texture associated with deformation. Twinned and un-twinned grains are treated as ellipsoids in a homogeneous matrix with average anisotropic properties.

6.2 Overview of the VPSC model

6.2.1 Local constitutive behaviour and homogenisation

In the present section the equations and definitions have been reproduced from [78]. Plastic deformation ensues when slip or twinning systems become active. Each system is characterised by a vector **n** normal to the plane they lie on, and a vector **b** (Burgers vector for slip and twin shear direction for twinning). The traceless symmetric Schmid tensor of a system (s), is given as $m_{ij}^s = \frac{1}{2}(n_i b_j + n_j n_i)$, with this, the resolved shear stress on a system (s) adopts:

$$\tau_r^s = \mathbf{m}_{ij}^s \sigma'_{ij} \tag{6.1}$$

This expression, including the Schmid tensor, can be recast to describe the plastic strain rate associated with the shear rate in a system (s), $\dot{\gamma}^s$ adopts:

$$\dot{\epsilon}_{ij} = \mathbf{m}^s_{ij}\dot{\gamma}^s. \tag{6.2}$$

When a given applied stress produces a shear rate in a system (s), it can be described by a rate sensitive criterion which (formally amounts) assumes a non-linear viscous response

$$\dot{\gamma}^s = \dot{\gamma}_0 \left(\frac{\tau^s_r}{\tau^s_c}\right)^n = \dot{\gamma}_0 \left(\frac{m^s_j \sigma'_j}{\tau^s_c}\right)^n \tag{6.3}$$

where $\dot{\gamma}_0$ is a reference rate, τ^s_c is a critical stress linked to $\dot{\gamma}_0$ and $\mathbf{n}$ is the inverse of the rate sensitivity. Using Equation 6.2 and 6.3, for a polycrystal, the viscoplastic constitutive behaviour of a material point $\mathbf{x}$ in a single crystal is described by the non-linear rate-sensitivity relation:

$$\dot{\epsilon}_{ij}(\mathbf{x}) = \dot{\gamma}^s \Sigma_s m^s_{ij}(\mathbf{x}) = \dot{\gamma}_0 \Sigma_s m^s_{ij}(\mathbf{x}) \left(\frac{\mid \mathbf{m}^s(\mathbf{x}) : \sigma'(\mathbf{x}) \mid}{\tau^s_0}\right)^n \times \mathrm{sign}(\mathbf{m}^s(\mathbf{x}) : \sigma'(\mathbf{x})) + \dot{\epsilon}^{tr}_{ij}(\mathbf{x}) \tag{6.4}$$

where $\dot{\epsilon}_{ij}(\mathbf{x})$ and $\sigma'_{ij}(\mathbf{x})$ are the strain rate and deviatoric stress tensors; $\dot{\gamma}^s$ is the shear rate on slip system (s) and $\dot{\epsilon}^{tr}_{ij}(\mathbf{x})$ is a generalised transformation strain rate, useful for accounting for non-external stress dependent deformation mechanisms. Within the domain of a grain (g), Equation (6.4) is linearised to:

$$\dot{\epsilon}(\mathbf{x}) = \mathbf{M}^{(g)} : \sigma'(\mathbf{x}) + \dot{\epsilon}^{0(g)} + \dot{\epsilon}^{tr(g)} \tag{6.5}$$

$$\sigma'(\mathbf{x}) = \mathbf{L}^{(g)} : \dot{\epsilon}(\mathbf{x} - \mathbf{L}^{(g)}) : \dot{\epsilon}^{0(g)} - \mathbf{L}^{(g)} : \dot{\epsilon}^{tr(g)} \tag{6.6}$$

where $\mathbf{L}^{(g)} = (\mathbf{M}^{(g)})^{-1}$, $\mathbf{M}^{(g)}$ and $\dot{\epsilon}^{0(g)}$ are the stiffness, linearised viscoplastic compliance and the back-extrapolated strain-rate for grain (g), respectively, and $\dot{\epsilon}^{tr(g)}$ is the average transformation strain rate. The moduli, $\mathbf{M}^{(g)}$ and $\dot{\epsilon}^{0(g)}$, can be chosen based on the linearisation used (e.g. secant or tangent). Performing homogenisation on this linearised heterogeneous medium at the polycrystal level requires linear relations comparable to Equation 6.5 and Equation 6.6.

$$\bar{\dot{\epsilon}} = \bar{\mathbf{M}} : \bar{\sigma'} + \bar{\dot{\epsilon}^{0}} \tag{6.7}$$

$$\bar{\sigma'} = \bar{\mathbf{L}} : (\bar{\dot{\epsilon}} - \bar{\dot{\epsilon}^{0}}) \tag{6.8}$$

where $\bar{\mathbf{L}} = (\bar{\mathbf{M}})^{-1}, \bar{\mathbf{M}}$, and $\bar{\dot{\epsilon}^{0}}$, are the polycrystals stiffness, viscoplastic compliance, and back-extrapolated strain rate. These effective moduli are deduced and adjusted self-consistently, $\bar{\dot{\epsilon}^{0}}$ here includes the average effect of the transformation strain rate in the grains (cannot be separated from the back-extrapolated term because of the linearisation). The volume averages of the local stress and strain tensors are denoted with brackets $\langle\rangle$ in $\bar{\dot{\epsilon}} = \langle\dot{\epsilon}(\mathbf{x})\rangle$ and $\bar{\sigma} = \langle\sigma(\mathbf{x})\rangle$, from [166]. The viscoplastic moduli at grain and polycrystal levels can be coupled via taking volumetric averages of Equations 6.5 & 6.6 and using Equations 6.7 & 6.8:

$$\bar{\mathbf{M}} : \bar{\sigma'} + \bar{\dot{\epsilon}^{0}} = \langle \mathbf{M}^{g} : \sigma'(\mathbf{x}\rangle + \langle \dot{\epsilon}^{0(g)} + \dot{\epsilon}^{tr(g)} \rangle \tag{6.9}$$

$$\bar{\mathbf{L}} : \dot{\epsilon} - \bar{\mathbf{L}} : \dot{\epsilon}^{0} = \langle \mathbf{L}^{g} : \dot{\epsilon}(\mathbf{x}\rangle - \langle \mathbf{L}^{g} : (\dot{\epsilon}^{0(g)} + \dot{\epsilon}^{tr(g)}) \rangle \tag{6.10}$$

In the simplest form the moduli $\bar{\mathbf{M}}$ and $\dot{\bar{\epsilon}}^0$ can be obtained from Equations 6.9 & 6.10 by assuming a uniform strain rate $\dot{\epsilon}(\mathbf{x}) = \bar{\dot{\epsilon}}$ in the aggregate i.e Taylor assumption [29]. To simplify the problem of a heterogeneous inclusion with different properties to the surrounding matrix, hcp grains with different crystallographic orientations, the concept of the equivalent inclusion [167] is used, Equation 6.5 is modified to obtain:

$$\dot{\epsilon}(\mathbf{x}) = \bar{\mathbf{M}} : \sigma'(\mathbf{x}) + \dot{\bar{\epsilon}}^0 + \dot{\epsilon}^*(\mathbf{x}) \tag{6.11}$$

and

$$\sigma'(\mathbf{x}) = \bar{\mathbf{L}} : (\dot{\epsilon}(\mathbf{x}) - \dot{\bar{\epsilon}}^0 - \dot{\epsilon}^*(\mathbf{x})) \tag{6.12}$$

which is the replacement of the inhomogeneous inclusion with a homogeneous inclusion, where $\dot{\epsilon}^*(\mathbf{x})$ is the eigenstrain rate field used to produce the same effect the inhomogeneous inclusion would have on the matrix.

$$\dot{\epsilon}^*(\mathbf{x})) = (\mathbf{M}^{(g)} - \bar{\mathbf{M}}) : \sigma'(\mathbf{x}) + (\dot{\epsilon} - \dot{\bar{\epsilon}}^0) + \dot{\epsilon}^{tr(g)} \tag{6.13}$$

The equivalent stress and strain fields of the inclusions are calculated with the matrix elastic moduli and the eigenstrain. Subtracting Equation 6.8 from 6.12 gives:

$$\tilde{\sigma}'(\mathbf{x}) = \bar{\mathbf{L}} : (\tilde{\dot{\epsilon}}(\mathbf{x}) - \dot{\epsilon}^*(\mathbf{x})) \tag{6.14}$$

The symbol "$\sim$" signifies local deviations of the corresponding tensor from macroscopic values: $\tilde{\sigma}'(\mathbf{x}) = \sigma'(\mathbf{x}) - \bar{\sigma}'$ and $\tilde{\dot{\epsilon}}(\mathbf{x}) = \dot{\epsilon}(\mathbf{x}) - \bar{\epsilon}$. The equilibrium equations in the absence of external body forces give:

$$\sigma_{ij,j}(\mathbf{x}) = 0 \tag{6.15}$$

$\sigma_{ij,j}(\mathbf{x})$ is the divergence of the Cauchy stress field. Writing the Cauchy stress field as the sum of its deviatoric and hydrostatic parts gives:

$$\sigma_{ij}(\mathbf{x}) = \sigma'_{ij} - p(\mathbf{x})\delta_{ij} \tag{6.16}$$

where $p(\mathbf{x})$ is the hydrostatic pressure field and δ_{ij} is the Kronecker delta (1 when i=j otherwise 0). Equation 6.15 can then be written as:

$$\sigma_{ij,j}(\mathbf{x}) = \tilde{\sigma}'_{ij,j} - \tilde{p_{,i}}(\mathbf{x}) = 0 \tag{6.17}$$

where $\tilde{p}(\mathbf{x}) = p(\mathbf{x} - \bar{p})$, $\bar{p}$ is the macroscopic hydrostatic pressure. Replacing 6.14 in 6.17 using the relation $\tilde{\dot{\epsilon}}_{ij}(\mathbf{x}) = \frac{1}{2}(\tilde{\dot{u}}_{i,j}(\mathbf{x}) + \tilde{\dot{u}}_{j,i}(\mathbf{x}))$ between strain rate and velocity gradient, accounting for minor symmetry $\bar{L}_{ijkl} = \bar{L}_{ijlk}$

$$\bar{L}_{ijkl}\tilde{\dot{u}}_{k,lj}(\mathbf{x}) - \tilde{p_{,i}}(\mathbf{x}) + f^b_i(\mathbf{x}) = 0 \tag{6.18}$$

where the fictitious body force field associated with the replaced heterogeneity is:

$$f^b_i(\mathbf{x}) = -\bar{L}_{ijkl}\dot{\epsilon}^*(\mathbf{x}) = \tilde{\sigma}'^*_{ij,j}(\mathbf{x}) \tag{6.19}$$

The deviatoric eigenstress field is $\sigma'^*(\mathbf{x}) = -\bar{\mathbf{L}} : \dot{\epsilon}^*(\mathbf{x})$, also known as the polarisation field representing the disturbance in the stress field arising from the eigenstrain of the inclusion. The Green function method and fourier transformations are used to efficiently solve the partial differential equations of the eigenstrain rate problem. Using convoluted integrals with green functions associated with the local deviation of; the velocity vector field () and the hydrostatic pressure field. The output is symmetric, $\mathbf{S}^{(g)}$, and anti-symmetric, $\mathbf{\Pi}^{(g)}$, Eshelby tensors, used to define the average strain-rate and rigid body

rotation rate deviations in the ellipsoidal inclusion (grain):

$$\tilde{\dot{\epsilon}}^{(g)} = \mathbf{S}^{(g)} : \dot{\epsilon}^{*(g)} \tag{6.20}$$

$$\tilde{\dot{\omega}}^{(g)} = \mathbf{\Pi}^{(\mathbf{g})} : \dot{\epsilon}^{*(g)} = \mathbf{\Pi}^{(\mathbf{g})} : \mathbf{S}^{(g)-1} : \tilde{\dot{\epsilon}}^{(g)} \tag{6.21}$$

the superscript (g) defines that in general, the grain shape and orientation may differ from grain to grain, so do their Eshelby tensors. Equation 6.14 relates local deviations in stress, strain rate and eigenstrain rate fields, this expression also holds for the same parameters in the grains with respect to macroscopic tensors:

$$\tilde{\sigma}'^{(g)} = \bar{\mathbf{L}} : (\tilde{\dot{\epsilon}}^{(g)} - \dot{\epsilon}^{*(g)}) \tag{6.22}$$

The eigenstrain given in Equation 6.20 used in Equation 6.22 gives the interaction equation:

$$\tilde{\dot{\epsilon}}^{(g)} = -\tilde{\mathbf{M}}^{(g)} : \tilde{\sigma}'^{(g)} \tag{6.23}$$

where the interaction tensor is defined as:

$$\tilde{\mathbf{M}}^{(g)} = (\mathbf{I} - \mathbf{S}^{(g)})^{-1} : \mathbf{S}^{(g)} : \bar{\mathbf{M}} \tag{6.24}$$

The Eshelby tensors from the solution to the strain-rate within a grain are coupled with the constitutive relations 6.5 & 6.7 and the interaction Equation 6.23 to give an expression describing the relationship between local fields and the macroscopic fields with

a localisation equation:

$$\sigma'^{(g)} = \mathbf{B}^{(g)} : \bar{\sigma}' + \mathbf{E}^{(g)} \tag{6.25}$$

where the localisation tensors are defined as:

$$\mathbf{B}^{(g)} = (\mathbf{M}^{(g)} + \tilde{\mathbf{M}}^{(g)})^{-1} : (\bar{\mathbf{M}} + \tilde{\mathbf{M}}^{(g)}) \tag{6.26}$$

$$\mathbf{E}^{(g)} = (\mathbf{M}^{(g)} + \tilde{\mathbf{M}}^{(g)})^{-1} : (\bar{\dot{\epsilon}}^{0} - \dot{\epsilon}^{0(g)} - \dot{\epsilon}^{tr(g)}) \tag{6.27}$$

describing the magnitude of influence the macroscopic field has on the inclusion.

Self-Consistent equations

Several approximations are required to construct a model regarding nonlinear grains in a real aggregate, when treating each grain as an ellipsoidal inclusion (with linearised behaviour) embedded in a linear homogeneous medium with the same properties of the homogenised polycrystal.

1. The deviations from the actual nonlinear viscoplastic behaviour (Equation 6.4) when using a linearisation assumption that requires the use Eshelby's inclusion formalism.

2. Grains are typically not ellipsoidal or surrounded by a homogenous medium. In practise, it is more observed that grains with identical orientation will be surrounded by neighbours with different orientations. The inhomogeneous stress fields induced inside each grain will therefore differ.

Thus, grain stress and strain rate given by the effective medium approximation (Equation 6.7) represents the average state of all grains having the same orientation in the aggregate.

Averaging Equation 6.25 gives:

$$\bar{\sigma}' = \langle \mathbf{B}^{(g)} \rangle^{-1} : (\langle \sigma'^{(g)} \rangle - \langle \mathbf{E}^{(g)} \rangle) \tag{6.28}$$

With a couple of steps:

1. Replacing this average stress localisation (Equation 6.28) in the local constitutive Equation 6.5.
2. Averaging and enforcing conditions of; the weighted average of the strain rate and stress over the aggregate has to coincide with the effective macroscopic strain rate and stress (i.e., $\bar{\dot{\epsilon}} = \langle \dot{\epsilon}^{(g)} \rangle$ & $\bar{\sigma}' = \langle \sigma'^{(g)} \rangle$)
3. Matching the linear and independent terms

the following self-consistent equations form:

$$\bar{\mathbf{M}} = \langle \mathbf{M}^{(g)} : \mathbf{B}^{(g)} \rangle : \langle \mathbf{B}^{(g)} \rangle^{-1} \tag{6.29}$$

$$\bar{\dot{\epsilon}}^0 = -\langle \mathbf{M}^{(g)} : \mathbf{B}^{(g)} \rangle : \langle \mathbf{B}^{(g)} \rangle^{-1} : \langle \mathbf{E}^{(g)} \rangle + \langle \mathbf{M}^{(g)} : \mathbf{E}^{(g)} + \dot{\epsilon}^{0(g)} + \dot{\epsilon}^{tr(g)} \rangle \tag{6.30}$$

$$= -\bar{\mathbf{M}} : \langle \mathbf{E}^{(g)} \rangle + \langle \mathbf{M}^{(g)} : \mathbf{E}^{(g)} + \dot{\epsilon}^{0(g)} + \dot{\epsilon}^{tr(g)} \rangle \tag{6.31}$$

From Equation 6.27, the localisation tensor $\mathbf{E}^{(g)}$ depends on $\bar{\dot{\epsilon}}^0$, therefore, Equation 6.31 is now:

$$\bar{\dot{\epsilon}}^0 = \langle \mathbf{B}^{\dagger(g)} \rangle^{-1} : \langle \mathbf{B}^{\dagger(g)} : (\dot{\epsilon}^{0(g)} + \dot{\epsilon}^{tr(g)}) \rangle \tag{6.32}$$

where

$$\mathbf{B}^{\dagger(g)} = (\bar{\mathbf{M}} + \tilde{\mathbf{M}}^{(g)}) : (\mathbf{M}^{(g)} + \tilde{\mathbf{M}}^{(g)})^{-1} \tag{6.33}$$

Linearisation

Choosing the linearisation scheme for the constitutive laws e.g. Equation 6.4 to 6.5 describing the relationship between stress and strain will strongly influence the result of the self-consistent scheme. This relationship is especially non-linear in viscoplasticity due to the time-dependent behaviour. The following linearisation schemes are available:

- Tangent, Secant & Intermediate, n^{eff}: The tangent and secant approaches offer interactions that tend to the classic; compliant lower bound (sachs) or stiff upper bound (taylor) respectively. To obtain an intermediate response between the upper and lower bound, an adjustable parameter n^{eff} allows the user to tune the linearisation between the lower and upper bound [168]. A further expansion of this scheme is the relative directional compliance (RDC) approach; this is favourable when grains exhibit large plastic anisotropy or there is a large difference between the compliance with respect to a deformation direction. Allowing for different grains to have different interaction n^{eff} with surrounding effective medium.

- Second Order: Very sophisticated ad computationally expensive, previous schemes were first order. Uses intergranular stress and strain fluctuations.

Hardening model

The threshold stress required to accommodate shear via activation of slip and twinning on corresponding crystallographic planes in the model is defined and evolved by a chosen hardening model. Shear rates 6.3 are calculated for the active deformation systems, the SC formulation only requires knowing the instantaneous values of threshold stress in the deformation systems, subroutines including the hardening model calculate these values and pass the stresses back to the VPSC algorithm.

The hardening law described in this section, defines the physical mechanisms that give the shear systems their threshold activation stresses. The hardening law is applied to single slip systems to describe the resistance propagating dislocations experience as a consequence of their interaction with lattice defects (e.g., dislocations, precipitates, second phases and grain boundaries). Several hardening models are available in the VPSC code, the popular extended Voce law, mechanical threshold stress (MTS) and the dislocation density hardening model. Each with their own benefits, the latter developed by Beyerlein and Tome [80], was preferred because the model explicitly accounts for the thermal activation of dislocations, temperature and strain rate dependence of yield stress and hardening. Linking the evolving dislocation densities in the slip systems with the threshold stress required to activate dislocations. This model also has the capability to perform lattice strain predictions that we attempt to use to match results from 4. The other models require different parameters for different temperatures and strain rates, this model is based on one set of parameters for different temperatures and strain rate conditions. Therefore, capturing the deformation behaviour of our alloys in these different conditions we can assume we have well calibrated material parameters that accurately describe dislocation evolution.

The law is applied to each slip mode, therefore, from this point (s) denotes basal, prismatic or pyramidal slip. Some parameters may be labelled with (s) but are the same

for every system such as elastic shear modulus $\mu^s H^s$.

The threshold stress for each system (s) is the sum of several dislocation interactions depicting different barrier mechanisms and stresses:

$$\tau^s = \tau_0^s + \tau_{for}^s + \tau_{sub}^s + \tau_{HP}^s \tag{6.34}$$

The first term τ_0^s is the resistance related to Peierls friction stress and microstructural obstacles such as precipitates and dislocations.

$$\tau_0^s = A_0^s + A_1^s exp(-T/A_2^s) \tag{6.35}$$

capturing the decrease of the initial CRSS with temperature for prismatic and pyramidal slip systems have shown exponential declines in CRSS in HCP materials.

The Hall-Petch term τ_{HP}^s provides the barrier effect by grain boundaries, accounting for dislocation pile-ups and other grain boundary interactions.

$$\tau_{HP}^s = \mu^s H^s \sqrt{\frac{b^s}{d_g}} \tag{6.36}$$

where H^s is the Hall-Petch coefficient for the mode, b^s is the magnitude of the Burgers vector of a dislocation and d_g is the grain size.

In this model it is assumed τ_0^s and τ_{HP}^s do not evolve during deformation. The terms τ_{for}^s and τ_{sub}^s in 6.34 are responsible for the level and development of strain hardening stemming from dislocation interactions. In the model the temperature influence on thermally-activated glide considers dislocations in motion to be obstructed by several different scenarios, e.g. interactions between other dislocations, attractive(annihilate or recombine, mechanisms that drive them require energy, temperature dependent) or repulsive (temperature independent). The rate at which such obstacles are overcome by glid-

ing dislocations using thermal energy controls the plastic strain rate. A stress-indpendent effective thermal activation energy (g) representing the likelihood of successful thermal activated processes is included. Considering the numerous dislocation interactions, jogs, forest, absorption into grain boundaries, junctions (Lomer-Cottrell locks) etc, the rate of density fluctuation for such dislocations looks like:

$$\begin{aligned}\frac{\delta\rho}{\delta\gamma} = \frac{\delta\rho_{generation}}{\delta\gamma} - \frac{\delta_{rem}}{\delta\gamma} = \frac{\delta\rho_{generation}}{\delta\gamma} - q\frac{\delta_{rem}}{\delta\gamma} - (1-q)\frac{\delta_{rem}}{\delta\gamma} \\ = \frac{\delta\rho_{generation}}{\gamma} - \frac{\delta\rho_{deb}}{\delta\gamma} - \frac{\delta\rho_{ann}}{\delta\gamma}\end{aligned} \tag{6.37}$$

where ρ_{rem} is the population of dislocations removed by forming defects ρ_{deb} or recovered ρ_{ann}, q and $(1-q)$ are the fractions of ρ_{rem} converted to debris or annihilated respectively.

Equation:6.37 for forest dislocations is expressed in the model for each mode via:

$$\frac{\delta\rho^s_{for}}{\delta\gamma^s} = k^s_1\sqrt{\rho^s_{for}} - k^s_2(\dot{\epsilon}, T)\rho_{for} \tag{6.38}$$

where k^s_1 is a rate-insensitive coefficient specific to the material, for a statistical account of the storage of dislocations in forest obstacles, $\sqrt{\rho^s_{for}}$ is inversely proportional to an effective mean-free path. The temperature and rate dependent coefficient k^s_2 accounts for dynamic recovery of dislocations.

$$k^s_2(\dot{\epsilon}, T) = k^s_1\frac{\chi_{for}\boldsymbol{b}^s}{g^s}\left(1 - \frac{kT}{D^s(\boldsymbol{b}^s)^3}\ln\left(\frac{\dot{\epsilon}}{\dot{\epsilon}_0}\right)\right) \tag{6.39}$$

where $T, k, \dot{\epsilon}, \dot{\epsilon}_0, D^s$ and g^s are, respectively, Boltzman's constant, effective macroscopic strain rate, reference effective strain rate (a material value that has units of strain rate [80]), a drag stress, and the normalised effective activation enthalpy mentioned earlier. For a typical value of $\dot{\epsilon_0} = 10^7\,\mathrm{s}^{-1}$ for magnesium, it is is linked to the incremental strain achieved from successful thermally activated dislocation glide. From Equation6.39 we can see k^s_2 in Equation 6.38 acts to increase the rate of dislocation recombination with

a decrease in strain rate or increase in temperature, the overall flow stress will decrease with a lower storage rate of dislocations. Equation 6.38 predicts with evolving strain the rate of removal will catch up with the rate generation, reaching a dislocation density steady state $\rho^s_{sat} = (k^s_1/k^s_2)^2$.

Experimentally, effective slip resistance is linked with the barrier posed by dislocation densities such as forest and substructure dislocations. For forest dislocations spaced l apart, the resistance is $\sim \mu b/l$, and the spacing $l \sim 1/\sqrt{\rho}$ for a random forest arrangement, representing an effective mean-free path before dislocation storage. The slip resistance from forest dislocations follows the general rule of the Taylor law:

$$\tau^s_{for} = \chi_{for}\mu^s b^s \sqrt{\sum_s \rho^{s'}_{for}} \tag{6.40}$$

where χ_{for} is a dislocation interaction coefficient, typically $\chi_{for} < 1.0$. The density $\rho^{s'}_{for}$ is assigned an initial value typically 5×10^5 for each mode and updated at each strain increment utilising Equation 6.38. The resistance from substructures is treated differently because the dislocation densities ρ_{sub} within can accumulate with greater density than ρ_{for}, at which the Taylor law may not apply. To better represent dislocations moving through closely spaced obstacles the relationship looks like:

$$\tau^s_{sub} = \chi_{sub}\mu^s b^s \sqrt{\rho_{sub}} \ln\left(\frac{1}{b^s\sqrt{\rho_{sub}}}\right) \tag{6.41}$$

where ρ_{sub} doesn't have the superscript (s) because it includes dislocations from all active systems, for low values of ρ_{sub} the constant χ_{sub} ensures Equation 6.41 converges to the Taylor law 6.40. The rate of ρ_{sub} development is coupled to the dynamic recovery of active dislocations, $[k^s_2$:

$$\mathrm{d}\rho_{sub} = \sum_s q^s \left[k^s_2 \rho^s_{for}\right] \mathrm{d}\gamma^s \tag{6.42}$$

where the coefficient q^s is dependent on ρ_{sub}, showing how a higher dislocation density within substructures immobilises a larger fraction of dislocation densities:

$$q^s = F^s_{(T,\dot{\epsilon})} b^s \sqrt{]\rho_{sub}} \tag{6.43}$$

Dependence of q^s on temperature and strain rate is obtainable by research at lower length scales. The parameter $F^s_{(T,\dot{\epsilon})}$ links substructure development to temperature and strain rate, in this version of the code it is empirically described by an exponential function for temperature dependence:

$$F^s_{(T,\dot{\epsilon})} = F^s_0 + F^s_1 \exp\left(T_{ref} - T/F^s_2\right) \tag{6.44}$$

from Knezevic et al [169]. For twinning, the threshold stress τ^t, dictates the resistance to twin propagation through a relationship that follows

$$\tau^t = \tau^t_0 + \tau^t_{slip} \tag{6.45}$$

where τ^t_{slip} represents the stress barrier posed by stored dislocations to twin propagation, and τ^t_0 is the intrinsic resistance to nucleation and propagation.

Twin nucleation and growth arise from different conditions, nucleation has links to high local stresses typically at grain boundaries, in contrast, growth is generally driven by average stresses in the grain. The crystal plasticity formulation employed in VPSC doesn't offer local stresses, using previous work on a probabilistic approach to twin nucleation [37], VPSC implements the critical stress for twinning as a probabilistic function P_{nucl} of a nucleation τ^t_{nucl} and propagation τ_{prop} stress. Local stresses can be related to hardening and dislocation density evolution, P_{nucl} is assumed to increase when local

stresses increase.

$$P_{nucl} = 1 - \exp\left(\sum_s \rho^s_{for} \frac{k^s_2}{k^s_1}\right) \tag{6.46}$$

The overall threshold stress for twinning is given:

$$\tau^t_0 = \tau_{prop} P_{nucl} + \tau^t_{nucl}(1 - P_{nucl}) \tag{6.47}$$

where the thermal relationship of nucleation and propagation for a twinning mode t are empirically described as:

$$\begin{aligned} \tau^t_{nucl} &= T^t_{0,nucl} + T^t_{1,nucl} \exp(-T/T_{2,nucl}) \\ \tau^t_{prop} &= T^t_{0,prop} + T^t_{1,prop} \exp(-T/T_{2,prop}) \end{aligned} \tag{6.48}$$

In this model the interaction between slip and twinning is given as a stress required to overcome stored dislocations ρ^s_{for} on slip planes:

$$\tau^t_{slip} = \mu^t \sum_s C^{ts} b^t b^s \rho^s_{for} \tag{6.49}$$

where b^t is the Burgers vector of the twinning dislocation, μ^t is the elastic shear modulus in the twin plane and C^{ts} is a slip-twin interaction matrix adjusting the level dislocations on system *s* hinder the growth of system *t* twins.

Twinning Scheme

Modelling the deformation of HCP magnesium requires an accurately capturing twinning. Deformation twinning is a shearing mechanism induced by an applied stress, it transforms grains though large reorientation's of the crystal, lenticular domains that can grow to lamellar structures of twin and parent within a grain. Twinning is a complex sequential

process, modelling the processes involved is very challenging and requires modelling and experiments at various length scales, the version of the VPSC code we use employs twinning schemes to deal with twin growth after the statistical nucleation represented in Equation 6.46. As described in the hardening section, twinning is given associated CRSS of activation, it differs from slip with directionality, only activating if the resolved shear stress is positive along the shear direction of the twin. Similar to the implementation of the hardening model, the VPC model offers the flexibility to use several different twinning schemes to describe the reorientation due to twinning:

1. The predominant twin reorientation(PTR) - The parent orientation (grain) is replaced with a twin orientation upon a condition of volume fraction being met, this keeps the number of grains in the aggregate constant. Accumulated shear strain from each system is tracked and the associated volume fraction is calculated via:

$$v^{t,g} = \gamma^{t,g}/S^t \tag{6.50}$$

where S^t is the characteristic twin shear. The weighted sum of twin volume fraction over all grains, for all variants belonging to a twin mode is expressed as:

$$V^{acc,tmode} = \sum_g \sum_t \frac{\gamma^{t,g}}{S^t} w^g \tag{6.51}$$

where w^g is the weight of the parent in the aggregate. This volume fraction is similar to the data we would obtain by orientation techniques such as EBSD. The volume fraction of fully reoriented grains is tracked by:

$$V^{eff,tmode} = \sum_g w^{g,reoriented} \tag{6.52}$$

$V^{eff,tmode}$ and $V^{acc,tmode}$ are kept consistent with a threshold volume fraction:

$$V^{th,tmode} = A^{th1} + A^{th2}\frac{V^{eff,tmode}}{V^{acc,tmode}} \tag{6.53}$$

At the end of each strain increment, grains are picked at random, where a grain is selected with a twin mode that meets a criteria $v^{t,g} > V^{th,tmode}$ the grain is fully reoriented. Subsequently, $V^{eff,tmode}$ increases and grains are continually selected until all grains are checked or $V^{eff,tmode} > V^{acc,tmode}$, if the latter is reached then the next deformation step is invoked. The parameters A^{th1} and A^{th2} are typically 0.10 and 0.50 respectively, larger values can have the effect of slowing down the rate of twin reorientation.4

2. Monte-Carlo (MC) - This scheme adapts the PTR scheme where reorientation is based on most active twin, the MC scheme makes it a stochastic choice. Every twin system is assigned a probability proportional to the volume fraction associated.

3. Volume Fraction Transfer (VFT) - same name but different to [85, 170]. Better computers has given the flexibility to allow more grains in the simulation, therefore, creating more grains is less of a problem. Volume fraction is transferred from the parent grain to the chosen twin (child) grain, $\Delta w^{t,g} = \frac{\Delta\gamma^{t,g}}{S} w^g$ following the shear on that system $\Delta\gamma^{t,g}$. VFT has the advantage over PTR and MC when simulating strain path reversals due to the ability to transfer back the volume fraction from child to parent. Similar concepts used in VFT from PTR and MC, when creating a twin grain it is the twin variant contributing the most shear exceeding the threshold volume fraction A^{th1}.

Back stresses involved in twinning transformations are accommodated by a simple adjustment, the current τ_{CRSS} for slip and twin in the parent is given to the slip and twin system in the child, except for the twin system used to create the child, in this system the τ_{CRSS} is halved. The PTR and VFT scheme were identified as the ideal schemes

to use. Both generated the distribution of Schmid factors and twin variants associated with the twins created. There are 6 variants total (symmetry) labelled by the decreasing value of their Taylor factor. They difference between both is the accumulated volume fraction of primary and secondary twins is given for PTR, essentially, grains reoriented once are allowed to undergo a second reorientation if this option is selected. Utilising the VFT scheme, you get an evolving volume fraction of parent and child phases, only one child per parent is allowed to keep the total number of grains manageable.

Microstructure evolution

Alongside twinning, texture evolution during deformation by slip, induces crystal lattice rotations within each grain. The rate of rotation $\dot{\Omega^{(g)}}$ is treated as a function of the shear rate $\gamma^{s(g)}$. For the VPSC formulation with an ellipsoidal inclusion, deformation is imposed via a macroscopic velocity gradient $\bar{L}$, within a grain you get the grain-averaged velocity gradient;

$$L^{(g)} = \dot{\epsilon}^{(g)} + \dot{\omega}^{(g)} \tag{6.54}$$

where $\dot{\epsilon}^{(g)}$ is the symmetric(strain rate) and $\dot{\omega}^{(g)}$ is the skew symmetric (rigigd-body rotation) part. From this the plastic grain-averaged velocity gradient is expressed as:

$$L_{ij}^{p(g)} = \dot{\epsilon}_{ij}^{p(g)} + \dot{\omega}_{ij}^{p(g)} = \sum_s \dot{\gamma}^s m_{ij}^s + \sum_s \dot{\gamma}^s q_{ij}^s \tag{6.55}$$

where q_{ij}^s is the skew-symmetric Schmid tensor. The interaction between the ellipsoid and effective medium equates a rigid-body rotation rate:

$$\dot{\omega}^{(g)} = \bar{\dot{\omega}} + \tilde{\dot{\omega}}^{(g)} \tag{6.56}$$

where the first component is the rate imposed on the effective medium, the latter hearkens back to the inhomogeneous response of the ellipsoid and the local deviation associated with it 6.21. To find the crystal lattice rotation the plastic spin is subtracted from the rigid body rotation of the ellipsoid:

$$\dot{\Omega}^g \cong \left(\bar{\dot{\omega}} + \tilde{\dot{\omega}}^{(g)} - \dot{\omega}_{ij}^{p(g)}\right) \tag{6.57}$$

If $\dot{\Omega}^g$ is assumed to be constant for a time increment Δt, the solution for the rotation matrix $R(t)$ that couples the specimen and crystal lattice reference systems is an exponential:

$$R(t + \Delta t) = R(t) \cdot exp(\dot{\Omega}^{(g)} \Delta t) \tag{6.58}$$

.

It is important to consider the effect of neighbouring grains on the above described rotation of crystal lattice and rigid body rotation of the ellipsoid. Interactions across grain boundaries between grains with different rotation rates and preferred reorientation will inflict local stresses at boundaries affecting slip. To mimic this the effect is implemented empirically, each grain (g) is assigned one or more neighbours (g') at random, these grains remain consistent throughout deformation. In our case, using the MTEX toolbox [102] with EBSD data, we found the average number of neighbours to be in the range of 4-6. At each incremental strain step the solved lattice spin $\dot{\Omega}^{(g')}$ of neighbours is coupled to the spin of grain (g). The effective medium approach ensures grains with the same initial orientation and morphology reorient the same way. The random coupling to other grains slows down and spreads these texture trends. The result is a reduced intensity for strong texture components.

The inputs and outputs of the code are summarised in Fig. 6.1.

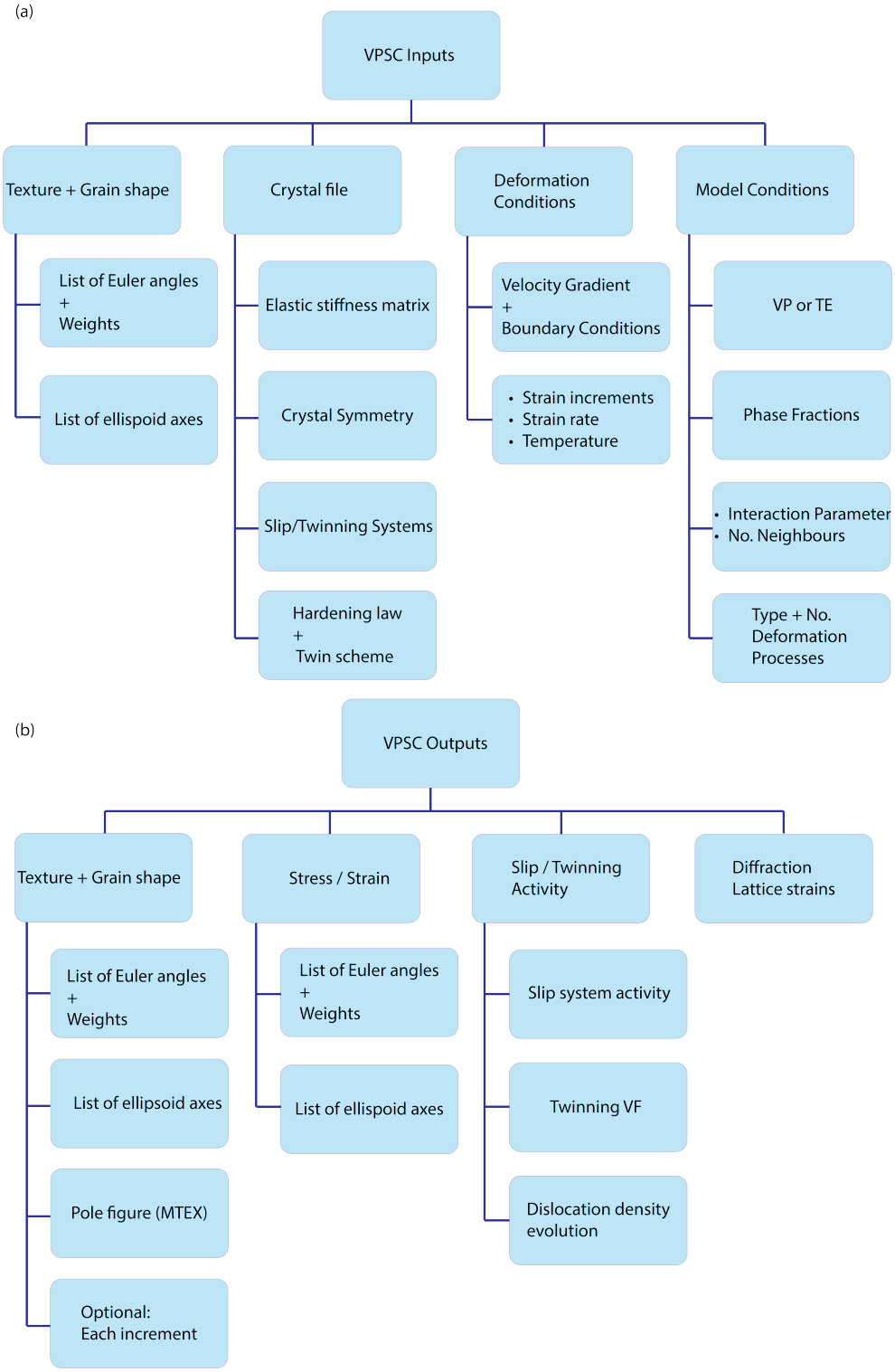


Figure 6.1: A summary of (a) the inputs that feed the model and (b) the outputs generated.

6.3 Results

6.3.1 Calibration of the VPSC model with macroscopic tensile data

To calibrate the model we simulated the uni-axial tensile experiments at RT and elevated temperatures, the samples and experiment conditions are detailed in Chapter 3. The initial microstructure of the alloys were converted from EBSD scans containing > 2000 grains. The average grain orientation was used to represent each grain and the grain size in pixels to weight them. The initial grain shape for all grains was defined as spherical, this implies no initial geometric anisotropy in the grain for numerical efficiency in the convergence scheme. This setting is standard in the VPSC simulation for simplicity unless a file with each grain morphology is used, this application is more important for severely deformed grains, e.g., after rolling.

For simplicity, for all alloys, we found the intermediate linearisation $n^{\text{eff}} = 10$ was sufficient for the simulations. The $\chi_s ub$ interaction parameter was kept at a default of 0.086. The initial $\rho^{s'}_{for}$ and ρ_{sub} kept to default values 5×10^5 and 1×10^{11} respectively. The temperature and strain rate references used were $298(K)$ and $0.001(s^{-}1)$ respectively. To simulate high levels of deformation along two seperate loading directions and elevated temperatures, we found it necessary to include the following deformation systems; prismatic $\langle a \rangle$, basal $\langle a \rangle$, and pyramidal $\langle c + a \rangle$. Experimentally, twinning was observed in these alloys and was suspected to contribute significantly to the anisotropy observed between the rolling direction (RD) and transverse direction (TD) in some of the alloys. As a result, tensile $10\bar{1}2$ and compression $11\bar{2}2$ twinning systems were included in our simulations. The hardening parameters for each alloy are defined in Tables 6.1, 6.2, 6.3, 6.4, 6.5 & 6.6.

Parameters

Alloy	$b^s[m]$	g^s	$K_1^s[m^-1]$	$\dot{\epsilon}_0[s^-1]$	HP^s	
AZ31						
Prismatic	3.21×10^{-10}	3×10^{-3}	2×10^8	1×10^7	0.10	
Basal	3.21×10^{-10}	3×10^{-3}	3.85×10^8	1×10^7	0.17	
Pyramidal	6.12×10^{-10}	4×10^{-3}	4×10^9	1×10^7	0.06	
Twinning		τ_{crit}	τ_{prop}	$TTWSL$	$Threshold$	
TTwin	4.92×10^{-11}	60	20	$44, 119, 9$	0.1	0.5
CTwin	1.09×10^{-9}	200	200	$10, 10, 3$	$0.1, 0.5$	

Table 6.1: Temperature independent parameters for AZ31.

Alloy	$b^s[m]$	g^s	$K_1^s[m^-1]$	$\dot{\epsilon}_0[s^-1]$	HP^s
AZX					
Prismatic	3.21×10^{-10}	3×10^{-3}	1×10^8	1×10^7	0.10
Basal	3.21×10^{-10}	3×10^{-3}	2.85×10^8	1×10^7	0.11
Pyramidal	6.12×10^{-10}	4×10^{-3}	4×10^8	1×10^7	0.06
Twinning		τ_{crit}	τ_{prop}	$TTWSL$	$Threshold$
TTwin	4.92×10^{-11}	60	30	$44, 119, 9$	$0.1, 0.5$
CTwin	1.09×10^{-9}	170	170	$265, 347, 3$	$0.1, 0.5$

Table 6.2: Temperature independent parameters for AZX.

To accurately capture the stress strain response at elevated temperatures it was necessary for the material dislocation interaction parameter χ_{for} and slip mode dependent drag stress D^s to be modified to vary with temperature. Early studies for forest dislocation interactions [171, 77] found χ_{for} to vary with temperature and strain rate, we utilise the relationship described by Beyerlein and Tome 2008 [80]:

$$\chi_{for} = \hat{\chi} * s(\dot{\epsilon}, T) \tag{6.59}$$

where $\hat{\chi}$ is 0.9 and $s(\dot{\epsilon}T)$ decreases from 1 to 0 with increasing temperature.

Alloy	$b^s[m]$	g^s	$K_1^s[m^-1]$	$\dot{\epsilon}_0[s^-1]$	HP^s
ZXK					
Prismatic	3.21×10^{-10}	3×10^{-3}	1×10^8	1×10^7	0.10
Basal	3.21×10^{-10}	3×10^{-3}	2.85×10^8	1×10^7	0.11
Pyramidal	6.12×10^{-10}	4×10^{-3}	4×10^8	1×10^7	0.06
Twinning		τ_{crit}	τ_{prop}	$TTWSL$	$Threshold$
TTwin	4.92×10^{-11}	60	20	$44, 119, 9$	$0.1, 0.5$
CTwin	1.09×10^{-9}	120	120	$265, 347, 3$	$0.1, 0.5$

Table 6.3: Temperature independent parameters for ZXK.

Alloy	$\tau_0^s[MPa](A_0^s, A_1^s, A_2^s)$	$F^s_{(T,\dot{\epsilon})}(F_0^s, F_1^s, F_2^s)$
AZ31		
Prismatic	-19.4 | 673.0 | 151.8	-1.1 | 41.1 | 65.7
Basal	5 | 0 | 298.0	-0.8 | 60.8 | 53.1
Pyramidal	-2.6 | 23467.5 | 62.7	-0.8 | 60.8 | 53.1

Table 6.4: Temperature dependent parameters for AZ31.

Tam et al 2020 [96] recently modelled the behaviour of AZ31 at elevated temperatures and found the same relationship with χ_{for}, in addition they found drag stress to decrease with temperature. Similarly we found the same monotonic relationship between drag stress and temperature, however, through iterations the drag stress was found to exponentially decay in our case, via the same relationship as the initial slip resistance τ_0^s:

$$D^s(T) = A^s + B^s * exp(-T/C^s) \tag{6.60}$$

Simulation curves

In this section the simulated stress strain curves are represented by triangles in Figures 6.2, 6.3, & 6.4. Utilising the dislocation density hardening models ability to capture tem-

Alloy	$\tau_0^s[MPa](A_0^s, A_1^s, A_2^s)$	$F^s_{(T,\dot{\epsilon})}(F_0^s, F_1^s, F_2^s)$
AZX		
Prismatic	0 | 677.6 | 131.3	-120.5 | 160.5 | 914.7
Basal	8.0 | 0 | 298.0	-9.2 | 69.2 | 142.0
Pyramidal	3.7 | 4330.0 | 88.0	-8.4 | 68.4 | 138.0

Table 6.5: Temperature dependent parameters for AZX.

Alloy	$\tau_0^s[MPa](A_0^s, A_1^s, A_2^s)$	$F^s_{(T,\dot{\epsilon})}(F_0^s, F_1^s, F_2^s)$
ZXK		
Prismatic	-2040.0 | 2190.2 | 8093.0	-1.1 | 41.1 | 65.7
Basal	8 | 0 | 298.0	-0.8 | 60.8 | 53.1
Pyramidal	0.3 | 12930 | 75.5	-0.8 | 60.8 | 53.1

Table 6.6: Temperature dependent parameters ZXK.

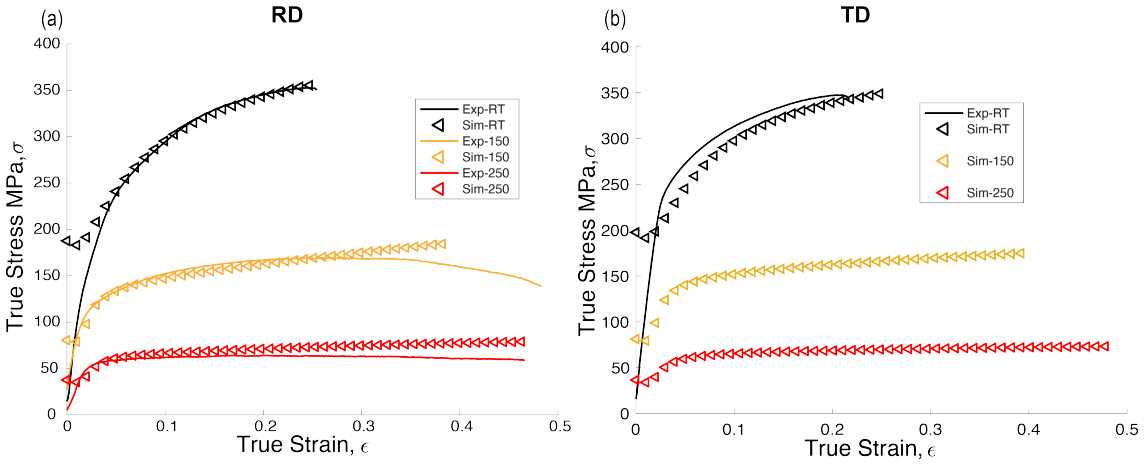


Figure 6.2: Stress-strain curves for AZ31 for loading in the (a) RD and (b) TD. Only the RD has experimental data at the elevated temperatures. The dotted lines represent the simulation results.

perature sensitive variation in flow stress behaviour, we have captured the experimental tensile behaviour of the 3 alloys with reasonable accuracy. Noting that both the trend in flow stress and hardening rate are well predicted. To simulate tensile stress parallel to the RD and TD direction of the sheet, the EBSD scans for tensile specimens with RD parallel to the loading axis in the x direction were rotated 90°, creating two separate texture files. The same result can be achieved with a change in the VPSC process file, by specifying the velocity gradient to be applied in the y-direction, both methods were

Alloy			
Temperature(°C)	RT	150	250
AZ31	1	0.888	0.222
AZX	1	0.833	0.222
ZXK	1	0.888	0.444

Table 6.7: Interaction parameter

AZ31	D^s		
Slip mode	A^s	B^s	C^s
Prismatic	7.45	2.78E+6	52.94
Basal	-2.13E+3	3.14E+4	201.05
Pyramidal	43.49	2.50E+5	43.50

Table 6.8: AZ31 Drag stress matrix

tested to sanity check the results. Producing two texture files was found to be more efficient when using a modified version of the VAMPYR MTEX based optimisation code [103] for finding suitable hardening parameters.

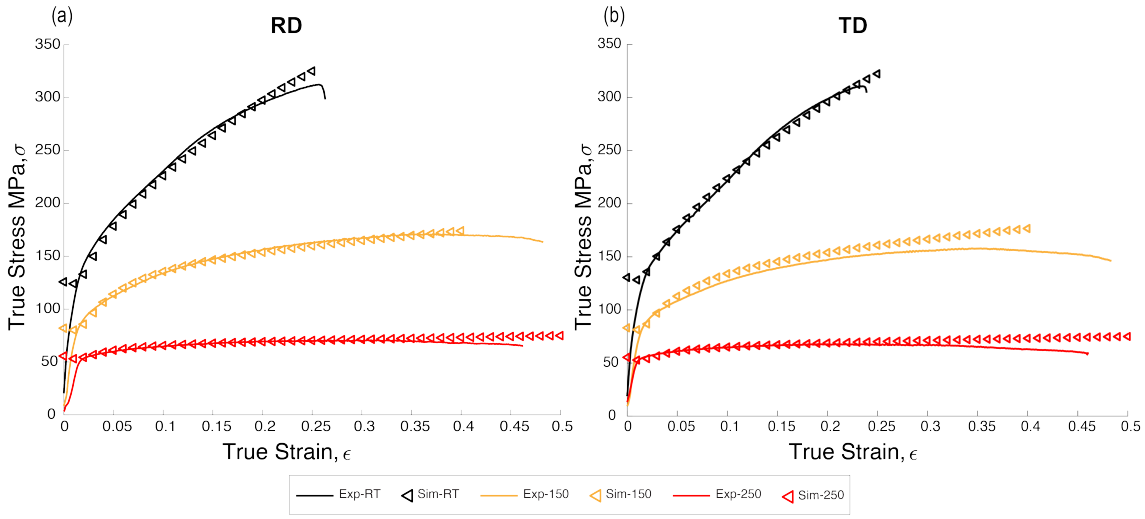


Figure 6.3: Stress-strain curves for AZX for loading in the (a) RD and (b) TD. The dotted lines represent the simulation results.

At room temperature (RT), the anomalous difference in hardening behaviour between directions for the ZXK alloy is more pronounced than for AZ31 and AZX. The model attempts to replicate the sigmoidal hardening curve to some extent but falls short in reproducing the dip observed after yield and before the second hardening stage. How-

AZX	D^s		
Slip mode	A^s	B^s	C^s
Prismatic	-32.28	3.76E+6	53.96
Basal	-1.91E+5	1.98E+5	1.56E+4
Pyramidal	-2.29E+3	1.77E+4	310.58

Table 6.9: Drag stress matrix for AZX

ZXK	D^s		
Slip mode	A^s	B^s	C^s
Prismatic	-1.41E+5	1.52E+5	7.03E+3
Basal	428.34	9.27E+4	83.12
Pyramidal	-1.09E+4	2.65E+4	619.05

Table 6.10: Drag stress matrix for ZXK

ever, it does effectively represent the early yield and second hardening phase, though the latter occurs immediately after yield, preventing the formation of the curve's indent. The hardening behaviour in the RD is accurately modelled. At 150°C, the temperature-dependent variation in initial slip resistance reflects the expected reduction in yield stress. The less pronounced difference in hardening behaviour is well handled by the model. At 250°C, the immediate plateau of flow stress after yielding, with minimal hardening and a prolonged period of stable stress with increasing strain, is well described. However, in the RD, the simulated initial yield point is slightly skewed. This directional discrepancy suggests inaccuracies in modelling the combination of active deformation modes contributing to stage 1 hardening. Experimental curves for AZX at RT show similar trends, and this is reflected in the model, where the simulated curves are almost indistinguishable. The difference in initial yield is accurately predicted, though experimentally, the TD shows a more pronounced sigmoidal shape, which the model does not fully replicate. Both simulated curves indicate twinning-influenced hardening. Similar to ZXK TD at 150°C, the TD experiences a larger post-yield drop than the RD. However, both simulated curves at 150°C display more regular flow stress patterns. At 250°C, the model accurately predicts the experimental response in both sheet directions. For AZ31 at RT,

the simulated curves predict the more consistent hardening response seen compared to the Ca-containing alloys. However, the model struggles to replicate the stiffer yield in the TD compared to the RD. At elevated temperatures, only RD data were available for model calibration. While the yield response is captured well at these temperatures, the simulated curves quickly exceed the experimental stress levels in the later stages of hardening.

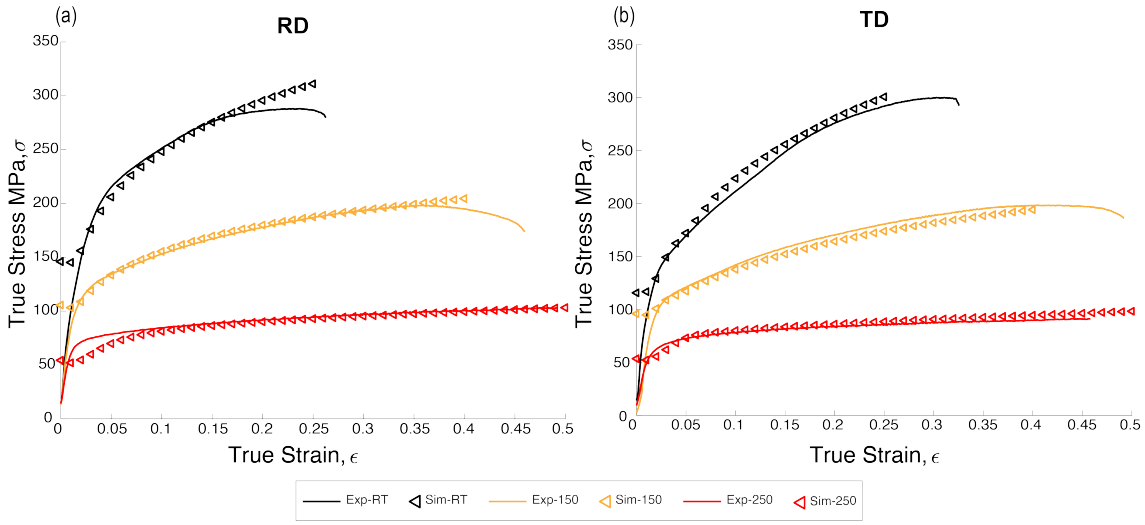


Figure 6.4: Stress-strain curves for AZX for loading in the (a) RD and (b) TD. The dotted lines represent the simulation results.

The calibration of the model with the experimental data was crucial for the subsequent analysis into the active deformation modes and texture development. The CRSS used for the predictions are shown in Fig. 6.5.

6.3.2 Extracting slip and twinning activity

The activity of deformation modes is deduced by the model as the relative amount of shear rate contributed by each mode available. In addition to twinning volume fraction, the volume fraction of grains that have been reoriented by twinning is also reported. The deformation activities, dislocation density (DD) evolution via forest and debris/substructure evolution predicted for the stress strain responses above are shown

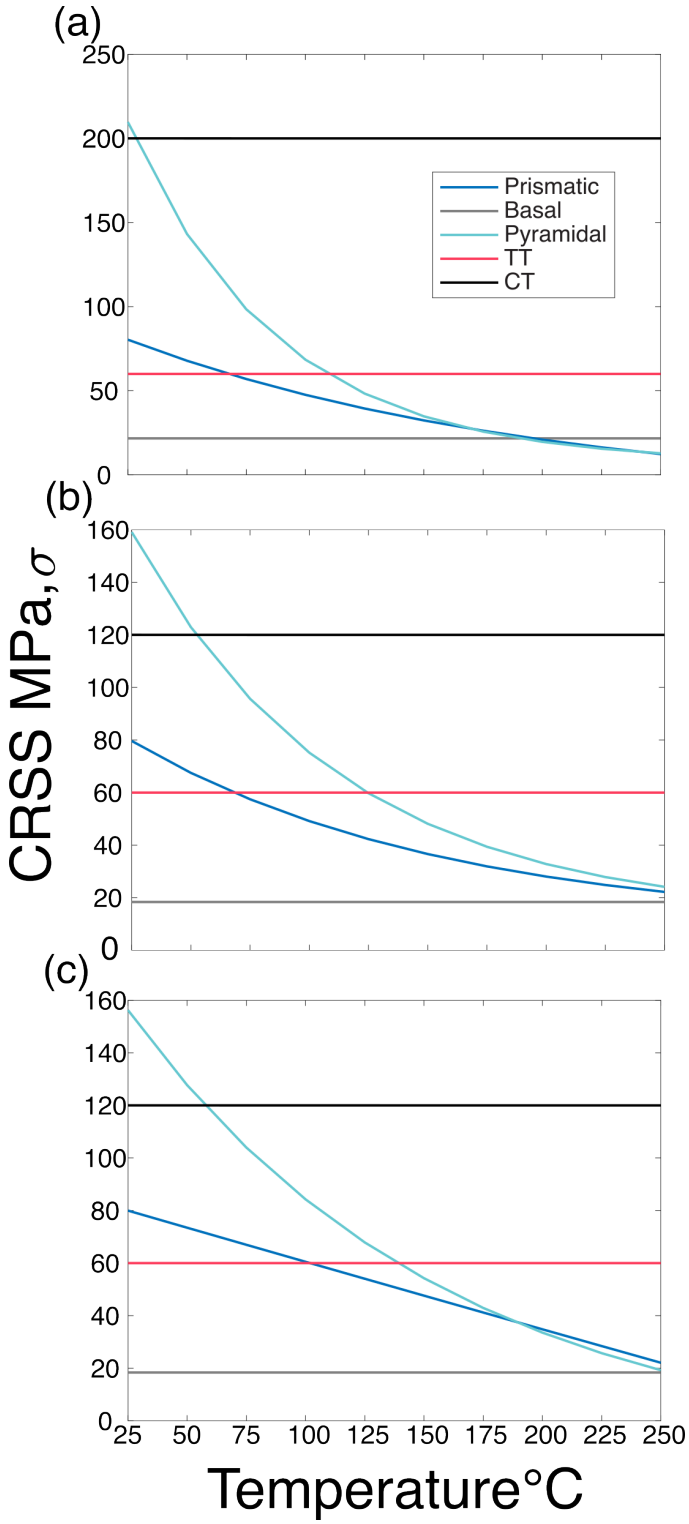


Figure 6.5: Evolution of initial CRSS with increasing temperature for considered deformation modes, for (a) AZ31, (b) AZX and (c) ZXK.

in Figures. 6.6, 6.7, 6.8, 6.9, 6.10 & 6.11.

In the following sections 'pyramidal activity' refers to pyramidal $\langle c+a \rangle$ slip activity.

Deformation behaviour of alloy AZ31

At RT, fig 6.6 shows very early deformation in the RD is highly reliant on basal slip, as expected with the lowest τ_{CRSS}. This is only true for a very short period of strain, prismatic slip quickly overtakes and dominates deformation there on. In contrast, the TD case is dominated by prismatic slip from the beginning and the overall contribution by basal slip is reduced. Both cases evolve small fractions of twinning, with slight differences. The RD case is predicted to have tensile twinning early in deformation followed by compression twinning. The fraction of twinning is smaller in the TD case. Pyramidal activity in both cases was minimal as expected because of a large τ_{CRSS}. The dislocation density evolution on the prismatic system dominated both cases, showing the majority of hardening predicted in the RT tensile curves to be a result of prismatic activity.

Increasing temperature resulted in a significant increase in pyramidal activity at the beginning of deformation in both RD and TD cases, the exponential decay in the τ_{CRSS} gives ease to pyramidal slip. At strains post-yield, the relative activity of prismatic slip remained dominant, predicting deformation to proceed mainly via prismatic and basal. The dislocation density evolution reveals a significant level on the pyramidal system compared to the prismatic and basal at 150°C, and even greater at 250°C. The twinning activity was greatly reduced as slip on the pyramidal systems became available. The development of debris and substructure also declined with increasing temperature.

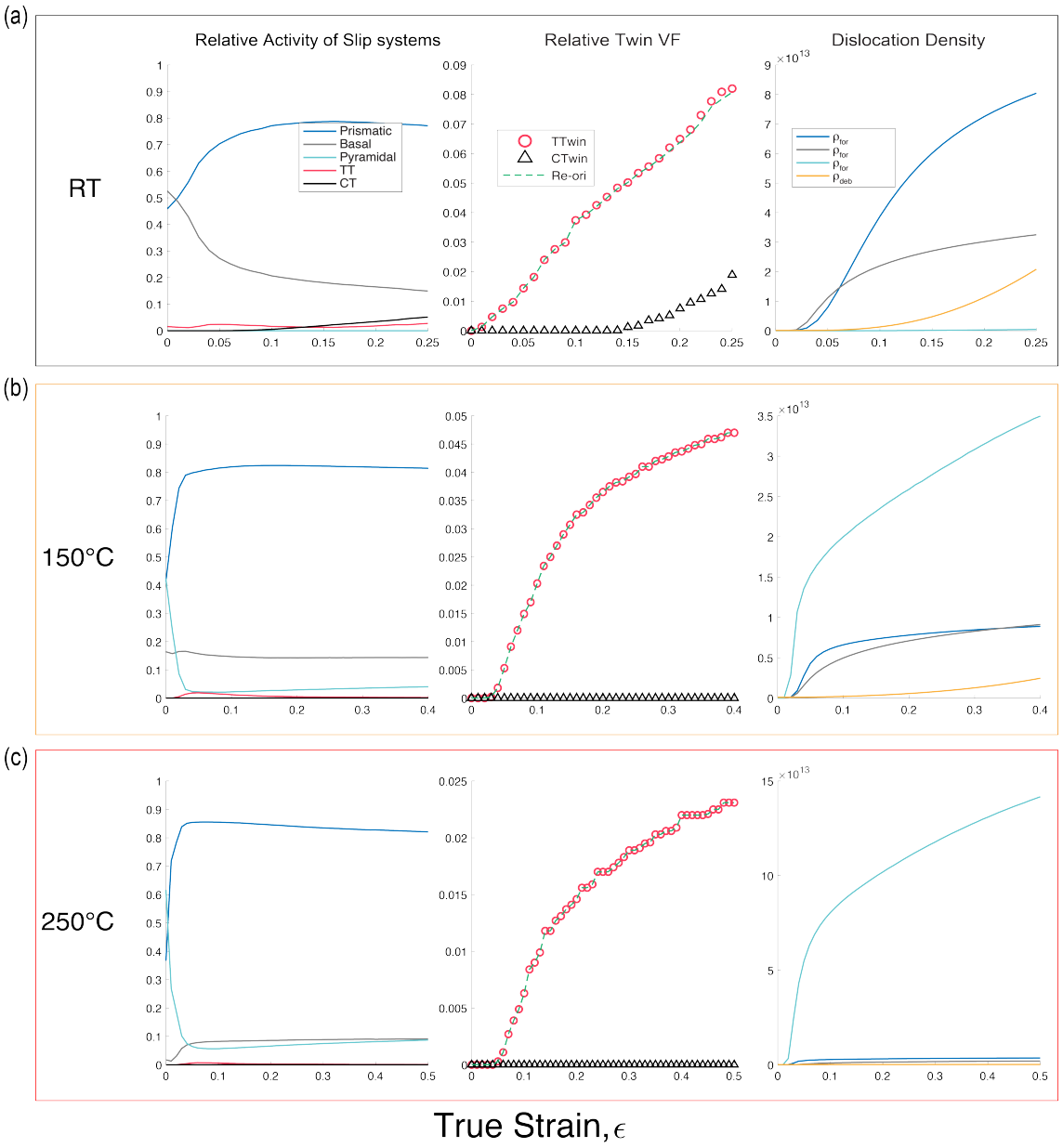


Figure 6.6: AZ31-RD. Predictions from left to right, the evolution of: slip system shear activity, twinning volume fraction and dislocation density on considered deformation modes. For increasing temperatures (a)-(c).

Deformation behaviour of alloy AZX

At RT for both RD and TD cases, deformation begins dominant via basal slip, this steadily decreases as prismatic slip activity increases, eventually superseding basal activity. The slip activity and dislocation density evolution of both are relatively identical, the development of substructures increases exponentially towards higher strains. A slight

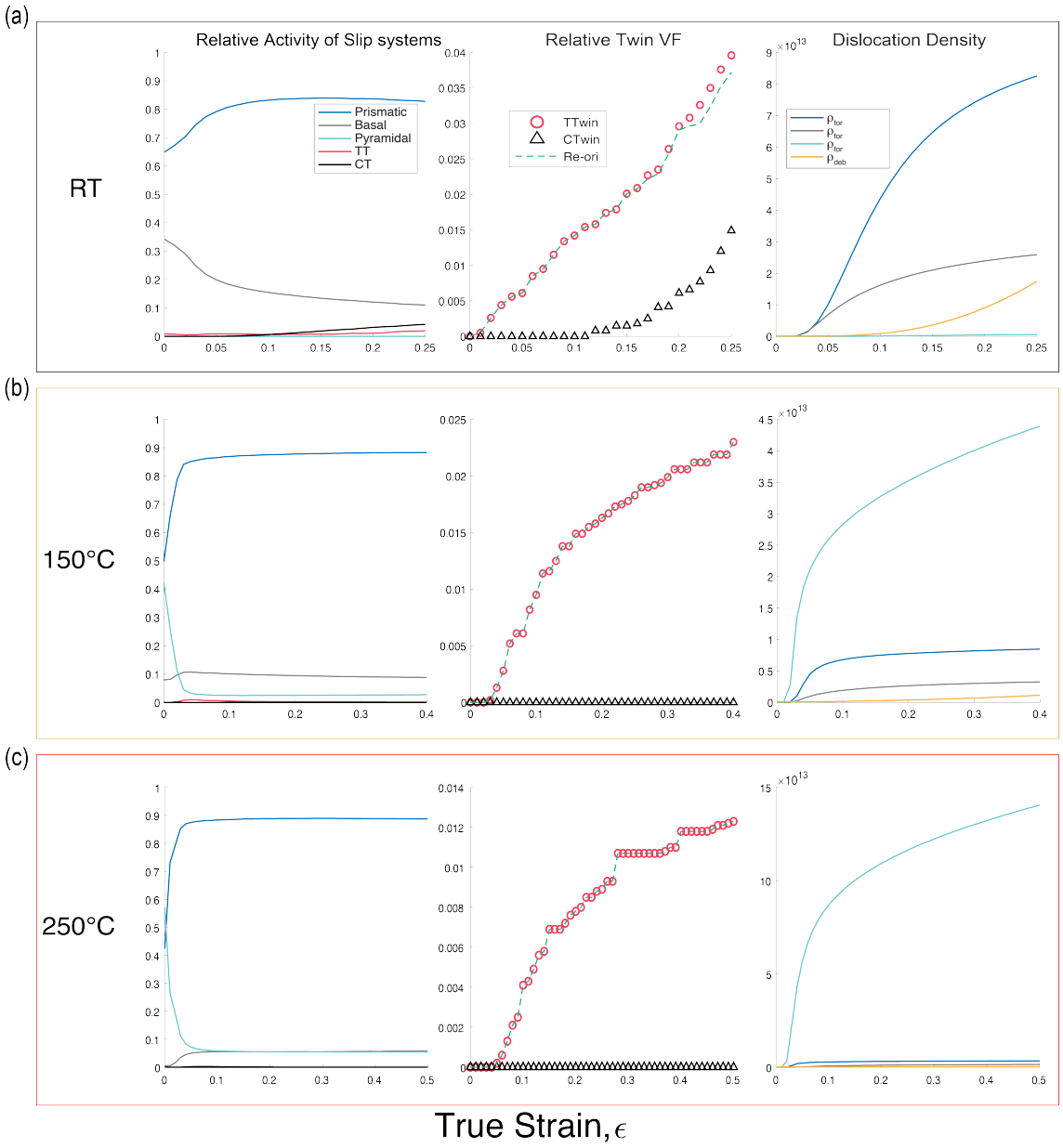


Figure 6.7: AZ31-TD. Predictions from left to right, the evolution of: slip system shear activity, twinning volume fraction and dislocation density on considered deformation modes. For increasing temperatures (a)-(c).

contrast between the directions at RT is evident in the twinning behaviour, loading along the TD triggers a larger increase in volume fraction of tensile twinning immediately at lower strains. Both directions reach peak shear contribution from tensile twinning at 0.05 strain. Compression twinning develops very late on in strain, a very small volume fraction of compression twins are formed, the relative volume fraction of twinning is larger in the TD case.

At elevated temperatures pyramidal slip becomes more active for both cases, and the transition between prismatic and basal slip occurs at very early strains, at 250°C prismatic and pyramidal are more dominant than basal from the beginning. The dislocation density due to substructures is significantly reduced. There are no significant changes in the volume fraction of twins at 150°C, tensile twinning is delayed due to access to pyramidal slip. Compression twinning is completely suppressed at elevated temperatures.

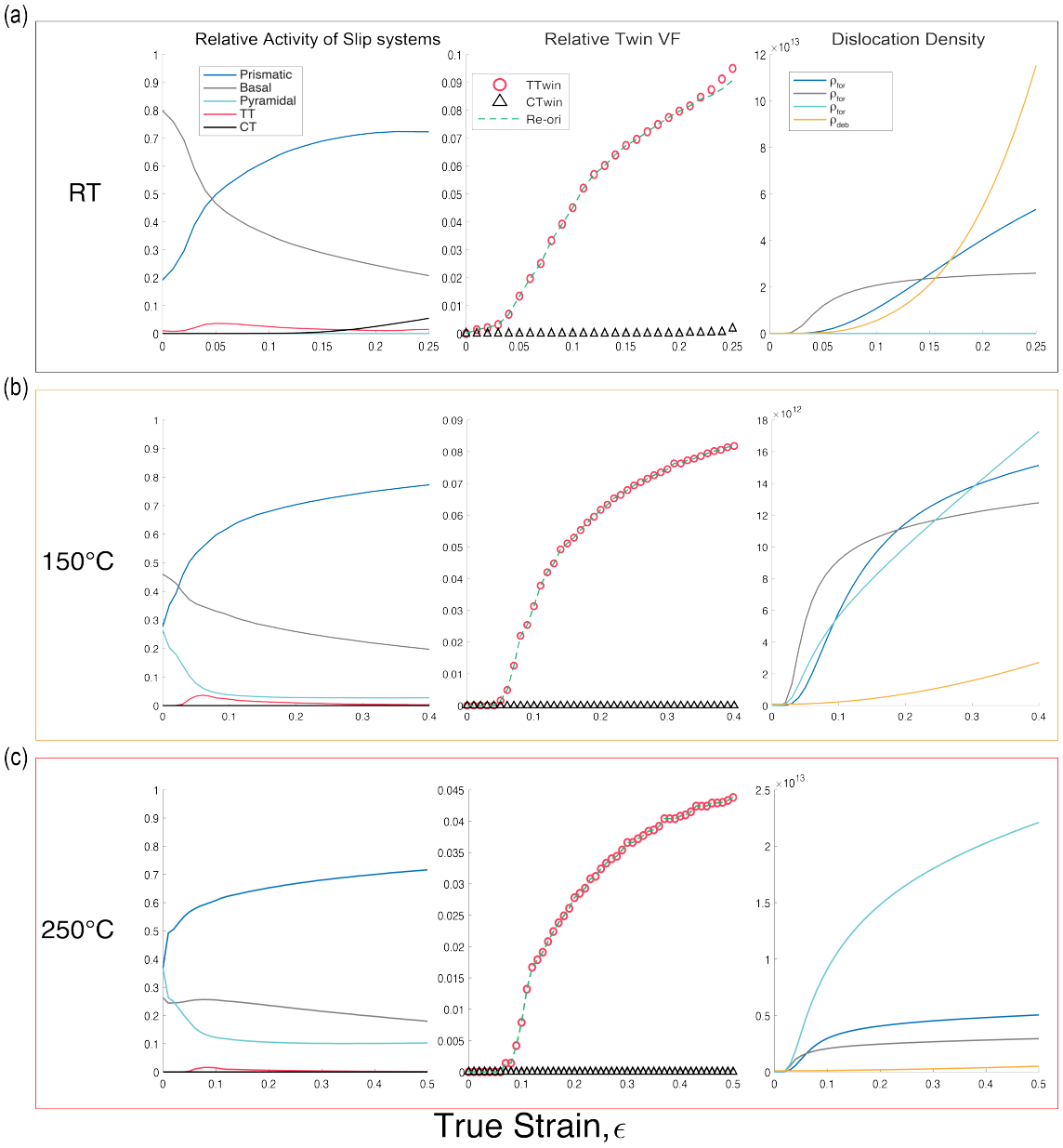


Figure 6.8: AZX-RD. Predictions from left to right, the evolution of: slip system shear activity, twinning volume fraction and dislocation density on considered deformation modes. For increasing temperatures (a)-(c).

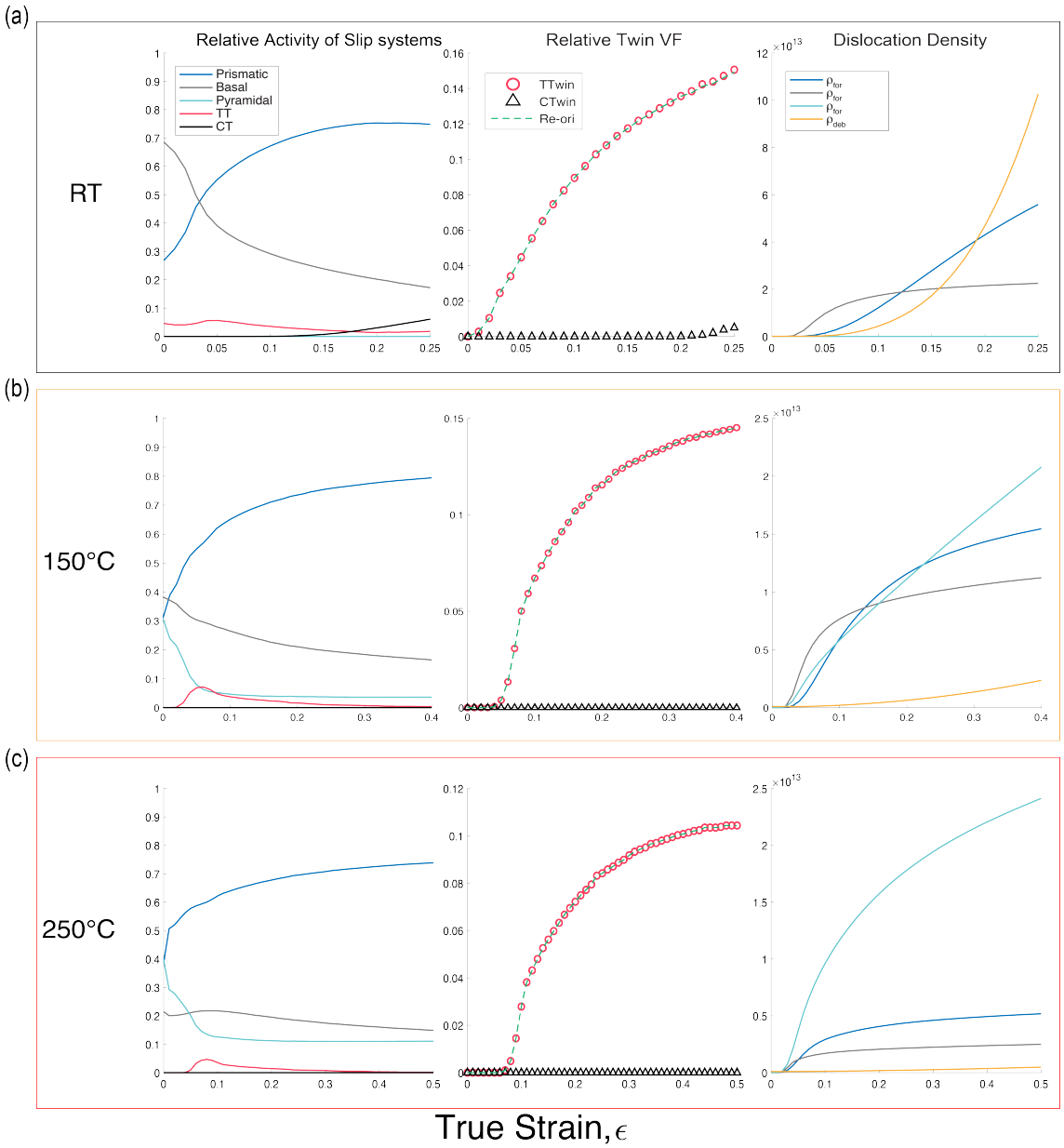


Figure 6.9: AZX-TD. Predictions from left to right, the evolution of: slip system shear activity, twinning volume fraction and dislocation density on considered deformation modes. For increasing temperatures (a)-(c).

Deformation behaviour of alloy ZXK

For the ZXK alloy larger differences in RT behaviour are observed between the RD and TD cases. Generally, a similar trend is observed to the AZX alloy, where basal slip activity contributes a greater amount to deformation in the initial stages of strain before prismatic overtakes, for ZXK this transition occurs at a higher strain. In the TD case

there is a significant delay in the growth of prismatic activity, the promotion of twinning reduces the requirement for prismatic activity. The stark difference in twinning activity is clear, an interesting observation is the insignificant level of compression twinning. Pyramidal activity is again suppressed at RT.

Surprisingly, pyramidal slip activity is not significant in either case until 250°C, this is in contrast with the other alloys. The level of pyramidal slip activity is similar for both cases, with the transition from basal to prismatic slip occurring earlier at higher temperatures. Tensile twinning persists at elevated temperatures for the TD case, with increasing pyramidal activity comes a greater delay in the start of twinning. Overall volume fraction of tensile twinning does reduce at elevated temperatures. For the RD case twinning is very suppressed at elevated temperatures.

Figure6.12 shows the overall contribution from each deformation mode evolving with temperature for our alloys. The model predicts for AZ31 and AZX cases that slip on prismatic systems is the preferred deformation mode in this temperature range. The Ca-containing alloys are predicted to rely less on twinning in the RD case than AZ31, but display more twinning in TD cases. In both RD and TD cases pyramidal activity grows with increasing temperature and twinning activity decreases.

6.3.3 Pole figure predictions

The initial textures and evolution following uniaxial tension are presented in Figures 6.13, 6.14 and 6.15. To note, the calculated intensities from the VPSC output are overall slightly higher than the measured values, they could be scaled for better interpretation.

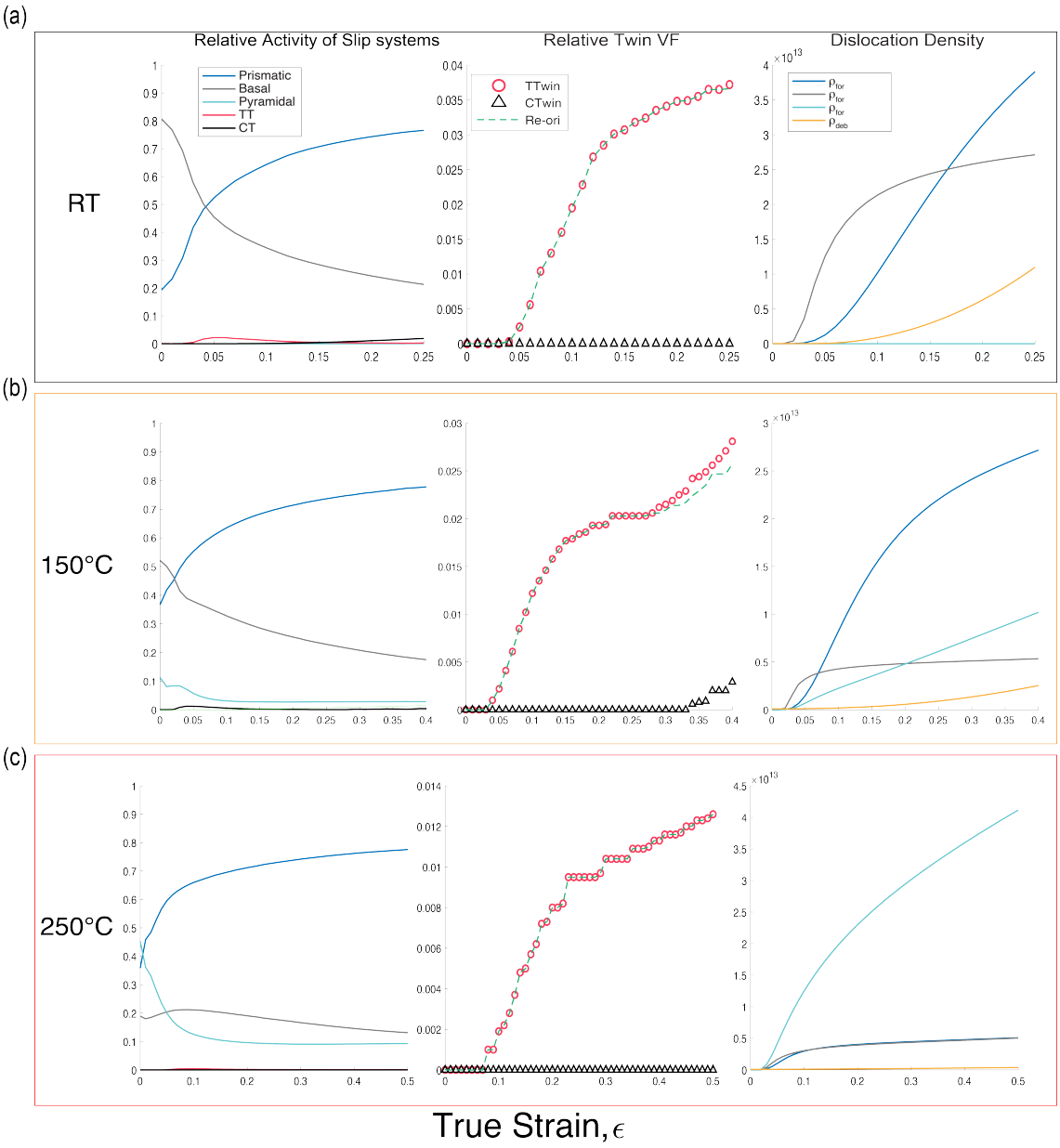


Figure 6.10: ZXK-RD. Predictions from left to right, the evolution of: slip system shear activity, twinning volume fraction and dislocation density on considered deformation modes. For increasing temperatures (a)-(c).

AZ31

In Fig. 6.13, for both RD and TD cases, the basal intensity profile of the basal pole figure remains relatively unchanged post deformation, while the prismatic intensity profile undergoes a significant transformation from a distribution that is symmetrically constant. The spread of basal poles in the initial texture towards the RD is most disrupted for the

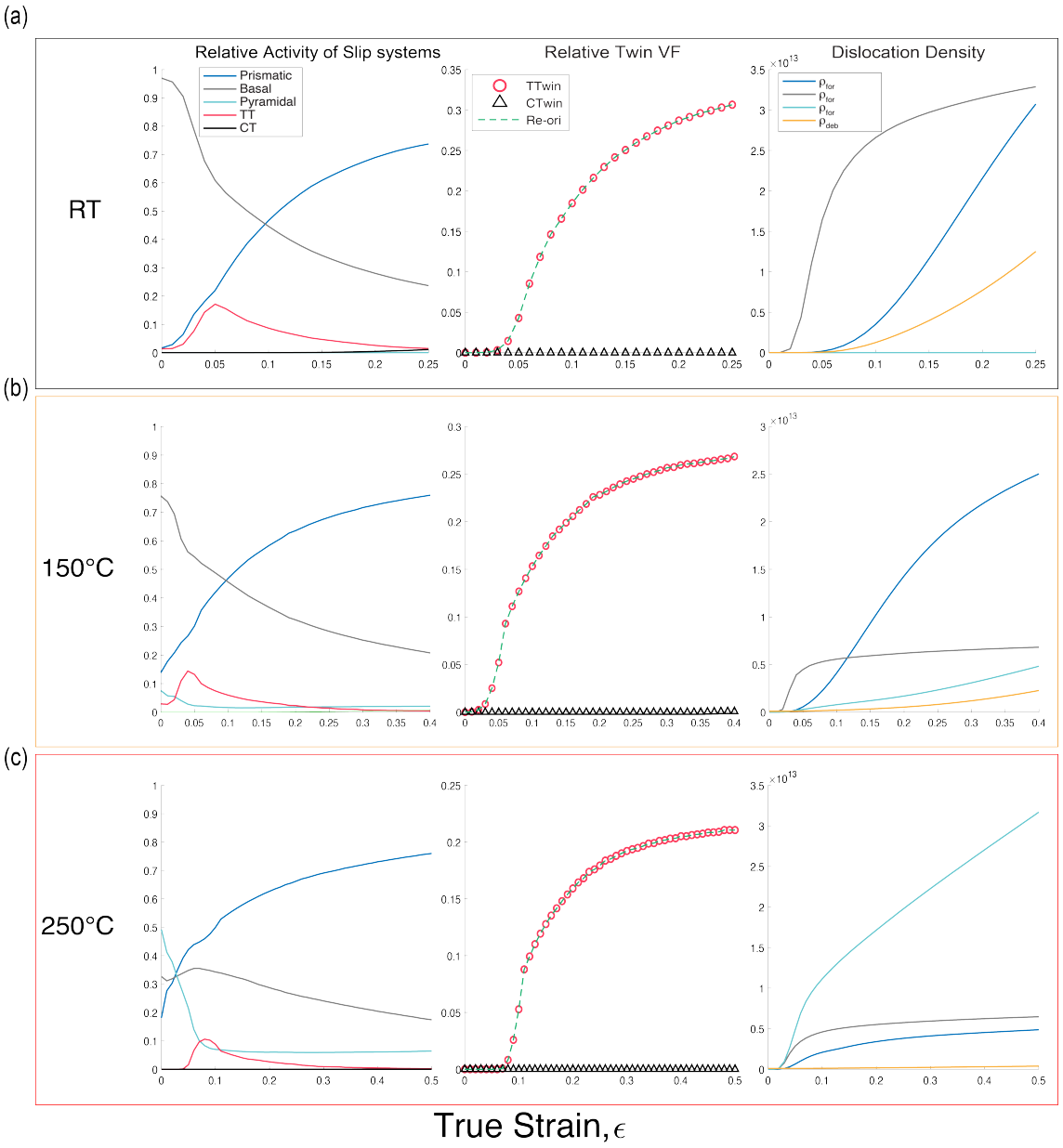


Figure 6.11: ZXK-TD. Predictions from left to right, the evolution of: slip system shear activity, twinning volume fraction and dislocation density on considered deformation modes. For increasing temperatures (a)-(c).

RD case at RT compared to elevated temperature tests, with no preferred direction bias. In both cases, the prismatic pole figures develop a 6-fold symmetry, which becomes more pronounced at higher temperatures.

The basal pole intensity in the initial condition indicates a significant fraction of grains have a Schmid factors close to 0 for basal slip (c-axis parallel to the sheet normal),

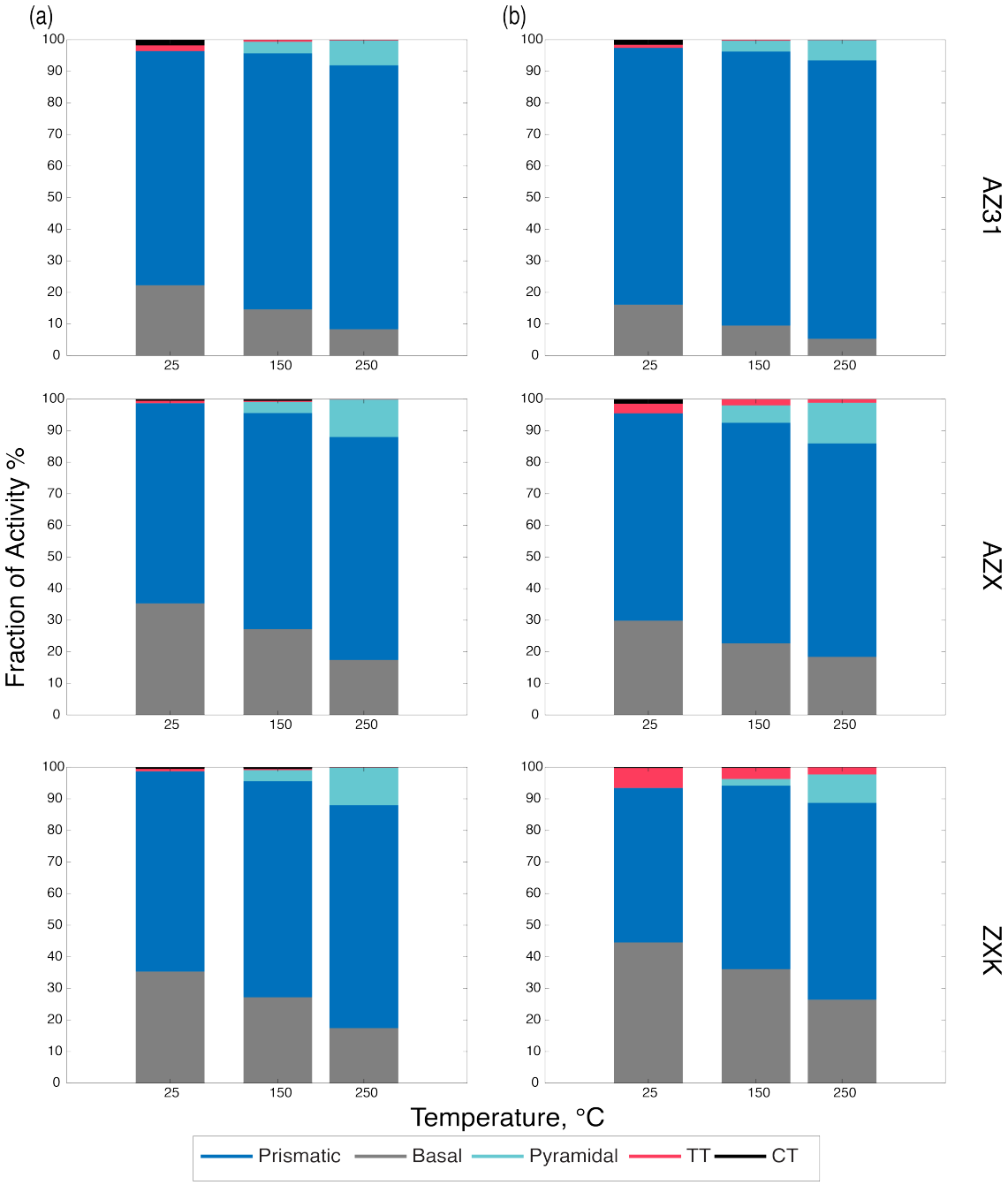


Figure 6.12: Active deformation modes relative contribution to total shear for all 3 alloys, for the (a) RD case, and (b) TD case.

corresponding to a lower fraction of basal activity observed for AZ31, as shown in Figure 6.12. The retention of the basal peak profile in the (0001) pole figure is more evident at higher temperatures in the RD case and overall in the TD case, which is also reflected in the reduced basal slip activity.

The strength of the basal texture does not change for all tested temperatures, as shown in the (0001) pole figure. This suggests that the active slip systems activity have had no influence on the basal texture.

Less twinning activity in the TD case at room temperature correlates to the change in texture with a more uniform basal peak intensity in the loading direction compared to the marginally larger spread in the RD case. The presence of basal poles around the periphery of the (0001) pole figure indicates re-orientation consistent with the 86.3°extension twin relationship about the $\langle 11\bar{2}0\rangle$ axis [172].

AZX

In Fig. 6.14, for the RD case, in the (0001) pole figure, the splitting of the basal pole peak intensity is more present after deformation. Additionally, splitting is stronger at higher temperatures, with the intensity of the peaks increasing to better match the contrast in intensity seen at RT. In contrast, the TD case shows a less distinctive split peak (a lower intensity). The angular spread of basal poles outside the peaks consistently favours a spread away from the loading axis (TD); this is true for both RD & TD cases despite the 90° difference in initial orientation spread.

Six-fold symmetry is present in the prismatic pole figures, and there is a larger increase in peak intensity in the temperature change from RT to 150° C compared to 150° C to 250° C. The symmetry is better produced in the RD case.

The weaker initial basal peak intensity compared to AZ31 coincides with increased basal slip activity.

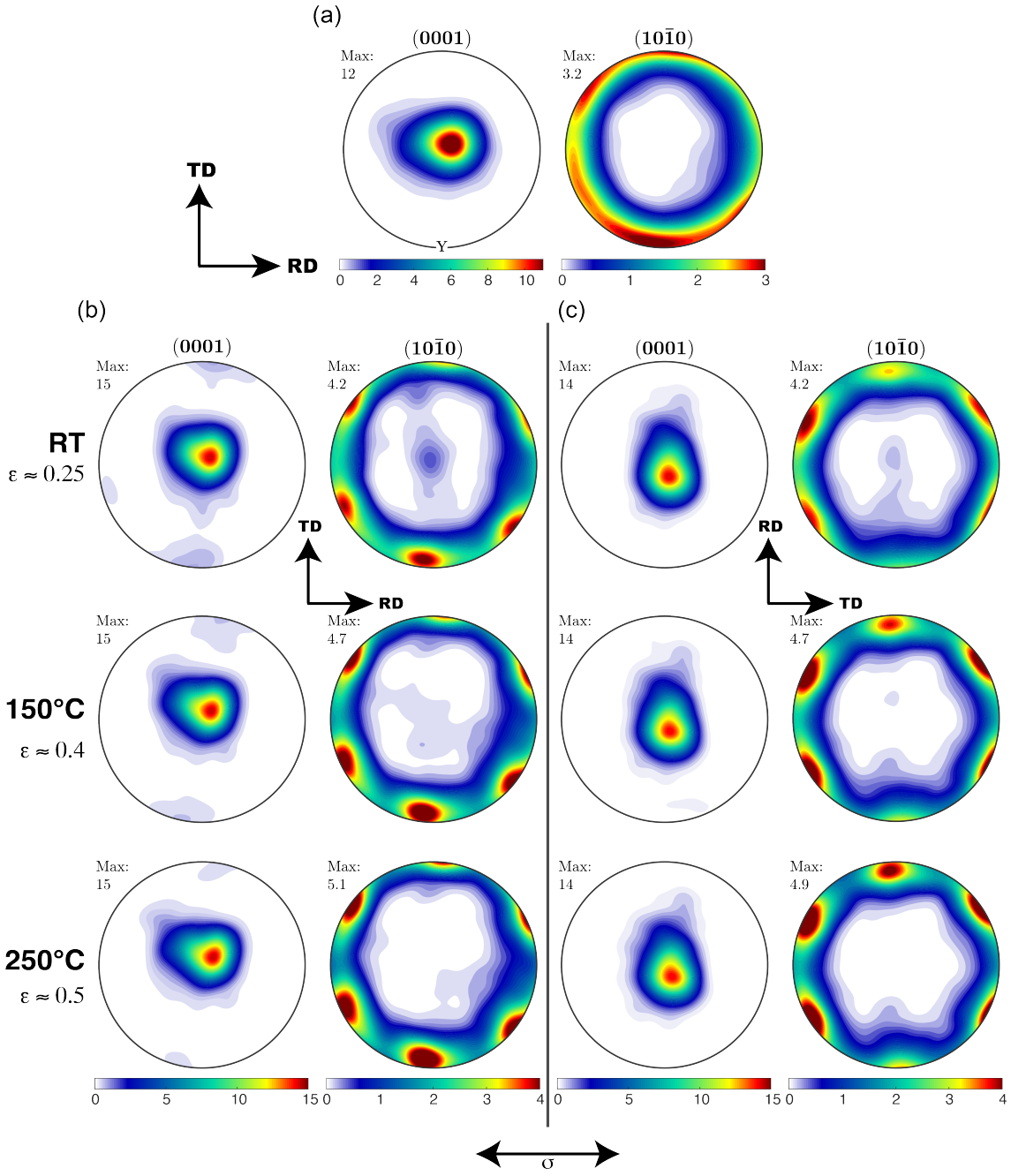


Figure 6.13: AZ31 - Texture predictions to end strains for loading in both directions, (b) RD case and (c) TD case. The initial experimental texture at RT (a) for reference.

ZXK

The influence of the weaker and more asymmetric initial basal peak intensity for ZXK compared to AZ31 & AZX is evident in the increased basal slip activity.

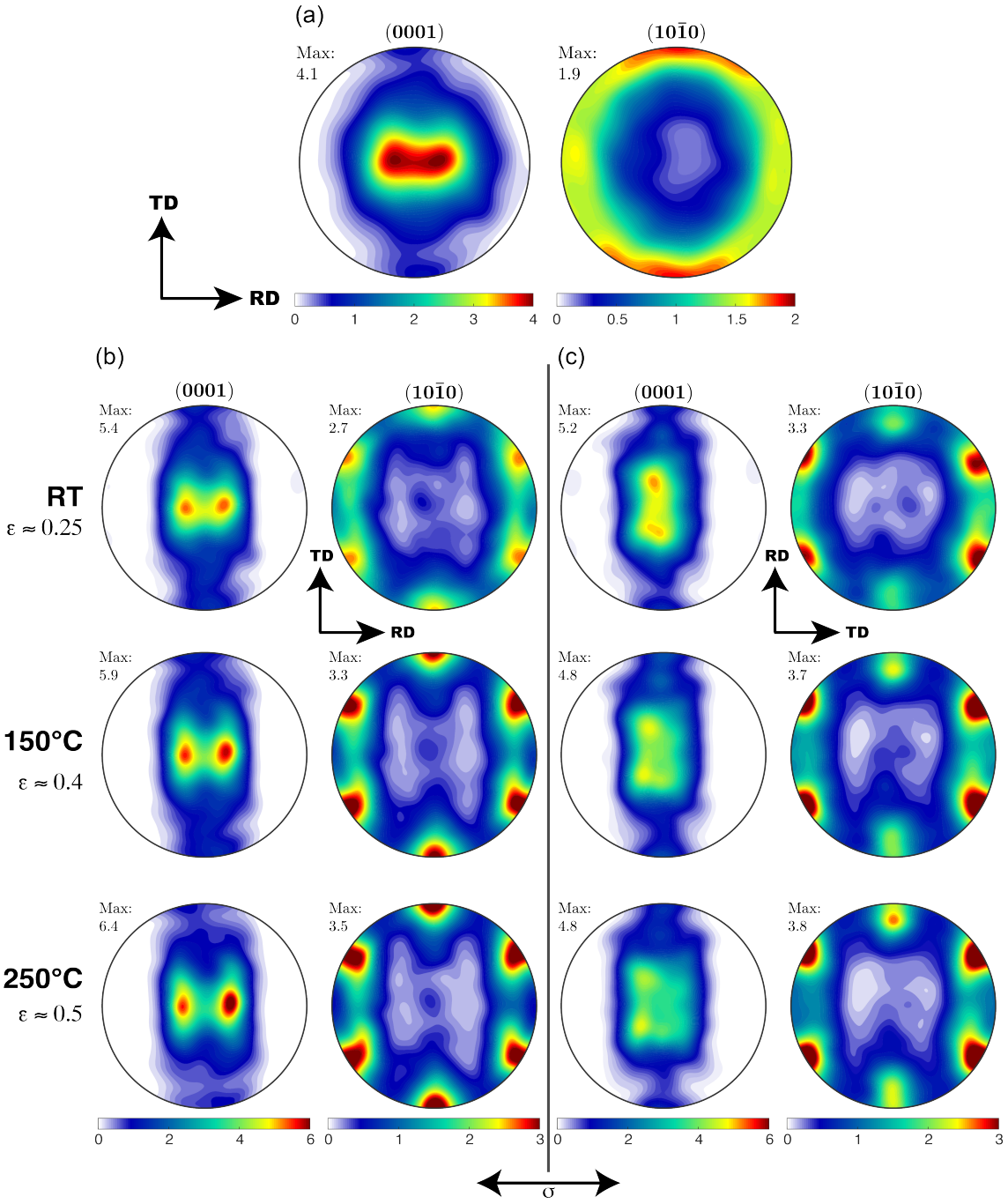


Figure 6.14: AZX - Texture predictions to end strains for loading in both directions, (b) RD case and (c) TD case. The initial experimental texture at RT (a) for reference.

In Fig. 6.15, for the TD case, the transformation of the basal pole peaks was most evident at room temperature, the split basal peaks towards TD directions are drawn to the centre. At 250°C this split is still evident, however, the spread of poles within the peaks are more strictly oriented towards the RD. For the RD case at all temperatures, the

peaks either side of the z direction split into further peaks, developing a 4 fold symmetry. This change is more evident at higher temperatures and can also be deduced in the TD case at 250°C. The decrease in twinning for the TD case at 150 & 250°C could lend to the more similar orientation spread of the basal poles with the RD case.

Similar to AZ31 and AZX, the prismatic pole figures for both cases develop a 6-fold symmetry. In both cases the symmetric peaks in the respective RD and TD directions tend to spread towards each other, but, they do this in a radial fashion towards Z(sheet normal) and avoid merging.

The texture developed at 250°C for the TD case is closer to the RD case, in the both pole figures. This is reflected in the active slip modes and the macroscopic flow curves. Figures 6.11 and 6.12 show at 250°C, twinning is seen to persist for the TD case at elevated temperatures and suppressed in the RD case. However, the volume fraction of grains reoriented is relatively low ≈ 0.2.

6.3.4 VPSC calculations of lattice strains

Nominally, crystallographic lattice strains from individual planes tend to be simulated by elasticity outputs from crystal plasticity models. The version of the VPSC model used in this study has the capability to calculate the micro-strains obtainable by neutron/high energy X-ray diffraction experiments. With this, the possibility to verify the simulated material response with experimental data exists.

To extract crystallographic strains, the model needs the elastic strain tensor in each grain. This would regularly be calculated from the Cauchy stress tensor, however, the viscoplastic deformation only accounts for the deviatoric stress tensor in each grain. The code instead leverages the macroscopic Cauchy stress to calculate the hydrostatic pressure in the grains. The pressure is added to the deviatoric stress with some assumptions

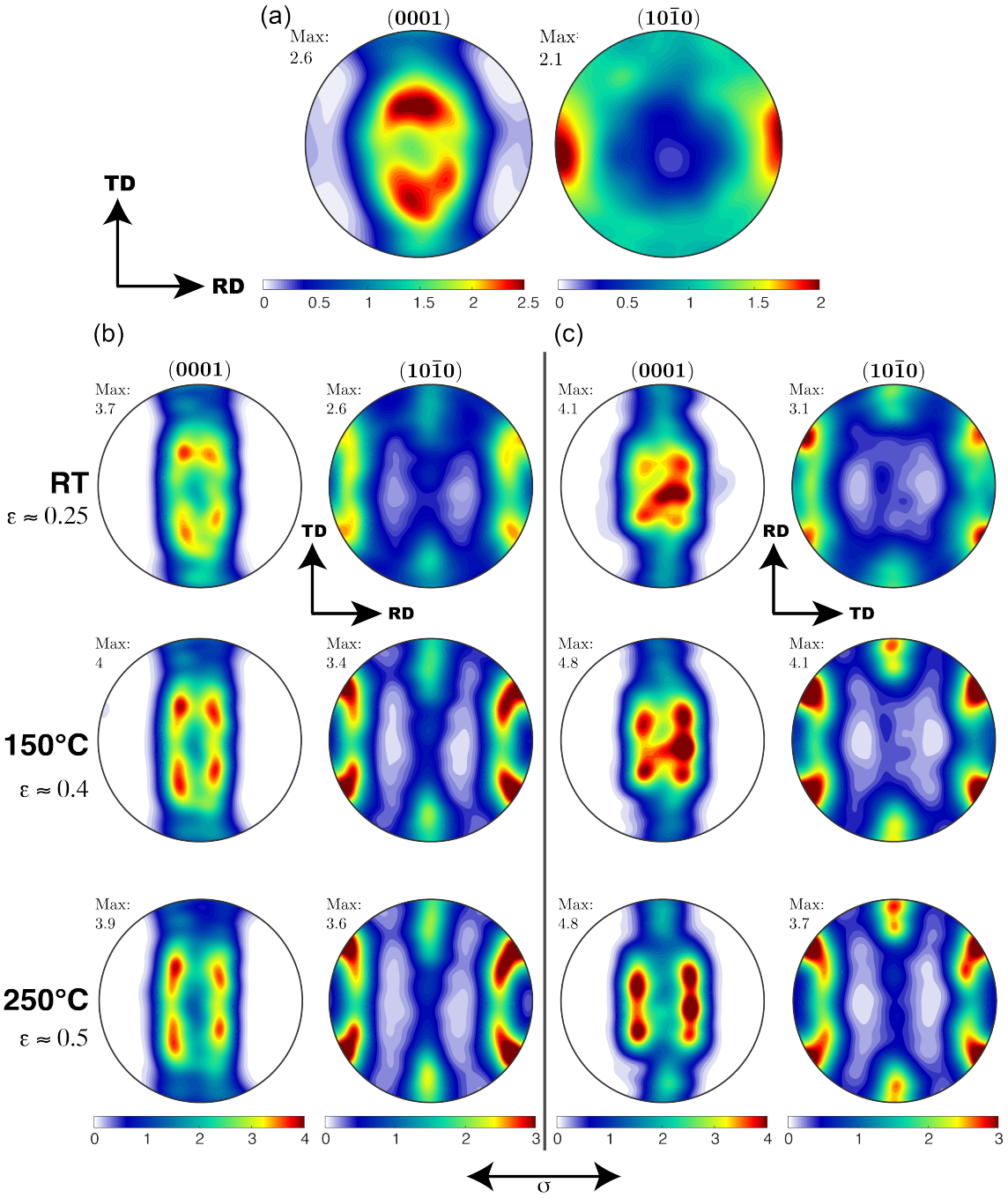


Figure 6.15: ZXK - Texture predictions to end strains for loading in both directions, (b) RD case and (c) TD case. The initial experimental texture at RT (a) for reference.

and the elastic strain tensor is then extracted [78].

The VPSC model identifies subsets of grains in the aggregate with crystallographic plane normals of interest that are well aligned for diffraction in directions specified. The average elastic strain perpendicular to the diffracting plane for these subsets is considered

synonymous to the shift in diffraction peak position observed in experiments [78]. The analysis presented here targets lattice strains on specific planes, predicted both parallel to the loading axis and perpendicular, to compare with experimental X-ray synchrotron data collected. Lattice strains parallel and perpendicular to the loading axis are referred to as 0°strains and 90°strains respectively.

To accompany this data, the model provides a weighting in the form of a relative volume fraction of grains contributing to each diffraction prediction. As a result, predictions originating from very small volume fraction may not be reliable. In addition, changes in volume fraction during deformation are an indication of grain rotation changes via slip and/or twinning. 0°lattice strains for the basal planes are unreliable due a to a low volume fraction of commonly oriented grains with the basal plane normal in this diffraction condition, Therefore have been omitted most cases. The remaining planes 0°lattice strains calculated by the model have relatively good volume fractions.

For almost all planes, the volume fraction of grains contributing to the 90°lattice strains lie between 1-4%, shown in Figures. 6.17, 6.19 & 6.21. This indicates these predictions may not be representative of the aggregate response.

In Figures. 6.16, 6.18 & 6.20, for 0° strains the prismatic planes exhibit more hardening compared to the pyramidal plane at RT and 150°C. This is true for both RD and TD cases, and for all alloys. The trends displayed in the RD and TD cases are similar. At RT, ZXK (Fig. 6.20) shows a considerable change in lattice strain behaviour between loading directions. A distinct increase in the 0°lattice strain around 0.075 strain on the $11\bar{2}0$ plane. This corresponds to a change in volume fraction, however, this value is relatively consistent in all temperatures.

The predicted lattice strains trends are consistent between the alloys, with the prismatic planes experiencing larger lattice strains than the second order pyramidal with

little difference between the prismatic planes. Comparing 150°C condition between alloys, prismatic planes on AZ31 exhibit the largest increase in lattice strains.

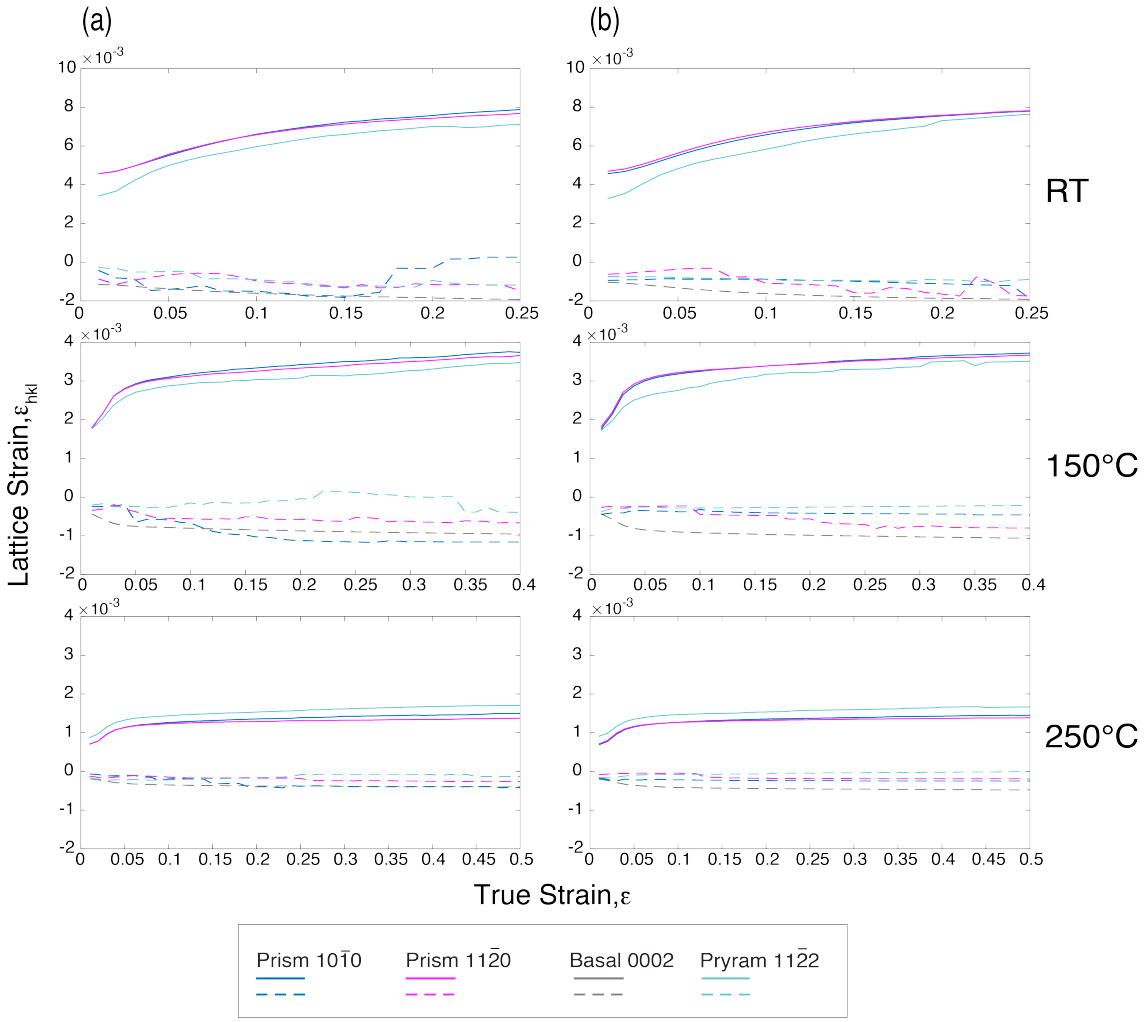


Figure 6.16: AZ31 - Lattice strain predictions for deformation at at RT and elevated temperatures, plotted against true strain. With respect to the (a) RD case or (b) TD case. Solid lines represent lattice strains evolving parallel to the loading axis, dashed lines are 90°to the loading axis.

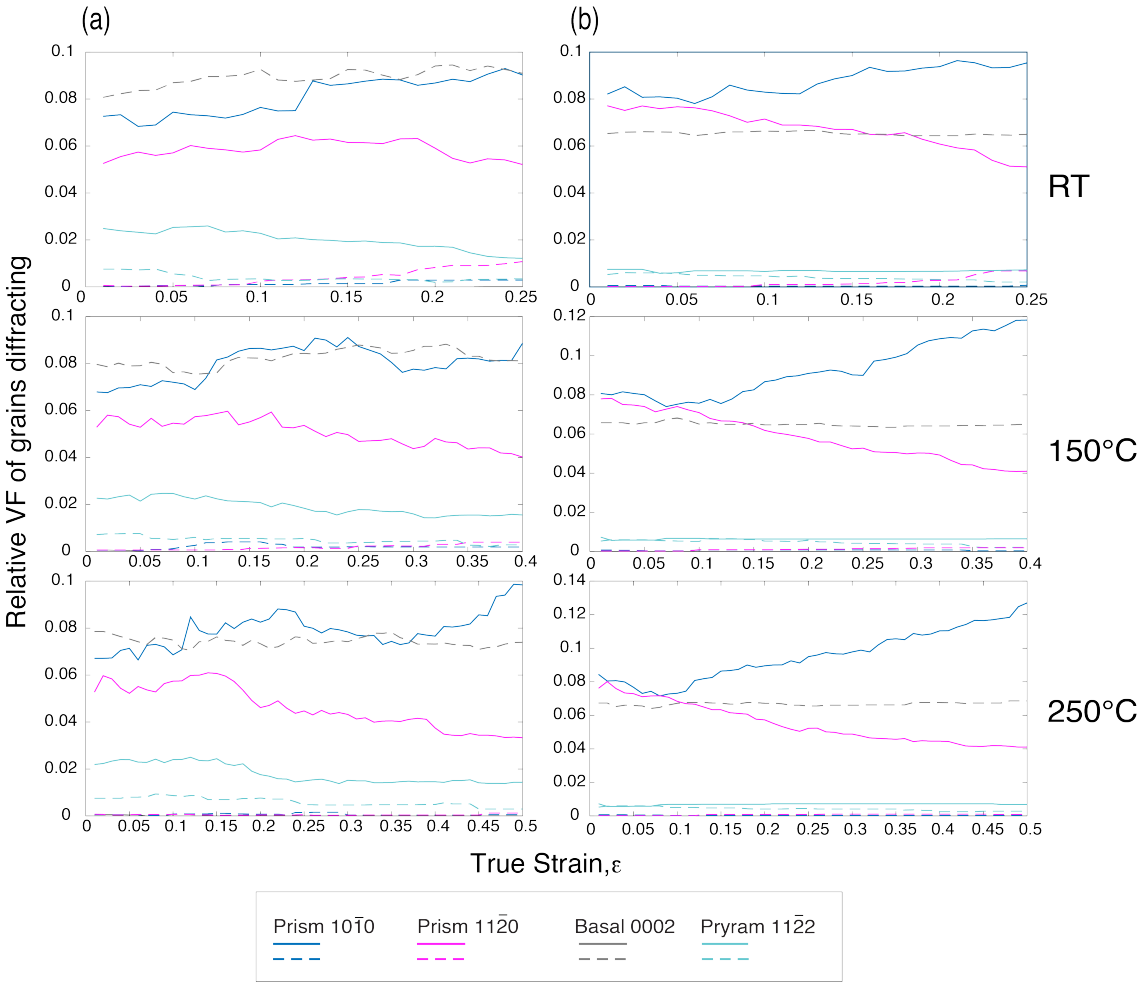


Figure 6.17: AZ31 - Relative volume fraction of grains contributing to the lattice strain predictions in Figure6.16. With respect to the (a) RD case or (b) TD case. Solid lines represent lattice strains evolving parallel to the loading axis, dashed lines are 90°to the loading axis.

6.4 Discussion

6.4.1 Dislocation interactions and Drag stress

This aspect of the study attempted to produce a single set of dislocation density hardening parameters for each alloy to predict the stress-strain behaviour at various temperatures. The interaction parameter χ_{for} and drag stress D^s values were initially kept constant. However, through many iterations it became obvious this was not feasible. The calculated stresses for the evolution of flow stress were overestimated and the hardening

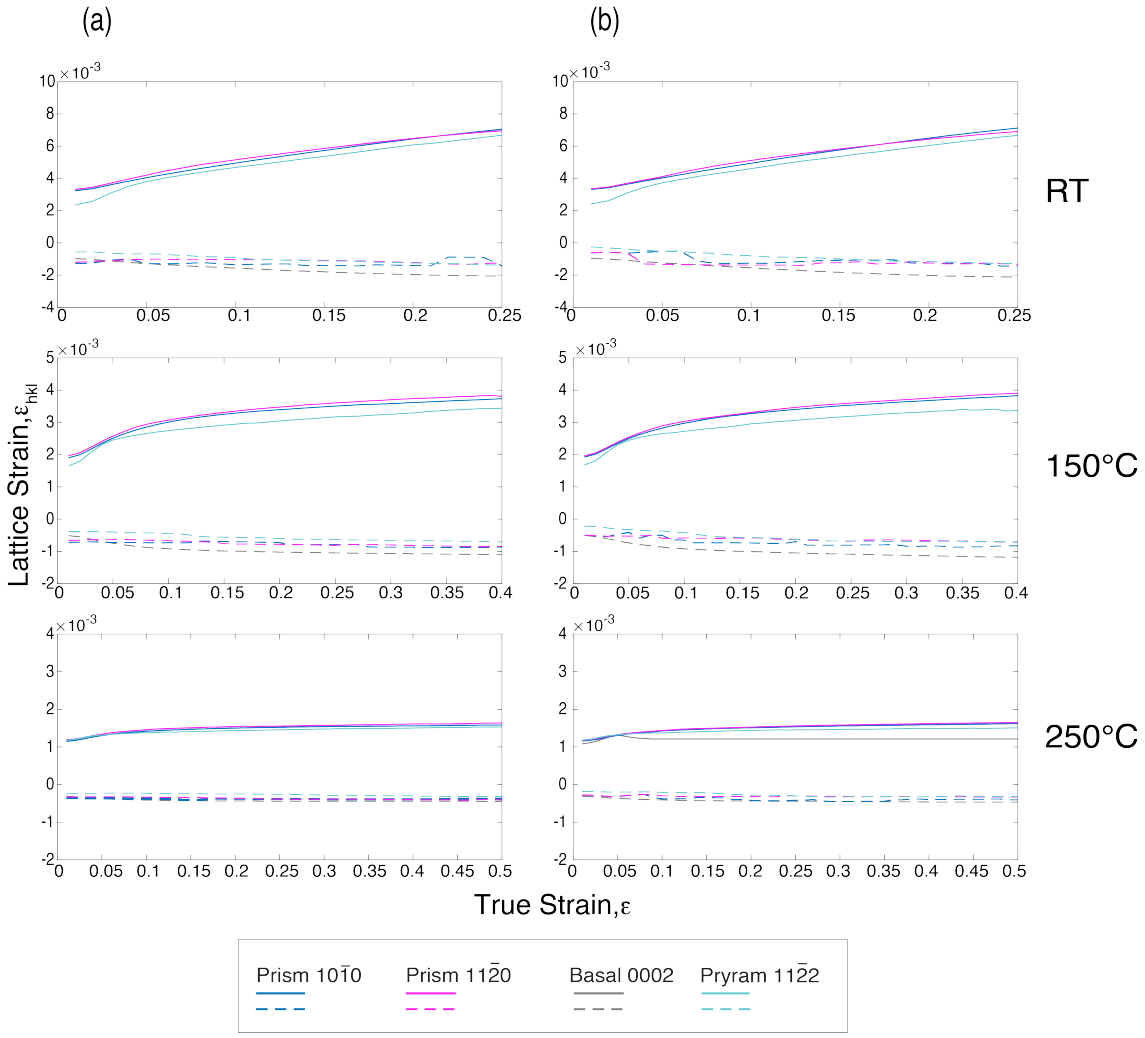


Figure 6.18: AZX - Lattice strain predictions for deformation at RT and elevated temperatures, plotted against true strain. With respect to the (a) RD case or (b) TD case. Solid lines represent lattice strains evolving parallel to the loading axis, dashed lines are 90°to the loading axis.

rate continued to grow beyond strains that were experimentally measured. Equation 6.40 for the slip resistance (τ^s_{for}) due to forest dislocations shows the relationship between χ_{for} and forest dislocation densities in the corresponding slip mode. With increasing strain, ρ_{for} tends to increase. In combination with χ_{for}, the interaction between dislocations on slip systems grows, forming greater barriers for further dislocation movement, requiring larger shear stresses and further increasing the flow stress [77, 5, 173]. The experimental curves at higher temperatures were better simulated with lower values of χ_{for}, listed in Table 6.7. With lower values of χ_{for} there is a weaker interaction alongside

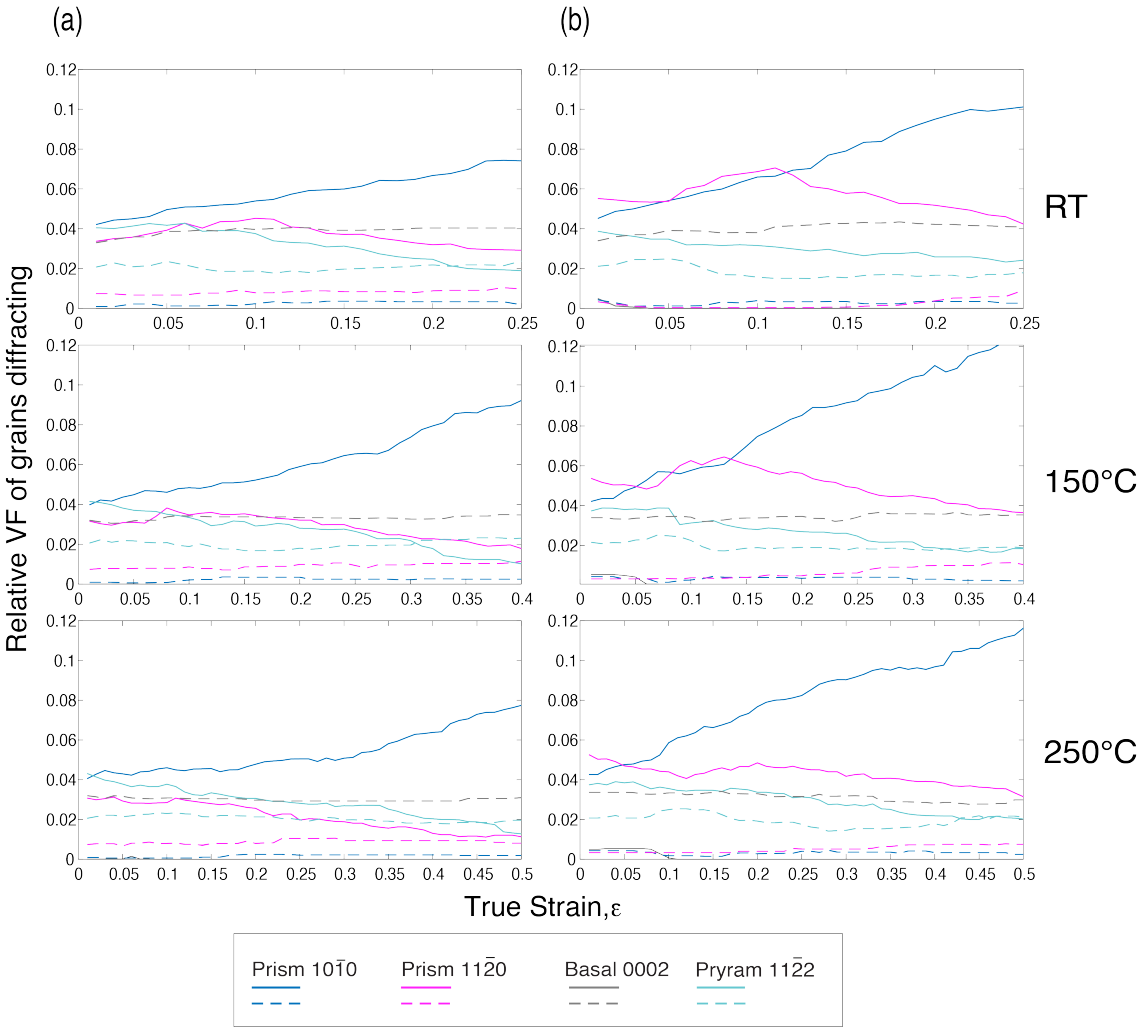


Figure 6.19: AZX- Relative volume fraction of grains contributing to the lattice strain predictions in Figure6.18 With respect to the (a) RD case or (b) TD case. Solid lines represent lattice strains evolving parallel to the loading axis, dashed lines are 90°to the loading axis.

an increasing dislocation mobility, aiding slip. The reduction in χ_{for} from 150-250°C is greater than the initial 25-150°C temperature change, suggesting the sensitivity to thermally activated mechanisms for overcoming dislocation interactions is greater at higher temperatures. This result corroborates observations shown by others [96]. To simulate deformation at intermediate temperatures and temperatures outside of the current experiment, it would be necessary to set this parameter to be a temperature dependant function. However, it anticipated that accurate characterisation of this parameter would require modelling at smaller length scales.

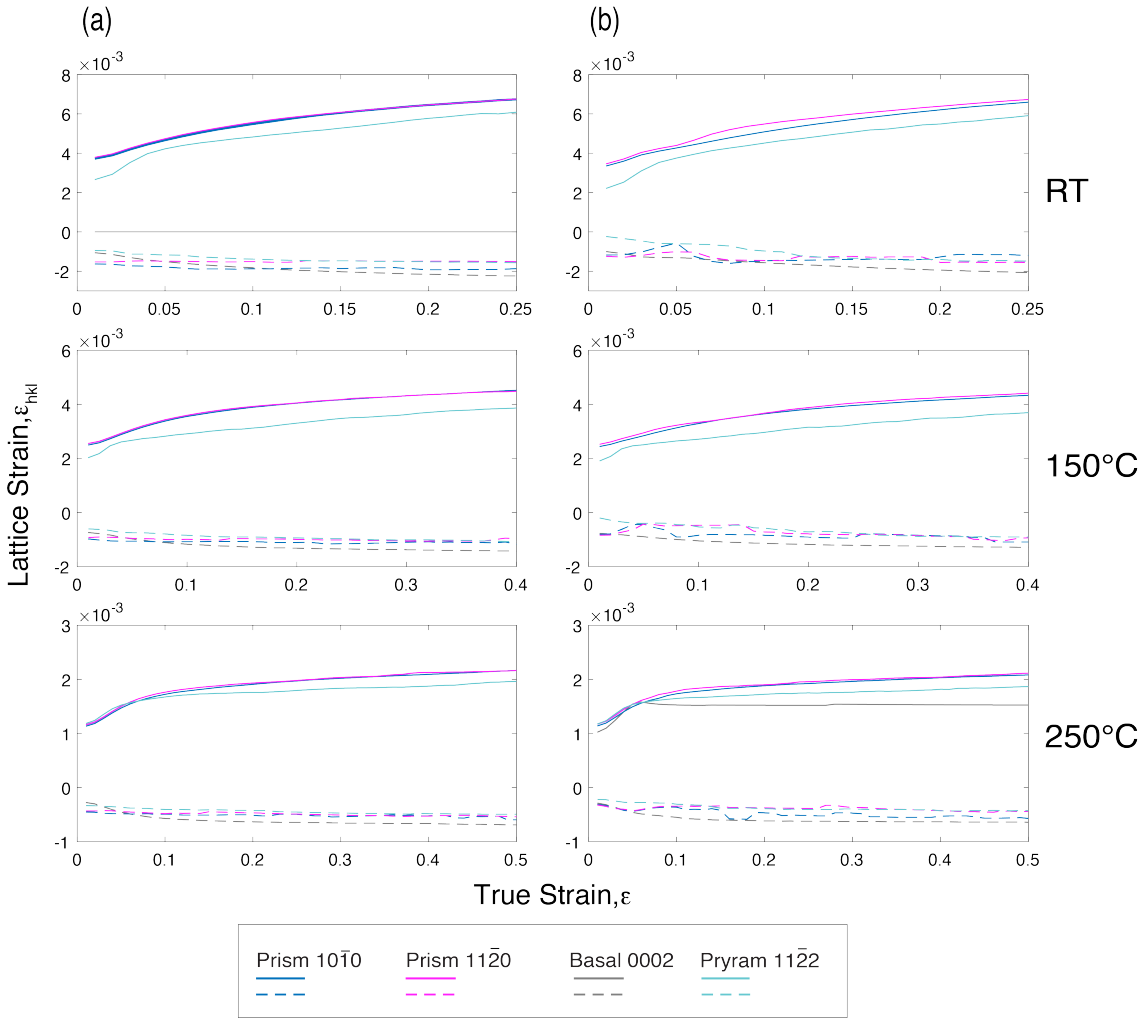


Figure 6.20: ZXK - Lattice strain predictions for deformation at at RT and elevated temperatures, plotted against true strain. With respect to the (a) RD case or (b) TD case. Solid lines represent lattice strains evolving parallel to the loading axis, dashed lines are 90°to the loading axis.

The dislocation interaction parameter used in this study is a simplification of a version used in previous work [96, 5, 169], where $\tau^s_{for} = \mu^s b^s \sqrt{\chi^{\alpha\prime\alpha} \rho^{s'}_{for}}$ is based on suggestions made in [80]. The interaction parameter, mathematically, is a matrix that couples the dislocation densities of all modes, This interaction parameter captures the effects of interactions between dislocations of different types clearly present in our alloys at elevated temperatures.

Another factor influencing the modelled calculation of flow stress at higher temperatures is the temperature dependence of dislocation density evolution. Equation 6.38

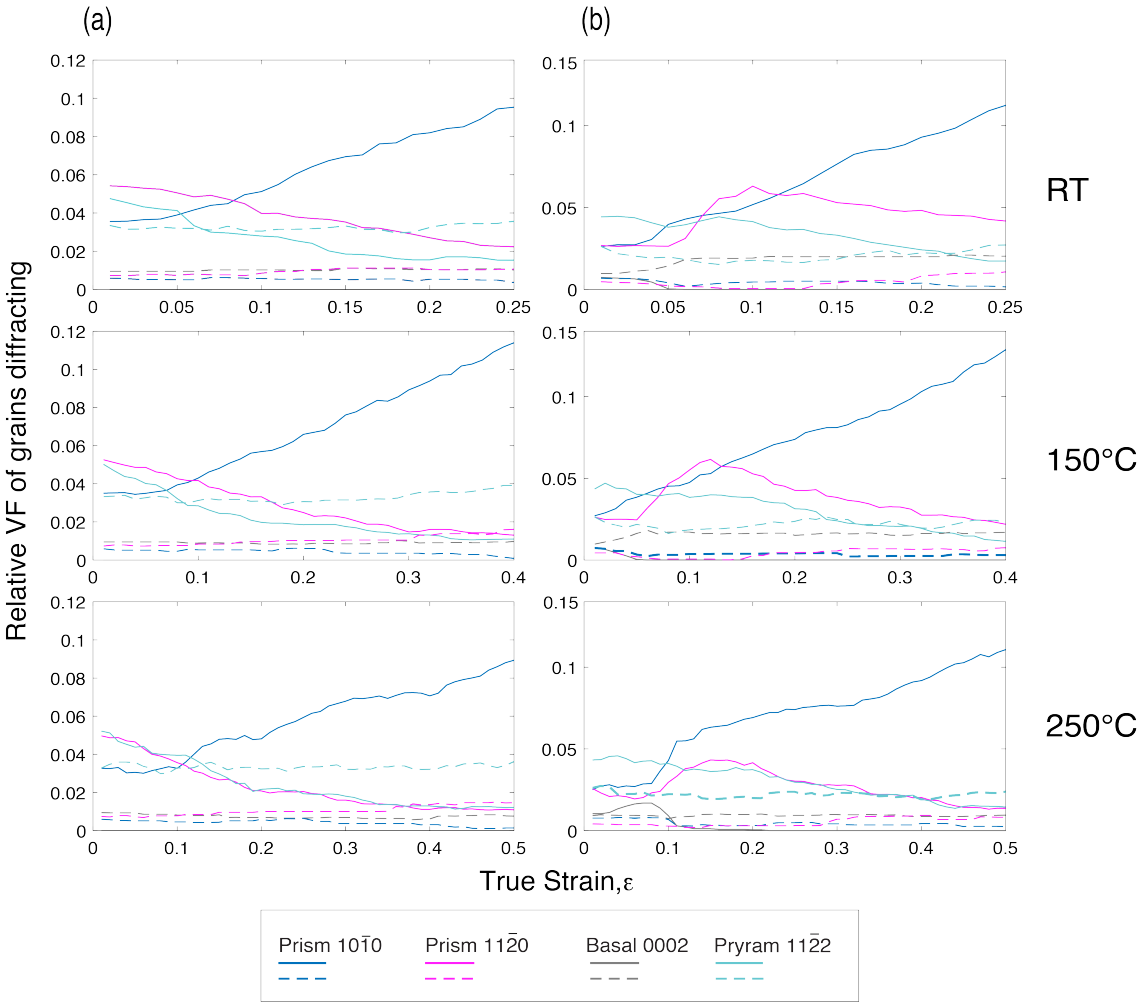


Figure 6.21: ZXK- Relative volume fraction of grains contributing to the lattice strain predictions in Figure6.20 With respect to the (a) RD case or (b) TD case. Solid lines represent lattice strains evolving parallel to the loading axis, dashed lines are 90°to the loading axis.

describes this evolution as the competition between k_1 and k_2, a storage/recovery ratio for each slip mode, calculated per grain. Larger k_2 values result in a lower rate of ρ^s_{for} development. As deformation proceeds it contributes to a decrease in flow stress in the latter stages of the stress-strain curve [80]. At higher temperatures, Equation 6.39 shows the temperature dependence of k_2. This dependence was insufficient. The drag stress is responsible for opposing dislocation motion, reducing it significantly and influences k_2. This accelerates the rate at which dislocation annihilation over their generation and storage [78]. At elevated temperatures, there are lower levels of twinning as slip dependence grows, owing more importance to the drag stress parameter. Varying this parameter

for individual slip modes gave the model more flexibility at higher temperatures. The flow stress behaviour was influenced via altering the drag stress for the most active slip mode or with the steepest gradient of ρ^s_{for} evolution. The exponential relationship of drag stress with temperature was clear, however, the exact relationship on individual slip modes would be difficult to assess between alloys. The reduction in drag stress was coupled to the value of k_1 and the activity of the slip system.

6.4.2 Active deformation modes & Texture

By varying the initial τ_{CRSS} for the available deformation modes, we iterated through various τ_{CRSS} ranges to achieve relatively accurate predictions for the initial flow stress behaviour for all samples. Established τ_{CRSS} trends for the deformation modes based on previous polycrystal simulations for similar alloys worked as a base [174, 81, 175, 96]. The ratios of non-basal/basal τ_{CRSS} obtained aligned reasonably well with ratios reported by [152]: $CRSS_{Prism}/CRSS_{basal} = 2-4$, $CRSS_{Pyram}/CRSS_{Basal} = 3.4-5.3$ and $CRSS_{twinning}/CRSS_{basal} = 1.2-2.5$. The largest deviations were seen from the values obtained for AZ31, a lower τ_{CRSS} for basal and a larger τ_{CRSS} for pyramidal slip and compression twinning resulted in higher ratios at RT. τ_{CRSS} ratios have been considered important when simulating anisotropy sensitive parameters such as r-values [25, 97].

Comparing the slip system activity with reported results provides a good measurement of the relative success of the predictions calculated here. However, differences in sample dimensions, grain size, texture and mechanical loading rigs used can add deviations in the comparisons. Tam et al 2020 [96] used a DD model for AZ31 in the TD case at temperatures similar to those used here. At RT their trend in slip system activity trends more to the predicted AZX behaviour shown here. Basal slip was the dominant mechanism followed by prismatic. The overall contribution between prismatic and basal was $\approx 50/50$. In contrast our predictions for the TD case were heavily prismatic dom-

inant. The τ_{CRSS} value for prismatic slip used in our simulation is $\approx 40\%$ lower, this could explain the difference. However, qualitatively comparing the fits there is not a discernible difference in accuracy. The most notable difference at elevated temperatures was the persistence of prismatic slip after activation of pyramidal slip. The predictions of the authors exhibited a large reduction in prismatic slip at elevated temperatures beginning at 100°C. In the RD case our slip activity is in better agreement with more basal contribution. Predictions in other work corroborate the prediction of more basal slip than predicted in this study for AZ31 [107, 6]. Due to the difficulty of finding relevant studies investigating the same deformation conditions, it would be necessary to apply alternate deformation conditions to our material parameters and compare the result with the literature to obtain a better view of the parameters for AZ31.

Studies for alloy compositions nearing AZX and ZXK [107, 6, 109, 108, 176] reflect the slip activity predicted. Larger basal activity to initiate deformation. For AZX at room temperature the τ_{CRSS} value for prismatic slip was lower than predicted for AZ31 and ZXK, without a significantly larger fraction of prismatic slip, this suggests the initial texture for AZX prompts a lower τ_{CRSS} for prismatic slip to achieve similar activities. Pyramidal activity increased more at elevated temperatures in AZX and ZXK compared to AZ31. However, pyramidal activity may be insufficiently modelled here, this could have been an artefact of the choice for k_1 being too large for the pyramidal slip systems. The burgers vector of pyramidal slip is considerably larger than prismatic and basal slip, generating higher slip resistance on the pyramidal system wtih dislocation density [5], forcing a reduction in its activity. The τ_{CRSS} values are updated at every strain increment with the developing dislocation densities, the competition between k_1 and k_2 is very influential on the relative activity after early deformation. More probing into research on dislocation density evolution on individual slip systems may aid the choice of this value. The model clearly predicts that deformation mode activity rests on texture as well as the initial τ_{CRSS}. The ZXK alloy showed a significant increase in twinning

behaviour at room temperature loading in the TD case compared to RD.

The model predictions provide an insight to how uni-axial deformation is accommodated in the different alloys. The Ca-containing alloys undergo a larger share of basal slip at RT compared to AZ31. Despite a higher CRSS for compression twinning compared to ZXK, AZ31 and AZX exhibit more compression twinning at RT to accommodate a small fraction of shear in the latter stages of deformation. Compression twinning has been observed in AZ31 simulations accompanied by experimental evidence [106]. This evidence aligns with observations of the failure mechanisms for magnesium alloys sheets, compression twin activity is associated with voids observed near fracture surfaces [177]; a possible explanation for the improved formability of ZXK alloys at low temperatures[20]. The larger spread and split of the basal peaks in the (0002) pole figure for initial ZXK texture gives a larger fraction of grains preferential orientated for basal slip and twinning. Loading in the TD case further increases tensile twinning and basal slip [176], leading to the characteristic difference in flow stress [21].

The competition between twinning and pyramidal slip to accommodate $\langle \mathrm{c} \rangle$ axis deformation can be seen at 250°C for ZXK in the TD case. At saturation of twinning the shear accommodated by pyramidal slip stops declining and remains constant.

The evolution of a 6-fold symmetry in the prismatic pole figure shown in Figure 6.13 is common in Mg texture studies for samples with strong strong basal textures like AZ31[25, 101, 178, 179, 180]. The symmetric poles in the prismatic pole figures are not as uniform for the AZX and ZXK alloys, their is a greater spread of prismatic poles towards the z axis of the pole figure. For AZX and ZXK (Figures. 6.14-6.15) the initial prismatic pole figure exhibits symmetric intensities either side of the RD or TD parallel to these directions. The AZX alloy forms a similar 6-fold symmetry to AZ31 compared to ZXK, with a closer starting texture. Both cases for ZXK exhibit a more complex evolution. The pole figure predictions for AZ31 in Fig. 6.13 showed very little variability

with increasing temperature and direction compared to the Ca-containing alloys. An extensive study of mechanical properties by Khan *et al.* [178] for AZ31 found post deformation textures that mirror our predictions at RT and 150°C for the RD case. The macroscopic tensile curves for AZ31 in RD and TD are relatively similar, therefore similarities in the texture evolution would be expected.

The predictions reinforce that increased ductility and lower flow stress seen at elevated temperatures are due to an increase in the number of slip system active at the beginning of deformation, a reduction in the strength of dislocation interactions and overall increase in dislocation recovery mechanisms compared to dislocation storage.

Important to note that pyramidal activity was considered to be inactive at room temperature for these simulations, there is evidence of pyramidal slip at room temperature for Mg alloys [51], this would likely have altered the predicted activities, experimental examination of slip traces and TEM work would be beneficial in elucidating the strength of pyramidal activity at room temperature.

Chapter 7

Discussion

In chapter 4 the results in Fig. 4.9 strongly suggested the macroscopic behaviour observed is determined by a complex balance of load sharing between the different deformation modes available, depending on the spread of crystallographic grain orientations and the hardness of each slip mode. The ranking of lattice strain accumulation across families of planes from commonly orientated grains was found to vary considerably more with loading direction for the Ca-containing alloys. It is confirmed that the strong basal texture of the AZ31 alloy provides less freedom or choice for load sharing across different deformation modes, incorporating twinning and slip. It was inferred that the difference in twinning for the ZXK alloy between loading in the RD and TD was significant, based on the observation of inflections in the (0002) basal plane transverse lattice strain behaviour. From this inflection it was inferred that the AZX alloy experienced twinning in the RD and TD, with less twinning in the RD showed from a less pronounced inflection.

The weak basal texture and split basal poles observed for AZX and ZXK alloys, led to more complex interactions between deformation modes, with twinning playing a greater role in accommodating strain during early plastic deformation. The reduced directional anisotropy at elevated temperatures shows the direct link between twinning-

induced microstructural changes and the observed decrease in yield anisotropy. The role of Ca in texture modification is generally attributed to two mechanisms. In no particular order, first, Ca has a strong tendency to segregate to grain boundaries during processing [181, 7, 117]. This segregation influences recrystallisation kinetics by solute interactions, retarding the preferential growth of grains with the c-axis parallel to the sheet normal. Second, studies show that Ca promotes non-basal slip during deformation (e.g., rolling before annealing), increasing non-basal activity and twinning, which tilts basal poles away from the sheet normal. This texture weakening is further enhanced after heat treatment via the first mechanism. An investigation by Yuasa et al. [182] on the addition of Group II elements in the Mg-Zn system found that Ca most effectively reduced basal texture intensity. After rolling, basal poles tilted toward the TD, an effect further amplified by annealing; unique to addition of Ca compared to the other Group II elements. We observed the same tilt in the pole figure for the ZXK alloy (Fig. 4.3). It was suggested that changes in the unstable stacking fault energy ratio of non-basal slip to basal slip promotes the increased non-basal slip. The argument for Ca solutes driving texture weakening reinforced when considering the effect of Al addition. Al is critical for solid solution strengthening and castability (widens the freezing range [1]) in Mg alloys. However, studies by Delis et al., [117] & Jo et al., [116] revealed that higher Al content preserves basal textures in Ca-containing alloys. This occurs because Al reduces the Ca concentration in solid solution via precipitation of secondary phases with Ca due to their strong affinity to form intermetallics. These studies confirm that Al_2Ca formation is preferred when the Al amount is greater than 2 wt.% and Ca content is above its solid solution limit in Mg (0.11 wt.%), conditions met with AZX. Consequently, the AZX alloy exhibited a stronger initial basal texture than ZXK, along with Al-Ca intermetallics, suggesting less solute Ca was available to disrupt texture during recrystallisation.

Reports of Al-driven twin suppression in Mg alloys [56, 183, 161] show some correlation with the twin volume fraction results in Fig. 7.1, particularly in the TD, where

twin volume fraction follows and Al content are AZ31(Al 3 wt.%) $<$ AZX(Al 2.3 wt.%) $<$ ZXK (Al 0 wt.%). However, the VPSC predictions for the CRSS (Fig. 6.5) do not indicate an increased CRSS for twinning in AZ31 and AZX compared to ZXK. Instead, the VPSC predicted higher twinning CRSS for Ca-containing alloys than AZ31, yet more twinning in AZ31 and AZX compared to ZXK when loading in the RD. These predictions, alongside experimental observations suggest that twinning behaviour here was primarily governed by the degree of basal texture weakening and the direction of the basal pole tilt (Figs. 4.2 & 4.3). While the influence of Al solutes on twinning cannot be dismissed, its effect here is better explained indirectly; through its reduction of Ca-induced basal texture weakening. The larger twin volume fraction in the TD versus RD for both Ca-prototype alloys supports this texture driven effect. For ZXK, the difference was pronounced in EBSD and VPSC predictions: the TD-split basal poles and more intense TD spread meant more grains were oriented with their c-axis aligned with the TD compared to AZX, where the TD spread had lower intensity. The Schmid factor calculations shown in Fig. 5.11 strongly confirmed the dependence of twinning on the grain orientation with respect to the loading direction for these alloys. The average Schmid factor for twinning in the ZXK alloy correlates with the subsequent volume fraction measurements shown in Fig. 7.1, this further reinforces the texture dependence of twin activation. The twin volume fraction calculations align with the inflections in the lattice strain observations for AZX and ZXK, and the lack there of for AZ31 in both directions and ZXK in the RD. The sigmoidal flow stress in the macroscopic tensile curves, inflections in the lattice strains and twin volume fraction from the EBSD measurements all corroborate the twinning on influence on the mechanical behaviour.

It could be argued that the difference in average tensile twin Schmid factor between AZX and ZXK alloys for loading parallel to TD was not significant enough for double the volume fraction to be present in the ZXK alloy. Assuming the average Schmid factor is representative of the microstructure, the difference in lattice strain behaviour between the

alloys loaded in the TD may provide some insights for further investigation. The tensile lattice strains were very similar, however, the distribution of transverse lattice strains showed higher magnitudes of lattice strains on the $(10\bar{1}0)$ prismatic plane through out deformation.

The observed strain rate and temperature dependence of the serrated behaviour at elevated temperatures strongly correlated with DSA [128, 184, 185]. At 150°C, thermal energy was insufficient for rapid solute diffusion, even at slower strain rates. Solute atmospheres could not form effectively to consistently pin dislocations. At 250°C, increased thermal energy enhanced solute mobility. However, at a strain rate of 10^{-3}s^{-1}, dislocation velocities may still be too quick for the solute diffusion mechanism, reducing effective pinning and serration amplitude. Only at 250°C and 10^{-3}s^{-1} did the timescale for dislocation motion and solute migration result in pronounced serrations for AZ31 and ZXK. For AZX, the suspected DSA behaviour at elevated temperatures appears further influenced by the Al-Ca second-phase formation, which removes Al & Ca from solid solution. This weakened the DSA effect compared to AZ31 and ZXK, observations here strongly suggested Ca solutes contributed to DSA in ZXK, while Al dominates for AZ31.

The SRS for ZXK and AZX was greater at room temperature compared to AZ31 (Fig. 4.16 indicating the modified basal texture made them less prone to localised deformation and failure. The off-basal texture is reported to provide increased Schmid factors for basal and non-basal slip compared to the strong basal texture (AZ31) that facilitates unfavourable 'hard' orientations. EBSD analysis revealed higher Schmid factors for basal slip in the Ca-containing alloys, however, did not agree with an obvious increase in non-basal Schmid factors. The choice for scaling of the Schmid factor analysis could be speculated as the probable cause and analysis of the raw Schmid factors could provide a better correlation. Regardless, VPSC predictions for slip activity showed the Ca-containing alloys underwent significantly more basal slip with prismatic slip while the AZ31 alloy primarily relied on prismatic slip. With less easy basal slip and higher

stresses required for dislocation glide on prismatic planes AZ31 could suggest it was more susceptible to stress concentrations.

Validating VPSC predictions with experimental micro-mechanical behaviour

The combination of these experiments and analysis was less adequate in assessing the influence of the weakened textures on slip system activation and contribution to deformation. This is especially true at elevated temperatures where pyramidal $\langle c+a \rangle$ slip is reported to increase significantly. The Viscoplastic Self-Consistent (VPSC) crystal plasticity model was identified as a promising tool to obtain this information without further experimental work. The capability of the model to capture the evolution of texture and slip system activity in anisotropic HCP polycrystals prone to twinning, suited the alloys in this investigation.

The VPSC model calibrated with the macroscopic tensile curves aligned well with published data for the Ca-containing alloys, specifically how basal and prismatic slip activity evolve during deformation. Additionally, the prediction for twin activity in Ca-containing alloys compared to AZ31 and depending on the loading direction shown in Fig. 6.12 aligned well with EBSD analysis.

Interesting work by Kadiri et al [186], showed the absorption of basal dislocations at $(10\bar{1}2)$ twin boundaries enabling the profuse growth of twins, effectively describing twins as a sink for basal dislocations. Chapter 5 corroborated these findings for grains that twinned; combining this with the predictions from the VPSC model in Chapter 6 showing a larger activity of basal slip in TD loading for ZXK at room temperature in comparison with the AZX alloy. The larger volume fraction measured in the ZXK alloys could be influenced by more basal dislocations to drive $10\bar{1}2$ growth.

To validate the accuracy of the twin statistics obtained using the predominant twin

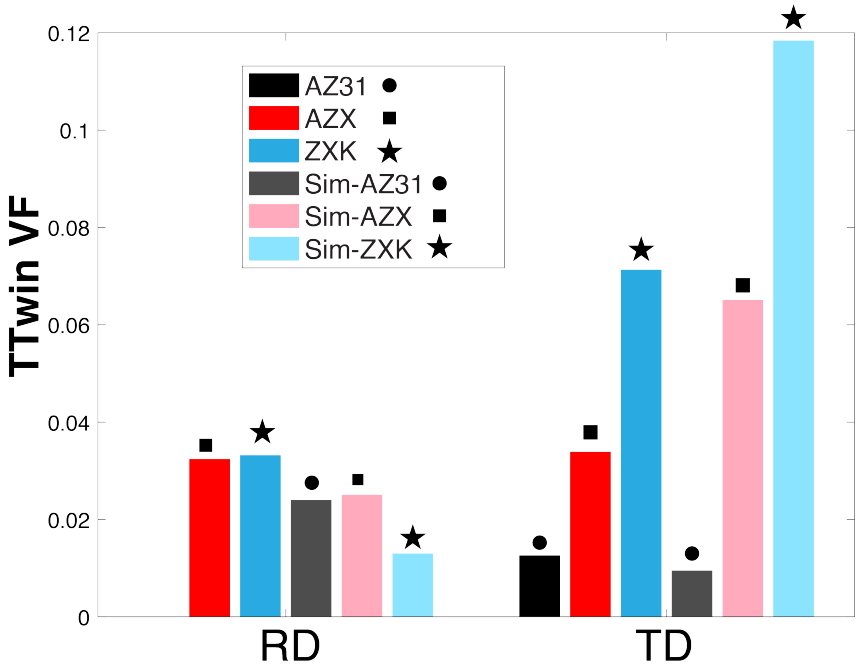


Figure 7.1: Comparison of the tension twin volume fractions calculated from In-situ EBSD samples post-experiment and predictions from the VPSC model.

reorientation (PTR) twinning model, Fig. 7.1 compares the measured twin volume fraction for tensile twins from Chapter 5 with the predictions from Chapter 6. Notably, the predictions in the TD direction align well with the trends from the measured data. However, the predictions are significantly over estimated. The RD predictions have a weaker correlation but the magnitudes closer to the measured data. Considering the lower estimates in the RD and larger estimates in the TD, a simple adjustment of the threshold values for reorientation would not converge the predictions towards a better estimation for either. The PTR model is relatively simple in comparison with more complex models employed in other studies [83, 187], many of which better capture the interaction between mobile dislocations and twin boundaries. The GND density interactions within twins and at twin boundaries in Chapter 5 indicate such interactions should be considered in more detail to accurately predict the twinning behaviour. The complete reorientation of grains by the PTR scheme is the likely source of the overestimations.

There were deviations in the slip activity predictions for AZ31 with published data,

suggesting that calibrating the model with macroscopic tensile curves may lead to a number of solutions in slip activity that cannot all hold true. However, there are numerous versions of the VPSC code and extensions of the hardening/twin models utilised in the code, as well as differences in the initial texture of AZ31 alloys studied, therefore, it becomes difficult to evaluate where errors may arise in the parameters used for the model. A more robust test of the calibration is displayed in Fig. 7.2. Predictions of lattice strains are compared to the X-ray diffraction measurements in Chapter 4 for similar planes. The model has captured the effects of texture, for example the (0002) basal plane lattice strain predictions align with the dominance of the transverse lattice strains from that plane, additionally the ranking of prismatic and pyramidal plane lattice strains is in reasonable agreement. However, the model does not accurately predict the distribution of the lattice strains, likely driven by the effect of residual stresses within the material that are not captured by the VPSC model. An anecdotal method to mirror this may come from increasing the starting dislocation density on the specified planes, this was kept as standard. Consequently, this would likely influence the predictions of the macroscopic curves. Therefore, calibration of the model and parameter optimisation initially using experimental lattice strain observations from Chapter 4 could provide more robust predictions, Results from this feature of the model are seldom reported, modelling of lattice strains is typically performed with Elasto-plastic or Elastic viscoplastic self consistent models [188, 189, 190], these models are designed for predicting the elastic portion of deformation.

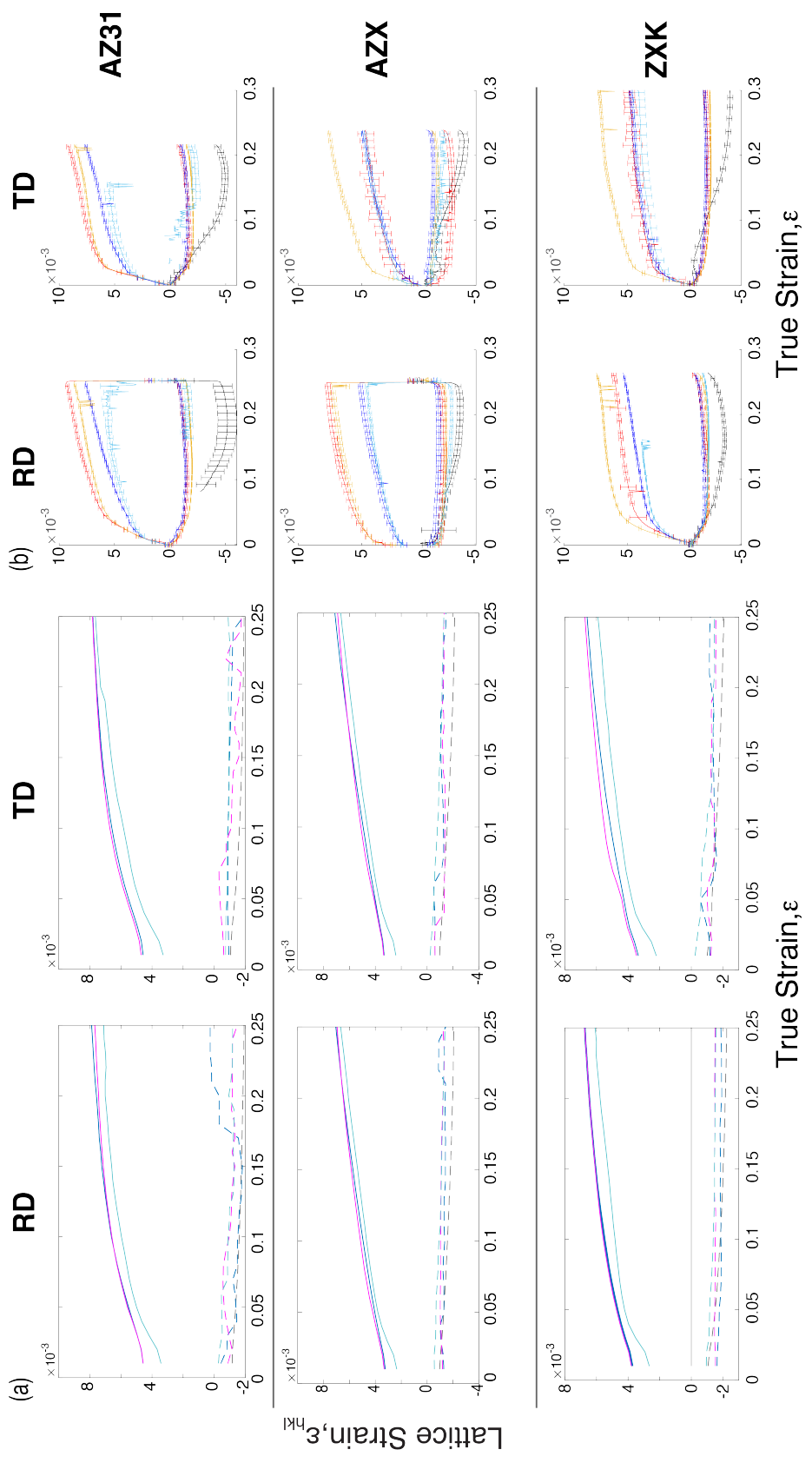


Figure 7.2: Comparison of lattice strains from (a) predictions from the VPSC model, and (b) calculated In-situ with X-ray synchrotron.

The choice of alloys, commercial AZ31 (Mg-Al-Zn) alongside two Ca-containing variants (ZXK: Mg-Zn-Ca and AZX: Mg-Al-Zn-Ca) was motivated by the need to investigate the interplay between Ca addition and texture evolution. While the presence of Al in AZX complicates the isolation of Ca's individual effects, the pronounced differences in initial textures provided a unique opportunity to explore how distinct texture configurations from Ca addition influence deformation mechanisms, particularly twinning and anisotropy. The inclusion of AZ31 as a benchmark further allowed comparisons to conventional Mg-Al-Zn alloys, highlighting the role of Ca in modifying recrystallization behaviour and slip/twinning activity.

Chapter 8

Conclusions and future work

This work aimed to gain insight into the micromechanical changes in Ca-containing magnesium alloys with mechanical properties that are distinctively different compared to a commercial AZ31 alloy. This addition of Ca to magnesium alloys are known to produce wrought texture weakened microstructures, previously achieved with the addition of rare earth elements. However, more detailed explanations, particularly at the grain and mesoscale have seldom been explored. Given that texture weakened magnesium alloys are known to improve the low temperature formability of Mg sheet alloys, understanding the governing micromechanic is considered extremely important for mocrostructure control of existing alloys and to guide the design of future alloys. To achieve this, experiments coupled with modelling provide insights during plastic deformation based on (1) the grain average response, (2) per-grain behaviour, and (3) the intragranular response.

The following key conclusions from the work can be drawn:

1. The significance of strain rate sensitivity has been emphasised by; the correlation of detrimental formability for ZXK reported at warm temperatures with a significantly reduced SRS measured here at 150°C; and, a higher SRS for AZX than AZ31 at

the same temperature aligning with the improved formability reported for a similar AZX series alloy directly compared to AZ31.

2. Twinning behaviour in the ZXK alloy exhibited significant anisotropy between the RD and TD loading directions, as observed through yield behaviour and work hardening differences. The twinning behaviour strongly correlated with c-axis alignment relative to the loading direction and nucleation followed local stress concentrations at grain boundaries.

3. The Ca-containing alloys modified texture led to the prediction of both basal and prismatic slip being accumulated during the early stages of deformation in the elastic-plastic transition. The modelled predictions are corroborated by lattice strain measurements where their distribution shows greater variation compared to AZ31, indicative that dislocation accumulation is comparably more homogeneous.

4. DSA signatures (serrated flow) at 250°C were solute-dependent. AZ31 was dominated by Al, the absence of Al in ZXK supports Ca solutes mediating dislocation pinning, weak serration magnitudes in AZX and evidence of Al-Ca precipitation points towards reduced solute availability for effective DSA.

5. VPSC predictions at elevated temperatures (250°), showed the activation of pyramidal $\langle$c+a$\rangle$ slip in the Ca-containing alloys was higher compared to AZ31. The CRSS predictions for pyramidal $\langle$c+a$\rangle$ were relatively equal between 150-250°C. The resulting difference in pyramidal $\langle$c+a$\rangle$ is expected to be governed by the initial texture. Enhanced ductility at elevated temperatures was linked to an increase in pyramidal slip activity, the improvement in accommodating deformation along the $\langle$c$\rangle$ axis via slip reduced the necessity for twinning, especially in the ZXK alloy along the TD where twinning at RT was profuse.

The predictions of twinning using the VPSC model could be improved to develop more accurate twin statistics and subsequent texture evolution. To achieve this, a twin model

that treats the grain reorientation more conservatively, such as the composite grain model [83] could be implemented. In addition, the model accounts for the directional barrier effect of twins on slip in planes intersecting a twin boundary, by giving the predominant twin within a grain a twin plane with a specific orientation with respect to other active slip and twin planes.

There is also scope to provide improved hardening laws between the alloys predicted by the VPSC. This includes

1. Expanding the VPSC study to fit data from the available lattice strains across temperature ranges.

2. Using a EVPSC model with measured lattice strains to better predict the elastic behaviour, which can then be better compared to the predicted CRSS and slip activity [36, 188].

3. Performing texture measurements on deformed samples at interrupted strains, varying temperatures and strain rates will provide a more robust dataset to calibrate the model by capturing texture components arising from specific deformation modes. This will build on complementary studies in the literature[98, 97, 180].

In-situ testing at elevated temperatures was conducted with high energy X-ray diffraction to probe lattice strain development and flow stress behaviour, comparing RT and high temperature conditions. This approach revealed distinct differences in SRS and rate dependent dynamic strain ageing. However, in-situ HR-EBSD was limited to RT. Extending the HR-EBSD to high temperatures would enable direct comparisons for GND density and stress evolution across a temperature range that promotes increased non-basal slip (e.g., pyramidal $\langle c + a \rangle$) and reduced twinning activity. Furthermore, investigating localised mechanisms such as dynamic recrystallisation (both static and continuos) and

grain boundary sliding would provide more comprehensive insights into the high temperature behaviour.

Forming relevant testing to assess the behaviour of the Ca-containing alloys under complex loading conditions relevant to automotive forming conditions would be extremely valuable. By building on the modelling parameters established in this work and extending the model for multi-axial deformation [123, 191]. Additionally, extracting formability relevant parameters such as the 'r' parameter for plastic anisotropy from the explored and additional loading directions, as well as strain hardening, using the calibrated hardening parameters [25]. This will facilitate a complete simple analysis of formability.

Further analysis on grain misorientation and GND distribution for the HR-EBSD data on the RD samples may reveal more on the relationships between soft and hard grains. Adding slip trace analysis to the HR-EBSD measured lattice rotations and plane specific GND density within grains. Will aid in revealing the true experimental difference in slip system activity between the alloys and provide more proof for the VPSC model.

In-situ analysis with EBSD is limited low strain ranges ($< 10\%$). One method to extend the strain range of in-situ orientation analysis could be achieved by developing a polarised light set up to work in-situ. This will enable the broad testing of Ca-containing alloys to capture the c-axis dependent texture evolution and twinning influence at strains beyond in-situ EBSD diffraction limits for these alloys [192, 193].

Exploring the use of other modelling tools such as DFT [56, 194, 182] to understand the intrinsic effect of Ca additions on the behaviour of Mg alloys. First principle calculations of Ca additions typically describe a lowering of stacking fault energies (compared to pure Mg) leading to lower activation stresses for non-basal slip associated dislocation mobility, influencing ductility.

8.1 Table of Symbols and definitions

Symbol	Definition	Equation/Context
n^{eff}	Linearization adjustment parameter	In between Tangent/Secant approaches
τ^s	Total threshold stress for slip system s	Eq. 6.34
τ_0^s	Peierls friction + obstacle resistance	Temperature-dependent
τ_{for}^s	Forest dislocation resistance	Taylor law (Eq. 6.40)
τ_{sub}^s	Substructure dislocation resistance	Eq. 6.41
τ_{HP}^s	Hall-Petch grain boundary resistance	Grain size dependent
μ^s	Elastic shear modulus	Slip system dependent
b^s	Burgers vector magnitude	Slip system specific
d_g	Grain size	Hall-Petch term
ρ_{for}^s	Forest dislocation density	Evolves with strain (Eq. 6.38)
ρ_{sub}	Substructure dislocation density	Includes all systems
χ_{for}	Dislocation interaction coefficient	Typically < 1.0
χ_{sub}	Substructure interaction constant	Ensures Taylor law convergence
k_1^s	Dislocation storage coefficient	Rate-insensitive
k_2^s	Dynamic recovery coefficient	Temperature dependent (Eq. 6.39)
g^s	Normalized activation enthalpy	Thermal activation

Table 8.1: Important Symbols and Definitions from Chapter 6

Symbol	Definition	Equation/Context
D^s	Drag stress	Temperature dependent
q^s	Debris formation fraction	Substructure development
$F^s_{(T,\dot{\epsilon})}$	Substructure temperature/strain rate factor	Empirical function
τ^t	Twinning threshold stress	Nucleation + propagation
S^t	Characteristic twin shear	Volume fraction calculation
$v^{t,g}$	Twin volume fraction in grain g	$\gamma^{t,g}/S^t$
$V^{acc,tmode}$	Accumulated twin volume fraction	Weighted sum over grains
$V^{eff,tmode}$	Effective reoriented volume fraction	Tracking fully twinned grains
$\dot{\Omega}^{(g)}$	Crystal lattice rotation rate	Texture evolution

Table 8.2: Important Symbols and Definitions from Chapter 6 (Continued table 8.1...).

Symbol	Definition	Equation/Context
ε^{hkl}_{ψ}	Lattice strain for (hkl) reflection	Dimensionless
d^{hkl}_0	Reference d-spacing (pre-load)	nm
d^{hkl}_{ψ}	Measured d-spacing	nm
$\delta\varepsilon^{hkl}_{\psi}$	Lattice strain uncertainty	Dimensionless
ψ	Azimuthal sector angle	$36 \times 10^{\circ}$ sectors
m	Strain rate sensitivity index	Dimensionless
σ	Flow stress	MPa
$\dot{\epsilon}$	Strain rate	s^{-1}
σ_{VM}	von Mises stress	GPa
ρ_{GND}	Geometrically Necessary Dislocation Density	m^{-2}
ε	Strain	Dimensionless
Φ	Inclination angle	Between crystal c-axis & sheet ND

Table 8.3: Important Symbols and Definitions from Chapter 4 and 5.

Bibliography

[1] C. J. Bettles and M. Barnett, *Advances in wrought magnesium alloys: Fundamentals of processing, properties and applications*. Woodhead Publishing, 2012.

[2] D. Klaumünzer, J. V. Hernandez, S. Yi, D. Letzig, S. hyun Kim, J. J. Kim, M. H. Seo, and K. Ahn, "Magnesium process and alloy development for applications in the automotive industry," in *Minerals, Metals and Materials Series*, pp. 15–20, 2019.

[3] I. Polmear, D. S. John, J.-F. Nie, and M. Qian, *The Light Metals - Light Alloys*. Elsevier Ltd., 2017.

[4] I. J. Beyerlein and C. N. Tomé, "A probabilistic twin nucleation model for HCP polycrystalline metals," *Proceedings of the Royal Society A: Mathematical, Physical and Engineering Sciences*, vol. 466, pp. 2517–2544, 9 2010.

[5] M. Zecevic, M. Knezevic, B. McWilliams, and R. A. Lebensohn, "Modeling of the thermo-mechanical response and texture evolution of WE43 Mg alloy in the dynamic recrystallization regime using a viscoplastic self-consistent formulation," *International Journal of Plasticity*, vol. 130, p. 102705, 7 2020.

[6] U. M. Chaudry, T. H. Kim, S. D. Park, Y. S. Kim, K. Hamad, and J. G. Kim, "Effects of calcium on the activity of slip systems in AZ31 magnesium alloy," *Materials Science and Engineering: A*, vol. 739, pp. 289–294, 1 2019.

[7] M. Pekguleryuz, K. Kainer, and A. A. Kaya, *Fundamentals of Magnesium Alloy Metallurgy*. Elsevier Ltd., 2013.

[8] K. Nishino, "Development of fuel economy regulations and impact on automakers.," tech. rep., Mitsui Global Strategic Studies Institute Monthly Report, 3 2017.

[9] C. Satterfield and K. Schefter, "Electric vehicle sales and the charging infrastructure required through 2030," *Edison Electric Institute*, 6 2022.

[10] Z. Li, A. Khajepour, and J. Song, "A comprehensive review of the key technologies for pure electric vehicles," *Energy*, vol. 182, pp. 824–839, 9 2019.

[11] X. Zeng, M. Li, D. A. El-Hady, W. Alshitari, A. S. Al-Bogami, J. Lu, and K. Amine, "Commercialization of lithium battery technologies for electric vehicles," *Advanced Energy Materials*, vol. 9, 7 2019.

[12] B. Powell, P. Krajewski, and P. M. A.A. Luo, *Materials, Design and Manufacturing for Lightweight Vehicles (Second Edition)*. Woodhead Publishing, 2020.

[13] F. Czerwinski, "Current trends in automotive lightweighting strategies and materials," *Materials 2021, Vol. 14, Page 6631*, vol. 14, p. 6631, 11 2021.

[14] E. Aghion, B. Bronfin, and D. Eliezer, "The role of the magnesium industry in protecting the environment," *Journal of Materials Processing Technology*, vol. 117, pp. 381–385, 11 2001.

[15] M. K. Kulekci, "Magnesium and its alloys applications in automotive industry," *International Journal of Advanced Manufacturing Technology*, vol. 39, pp. 851–865, 2008.

[16] W. J. Joost and P. E. Krajewski, "Towards magnesium alloys for high-volume automotive applications," *Scripta Materialia*, vol. 128, pp. 107–112, 2 2017.

[17] W. Zhang and J. Xu, "Advanced lightweight materials for Automobiles: A review," *Materials & Design*, vol. 221, p. 110994, 9 2022.

[18] J. Song, J. She, D. Chen, and F. Pan, "Latest research advances on magnesium and magnesium alloys worldwide," *Journal of Magnesium and Alloys*, vol. 8, pp. 1–41, 3 2020.

[19] P. Mansoor and S. M. Dasharath, "Microstructural and mechanical properties of magnesium alloy processed by severe plastic deformation (SPD) – A review," *Materials Today: Proceedings*, vol. 20, pp. 145–154, 1 2020.

[20] J. Victoria-Hernández, S. Yi, D. Klaumünzer, and D. Letzig, "Comparison of the Mechanical Properties and Forming Behavior of Two Texture-Weakened Mg-Sheet Alloys Produced by Twin Roll Casting," *Frontiers in Materials*, vol. 6, pp. 1–11, 2019.

[21] M. R. Barnett, "Twinning and the ductility of magnesium alloys. part i: "tension" twins," *Materials Science and Engineering A*, vol. 464, pp. 1–7, 2007.

[22] C. S. Roberts, "The deformation of magnesium.," *Magnesium and Its Alloys*, pp. 81–107, 1964.

[23] B. C. Wonsiewicz and W. A. Backofen, "Plasticity of magnesium crystals," *Trans.TMS-AIME*, pp. 1422–1431, 1967.

[24] M. Niewczas, A. Kula, H. Kitahara, and S. Ando, "Dislocation distribution and patterning in $\langle a \rangle$-axis Mg single crystals during early compression," *Acta Materialia*, vol. 164, pp. 714–727, 2 2019.

[25] S. R. Agnew and Özgür Duygulu, "Plastic anisotropy and the role of non-basal slip in magnesium alloy AZ31B," *International Journal of Plasticity*, vol. 21, pp. 1161–1193, 6 2005.

[26] L. Y. Chen, L. Chai, and L. C. Zhang, "Editorial: Hexagonal close-packed metals and alloys: Processing, microstructure and properties," *Frontiers in Materials*, vol. 8, pp. 1–2, 2021.

[27] A. Orozco-Caballero, D. Lunt, J. D. Robson, and J. Q. da Fonseca, "How magnesium accommodates local deformation incompatibility: A high-resolution digital image correlation study," *Acta Materialia*, vol. 133, pp. 367–379, 2017.

[28] R. v. Mises, "Mechanik der plastischen formänderung von kristallen," *ZAMM-Journal of Applied Mathematics and Mechanics/Zeitschrift für Angewandte Mathematik und Mechanik*, vol. 8, no. 3, pp. 161–185, 1928.

[29] G. I. Taylor, "Plastic strain in metals," *J. Inst. Met.*, pp. 307–324, 1938.

[30] J. Koike, R. Ohyama, T. Kobayashi, M. Suzuki, and K. Maruyama, "Grain-Boundary Sliding in AZ31 Magnesium Alloys at Room Temperature to 523 K," *MATERIALS TRANSACTIONS*, vol. 44, pp. 445–451, 2003.

[31] M. H. Yoo, "Slip, twinning, and fracture in hexagonal close-packed metals," *Metallurgical Transactions A*, vol. 12, pp. 409–418, 1981.

[32] K. Sofinowski, T. Panzner, M. Kubenova, J. Čapek, S. V. Petegem, and H. V. Swygenhoven, "In situ tension-tension strain path changes of cold-rolled Mg AZ31B," *Acta Materialia*, vol. 164, pp. 135–152, 2019.

[33] M. W. Vaughan, W. Nasim, E. Dogan, J. S. Herrington, G. Proust, A. A. Benzerga, and I. Karaman, "Interplay between the effects of deformation mechanisms and dynamic recrystallization on the failure of Mg-3Al-1Zn," *Acta Materialia*, vol. 168, pp. 448–472, 2019.

[34] D. Hull and D. J. Bacon, *Introduction to Dislocations, Fifth Edition*. Elsevier, 1 2011.

[35] F. Kocks, C. Tomé, and H.-R. Wenk, *Texture and Anisotropy. Preferred Orientations in Polycrystals and Their Effect on Material Properties*. Cambridge University Press, 5 1998.

[36] J. Wang, I. J. Beyerlein, and C. N. Tomé, "An atomic and probabilistic perspective on twin nucleation in mg," *Scripta Materialia*, vol. 63, pp. 741–746, 10 2010.

[37] I. J. Beyerlein, L. Capolungo, P. E. Marshall, R. J. McCabe, and C. N. Tome, "Statistical analyses of deformation twinning in magnesium," *Philosophical Magazine*, vol. 90, pp. 2161–2190, 5 2010.

[38] P. Chen, F. Wang, J. Ombogo, and B. Li, "Formation of 60° $\langle 01\bar{1}0\rangle$ boundaries between $10\bar{1}2$ twin variants in deformation of a magnesium alloy," *Materials Science and Engineering: A*, vol. 739, pp. 173–185, 1 2019.

[39] A. Chapuis and J. H. Driver, "Temperature dependency of slip and twinning in plane strain compressed magnesium single crystals," *Acta Materialia*, vol. 59, pp. 1986–1994, 2011.

[40] M. A. Meyers, O. Vöhringer, and V. A. Lubarda, "The onset of twinning in metals: A constitutive description," *Acta Materialia*, vol. 49, pp. 4025–4039, 2001.

[41] J. Koike, "Enhanced deformation mechanisms by anisotropic plasticity in polycrystalline mg alloys at room temperature," *Metallurgical and Materials Transactions A: Physical Metallurgy and Materials Science*, vol. 36, pp. 1689–1696, 2005.

[42] S. R. Agnew, D. W. Brown, and C. N. Tomé, "Validating a polycrystal model for the elastoplastic response of magnesium alloy AZ31 using in situ neutron diffraction," *Acta Materialia*, vol. 54, pp. 4841–4852, 10 2006.

[43] H.-J. Bunge, *Texture Analysis in Materials Science*. Butterworth-Heinemann, 1982.

[44] Y. N. Wang and J. C. Huang, "Texture analysis in hexagonal materials," *Materials Chemistry and Physics*, vol. 81, pp. 11–26, 7 2003.

[45] M. Zhao, V. Kannan, and K. T. Ramesh, "The dynamic plasticity and dynamic

failure of a magnesium alloy under multiaxial loading," *Acta Materialia*, vol. 154, pp. 124–136, 2018.

[46] X. Huang, K. Suzuki, and N. Saito, "Textures and stretch formability of Mg-6Al-1Zn magnesium alloy sheets rolled at high temperatures up to 793 K," *Scripta Materialia*, vol. 60, pp. 651–654, 2009.

[47] H. Dieringa, "Influence of cryogenic temperatures on the microstructure and mechanical properties of magnesium alloys: A review," *Metals*, vol. 7, 2017.

[48] K. Zhang, J. H. Zheng, C. Hopper, C. Sun, and J. Jiang, "Enhanced plasticity at cryogenic temperature in a magnesium alloy," *Materials Science and Engineering: A*, vol. 811, p. 141001, 4 2021.

[49] D. Griffiths, "Explaining texture weakening and improved formability in magnesium rare earth alloys," *Materials Science and Technology (United Kingdom)*, vol. 31, pp. 10–24, 2015.

[50] N. Stanford, M. D. Callaghan, and B. de Jong, "The effect of rare earth elements on the behaviour of magnesium-based alloys: Part 1-Hot deformation behaviour," *Materials Science and Engineering A*, vol. 565, pp. 459–468, 2013.

[51] S. Sandlöbes, M. Friák, J. Neugebauer, and D. Raabe, "Basal and non-basal dislocation slip in Mg–Y," *Materials Science and Engineering A*, vol. 576, pp. 61–68, 2013.

[52] S. R. Agnew, L. Capolungo, and C. A. Calhoun, "Connections between the basal I1 "growth" fault and $\langle c+a \rangle$ dislocations," *Acta Materialia*, vol. 82, pp. 255–265, 1 2015.

[53] S. Sandlöbes, M. Friák, S. Zaefferer, A. Dick, S. Yi, D. Letzig, Z. Pei, L. F. Zhu, J. Neugebauer, and D. Raabe, "The relation between ductility and stacking fault energies in Mg and Mg-Y alloys," *Acta Materialia*, vol. 60, pp. 3011–3021, 2012.

[54] Y. Chino, X. Huang, K. Suzuki, and M. Mabuchi, "Enhancement of stretch formability at room temperature by addition of Ca in Mg-Zn alloy," *Materials Transactions*, vol. 51, pp. 818–821, 2010.

[55] S. R. Agnew, C. E. Dreyer, F. J. Polesak, W. V. Chiu, C. J. Neil, and M. Rodriguez, "Constitutive behavior of four wrought magnesium alloys under warm forming conditions," *Magnesium Technology*, pp. 159–164, 2008.

[56] M. Ghazisaeidi, L. G. Hector, and W. A. Curtin, "Solute strengthening of twinning dislocations in mg alloys," *Acta Materialia*, vol. 80, pp. 278–287, 11 2014.

[57] Z. Ding, W. Liu, H. Sun, S. Li, D. Zhang, Y. Zhao, E. J. Lavernia, and Y. Zhu, "Origins and dissociation of pyramidal dislocations in magnesium and its alloys," *Acta Materialia*, vol. 146, pp. 265–272, 3 2018.

[58] J. Wang, J. P. Hirth, and C. N. Tomé, "$(\bar{1}012)$ twinning nucleation mechanisms in hexagonal-close-packed crystals," *Acta Materialia*, vol. 57, pp. 5521–5530, 10 2009.

[59] R. Namakian and G. Z. Voyiadjis, "An atomic displacive model for $\{10\bar{1}2\}$ $\langle\bar{1}011\rangle$ twinning in hexagonal close packed metals with the emphasis on the role of partial stacking faults in formation of $\{10\bar{1}2\}$ twins," *Acta Materialia*, vol. 150, pp. 381–393, 5 2018.

[60] Q. Zu, X. Z. Tang, S. Xu, and Y. F. Guo, "Atomistic study of nucleation and migration of the basal/prismatic interfaces in mg single crystals," *Acta Materialia*, vol. 130, pp. 310–318, 5 2017.

[61] R. Namakian, G. Z. Voyiadjis, and P. Kwaśniak, "On the slip and twinning mechanisms on first order pyramidal plane of magnesium: Molecular dynamics simulations and first principal studies," *Materials & Design*, vol. 191, p. 108648, 6 2020.

[62] H. Fan, S. Aubry, A. Arsenlis, and J. A. El-Awady, "The role of twinning deformation on the hardening response of polycrystalline magnesium from discrete dislocation dynamics simulations," *Acta Materialia*, vol. 92, pp. 126–139, 6 2015.

[63] D. A. Wei, M. Zaiser, Z. Feng, G. Kang, H. Fan, and X. Zhang, "Effects of twin boundary orientation on plasticity of bicrystalline copper micropillars: A discrete dislocation dynamics simulation study," *Acta Materialia*, vol. 176, pp. 289–296, 9 2019.

[64] M. Yaghoobi, G. Z. Voyiadjis, and V. Sundararaghavan, "Crystal plasticity simulation of magnesium and its alloys: A review of recent advances," *Crystals*, vol. 11, p. 435, 4 2021.

[65] R. A. Lebensohn and C. N. Tomé, "A self-consistent anisotropic approach for the simulation of plastic deformation and texture development of polycrystals: Application to zirconium alloys," *Acta Metallurgica et Materialia*, vol. 41, pp. 2611–2624, 9 1993.

[66] P. A. Turner, C. N. Tomé, and C. H. Woo, "Self-consistent modelling of nonlinear visco-elastic polycrystals: An approximate scheme," *Philosophical Magazine A: Physics of Condensed Matter, Structure, Defects and Mechanical Properties*, vol. 70, pp. 689–711, 1994.

[67] J. Bishop and R. Hill, "A theoretical derivation of the plastic properties of a polycrystalline face-centred metal," *The London, Edinburgh, and Dublin Philosophical Magazine and Journal of Science*, vol. 42, pp. 1298–1307, 11 1951.

[68] A. Molinari, G. R. Canova, and S. Ahzi, "A self consistent approach of the large deformation polycrystal viscoplasticity," *Acta Metallurgica*, vol. 35, pp. 2983–2994, 12 1987.

[69] R. A. Lebensohn, Y. Liu, and P. Castañeda, "Macroscopic properties and field fluc-

tuations in model power-law polycrystals: full-field solutions versus self-consistent estimates," *Proc. R. Soc. Lond. A*, vol. 460, pp. 1381–1405, 2 2004.

[70] H. Abdolvand and A. J. Wilkinson, "Assessment of residual stress fields at deformation twin tips and the surrounding environments," *Acta Materialia*, vol. 105, pp. 219–231, 2 2016.

[71] F. Roters, P. Eisenlohr, L. Hantcherli, D. D. Tjahjanto, T. R. Bieler, and D. Raabe, "Overview of constitutive laws, kinematics, homogenization and multiscale methods in crystal plasticity finite-element modeling: Theory, experiments, applications," *Acta Materialia*, vol. 58, pp. 1152–1211, 2 2010.

[72] C. S. Hyun, M. S. Kim, S. H. Choi, and K. S. Shin, "Crystal plasticity fem study of twinning and slip in a mg single crystal by erichsen test," *Acta Materialia*, vol. 156, pp. 342–355, 2018.

[73] M. A. Kumar, I. J. Beyerlein, R. A. Lebensohn, and C. N. Tomé, "Role of alloying elements on twin growth and twin transmission in magnesium alloys," *Materials Science and Engineering: A*, vol. 706, pp. 295–303, 10 2017.

[74] S. H. Choi, D. W. Kim, B. S. Seong, and A. D. Rollett, "3-D simulation of spatial stress distribution in an AZ31 Mg alloy sheet under in-plane compression," *International Journal of Plasticity*, vol. 27, pp. 1702–1720, 10 2011.

[75] J. Zhang and S. P. Joshi, "Phenomenological crystal plasticity modeling and detailed micromechanical investigations of pure magnesium," *Journal of the Mechanics and Physics of Solids*, vol. 60, pp. 945–972, 5 2012.

[76] G. Sachs, "Plasticity problems i n metals."

[77] H. Mecking and U. F. Kocks, "Kinetics of flow and strain-hardening," *Acta Metallurgica*, vol. 29, pp. 1865–1875, 11 1981.

[78] C. N. Tomé and R. A. Lebensohn, *Material Modeling with the Visco-Plastic Self-Consistent (VPSC) Approach: Theory and Practical Applications*. Elsevier, 1 2023.

[79] C. Tome, G. R. Canova, U. F. Kocks, N. Christodoulou, and J. J. Jonas, "The relation between macroscopic and microscopic strain hardening in f.c.c. polycrystals," *Acta Metallurgica*, vol. 32, pp. 1637–1653, 10 1984.

[80] I. J. Beyerlein and C. N. Tomé, "A dislocation-based constitutive law for pure Zr including temperature effects," *International Journal of Plasticity*, vol. 24, pp. 867–895, 5 2008.

[81] A. L. Oppedal, H. E. Kadiri, C. N. Tomé, G. C. Kaschner, S. C. Vogel, J. C. Baird, and M. F. Horstemeyer, "Effect of dislocation transmutation on modeling hardening mechanisms by twinning in magnesium," *International Journal of Plasticity*, vol. 30-31, pp. 41–61, 3 2012.

[82] M. Knezevic, M. Zecevic, I. J. Beyerlein, J. F. Bingert, and R. J. McCabe, "Strain rate and temperature effects on the selection of primary and secondary slip and twinning systems in hcp zr," *Acta Materialia*, vol. 88, pp. 55–73, 4 2015.

[83] G. Proust, C. N. Tomé, and G. C. Kaschner, "Modeling texture, twinning and hardening evolution during deformation of hexagonal materials," *Acta Materialia*, vol. 55, pp. 2137–2148, 4 2007.

[84] C. N. Tomé, R. A. Lebensohn, and U. F. Kocks, "A model for texture development dominated by deformation twinning: Application to zirconium alloys," *Acta Metallurgica et Materialia*, vol. 39, pp. 2667–2680, 11 1991.

[85] R. A. Lebensohn and C. N. Tome, "Modelling twinning in texture development codes," *Textures and Microstructures*, vol. 14, pp. 959–964, 1991.

[86] R. A. Lebensohn and C. N. Tomé, "A self-consistent viscoplastic model: prediction of rolling textures of anisotropic polycrystals," *Materials Science and Engineering*, vol. 175, pp. 71–82, 1994.

[87] P. V. Houtte, "Simulation of the rolling and shear texture of brass by the taylor theory adapted for mechanical twinning," *Acta Metallurgica*, vol. 26, pp. 591–604, 4 1978.

[88] G. C. Kaschner, C. N. Tomé, I. J. Beyerlein, S. C. Vogel, D. W. Brown, and R. J. McCabe, "Role of twinning in the hardening response of zirconium during temperature reloads," *Acta Materialia*, vol. 54, pp. 2887–2896, 6 2006.

[89] D. W. Brown, S. R. Agnew, M. A. Bourke, T. M. Holden, S. C. Vogel, and C. N. Tomé, "Internal strain and texture evolution during deformation twinning in magnesium," *Materials Science and Engineering: A*, vol. 399, pp. 1–12, 6 2005.

[90] S. R. Agnew, M. H. Yoo, and C. N. Tomé, "Application of texture simulation to understanding mechanical behavior of mg and solid solution alloys containing li or y," *Acta Materialia*, vol. 49, pp. 4277–4289, 12 2001.

[91] S. R. Agnew, J. A. Horton, and M. H. Yoo, "Transmission electron microscopy investigation of $\langle c + a \rangle$ dislocations in Mg and α-solid solution Mg-Li alloys," *Metallurgical and Materials Transactions A: Physical Metallurgy and Materials Science*, vol. 33, pp. 851–858, 2002.

[92] E. Dogan, M. W. Vaughan, S. J. Wang, I. Karaman, and G. Proust, "Role of starting texture and deformation modes on low-temperature shear formability and shear localization of Mg–3Al–1Zn alloy," *Acta Materialia*, vol. 89, pp. 408–422, 5 2015.

[93] R. A. Lebensohn, M. Zecevic, M. Knezevic, and R. J. McCabe, "Average intragranular misorientation trends in polycrystalline materials predicted by a viscoplastic self-consistent approach," *Acta Materialia*, vol. 104, pp. 228–236, 2 2016.

[94] M. Zecevic, R. A. Lebensohn, R. J. McCabe, and M. Knezevic, "Modeling of intragranular misorientation and grain fragmentation in polycrystalline materials using the viscoplastic self-consistent formulation," *International Journal of Plasticity*, vol. 109, pp. 193–211, 10 2018.

[95] M. Zecevic, R. A. Lebensohn, R. J. McCabe, and M. Knezevic, "Modelling recrystallization textures driven by intragranular fluctuations implemented in the viscoplastic self-consistent formulation," *Acta Materialia*, vol. 164, pp. 530–546, 2 2019.

[96] K. J. Tam, M. W. Vaughan, L. Shen, M. Knezevic, I. Karaman, and G. Proust, "Modelling the temperature and texture effects on the deformation mechanisms of magnesium alloy AZ31," *International Journal of Mechanical Sciences*, vol. 182, p. 105727, 9 2020.

[97] V. M. Miller, T. D. Berman, I. J. Beyerlein, J. W. Jones, and T. M. Pollock, "Prediction of the plastic anisotropy of magnesium alloys with synthetic textures and implications for the effect of texture on formability," *Materials Science and Engineering: A*, vol. 675, pp. 345–360, 10 2016.

[98] V. M. Miller, T. D. Berman, I. J. Beyerlein, and T. M. Pollock, "Prediction of magnesium alloy formability: The role of texture," *Magnesium Technology*, pp. 257–262, 2016.

[99] W. Ren, R. Xin, J. Xu, B. Song, L. Zhang, and Q. Liu, "Effects of precipitate type on twin/slip activity in zk60 alloys and yield asymmetry," *Journal of Alloys and Compounds*, vol. 792, pp. 610–616, 7 2019.

[100] I. J. Beyerlein, R. A. Lebensohn, and C. N. Tomé, "Modeling texture and microstructural evolution in the equal channel angular extrusion process," *Materials Science and Engineering: A*, vol. 345, pp. 122–138, 3 2003.

[101] V. M. Miller, S. L. Semiatin, C. Szczepanski, and A. L. Pilchak, "Optimization of vpsc model parameters for two-phase titanium alloys: Flow stress vs orientation distribution function metrics," *Metallurgical and Materials Transactions A: Physical Metallurgy and Materials Science*, vol. 49, pp. 3624–3636, 8 2018.

[102] F. Bachmann, R. Hielscher, and H. Schaeben, "Texture Analysis with MTEX-Free and Open Source Software Toolbox," *Solid State Phenomena*, pp. 63–68, 2 2010.

[103] B. A. Begley and V. M. Miller, "Vampyr: A matlab-based toolset leveraging mtex for automating vpsc," *Integrating Materials and Manufacturing Innovation*, vol. 12, pp. 277–288, 12 2023.

[104] Q. Chen, L. Hu, L. Shi, T. Zhou, M. Yang, and J. Tu, "Assessment in predictability of visco-plastic self-consistent model with a minimum parameter approach: Numerical investigation of plastic deformation behavior of AZ31 magnesium alloy for various loading conditions," *Materials Science and Engineering: A*, vol. 774, p. 138912, 2 2020.

[105] J. Jain, W. J. Poole, and C. W. Sinclair, "The deformation behaviour of the magnesium alloy az80 at 77 and 293 k," *Materials Science and Engineering: A*, vol. 547, pp. 128–137, 6 2012.

[106] B. Hutchinson, J. Jain, and M. R. Barnett, "A minimum parameter approach to crystal plasticity modelling," *Acta Materialia*, vol. 60, pp. 5391–5398, 9 2012.

[107] S. J. Kim, Y. S. Lee, and D. Kim, "Analysis of formability of Ca-added magnesium alloy sheets at low temperatures," *Materials Characterization*, vol. 113, pp. 152–159, 3 2016.

[108] S. J. Park, H. C. Jung, and K. S. Shin, "Deformation behaviors of twin roll cast Mg-Zn-X-Ca alloys for enhanced room-temperature formability," *Materials Science and Engineering: A*, vol. 679, pp. 329–339, 1 2017.

[109] U. M. Chaudry, K. Hamad, and J. G. Kim, "Ca-induced Plasticity in Magnesium Alloy: EBSD Measurements and VPSC Calculations," *Crystals 2020, Vol. 10, Page 67*, vol. 10, p. 67, 1 2020.

[110] J. Victoria-Hernández, S. Yi, and D. Letzig, "Role of non-basal slip systems on the microstructure and texture development of ZXK-Mg alloy deformed in Plane Strain Compression at elevated temperature," *Scripta Materialia*, vol. 208, p. 114322, 2 2022.

[111] J. Blaber, B. Adair, and A. Antoniou, "Ncorr: Open-Source 2D Digital Image Correlation Matlab Software," *Experimental Mechanics*, vol. 55, pp. 1105–1122, 2015.

[112] J. Filik, A. W. Ashton, P. C. Chang, P. A. Chater, S. J. Day, M. Drakopoulos, M. W. Gerring, M. L. Hart, O. V. Magdysyuk, S. Michalik, A. Smith, C. C. Tang, N. J. Terrill, M. T. Wharmby, and H. Wilhelm, "Processing two-dimensional X-ray diffraction and small-angle scattering data in DAWN 2," *urn:issn:1600-5767*, vol. 50, pp. 959–966, 5 2017.

[113] D. M. Collins, M. Mostafavi, R. I. Todd, T. Connolley, and A. J. Wilkinson, "A synchrotron x-ray diffraction study of in situ biaxial deformation," *Acta Materialia*, vol. 90, pp. 46–58, 5 2015.

[114] S. Pawar, T. J. Slater, T. L. Burnett, X. Zhou, G. M. Scamans, Z. Fan, G. E. Thompson, and P. J. Withers, "Crystallographic effects on the corrosion of twin roll cast AZ31 Mg alloy sheet," *Acta Materialia*, vol. 133, pp. 90–99, 7 2017.

[115] R. Pei, Y. Zou, D. Wei, and T. Al-Samman, "Grain boundary co-segregation in magnesium alloys with multiple substitutional elements," *Acta Materialia*, vol. 208, p. 116749, 4 2021.

[116] S. Jo, D. Letzig, and S. Yi, "Effect of Al Content on Texture Evolution and

Recrystallization Behavior of Non-Flammable Magnesium Sheet Alloys," *Metals 2021, Vol. 11, Page 468*, vol. 11, p. 468, 3 2021.

[117] W. J. Delis, P. C. Huckfeldt, B. Hallstedt, P. L. Sun, D. Raabe, S. Korte-Kerzel, and S. Sandlöbes-Haut, "Influence of Al and Ca on the Ductility of Mg–Al–Ca Alloys," *Advanced Engineering Materials*, vol. 26, p. 2301071, 2 2024.

[118] S. M. Liang, R. S. Chen, J. J. Blandin, M. Suery, and E. H. Han, "Thermal analysis and solidification pathways of Mg–Al–Ca system alloys," *Materials Science and Engineering: A*, vol. 480, pp. 365–372, 5 2008.

[119] R. Pei, Y. Zou, M. Zubair, D. Wei, and T. Al-Samman, "Synergistic effect of Y and Ca addition on the texture modification in AZ31B magnesium alloy," *Acta Materialia*, vol. 233, p. 117990, 7 2022.

[120] M. Z. Bian, T. T. Sasaki, B. C. Suh, T. Nakata, S. Kamado, and K. Hono, "A heat-treatable Mg–Al–Ca–Mn–Zn sheet alloy with good room temperature formability," *Scripta Materialia*, vol. 138, pp. 151–155, 9 2017.

[121] T. Wang, J. J. Jonas, H. Qin, and S. Yue, "Effect of dynamic strain aging on the deformation and twinning behavior of a Mg–2Zn–2Nd alloy," *Materials Science and Engineering: A*, vol. 645, pp. 126–135, 10 2015.

[122] C. Corby, C. H. Cáceres, and P. Lukáč, "Serrated flow in magnesium alloy AZ91," *Materials Science and Engineering: A*, vol. 387-389, pp. 22–24, 12 2004.

[123] C. J. Neil and S. R. Agnew, "Crystal plasticity-based forming limit prediction for non-cubic metals: Application to Mg alloy AZ31B," *International Journal of Plasticity*, vol. 25, pp. 379–398, 3 2009.

[124] T. Naka, Y. Nakayama, T. Uemori, R. Hino, F. Yoshida, M. Kohzu, and K. Higashi, "FLD of AZ31 sheet under warm stretching and its prediction," *International Journal of Modern Physics B*, vol. 22, pp. 6010–6015, 12 2008.

[125] N. Stanford, I. Sabirov, G. Sha, A. L. Fontaine, S. P. Ringer, and M. R. Barnett, "Effect of al and gd solutes on the strain rate sensitivity of magnesium alloys," *Metallurgical and Materials Transactions A: Physical Metallurgy and Materials Science*, vol. 41, pp. 734–743, 3 2010.

[126] S. R. Agnew, C. N. Tomé, D. W. Brown, T. M. Holden, and S. C. Vogel, "Study of slip mechanisms in a magnesium alloy by neutron diffraction and modeling," *Scripta Materialia*, vol. 48, pp. 1003–1008, 4 2003.

[127] A. A. Luo, R. Shi, J. Miao, and T. Avey, "Review: Magnesium sheet alloy development for room temperature forming," *JOM*, vol. 73, pp. 1403–1418, 5 2021.

[128] A. Cottrell, "A note on the Portevin-Le Chatelier effect," *The London, Edinburgh, and Dublin Philosophical Magazine and Journal of Science*, vol. 44, pp. 829–832, 8 1953.

[129] J. M. Robinson and M. P. Shaw, "Microstructural and mechanical influences on dynamic strain aging phenomena," *https://doi.org/10.1179/imr.1994.39.3.113*, vol. 39, pp. 113–122, 1 1994.

[130] D. Wu, R. S. Chen, and E. H. Han, "Serrated flow and tensile properties of a Mg–Gd–Zn alloy," *Materials Science and Engineering: A*, vol. 532, pp. 267–274, 1 2012.

[131] S. M. Zhu, X. Gao, and J. F. Nie, "Strain burst in creep of Mg–1Ca–0.5Zn–0.6Zr alloy," *Materials Science and Engineering: A*, vol. 384, pp. 270–274, 10 2004.

[132] G. Garcés, P. Pérez, J. Medina, R. Barea, A. Gómez, J. García, and P. Adeva, "On the Influence of Precipitation on the Dynamic Strain Aging in Mg-2%Nd," *JOM*, vol. 75, pp. 2385–2396, 7 2023.

[133] X. Y. Fang, D. Q. Yi, and J. F. Nie, "The serrated flow behavior of Mg-Gd(-Mn-

Sc) alloys," *Metallurgical and Materials Transactions A: Physical Metallurgy and Materials Science*, vol. 40, pp. 2761–2771, 8 2009.

[134] K. Huang and R. E. Logé, "A review of dynamic recrystallization phenomena in metallic materials," *Materials & Design*, vol. 111, pp. 548–574, 12 2016.

[135] H. K. Zhang, H. Xiao, X. W. Fang, Q. Zhang, R. E. Logé, and K. Huang, "A critical assessment of experimental investigation of dynamic recrystallization of metallic materials," *Materials & Design*, vol. 193, p. 108873, 8 2020.

[136] K. J. Tam, M. W. Vaughan, L. Shen, M. Knezevic, I. Karaman, and G. Proust, "Modelling dynamic recrystallisation in magnesium alloy AZ31," *International Journal of Plasticity*, vol. 142, p. 102995, 7 2021.

[137] Y. Xiong, P. Karamched, C. T. Nguyen, D. M. Collins, C. M. Magazzeni, E. Tarleton, and A. J. Wilkinson, "Cold creep of titanium: Analysis of stress relaxation using synchrotron diffraction and crystal plasticity simulations," *Acta Materialia*, vol. 199, pp. 561–577, 10 2020.

[138] A. J. Wilkinson, G. Meaden, and D. J. Dingley, "High-resolution elastic strain measurement from electron backscatter diffraction patterns: New levels of sensitivity," *Ultramicroscopy*, vol. 106, pp. 307–313, 3 2006.

[139] A. J. Wilkinson, G. Meaden, and D. J. Dingley, "High resolution mapping of strains and rotations using electron backscatter diffraction," *Materials Science and Technology*, vol. 22, pp. 1271–1278, 11 2006.

[140] J. Jiang, T. B. Britton, and A. J. Wilkinson, "Mapping type iii intragranular residual stress distributions in deformed copper polycrystals," *Acta Materialia*, vol. 61, pp. 5895–5904, 9 2013.

[141] T. B. Britton and A. J. Wilkinson, "Measurement of residual elastic strain and

lattice rotations with high resolution electron backscatter diffraction," *Ultramicroscopy*, vol. 111, pp. 1395–1404, 7 2011.

[142] T. B. Britton and A. J. Wilkinson, "High resolution electron backscatter diffraction measurements of elastic strain variations in the presence of larger lattice rotations," *Ultramicroscopy*, vol. 114, pp. 82–95, 3 2012.

[143] Y. Mikami, K. Oda, M. Kamaya, and M. Mochizuki, "Effect of reference point selection on microscopic stress measurement using ebsd," *Materials Science and Engineering: A*, vol. 647, pp. 256–264, 10 2015.

[144] M. F. Ashby, "The deformation of plastically non-homogeneous materials," *Philosophical Magazine*, vol. 21, pp. 399–424, 1970.

[145] O. Muránsky, L. Balogh, M. Tran, C. J. Hamelin, J. S. Park, and M. R. Daymond, "On the measurement of dislocations and dislocation substructures using ebsd and hrsd techniques," *Acta Materialia*, vol. 175, pp. 297–313, 8 2019.

[146] D. Kuhlmann-Wilsdorf, "Theory of plastic deformation: - properties of low energy dislocation structures," *Materials Science and Engineering: A*, vol. 113, pp. 1–41, 7 1989.

[147] J. F. Nye, "Some geometrical relations in dislocated crystals," *Acta Metallurgica*, vol. 1, pp. 153–162, 3 1953.

[148] R. Armstrong, I. Codd, R. M. Douthwaite, and N. J. Petch, "The plastic deformation of polycrystalline aggregates," *Philosophical Magazine*, vol. 7, pp. 45–58, 1962.

[149] Y. Zhu, Y. Xiang, and K. Schulz, "The role of dislocation pile-up in flow stress determination and strain hardening," *Scripta Materialia*, vol. 116, pp. 53–56, 4 2016.

[150] J. Koike, T. Kobayashi, T. Mukai, H. Watanabe, M. Suzuki, K. Maruyama, and K. Higashi, "The activity of non-basal slip systems and dynamic recovery at room temperature in fine-grained AZ31B magnesium alloys," *Acta Materialia*, vol. 51, pp. 2055–2065, 2003.

[151] E. Song, M. T. Andani, and A. Misra, "Quantification of grain boundary effects on the geometrically necessary dislocation density evolution and strain hardening of polycrystalline Mg-4Al using in situ tensile testing in scanning electron microscope and HR-EBSD," *Journal of Magnesium and Alloys*, vol. 12, pp. 1815–1829, 5 2024.

[152] B. Raeisinia, S. R. Agnew, and A. Akhtar, "Incorporation of solid solution alloying effects into polycrystal modeling of Mg alloys," *Metallurgical and Materials Transactions A: Physical Metallurgy and Materials Science*, vol. 42, pp. 1418–1430, 5 2011.

[153] L. Jiang, J. J. Jonas, A. A. Luo, A. K. Sachdev, and S. Godet, "Influence of $\{10\bar{1}2\}$ extension twinning on the flow behavior of AZ31 Mg alloy," *Materials Science and Engineering: A*, vol. 445-446, pp. 302–309, 2 2007.

[154] F. Mokdad, D. L. Chen, and D. Y. Li, "Single and double twin nucleation, growth, and interaction in an extruded magnesium alloy," *Materials & Design*, vol. 119, pp. 376–396, 4 2017.

[155] S. H. Park, S. G. Hong, and C. S. Lee, "Activation mode dependent $\{10\bar{1}2\}$ twinning characteristics in a polycrystalline magnesium alloy," *Scripta Materialia*, vol. 62, pp. 202–205, 2 2010.

[156] Y. Jia, S. Jiang, J. Tan, Z. Lu, J. Jiang, and X. Wang, "The evolution of local stress during deformation twinning in a Mg-Gd-Y-Zn alloy," *Acta Materialia*, vol. 222, p. 117452, 1 2022.

[157] M. A. Kumar and I. J. Beyerlein, "Local microstructure and micromechanical stress

evolution during deformation twinning in hexagonal polycrystals," *Journal of Materials Research 2020 35:3*, vol. 35, pp. 217–241, 2 2020.

[158] M. A. Kumar, A. K. Kanjarla, S. R. Niezgoda, R. A. Lebensohn, and C. N. Tomé, "Numerical study of the stress state of a deformation twin in magnesium," *Acta Materialia*, vol. 84, pp. 349–358, 2 2015.

[159] M. A. Kumar, I. J. Beyerlein, and C. N. Tomé, "Effect of local stress fields on twin characteristics in hcp metals," *Acta Materialia*, vol. 116, pp. 143–154, 9 2016.

[160] A. Fitzner, D. G. Prakash, J. Q. D. Fonseca, M. Thomas, S. Y. Zhang, J. Kelleher, P. Manuel, and M. Preuss, "The effect of aluminium on twinning in binary alpha-titanium," *Acta Materialia*, vol. 103, pp. 341–351, 1 2016.

[161] N. Tahreen, D. L. Chen, M. Nouri, and D. Y. Li, "Influence of aluminum content on twinning and texture development of cast Mg–Al–Zn alloy during compression," *Journal of Alloys and Compounds*, vol. 623, pp. 15–23, 2 2015.

[162] B. Clausen, C. N. Tomé, D. W. Brown, and S. R. Agnew, "Reorientation and stress relaxation due to twinning: Modeling and experimental characterization for Mg," *Acta Materialia*, vol. 56, pp. 2456–2468, 6 2008.

[163] M. R. Barnett, Z. Keshavarz, A. G. Beer, and D. Atwell, "Influence of grain size on the compressive deformation of wrought Mg–3Al–1Zn," *Acta Materialia*, vol. 52, pp. 5093–5103, 10 2004.

[164] S. Jiang, Y. Jia, X. Wang, and J. Jiang, "Precise measurement of strain accommodation in a Mg-Gd-Y-Zn alloy using cross-correlation-based high resolution EBSD," *Materials Characterization*, vol. 165, p. 110384, 7 2020.

[165] J. W. Hutchinson, "Bounds and self-consistent estimates for creep of polycrystalline materials," *Proceedings of the Royal Society of London. A. Mathematical and Physical Sciences*, vol. 348, pp. 101–127, 2 1976.

[166] R. Hill, "The essential structure of constitutive laws for metal composites and polycrystals," *Journal of the Mechanics and Physics of Solids*, vol. 15, pp. 79–95, 3 1967.

[167] T. Mura, *Micromechanics of defects in solids*, vol. 3. Springer Netherlands, 1987.

[168] A. Molinari and L. S. Tóth, "Tuning a self consistent viscoplastic model by finite element results—i. modeling," *Acta Metallurgica et Materialia*, vol. 42, pp. 2453–2458, 7 1994.

[169] M. Knezevic, R. J. McCabe, C. N. Tomé, R. A. Lebensohn, S. R. Chen, C. M. Cady, G. T. Gray, and B. Mihaila, "Modeling mechanical response and texture evolution of α-uranium as a function of strain rate and temperature using polycrystal plasticity," *International Journal of Plasticity*, vol. 43, pp. 70–84, 4 2013.

[170] R. A. Lebensohn and C. N. Tomé, "A study of the stress state associated with twin nucleation and propagation in anisotropic materials," *Philosophical Magazine A: Physics of Condensed Matter, Structure, Defects and Mechanical Properties*, vol. 67, pp. 187–206, 1993.

[171] F. Lavrentev, "The type of dislocation interaction as the factor determining work hardening," *Materials Science and Engineering*, vol. 46, pp. 191–208, 12 1980.

[172] J. Shen, L. Zhang, L. Hu, W. Liu, A. Fang, Z. Yao, Y. Ning, L. Ren, and Y. Sun, "Towards strength-ductility synergy through a novel technique of multi-pass lowered-temperature drawing in AZ31 magnesium alloys," *Journal of Alloys and Compounds*, vol. 873, p. 159604, 8 2021.

[173] F. F. Lavrentev and Y. A. Pokhil, "Relation of dislocation density in different slip systems to work hardening parameters for magnesium crystals," *Materials Science and Engineering*, vol. 18, pp. 261–270, 4 1975.

[174] I. J. Beyerlein, R. J. McCabe, and C. N. Tomé, "Effect of microstructure on the nucleation of deformation twins in polycrystalline high-purity magnesium: A multi-scale modeling study," *Journal of the Mechanics and Physics of Solids*, vol. 59, pp. 988–1003, 5 2011.

[175] M. Ardeljan, I. J. Beyerlein, B. A. McWilliams, and M. Knezevic, "Strain rate and temperature sensitive multi-level crystal plasticity model for large plastic deformation behavior: Application to AZ31 magnesium alloy," *International Journal of Plasticity*, vol. 83, pp. 90–109, 8 2016.

[176] J. Bohlen, M. R. Nürnberg, J. W. Senn, D. Letzig, and S. R. Agnew, "The texture and anisotropy of magnesium–zinc–rare earth alloy sheets," *Acta Materialia*, vol. 55, pp. 2101–2112, 4 2007.

[177] M. R. Barnett, "Twinning and the ductility of magnesium alloys: Part ii. "contraction" twins," *Materials Science and Engineering: A*, vol. 464, pp. 8–16, 8 2007.

[178] A. S. Khan, A. Pandey, T. Gnäupel-Herold, and R. K. Mishra, "Mechanical response and texture evolution of AZ31 alloy at large strains for different strain rates and temperatures," *International Journal of Plasticity*, vol. 27, pp. 688–706, 5 2010.

[179] J. Balík, P. Dobroň, F. Chmelík, R. Kužel, D. Drozdenko, J. Bohlen, D. Letzig, and P. Lukáč, "Modeling of the work hardening in magnesium alloy sheets," *International Journal of Plasticity*, vol. 76, pp. 166–185, 1 2016.

[180] N. Chandola, R. K. Mishra, and O. Cazacu, "Application of the VPSC model to the description of the stress-strain response and texture evolution in AZ31 Mg for various strain paths," *Journal of Engineering Materials and Technology, Transactions of the ASME*, vol. 137, 10 2015.

[181] R. Shi, J. Miao, T. Avey, and A. A. Luo, "A new magnesium sheet alloy with

high tensile properties and room-temperature formability," *Scientific Reports 2020 10:1*, vol. 10, pp. 1–10, 6 2020.

[182] M. Yuasa, N. Miyazawa, M. Hayashi, M. Mabuchi, and Y. Chino, "Effects of group II elements on the cold stretch formability of Mg–Zn alloys," *Acta Materialia*, vol. 83, pp. 294–303, 1 2015.

[183] F. Guo, D. Zhang, H. Wu, L. Jiang, and F. Pan, "The role of Al content on deformation behavior and related texture evolution during hot rolling of Mg-Al-Zn alloys," *Journal of Alloys and Compounds*, vol. 695, pp. 396–403, 2 2017.

[184] P. G. McCormigk, "A model for the portevin-le chatelier effect in substitutional alloys," *Acta Metallurgica*, vol. 20, pp. 351–354, 3 1972.

[185] A. V. D. Beukel, "On the mechanism of serrated yielding and dynamic strain ageing," *Acta Metallurgica*, vol. 28, pp. 965–969, 7 1980.

[186] H. E. Kadiri, C. D. Barrett, J. Wang, and C. N. Tomé, "Why are $\{101\bar{}2\}$ twins profuse in magnesium?," *Acta Materialia*, vol. 85, pp. 354–361, 2 2015.

[187] I. Chelladurai, D. Adams, D. T. Fullwood, M. P. Miles, S. Niezgoda, I. J. Beyerlein, and M. Knezevic, "Modeling of trans-grain twin transmission in AZ31 via a neighborhood-based viscoplastic self-consistent model," *International Journal of Plasticity*, vol. 117, pp. 21–32, 6 2019.

[188] H. Wang, P. D. Wu, C. N. Tomé, and J. Wang, "Study of lattice strains in magnesium alloy AZ31 based on a large strain elastic-viscoplastic self-consistent polycrystal model," *International Journal of Solids and Structures*, vol. 49, pp. 2155–2167, 8 2012.

[189] S. Kaboli and P. C. Burnley, "In-situ synchrotron X-ray diffraction deformation and EPSC modeling of AZ31 Mg alloy," *Materials Science and Engineering: A*, vol. 739, pp. 99–104, 1 2019.

[190] M. Zecevic, M. Knezevic, I. J. Beyerlein, and C. N. Tomé, "An elasto-plastic self-consistent model with hardening based on dislocation density, twinning and de-twinning: Application to strain path changes in hcp metals," *Materials Science and Engineering: A*, vol. 638, pp. 262–274, 6 2015.

[191] D. Steglich and Y. Jeong, "Texture-based forming limit prediction for Mg sheet alloys ZE10 and AZ31," *International Journal of Mechanical Sciences*, vol. 117, pp. 102–114, 10 2016.

[192] C. J. Newton and H. C. Vacher, "Correlation of polarized light phenomena with the orientation of some metal crystals," *Journal of Research of the National Bureau of Standards*, vol. 53, p. 1, 1954.

[193] K. W. Jin and M. D. Graef, "c-axis orientation determination of α-titanium using Computational Polarized Light Microscopy," *Materials Characterization*, vol. 167, p. 110503, 2020.

[194] B. Yin, Z. Wu, and W. A. Curtin, "Comprehensive first-principles study of stable stacking faults in hcp metals," *Acta Materialia*, vol. 123, pp. 223–234, 1 2017.